UNIVERSITY OF SOUTHAMPTON

FACULTY OF ENGINEERING, SCIENCE & MATHEMATICS

School of Engineering Sciences

Photodetector Calibration for Solar SXR and UV Dose Measurement for Correlation with Materials Degradation on the International Space Station

by

Duncan N.O. Goulty

Thesis submitted in satisfaction of the requirements for the degree of Doctor of Philosophy

May 2007

UNIVERSITY OF SOUTHAMPTON

ABSTRACT

FACULTY OF ENGINEERING, SCIENCE & MATHEMATICS

SCHOOL OF ENGINEERING SCIENCES

Doctor of Philosophy

PHOTODETECTOR CALIBRATION FOR SOLAR SXR AND UV DOSE MEASUREMENT FOR CORRELATION WITH MATERIALS DEGRADATION ON THE INTERNATIONAL SPACE STATION

by Duncan Neil Ormiston Goulty

Silicon and Aluminium Gallium Nitride photodetectors have been calibrated for use on the Southampton Transient Oxygen and Radiation Monitor (STORM), part of the Materials Exposure and Degradation Experiment on the European Technology Exposure Facility. The detectors will monitor the Solar SXR and UV dose levels over a period of three years while situated in Low Earth Orbit (LEO) on the International Space Station.

Calibration of the detectors included measuring their spectral responsivity, spectral transmission of filters, sensitivity to electron bombardment, sensitivity to angle of incidence of electromagnetic radiation, proportionality of response to electromagnetic radiation and ability to withstand launch-simulating vibration loads. With respect to the AlGaN detectors this calibration represents novel work and, consequently, the design and development of the STORM instrument suite represents a unique engineered structure for the application of LEO environment monitoring.

Additional material includes: literature reviews of space materials exposure research, Solar generation of SXR and UV, previous spacecraft usage of SXR and UV detectors for Solar dose monitoring, and the development of AlGaN photodiodes; and a discussion involving the expected behaviour of the detectors on-orbit, potential sources of interference with possible mitigation strategies, and predictions of the amount of data to be returned throughout the mission.

Contents

Tables of Figures

Acknowledgements

I would like to acknowledge the following people for their help towards the work carried out for this thesis:

My supervisor and STORM PI, Steve Gabriel, for his guidance and consultation throughout the Ph.D.

The other STORM team members, Graham Roberts, Alan Chambers, Neil Ross and Carl White who combined to make the project such a success.

Marc van Eesbeek, Barry Dunn, Adrian Tighe and Stan Heltzel of ESTEC for allowing and helping me to use the SORASI facility and other varied equipment within the Material Division laboratories.

Gerhard Ulm, Mathias Richter, Frank Scholze, and Michael Krumrey of PTB for carrying out the absolute spectral responsivity measurements on the detectors to my specifications at the BESSY II beamline facility.

Tim Stevenson of Leicester University for his design consultation in the early stages of the project.

The administration and workshop staff of the Astronautics Group and the School of Engineering Sciences for their behind-the-scenes support.

My colleagues in the Astronautics Group offices who made the difficult times bearable.

Last but by no means least my family and my girlfriend, Naomi Neoh, for their unwavering support, love and understanding over the past seven long years.

1 Introduction

The study of the orbital environment and its effects on spacecraft materials is of crucial importance to the design and longevity of space vehicles. However, gathering comprehensive, detailed analyses of degradation effects on-orbit is difficult, costly and usually of secondary importance to other scientific, commercial or military goals. With the duration of spaceflights constantly increasing, the huge costs of long-term missions and developing capabilities in other areas of spacecraft design, this situation is changing and on-orbit materials research is becoming ever more important.

This thesis describes the research and experimentation carried out towards the aim of calibrating and characterising the aluminium gallium nitride (AlGaN) and silicon (Si) photodetectors chosen for use on the Southampton Transient Oxygen and Radiation Monitor (STORM), a Low Earth Orbit (LEO) environment monitor, that will be placed on to the International Space Station (ISS) in late 2007 or early 2008 (depending on the U.S. Shuttle launch manifest for flight 1E).

The thesis is divided into three main sections: a literature review that endeavours to ascertain the contribution that this current research will provide, placing the STORM instrument and, in particular, the radiation detectors within the framework of current research and development; a description of the experimental work and results; and a discussion that explains how the results found will impact on-orbit operations and the ability of the radiation detectors to achieve their stated aims.

An overview of the STORM mission plus its situation on the ISS is provided later in this introduction, along with an explanation for the choice of radiation detectors picked to be included on the instrument.

The absolute calibration of the detectors has been carried out at the Physikalisch Technische Bundesanstalt (PTB) synchrotron facilities in Berlin, by way of spectral responsivity measurements from exposure to monochromatic radiation. The results and primary analysis of this data are presented within this thesis.

The characterisation of the detectors to other expected effects while on orbit has been mainly carried out at the Material Division of the European Spacecraft Technology Research Centre (ESTEC). This work includes exposure of the detectors to high flux soft x-ray (SXR), ultraviolet (UV), and electron sources. Other characterisation took the form of measurements regarding the angle of incidence response, linearity of response, plus checks on dark current that includes the amplifier offset that is integral to the circuit construction for the radiation detectors within the STORM module.

The novelty of the thesis revolves around the utilisation of the radiation detectors of STORM within a state-of-the-art materials exposure experiment and the characterisation of AlGaN for use as a space-based detector. The design of the STORM radiation detectors provides a low cost, power and mass system to monitor specific elements of the LEO environment and correlate these observations against others made by the remaining detectors onboard STORM and MEDET. Such novel, coordinated measurements aim to shed light on the various interactions between different environmental elements, such as the proposed SXR-enhanced degradation of polymer coatings and the synergistic effect of VUV and Atomic Oxygen (AO) degradation.

To this end a literature review of previous materials exposure experiments and UV detectors used in space to date has been provided, to demonstrate that this flight will be the first to use AlGaN detector technology and this specific combination of measurements within a novel materials exposure application. A literature review of the development of III-V semiconductor detectors has also been provided to emphasise the very recent emergence of this technology and the exploitation of its capabilities.

Lastly, the conclusions summarise the results and the main factors highlighted in the discussion that will have a significant impact on in-flight operations, together with proposed alterations to future versions of the STORM radiation detectors and directions in which this research can be developed.

1.1 The STORM Project

The Low Earth Orbit (LEO) environment is of great significance to spacecraft design considering that orbiters have to survive within this environment, yet not be over-engineered to keep development costs at a minimum. Detailed knowledge of this environment is therefore required to help produce adequate spacecraft design requirements and accurate simulation facilities for pre-flight ground testing of hardware.

As part of the Materials Exposure and Degradation Experiment on the European Technology Exposure Facility (MEDET on EuTEF) the Southampton Transient Oxygen and Radiation Monitor (STORM) aims to provide continuous detection of the SXR and UV flux (one measurement taken from each detector every three seconds), and periodic AO flux and fluence measurements (one data set captured every 24 hours) throughout the 3-year life-time of the mission. These major elements of the LEO environment are significant singular, and possibly synergistic, causes of degradation to delicate optical and polymer components on the exterior of spacecraft[1,2,3].

The MEDET design team provided the top-level requirements for the STORM unit (mass/power/size limits, data rates, survival limits for vibration launch loads and depressurisation) whilst the development, production and testing of the instruments themselves was the responsibility of the University of Southampton team.

The following sections describe the STORM mission in detail, with specific consideration given to the trade-offs in design of the instrumentation and highlighting the areas of research undertaken, for this thesis, to prepare the unit for spaceflight. In addition, an overview of the Monitor's position in the MEDET and EuTEF hierarchy is provided so that STORM can be seen in context with the complimentary instruments it will operate alongside.

1.1.1 Historic Project Overview

The University of Southampton was accepted into the MEDET program after responding to an announcement of opportunity from the European Space Agency (ESA) in 1999. The STORM module was the next logical step from earlier spaceflight hardware that was included on the Space Technology Research Vehicle (STRV) 1a[4] and 1c missions. Building on ten years of experience in the field of AO instrument construction and testing, the addition of radiation detectors would enable an opportunity to measure proposed synergistic degradation effects between radiation and AO environmental components.

Once Phase A studies for STORM were complete an Engineering and Physical Sciences Research Council (EPSRC) grant was awarded in 2001 to continue the design, construction, testing and delivery of the module for inclusion on MEDET. After almost four years of work by an inter-disciplinary team at Southampton, the STORM module was successfully delivered to ESA in December 2003, having met all of the design requirements. The laboratory work carried out for this thesis ran concurrent with the STORM development, construction and testing and continued up until December 2004 with submission of the final data analysis in September 2006.

1.2 The International Space Station

Currently under construction in LEO, the ISS will be the largest and most expensive manned space structure yet built. Sixteen nations are involved in its development and utilisation, including France, Holland, Italy and the UK, which are the member states directly involved with the design and construction of MEDET. Due to be complete by 2010, the ISS will provide a valuable orbiting laboratory capable of carrying out research across a number of academic disciplines.

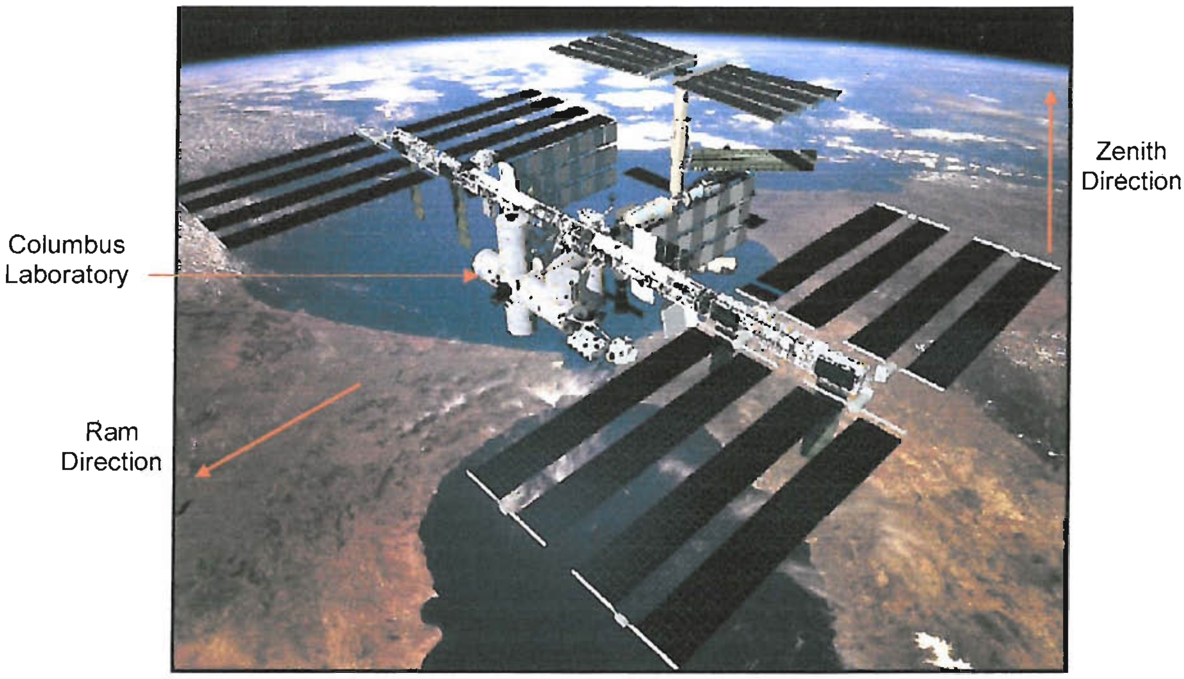

Figure 1: The International Space Station

The ISS orbits at a 51.6° inclination at an altitude of 370-460km[5] (mean altitude decreases due to atmospheric drag, requiring periodic thruster firing to return to a higher orbit to avoid re-entry). All measurements will therefore take place within LEO, under the Van Allen radiation belts but within the high-density plasma environment of the ionosphere. The ISS is Earth-centred so that one side (ram) always faces in the direction of travel and another (nadir) always faces towards the Earth. This generates a constantly changing viewing angle of the Sun for fixed instruments such as STORM. A number of important factors arise as a result, the primary one being that monitoring of the Sun is periodic depending on the ISS' orbital position and the orientation of its orbital plane with the ecliptic. These factors, that directly affect the data recorded by the radiation detectors on STORM, will be discussed in more detail later.

The time of launch will have some impact on the measurements recorded by STORM due to the level of solar activity. At solar maximum it is expected that the greater frequency of flares will produce a larger variation in SXR and Lyman-α data, and the generally higher levels of radiation will provide a stronger UV signal. The amount of AO will also be increased due to the higher levels of radiation dissociating more oxygen atoms from their molecules in the upper atmosphere.

At present, it appears that STORM will operate in a period leading up to the next solar maximum, forecast for 2011[6]. If so, it is expected that the amount of variation in the data caused by solar activity will increase as the mission progresses.

The UK is involved with the exploitation of the unmanned operations on board the ISS. This includes the MEDET project that will operate autonomously at its external location with only ground telemetry affecting its operation.

1.3 The Low Earth Orbit Environment

The LEO environment, within which the ISS will reside, is of great importance to the space industry as it is the primary repository for spacecraft, being the lowest and therefore most easily accessed orbit. Far from being a featureless vacuum, the LEO environment contains many elements that erode and degrade exposed materials on spacecraft outer surfaces. Provided here is a short summary of these different elements, more in-depth discussions can be found in other material noted in the bibliography. The relevance of these different environmental elements to the STORM mission is discussed in much greater detail in Section 5.3.

1.3.1 Ambient Pressure

The extremely low ambient pressure of the LEO environment (~0.3Pa at 100km altitude in comparison to 1MPa at sea level – essentially a vacuum) is the major environmental factor that enables the exotic reaction and degradation effects to occur that are so different from ground-based ones. The low pressure enables particles to have high thermal velocities (~1km/s) due to increased mean free paths, although this is small compared with the speed of orbiting craft (~8km/s).

In addition the tenuous atmosphere allows the penetration of greater levels of electromagnetic radiation and enables out-gassing of volatile substances from exposed surfaces (that in turn can contaminate other parts of the spacecraft).

1.3.2 Neutral Particles

The altitude band 100-550km is described as the Thermosphere of the Earth's atmosphere, a region of increased temperature (~770K) due to the high rates of absorption of incident solar electromagnetic radiation by the tenuous neutral atmosphere. Electrically neutral particles make up the majority of particulate species that are resident in this region. At the ISS' nominal 400km altitude the approximate abundances[7] of the major constituents at solar maximum are, in descending order: atomic oxygen ($10^{14}m^{-3}$); molecular nitrogen ($10^{13}m^{-3}$); helium ($10^{13}m^{-3}$); molecular oxygen ($3 \times 10^{11}m^{-3}$); and hydrogen ($10^{11}m^{-3}$).

Atomic oxygen (AO) is the most important of these constituents, not only due to it having the highest abundance but also due to its high chemical reactivity. It is this feature of the LEO environment that is of critical importance to material degradation, and the study of the processes with which AO attacks materials is of singular importance to the detection of other contributing factors such as the VUV and SXR flux.

1.3.3 Charged Particles

In addition to the neutral species of particles present in LEO, there is also a significant population of charged particles that interact with orbiting objects. The charged particles are generated by the photo-dissociation of a proportion of the neutral atoms and molecules present, the proportion being dependent on the solar UV flux that supplies the energy for ionisation. For a nominal 400km altitude, within the ionosphere (that overlaps the thermosphere, noted above), the plasma density varies between $3 \times 10^{10}m^{-3}$ and $2 \times 10^{12}m^{-3}$, depending on whether the ISS is in view of the Sun and the level of activity of the Sun itself.

A further major source is from the solar wind where charged particles are swept up by Earth's magnetic field and restricted to the regions known as the Van Allen radiation belts. There are only two situations where this source has a significant impact on LEO spacecraft with high orbital inclinations. The first is the increased flux due to the South Atlantic Anomaly where the trapped radiation is closer to

Earth due to the asymmetry of the geomagnetic field[8]. The second is a more variable phenomenon associated with increased solar wind production during solar storms. In such situations the Earth's magnetic field on the far side from the Sun becomes compressed due to the increased dominance of the solar magnetic field and the trapped plasma within the Van Allen belts is forced towards the Earth. This plasma surge then splits as the excess protons drift counter to the Earth's rotation whilst the electrons drift in the same direction to the Earth's rotation. The higher velocity of the electrons generates the adverse conditions as any charging effects cannot be as rapidly neutralised by the slower motion of protons and ions. During such geomagnetic events it is thus noted that more charging incidents occur between the midnight and 6am position of a spacecraft's orbit as they encounter this surge of electrons in the Earth's umbra.

The final source of charged particle radiation is in the form of cosmic rays. These have little impact on surface material properties and degradation due to their extremely low flux and ability to penetrate deep within materials. This is an issue for electronic systems on-orbit, but the effects on degradation are negligible compared to the factors above.

However, the flux of charged particles on to spacecraft surfaces is still far lower than the flux of AO due to the lower plasma density levels (the plasma density can never be higher than the neutral particle density as the plasma relies on the neutral particle population for its generation). Due to the most dominant neutral particle species being atomic oxygen, the most dominant ion in LEO is singly-charged oxygen that has similar degradation properties to AO. From a perspective of chemical degradation in LEO, oxygen is the major factor, eclipsing effects from other neutral and charged particle species.

Ion and electron impacts are important for differential charging of structures on-orbit that can lead to degradation through electric discharge. But for the LEO environment where the Debye length of the plasma is on the order of ~1cm, the instrumentation used will be effectively insulated by the plasma from surrounding objects at markedly different potentials and thus the threat of arcing causing significant damage/degradation is negligible.

1.3.4 Micrometeoroids and Orbital Debris

Alongside the atomic and molecular constituents of the LEO environment there are comparably larger particles that can cause degradation and erosion to surfaces through impact. These particles, being in the range from nanograms to grams, are split into two distinct groups: micrometeoroids are the remnants of dust from earlier asteroid and larger Solar System body impacts that pervades interplanetary space; and orbital debris are the ejecta from man-made operations in space due to rocket exhausts, grinding associated with the interaction of mechanical components, spacecraft impacts, and explosions, both designed and accidental. For LEO the frequency of spacecraft operations has massively increased the amount of man-made debris on-orbit to a level where it rivals and, in some size ranges, surpasses the micrometeoroid flux.

Impact velocities for micrometeoroids can range from 11 - 72km/s, averaging at approximately 19km/s, whereas orbital debris has an average impact velocity of the order of ~8km/s.

The effect of debris impacts is different from other orbital environment elements in that it is mechanical rather than chemical. It is the kinetic energy imparted by the impact that causes cratering, spallating and puncturing of exposed surfaces.

1.3.5 Electromagnetic Radiation

The prominent source of electromagnetic radiation in LEO is the Sun, although there are secondary sources such as Earth albedo and astronomical objects that are significant at certain wavelengths.

To the subject of material degradation only a narrow band of electromagnetic energies are of interest – those that are high enough to affect the atomic/molecular structure of exposed materials while being low enough to be predominantly absorbed. This range is from a few electron-volts, the ultraviolet, up to a few tens of thousands of electron-volts, the x-ray. The UV region of the solar spectrum has an irradiance of approximately 14 W/m^2 in LEO, compared with only a few mW/m^2 for the x-ray region. The UV region changes relatively little during the solar cycle, it fluctuates by approximately 10% at longer wavelengths (200-380nm) but can vary by up to 100% at and below the Lyman-α region (121.6nm). In contrast, the x-ray region, particularly soft x-rays from 1-10keV can change intensity over four or more orders of magnitude during high-energy solar events such as flares.

The study of these regions of the electromagnetic spectrum is of primary importance to the research carried out for this thesis. Not only does electromagnetic radiation affect materials directly, but it has also been found to act synergistically with AO attack to enhance degradation. This is a major issue for the current understanding of material degradation effects in LEO as no in-depth correlation between UV flux, x-ray flux, AO flux and rate of degradation of material samples has yet been actively monitored by a space-borne instrument. This issue will be discussed in further detail in Section 2.1.

The only remaining aspect of the LEO environment is the very high energy gamma radiation that is generated by extra-solar sources. Similar to particulate cosmic rays, these have little impact on surface material properties and degradation due to their extremely low flux and ability to penetrate deep within materials.

1.4 The European Technology Exposure Facility (EuTEF)

The European Technology Exposure Facility (EuTEF) is a Columbus External Payload Adapter (CEPA), a platform on which up to six experiments can be placed containing various instruments, mounted on the outside of the Columbus laboratory module. Originally, EuTEF was planned to be located on the zenith-outboard position on the S3 truss segment of the main boom of the ISS, as part of the Expedite the Processing of Experiments to Space Station (EXPRESS) pallet system. However, after changes to the construction schedule of the main space station elements, it is now planned to install EuTEF on the Columbus External Payload Facility (CEPF) at the zenith outboard (starboard facing) connection position (CEPF ExPA-XO) on the alternative CEPA carrier. Such a change in location has had some significant impact on the development of the Southampton instrument package, although little impact on the quality or amount of data that is expected to be returned.

EuTEF contains a variety of experimental platforms that are directly exposed to the LEO environment. The operation of these units is fully automated and so requires no intervention or monitoring by the onboard crew. Data and new command instructions are relayed directly to and from ground control.

EuTEF will be launched to the ISS in the near future, possibly at the end of 2007 but more probably in the first half of 2008. Due to the change in location from the S3 truss, EuTEF is currently scheduled for launch to the ISS on National Space Transportation System (NSTS) flight 1E to accompany the Columbus module. With EuTEF's planned operational lifetime of 3 years, MEDET and STORM will be operational for the period of approximately late 2007 to late/early 2010/2011. This, fortuitously, coincides with the run up to Solar maximum, as mentioned above, and should maximise the amount of pertinent data relating to materials degradation due to Solar radiation – the higher average flux of radiation from the Sun and the more frequent extreme flux changes due to active flare events will generate degradation that is more obvious than during the more quiet Solar conditions during the minimum of the solar-cycle.

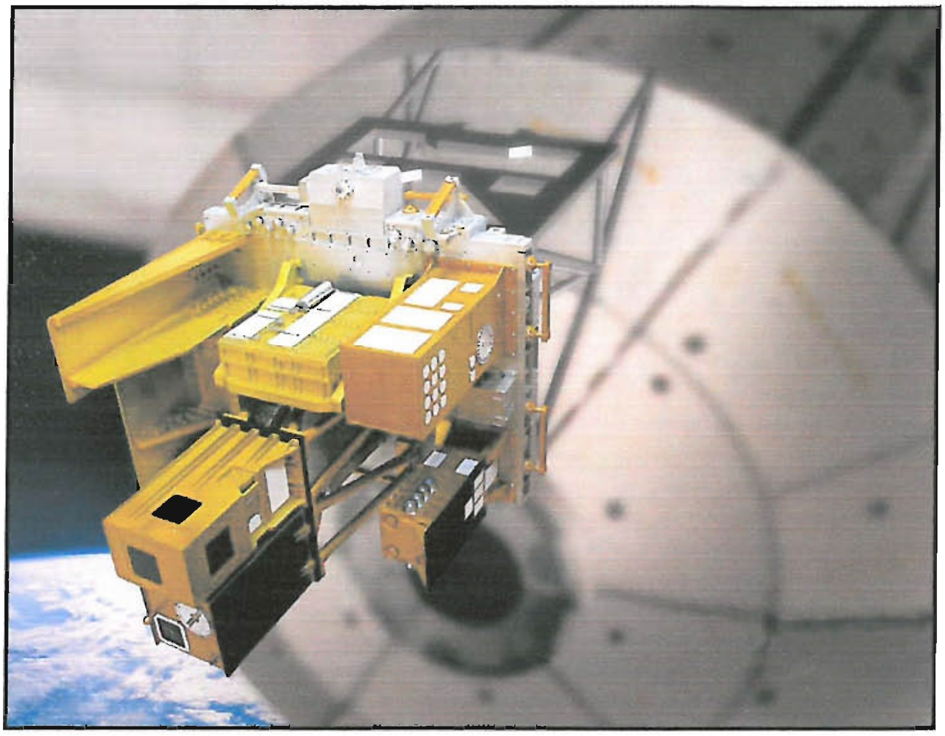

Figure 2: EuTEF on the starboard face of the Columbus Module[9]

EuTEF will be delivered to the ISS along with the Columbus Laboratory payload and one or more further CEPA platforms. Columbus will be attached to the ISS first before the CEPAs are manoeuvred from the Shuttle payload bay to their respective external positions. At the end of the mission the CEPAs will be 'swapped-out' for new platforms and the old ones will potentially be returned to Earth for post-flight analysis (this is an especially important step for materials experiments, such as MEDET, as it will allow post-flight calibration to reduce the impact of accumulated measurement errors caused by degradation throughout the mission). However, it is unfortunate that due to continuing budget concerns with the Shuttle programme and the strong possibility that no further flights will be made after the final ISS construction mission, the return of hardware has not yet been confirmed.

One of the experiments contained within EuTEF is MEDET.

1.5 The Materials Exposure and Degradation Experiment on EuTEF (MEDET)

MEDET is a project run jointly between the European Technology Research Centre (ESTEC), the Centre National d'Études Spatiales (CNES), the Office National d'Études et de Recherches Aérospatiales (ONERA), and the University of Southampton. Involvement with other bodies most notably includes the EuTEF integrators: Carlo Gavazzi Space.

As its name suggests, MEDET will be used primarily to monitor the degradation effects of the exposed LEO environment on a selection of materials. Included in the study will be measurements of optical and thermo-optical properties, molecular contamination of optical windows, and micro-particle debris flux dynamics.

Due to the on-orbit orientation of the ISS, the instrumentation of MEDET will be constantly facing into the direction of travel. Therefore, debris, charged particle and atmospheric species (including atomic oxygen) fluxes on to the detectors will be approximately constant throughout the mission lifetime (i.e. they will fluctuate only with changing environmental conditions, rather than changes in the ISS' attitude), allowing for a maximum return of data concerning these components of the environment.

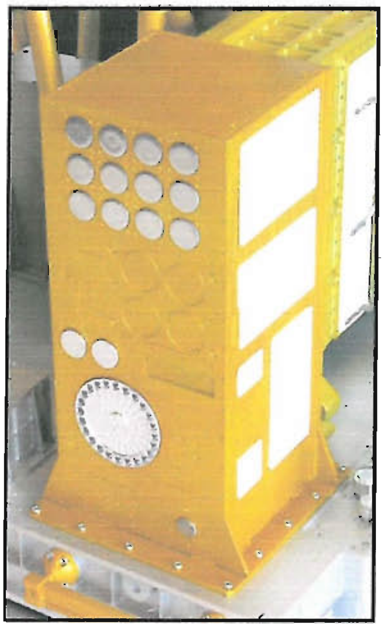

Figure 3: The MEDET module on EuTEF

The detailed analysis of such data will allow more accurate modelling of the performance of materials to be made available to future spacecraft designers. The pay-off from this data will be that spacecraft can be built to more accurate specifications, allowing designers to include less over-engineering. It will also allow designers to recognise more malignant environmental circumstances on orbit and take steps to protect vulnerable surfaces during such times. The resultant savings of money and effort for future spacecraft manufacture and the prolonged longevity of the spacecraft themselves will have a positive effect on the industry.

The other benefit to spacecraft design will be the scope of the measurements undertaken. By recording so many different variables MEDET will hopefully be able to analyse the different synergistic effects that occur between atmospheric particles (predominantly atomic oxygen) and Solar electromagnetic radiation (predominantly SXR and UV) in LEO. The analysis will allow designers to take into account degradation of this nature, plus it will demonstrate which are the most important environmental factors, with respect to synergistic effects, that then should be included as a priority in future ground-based testing facilities.

In addition, some new technologies that are new to space-based applications will be flown to evaluate their performance on orbit.

The instruments being included on MEDET are as follows:

- Orbital System for Active Detection of Debris (SODAD): will study micrometeoroids and dust particles using Metal-Oxide-Semiconductor components to detect discharge caused by impacting material.
- Quartz Crystal Microbalance (QCM): will study the temperature, atomic oxygen (AO) erosion, and the amount of deposited contamination by measuring the frequency generated across the solid-state detection component.
- Transmission Spectrometer: will study the degradation of a number of materials housed within a rotating wheel via spectrometric analysis. The spectrometer will be used in conjunction with sun-pointing detectors to increase the accuracy of the received data.
- Pressure Gauge: will measure the residual pressure around EuTEF using the Penning principle across a cold cathode.
- Microcalorimeters: will study the thermal heat balance of various materials using direct temperature measurements to discern the degradation of the thermo-optical characteristics of the test subjects.
- Aerogel: will passively collect micrometeoroids and dust particles for ground analysis.
- Zinc Oxide (ZnO) Detectors: will monitor the flux of AO by the increase in resistance of regenerated Zinc Oxide films when exposed to AO.
- Carbon Detectors: will monitor the accumulated AO fluence by the increase in resistance of the Carbon films as they erode throughout the mission.

- X-ray Detectors: will monitor the Solar soft X-ray flux using silicon photodiodes.
- UV Detectors: will monitor the Solar UV flux using Aluminium Gallium Nitride photodetectors.

Contained within the Southampton instrument package are the ZnO and Carbon atomic oxygen detectors, and the soft X-ray and UV detectors.

For a more detailed overview of the MEDET experiment please refer to Dinguirard et al.[10]

1.6 The Southampton Transient Oxygen and Radiation Monitor (STORM)

The Southampton instrument package is required as a complement to the other material-monitoring instruments onboard MEDET. It is an environment monitor for three sources of degradation in LEO: soft X-rays, UV-C and atomic oxygen. The data collected from STORM, when compared against the data collected for the degradation of the MEDET material samples, will provide an in-depth record of which eroding species affected which materials and at what rate degradation occurred with respect to the total absorbed fluence of those species.

The physical requirements for the STORM module as provided by the MEDET team and final values of the design are as follows in Table 1. In addition, electronic requirements were imposed for the rate at which data will be recorded and also, importantly for the design and calibration of the detectors, that the output signal should be within the range 0-10V.

Attribute	MEDET Requirement	Final Design Value
Mass	1kg (+/-10%)	943.6g
Power	≤5W	2W nominal operations 5W maximum (ZnO refresh)
Dimensions	130mm x 105mm x 85mm (with cut-outs)	As for requirement

Table 1: Physical requirements and final values for the STORM module

The STORM module was initially envisaged to be composed of two or three components, as the orientation of MEDET at its original position necessitated a different distribution of the instruments. However, with the move to a Columbus external payload site it was possible for the instrument package to be comprised of a single, cuboid-shaped component that contains all the AO, X-ray and UV detectors. The sets of detectors are split into two sections: those detectors that face towards the ram direction and those that face towards the zenith direction. STORM is the only instrument on MEDET to have detectors pointing in the zenith direction. This will allow a greater volume of data to be collected from the X-ray and UV solar radiation detectors and will allow for on-orbit analysis of the degradation of the ram-facing detectors due to the effects of AO erosion (the zenith detectors will receive a greatly reduced AO flux, so can operate as a control for the ram detectors).

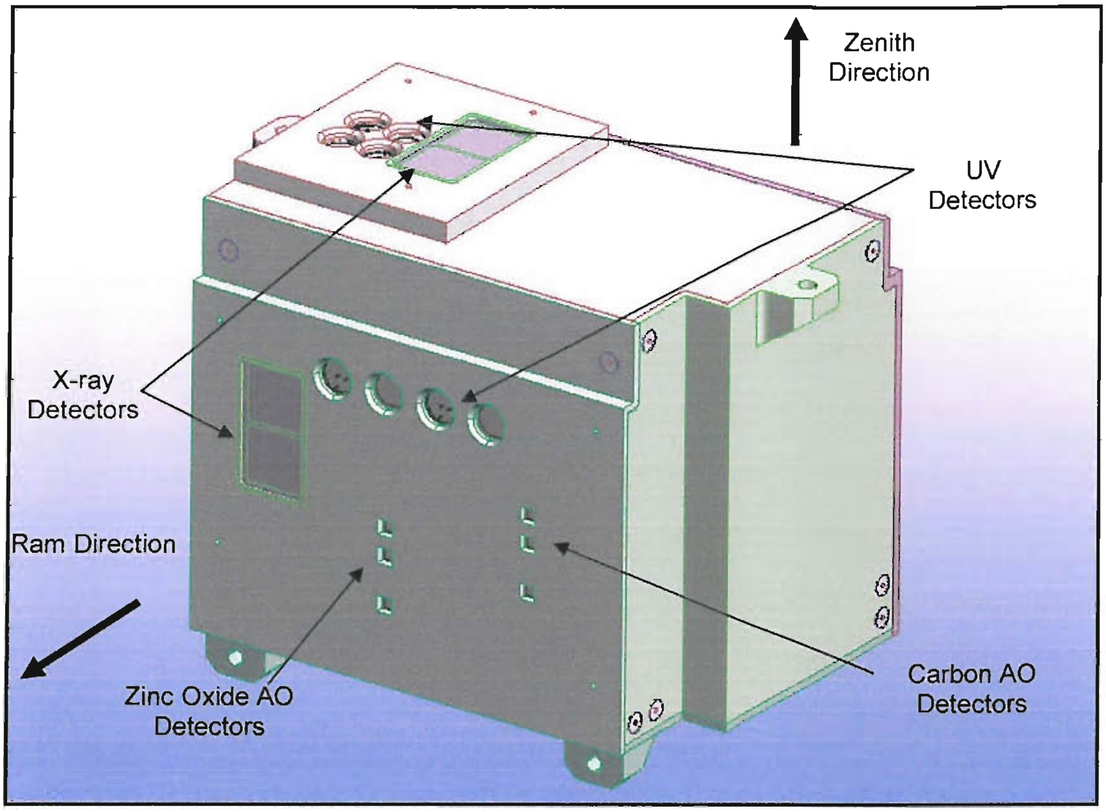

Figure 4: The STORM Instrument Unit

The ram-facing detector section contains all four ZnO and all four Carbon AO detectors, along with two X-ray detectors and four UV detectors. Two of the UV detectors will have fused silica filters; the other two will remain bare. The zenith-facing detector section will contain the remaining two X-ray detectors and four UV detectors. Similarly, two of the UV detectors will have fused silica filters while the remaining two are bare. All of the X-ray detectors on both faces have beryllium filters that are integrated into the surrounding instrument frame.

Each detector section is mounted on a sub-board that also contains the first stage of amplification, temperature sensors, and substrate heaters. Underneath the ram-facing detector sub-board, within a stack of five parallel boards, are housed the remainder of the electronics for the detectors, including further stages of amplification, signal line multiplexers, and power distribution circuitry. The electronics are directly connected to MEDET's Onboard Data Handling (OBDH) system and to the relevant Group Power Unit (GPU) via ribbon cables. STORM is attached to MEDET via four bolting points: two on the ram face and two on the zenith face.

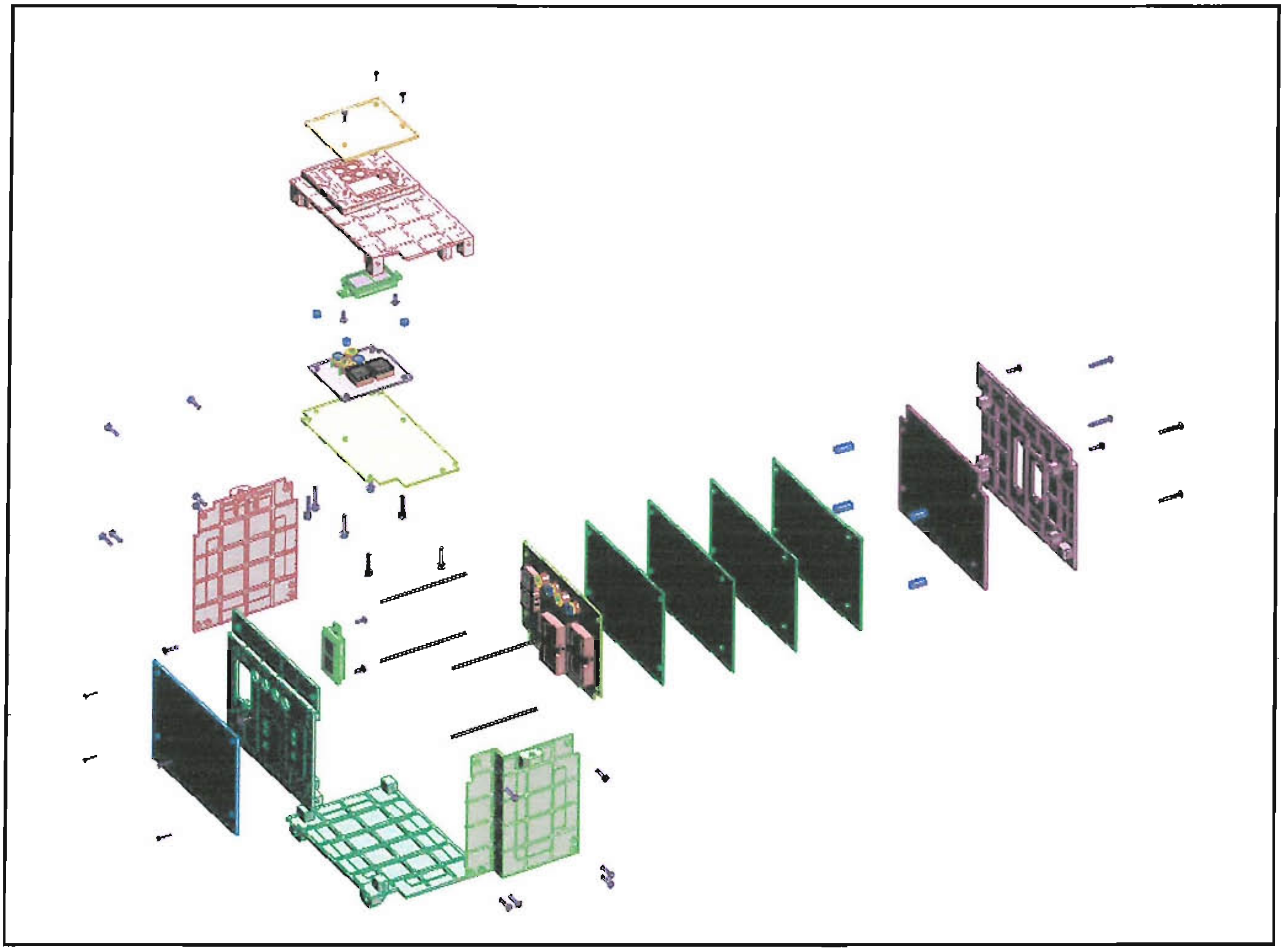

Figure 5: Exploded diagram of the STORM components

Contained within a six-panelled aluminium frame, the circuitry is held in a very rigid pin and spacer configuration that allows for precise positioning of the detectors to their apertures and associated filters and also minimises movement and possible damage due to vibration launch loads. The structural integrity was tested in incremental configurations to the predicted mechanical launch loads (see Section 4.3.1, below).

On the ram face one of the ZnO detectors is obscured by the sample windows of the spectrometer wheel to enable measurement of the response of a freshly regenerated ZnO detector's immediate exposure to AO. One each of the ZnO and Carbon detectors will also be covered by the external frame and will act as controls for the other active, exposed detectors to be compared against.

1.7 Radiation Detectors

Of primary concern to this thesis are the choices made for the inclusion of the specific radiation detectors. As a small instrument it was vital to use low volume, low mass instrumentation that could be operated on a minimum level of power. The decision to use solid state detectors was thus easy to justify: they fit the above criteria with the added bonus of being reasonably inexpensive for commercial off-the-shelf (COTS) items. Scintillation detectors introduce the mass and power-hungry nature of micro-channel plates (MCPs) and gas proportional counters would require too much volume to be feasible within STORM's tight requirements.

The soft X-ray detectors had to be sensitive to an energy spectrum of 1-10keV and the UV detectors to the UV-C spectrum. If possible the UV detectors would also supply flux information on the 121.6nm Lyman-α region. Both of these regions are of significant importance to the monitoring of LEO materials degradation due to their potential for synergistic action with other eroding species, most notably AO (see Section 2.1 for further details).

1.7.1 Soft X-ray Detectors

The detectors chosen for soft x-ray detection were Hamamatsu S3590-08 Silicon PIN photodiodes, a 500μm thick single-wafer device mounted in a flat, rectangular ceramic package. All the detectors were positioned under 50μm beryllium filters that were themselves mounted to aluminium frames for attachment to the STORM structure. The following Figure 6 displays the detector when mounted on a Macor ceramic block that is bolted to the underlying printed-circuit board (PCB). The square black area is the silicon wafer, the silver edging around this area are the electrodes that connect to the gold contacts (more clearly seen in Figure 7).

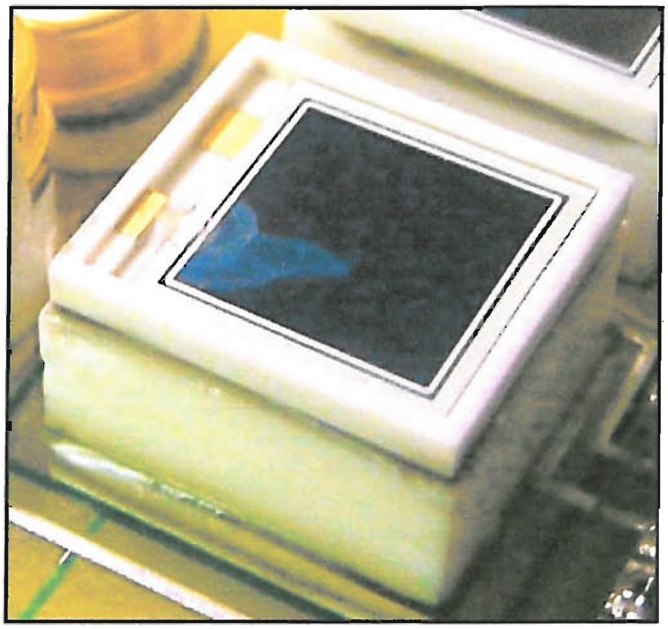

Figure 6: SXR Detector – Si PIN Photodiode mounted on PCB

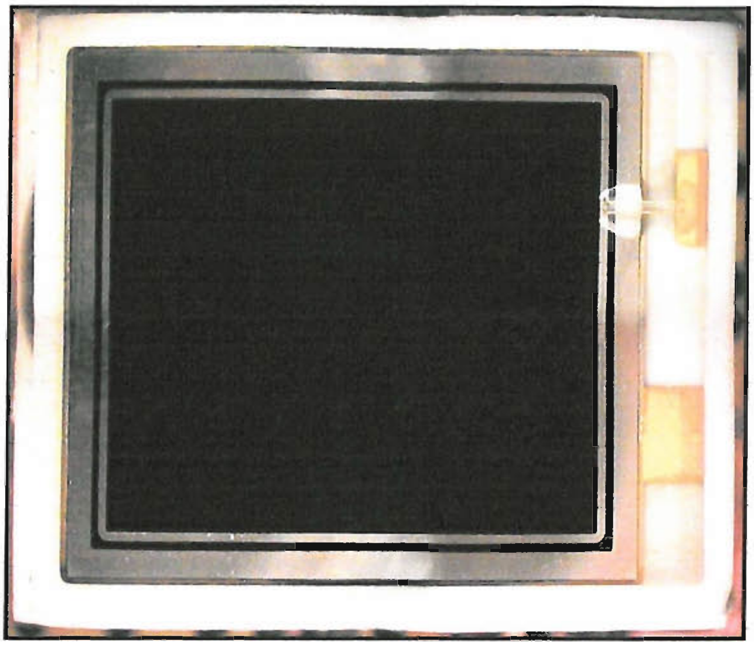

Figure 7: Si PIN photodiode close-up

The decision to use these silicon PIN photodiodes was due to a number of reasons:

- Readily available with low lead times (<6 weeks).
- Relatively inexpensive (<£100 each).
- Low mass (~1g for each detector, ~4g total).
- Low power requirements – only the associated amplifiers need to be powered (312mW each, 1248mW total).
- Reasonable quantum efficiency (reaching a maximum value of ~30%, see Section 4.1.1 for further details).
- Reasonable active area (within STORM dimensional constraints) to maximise flux gathered (9mm x 9mm).
- Approved space use (silicon is extensively incorporated in solar panels for electricity generation).

- Can be operated with simple electronics to help reduce volume and mass of the instrument (as opposed to alternative detector systems that require large potential difference supplies and have higher power demands).

The use of other solid state materials (such as germanium) was overruled due to the greater expense of photodiodes made from these more exotic substances.

The drawbacks to these silicon detectors were:

- Very low energy resolution – only a broad energy band can be monitored, the limits determined by the thickness of the detector and the thickness/material of a filter.
- Very low angular resolution – only limited to the field of view (FOV) of the photodiode in its instrument housing.
- Requires a filter to provide the high-band pass (50μm of beryllium).

However, as STORM is attempting to provide a quantitative measure of the total dose of the SXR flux to correlate against rates of degradation of material samples on MEDET, rather than a precise spectroscopic study of the Sun in SXR wavelengths, then these factors were considered subsidiary to those in favour of the detectors. The energy resolution will still determine when flares occur and, with calibration, will be able to establish their strength. The angular resolution is not required as the only source of x-rays powerful enough to be detected will be the Sun itself – the originator of the soft x-ray flux (although see Section 5.3.4 for further details).

The filter chosen was beryllium as this has the sharpest transmission curve of any metal (to provide as clean a cut-off below 1keV as possible) and has no K-transition lines within the energy range to be monitored. This provided the only technical drawback of the detector choice as a separate filter had to be mounted in front of the detector that would not allow any light leakage to the detector surface within the instrument casing.

The detectors operate by absorbing incident photons with the electrons in the valence band. These electrons will become excited and if the energy of the incident photon is higher than the band gap for the material (~1.12eV for silicon, equivalent to ~1108nm in the infrared) then the electron will be promoted to the conductance band while leaving a hole behind in the valence band. These electron-hole pairs occur throughout the photodiode in the positive (p), intrinsic (i) and negative (n) regions, but it is only those generated in the intrinsic, or depletion, layer that are important as these are the ones affected by the electric field generated across the layer by the proximity of the p and n layers. The electric field across the intrinsic layer causes the electrons and holes formed there to drift in opposite directions with holes collecting in the p-layer and electrons collecting in the n-layer.

In an isolated photodetector this current generated would quickly slow and stop as the charge-disparity across the p-i-n junction approached and reached the point where an opposing electric field was generated equal to that formed by the junction itself. However, once connected to a circuit, the current can be fed out of the detector and further illumination will continue to generate a current across the p-i-n junction that is proportional to the level of irradiance by photons of appropriately high energy.

The circuit used for the SXR detectors is as follows:

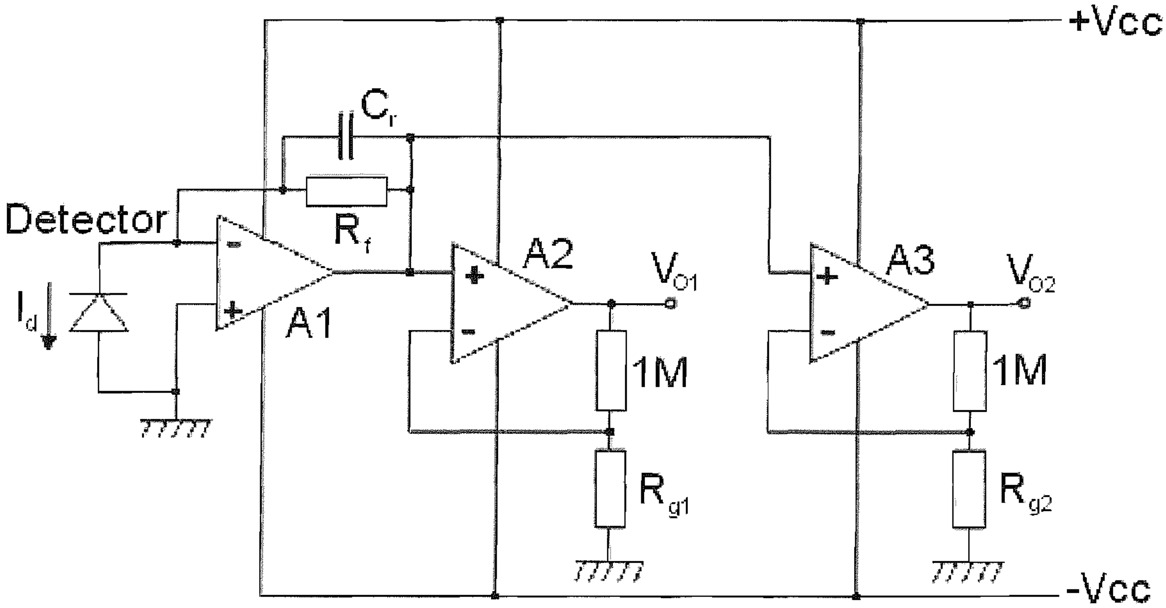

Figure 8: Circuit Diagram for SXR Detector

Note that the detector is operated without bias in the photovoltaic mode. This is to reduce the shot noise – the unwanted current produced by electron-hole pairs generated by thermal fluctuations in the depletion region. The downside is a lower response time as it takes longer for electron-hole pairs to drift apart across the depletion region, but this is of little consequence considering the relatively slow sample rate (one measurement every three seconds).

The output signal current from the detector is passed to the transimpedance amplifier A1 that transforms the current into a potential difference output. Due to the low SXR flux expected on-orbit a second stage of amplification is required. However, as the flux range is expected to be so large this second stage of amplification splits the output signal from the first to two separate amplifiers, A2 and A3, which have different gains. Thus, each detector produces two output signals, V_{O1} and V_{O2}, which cover different flux levels.

These signals are produced by the following relationships:

$$V_{O1} = I_d R_f \left(1 + \frac{1M\Omega}{R_{g1}}\right)$$

Equation 1: SXR Detector Potential Difference Output from the 2nd Stage Amplifier A2

$$V_{O2} = I_d R_f \left(1 + \frac{1M\Omega}{R_{g2}}\right)$$

Equation 2: SXR Detector Potential Difference Output from the 2nd Stage Amplifier A3

Where	I_d	Signal current generated by the photodetector
	R_f	Feedback resistance for the first stage of amplification
	R_{g1}	Feedback resistance for the second stage of amplification by A2
	R_{g2}	Feedback resistance for the second stage of amplification by A3
	V_{O1}	Potential Difference output from A2
	V_{O2}	Potential Difference output from A3

For the STORM flight model the resistor values used for the final detector circuits, calculated with respect to the expected on-orbit SXR flux, are:

R_f	10MΩ
R_{g1}	10kΩ *and* 3.3 kΩ
R_{g2}	100kΩ

With the calibrated responsivity of the detector and the expected on-orbit flux, it is possible to use these relationships to calculate the range of expected signals that will be measured during the mission (see Section 5.2). Note that for the four SXR detector output channels in total for each face of STORM, two of these channels will have the same R_{g2} value, while the remaining two will each have one of the R_{g1} values. This difference is simply to try to monitor the greatest dynamic range of the SXR flux possible, while retaining the redundancy of two channels amplified with the 100kΩ resistors as these will be able to monitor the more powerful flare events that are more likely to have a noticeable impact on material degradation.

The amplifiers used for the SXR detector circuit are an LM108A[11] for A1 and a dual LM158[12] for A2 and A3, both chosen for their low noise and low power requirements. Both are powered by +/-15V power rails (+Vcc and –Vcc respectively). Non-linear amplifiers (that could more easily cover the four orders of magnitude expected from the signal source) were not chosen for this application due to the limited volume of the STORM module – non-linear amplifiers entail using a number of additional control lines that would have increased the track-area on the PCBs. This would have required a concomitant increase in PCB size and therefore volume of the unit that was not possible given the MEDET-level requirements.

1.7.2 UV Detectors

The detectors chosen for UV detection were APA Optics Inc. DA2-3 Schottky-barrier Aluminium Gallium Nitride (AlGaN) photodetectors with a single, cuboid crystal detector element mounted inside a stainless steel TO-5 can – half of which have fused silica windows of 0.86mm thickness mounted to the TO-5 cap (the filtered detectors), the other half having no filter and the cap removed (the bare detectors).

Figure 9, below, displays both types of detector in their mounted configuration on a PCB. The detector crystals are tiny by comparison with the rest of the TO-5 can – they are mounted to the middle of the circular upper surface. The difference in configuration between having the filter and cap in place and having no cap is clear. The two wires leading from the bare detector are for the PT100 temperature sensor that is sandwiched between the can and the Macor block.

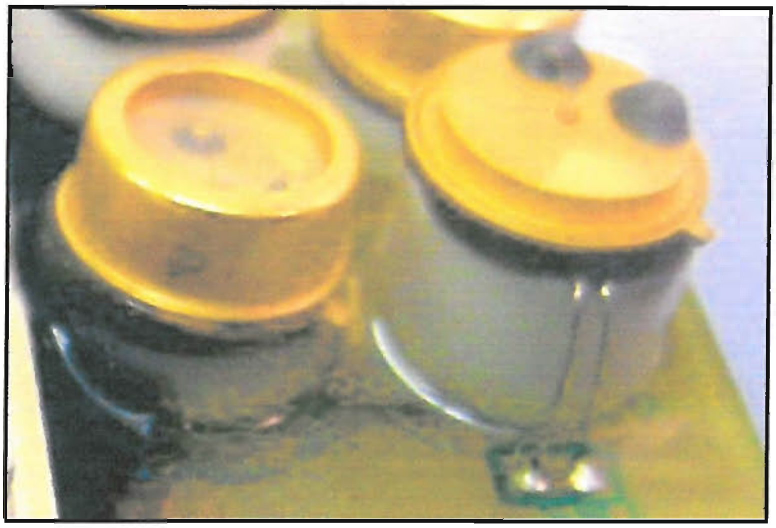

Figure 9: Filtered and Bare AlGaN detectors mounted on PCB

Figure 10 shows a plan view of the upper surface of a bare TO-5 can. The detector is in the centre with two contact wires leading from it to the terminals that connect to the TO-5 can leads. In the above Figure 9 it can be seen how the terminals of the bare detector have been covered in grey araldite to avoid unwarranted interference (see Section 4.1.2).

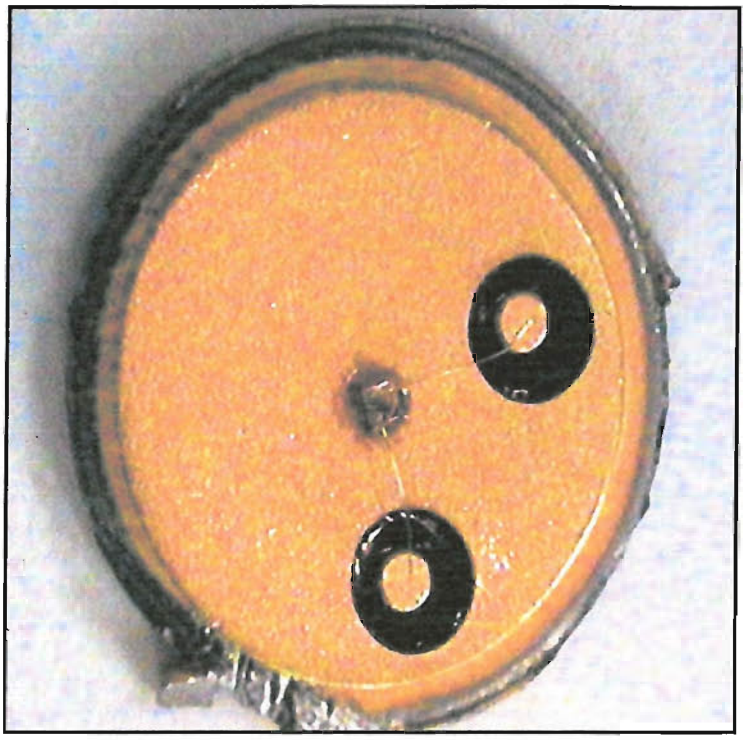

Figure 10: Surface of AlGaN TO-5 Can

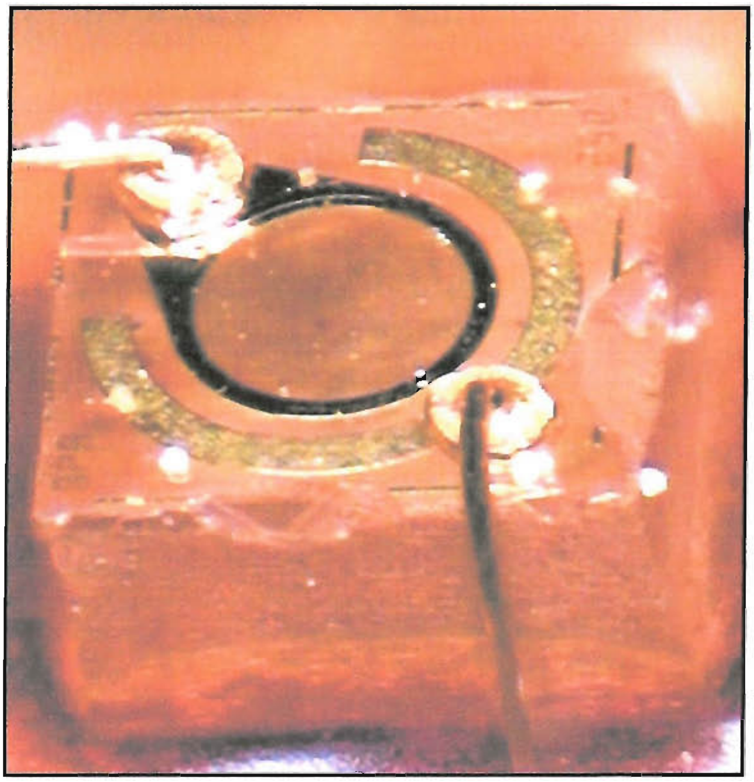

Figure 11: Elevated close-up of AlGaN crystal

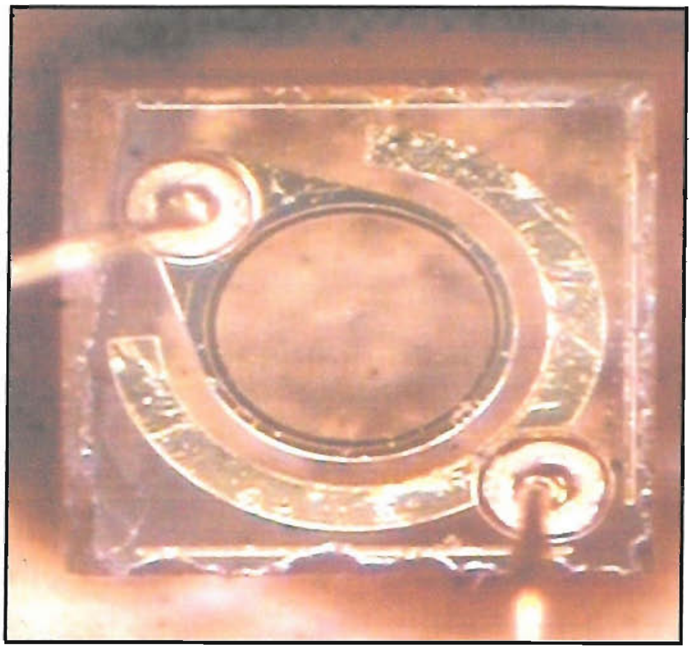

Figure 12: Plan close-up of AlGaN crystal

These two figures display more detailed close-ups of the AlGaN detector crystal itself. The two contact wires can clearly be seen leading to terminals that are attached to the two circular gold electrodes on the surface of the detector. Although the detectors are cuboid, the active area of the detector is circular and given as a diameter measurement due to the configuration of the electrodes. It is clear at the edges of the crystal how vulnerable to fracturing it is, with numerous chips caused by the shaping of the detector prior to adhesion to the can. The white flecks on the surface of the crystal in Figure 11 are tiny grains of zinc sulphide that were used in the electron-beam exposure to locate the beam by fluorescence (see Section 3.2.4).

The decision to use AlGaN photodiodes was based on a similar set of reasons:

- Relatively inexpensive. (<£100 each)
- Low mass. (~1g each, ~8g total)

- Low power requirements – only the associated amplifiers need to be powered (72mW each, 576mW total).
- Reasonable quantum efficiency (reaching a maximum value of ~20%, see Section 4.2.1).
- Can be operated with simple electronics to help reduce volume and mass of the instrument (as opposed to alternative detector systems that require large potential difference supplies and have higher power demands).
- Solar-blind – its physical properties provide the high-pass filter without the need for additional components.

The differences between the reasons for the choice of silicon and AlGaN detectors form the basis for research into its behaviour for use in the LEO environment. Unlike silicon it has never been used in space before and its quantum efficiency in the region of interest (around Lyman-α) is unknown.

Unlike silicon detectors they are more difficult to source due to the very low number of current fabricators and their short history has not allowed the crystal-growth technology to mature. This has a corresponding effect on the active area of the detectors ($0.79mm^2$ - 500μm diameter) although the far higher VUV flux from the sun is predicted to counterbalance this disadvantage.

It is the solar-blind nature of the detectors that is useful as it allows a greater FOV with no restricting filters in place. This will result in a greater proportion of data gathered due to the instruments not being fixed in orientation with respect to the Sun.

The detectors do suffer from the same deficiencies as the silicon ones: low energy and angular resolution, but the mitigating factors are also the same. However, the addition of fused silica filters to half of the detectors is an attempt to make up for this shortfall as this will allow greater energy resolution of the important Lyman-α region without compromising the increased level of data gathered from the unfiltered detectors.

The physical operation of the detectors is similar to the Si PIN photodiodes except that for Schottky photodiodes the depletion region is generated within the crystal in proximity to the metal-semiconductor contact-region. The solar-blind property is a function of the band gap between the valence and conduction bands that is determined by the ratio of AlN:GaN in the detector (see Section 2.3.2). The precise figure was not made available by the manufacturer, but was described as 36-40% of AlN (although see further comment in Section 5.1).

The following circuit in Figure 13 is that used for the UV detectors. It is simpler than that for the SXR detectors due to the lack of need for a second level of amplification – the Solar UV flux being far greater than the SXR flux and having a far lower range of variability (see Section 1.3.5).

The amplifier A4 acts in the transimpedance mode to convert the output current from the detector into a potential difference signal, V_0, produced by the following relationship:

$$V_0 = I_d R_f$$

Equation 3: UV Detector Potential Difference Output from Amplifier A4

Where	I_d	Signal current generated by the photodetector
	R_f	Feedback resistance for the amplifier
	V_0	Potential Difference output from A4

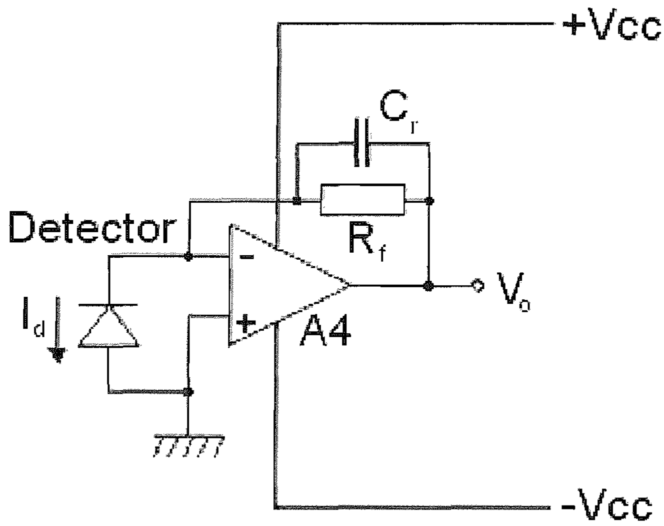

Figure 13: Circuit Diagram for UV Detector

For the STORM flight model the resistor value used for the final detector circuits is:

R_f 470MΩ

With the calibrated responsivity of the detector and the expected on-orbit flux, it is possible to use these relationships to calculate the range of expected signals that will be measured during the mission (see Section 5.1).

The amplifier used for the UV detector circuit is a LM108A, as used for the first stage of amplification in the SXR detector circuit.

2 Literature Review

The literature review is split into three main sections. First is a description of recent and current materials exposure experimentation that has been carried out in LEO. This will serve to place the MEDET experiment and STORM instrument within the current context of space-based materials research.

This is followed by an overview of the historic usage of UV and x-ray detectors in space in order to ascertain the previous role(s), if any, of the detectors employed on the STORM module. Such a review will provide an understanding of what experimentation carried out for the calibration of these detectors will be relevant to the respective research fields.

Lastly is a review of AlGaN detector development and usage to establish the novel areas of research that the experimentation necessary for STORM calibration can fill.

2.1 Space Materials Exposure Research

Over the course of spaceflight history it has become apparent that the various orbital and interplanetary environments are far from being benign regions within which to operate. This has immediate ramifications for the longevity of spacecraft operating for extended periods of time within these environments. Not only can delicate surfaces of spacecraft instrumentation be damaged, causing deterioration and loss of data, but thermo-optical properties can be slowly altered, producing changes in spacecraft thermal control and power generation that can degrade performance and, ultimately, lead to the premature loss of the vehicle.

Research into materials degradation is thus of great importance to mission planners and spacecraft designers due to the insidious effects that the environment produces. Indeed, with growing demand for flights of longer duration to make space utilisation more profitable and for the development of instruments of greater sophistication and delicacy, the requirement to understand the effects of, and interactions between, the different environmental components is becoming increasingly significant. This trend of increasing significance is unlikely to change in the short or long term as the capabilities of the various space agencies and private consortiums grow.

As important as space-based materials exposure research is, there are considerable problems associated with the field that have limited its development. An important requirement is that materials are returned to the ground after exposure for detailed laboratory analysis, without which it is only possible to infer degradation effects by monitoring vehicle performance. The high cost of such experimentation has undoubtedly been a major component in the somewhat limited materials exposure research that has been carried out to date. Whereas understanding the environmental effects on materials in LEO is vital, research is restricted due to the requirement of safely returning the test samples to evaluation facilities on the ground. As a result, almost all materials research has relied on manned spaceflight so that the return of exposure tests was coincident with the more important return of astronauts.

In addition, both returned samples and inferences based on performance data suffer from an inability to distinguish between the various environmental elements. The different space environments consist, in differing proportions, of: solar and albedo electromagnetic radiation; trapped and solar protons, electrons and ionised particles; cosmic rays; atomic oxygen; micrometeoroids; debris; direct and return-flux contamination; near vacuum; and thermal cycling due to orbital motion. Isolating the effects of each of these components is difficult enough, but the difficulty is further compounded by synergistic effects between the components that can enhance or reduce their combined effects compared to the sum of their individual contributions.

A comprehensive understanding of space degradation would further have to take into account the variety of space environments that include Low Earth Orbit (LEO), Medium Earth Orbit (MEO) including Sun-synchronous orbits, the CisLunar region including Geostationary Orbit (GEO) and Lagrange-point Halo Orbits, and the interplanetary region including the locales surrounding other Solar System bodies. These environments can also fluctuate depending on Solar activity, providing yet another layer of complexity.

The final issue concerning materials erosion is the difficulty involved with reproducing a specific space environment in ground test facilities. It is important to note that there are no current (commercial/academic) facilities that can recreate all the above factors of a space environment simultaneously. Thus, space-based testing is paramount to precisely deduce degradation effects until such time that accurate ground-based testing facilities become available.

The best that current facilities can provide (such as the Materials Division at ESTEC, the (US) Air Force Research Laboratory's Materials and Manufacturing Directorate, or the Boeing Company's Combined Radiation Effects Test Chamber (CRETC)) is exposure to two or three environment factors simultaneously. However, even in this case an accurate representation of the on-orbit energy/frequency spectrum for each factor is unlikely to be obtained – tuning equipment to precisely replicate, say, the full Solar UV spectrum is exceptionally difficult. Such tuning and calibrating of test equipment is also, necessarily, hampered by our incomplete understanding of the varied space environments and how they change with time, over both the short-term, which can generate transient events that affect spacecraft, and the long-term, which is important for predicting spacecraft longevity and changes to thermal and electrostatic charging characteristics.

Due to these current limits on ground testing, direct exposure to the space environment of interest remains the best method of assessing the resultant degradation and/or alteration of materials. At present the most important space environment for study is that of LEO, due to the fact that it is the most easily accessible and thus the most commercially and scientifically developed region. The LEO environment will also be essential, for the foreseeable future, as a staging ground for assembly and preparation of larger space projects that will ultimately be exposed to further environments.

2.1.1 Previous Exposure Research

The exploration of the space environments, and our understanding of the nature of the different components of which they are comprised, has developed greatly over the past 50 years. Indeed, the pioneering missions of the 1940s and 1950s were principally concerned with exploring the immediate space-environment within the Earth's thermosphere.

Various attempts to deduce the effects of the environment on spacecraft components, by using data from their in-flight performance, have been made, including the reduction over time of power generation of solar panels being linked to damage by dust during close cometary encounters[13] and by the synergistic effects of radiation and molecular contamination[14,15]. In such cases, the results are based on inference and so are subject to potentially unforeseen errors. They are also of limited use in estimating the same effects in other space environments due to the difficulty of scaling such effects without detailed knowledge of the environmental constituents.

To achieve a deeper understanding of the effects that the space environment has on the materials and operating components of spacecraft it was necessary to develop manned spaceflight with the concurrent return of space hardware to the ground; previous return missions were comprised exclusively of sub-orbital rockets that spent too little time in the space environment to be noticeably affected (although these were widely used to take direct measurements of the environment).

The design of manned return missions provided the opportunity to develop simple experiments to monitor conspicuous damage to materials, such as the micrometeoroid detectors on the Gemini[16] and Skylab[17] missions, the Thermal Control Coatings and Polymeric Films Experiment, also on Skylab[18], the Etalon space exposure experiment on Salyut 7, the Mir Environmental Effects Payload (MEEP)[19], and the Echantillons experiment[20,21] also on Mir. The return of space hardware to the ground also allowed for the analysis of exposed surfaces, such as Apollo windows[22] and the Surveyor III camera[23], a practice that has continued with the return and investigation of various solar panels, including those from the Hubble Space Telescope[24] and from the Mir Space Station[25]; thermal panels, also from Hubble[26] and the TREK cosmic ray detector on Mir[27]. Such investigations provided data on the combined effects of the environmental constituents, but were of little help in determining the different contributions to the degradation. It was also discovered that certain effects on materials were obscured by out-gassing contamination[18] and re-entry effects – notably that some degradation is obscured by materials curing on contact with atmospheric oxygen after returning to Earth, so more sophisticated exposure and recovery techniques were required.

This became possible with the development of the Shuttle, and the consequent return flights with the capacity to recover significant volumes of hardware from space. Due to the limited length of time that the Shuttle can remain on-orbit, the majority of materials experiments that it has carried out have been of short-duration, including the Atomic Oxygen Effects Experiment on STS-8[28], the Limited Duration Space Environment Candidate Materials Exposure (LDCE)[29] package on flights STS-46 (that included the Evaluation of Oxygen Interactions with Materials III (EOIM-III) experiment[30]), STS-51 (that included the Surface Effects Sample Monitors[31]), and STS-62, the Advanced Composite Material Exposure Experiment (ACOMEX)[32] on STS-41G[33], the Materials Exposure in LEO (MELEO)[34] package on STS-52 and the Solar Array Module Plasma Interactions Experiment (SAMPIE)[35] on STS-62.

However, the Shuttle was also instrumental in providing the capacity for long duration exposures by recovering other spacecraft, including the Solar Maximum satellite in 1984[36,37], the European Retrievable Carrier (EURECA)[38,39], and the first dedicated materials exposure vehicle, the Long Duration Exposure Facility (LDEF)[40], after a 69 month flight between 1984 and 1990.

This trend of using manned spacecraft to carry out materials research has continued with the utilisation of the ISS. The recent and current investigations have included the Material International Space Station Experiment (MISSE) pallets[41,42] (with the complementary Shuttle-based Polymer Erosion and Contamination Experiment (PEACE)[41], the Micro-Particle Capturer and Space Environment Exposure Devices (MPAC/SEEDS)[43,44], and the Russian flight experiments SKK, KROMKA, BKDO and KOMPLAST[45].

The vast majority of the above experiments have been completely passive in nature, the materials being situated or placed on an external spacecraft surface for a fixed length of time before being retrieved for ground analysis, without any discrimination as to which environmental factor, or combination of factors, caused any resulting degradation. The only exceptions are the use of Quartz-Crystal Microcalorimeters on LDEF and MELEO to record Atomic Oxygen fluence and the active monitoring of charge and plasma build-up by SAMPIE. The majority of experiments on the non-powered LDEF and even the most recent MISSE experiment on the ISS have relied on passive exposure where the only calibrating measurement was the duration of the flight.

In contrast there have been relatively few experiments that have actively monitored any aspect of the space environment while simultaneously observing the concurrent effects on samples of material. For example, the THERME experiments running on spacecraft in Medium Earth Orbit (MEO) at approximately 800km altitude (SPOT 2, 3, 4 and potentially on SPOT 5, HELIOS II, STENTOR, FBM, and DEMETER)[46]. These experiments make multiple measurements of the temperature of various spacecraft surfaces throughout the lifetime of the mission from which changes to the thermo-optical properties of the coatings/exterior surfaces can be inferred. Once again, however, such experiments have no capability to distinguish which environmental elements cause the majority of the degradation.

Other examples include: the Atomic Oxygen Experiments (AOE)[47,48,49] on the Space Technology Research Vehicle 1a (STRV-1a) and 1c, that measured the atomic oxygen fluence and degradation to thin films coating the detectors; the Spacecraft Active Modular Materials Experiments (SAMMES) instrumentation[50,51], to monitor atomic oxygen erosion, thermo-optical properties, contamination, ionising radiation fluence and solar irradiance/shadowing, that was unfortunately lost on the Space Test Experiment Platform mission 3 (STEP-3) but then successfully flown as part of the STRV-2 payload on the Tri-Service Experiments Mission 5 (TSX-5) in 2000; and the contamination experiments[52] on the Midcourse Space Experiment (MSX) satellite[53], to measure pressure, condensed masses, distribution of contaminant particles and sizes, and provide chemical composition analysis of the contaminants.

There have been a host of further experiments to monitor contamination on various spacecraft, as this is a crucial issue that affects delicate optical components in imaging applications. However, as such experiments are primarily concerned with maintaining on-orbit calibration and not specifically with directly monitoring and measuring the causes of this environment-induced degradation, they have been omitted from this review.

2.1.2 SXR and UV Ground-Based Materials Exposure Research

During the Hubble Space Telescope second servicing mission (SM2) it was found that a region of multi-layer insulation had become severely cracked and embrittled[26]. The ensuing investigation to determine the cause of the damage exposed samples of the aluminised Teflon fluorinated ethylene propylene (Al-FEP) to charged-particle radiation, simulated solar flare X-ray radiation and thermal cycling under load[54] and succeeded in producing similar results. Comparable damage was also observed on recovered experiments from LDEF[55], prompting further interest into the degradation effects.

It is well known that UV radiation rapidly affects polymers by causing degradation in mechanical and chemical structure[56,57] due to these synthetic, organic materials being particularly vulnerable to photons at and above these energies. This can have a significant impact on various polymers used in spacecraft applications, including the discolouration and darkening of thermo-optical films due to increased polymerisation[58,59] that can have a severe impact on the vehicle's thermal performance.

Such UV damage has been observed in laboratories elsewhere[60,61], including specific observations of decreases in the spectral reflectance, in the UV-visible range, of polyimides[62] that, again, has direct relevance to thermal control when using such materials.

It is similarly known that soft X-rays also produce degradation in polymers[63,64] through equivalent processes to UV deterioration. Due to the similarity in effect it is, consequently, difficult to ascertain which frequencies of radiation generate the most damage. This difficulty is apparent in the suggestion that solar flare X-rays are primarily responsible for the FEP degradation[65,66] on Hubble, whereas further tests with exposure to X-rays[67] and a combination of VUV and SXR[68] apparently demonstrate that SXR cannot be the primary degradation factor.

With respect to the LEO environment this picture is further complicated by the potential for non-linear, synergistic degradation processes to arise with the addition of atomic oxygen. As it is the most abundant particle species in LEO and also highly reactive, AO has been well investigated for its contribution to on-orbit materials degradation[69]. With regard to synergistic effects, it has been demonstrated that UV can increase the reactivity of FEP Teflon, PCTFE and Kapton to AO in vacuum[70], and that AO and UV can act synergistically in the erosion of polyethylene[71], Teflon FEP and silicon carbide[72]. It has been similarly alleged that degradation on all surfaces of Hubble (not just Sun-pointing surfaces) make clear that an atmospheric component (AO/charged particles) is primarily responsible and that this acts synergistically with SXR and UV[68].

This currently confused and complex outlook on degradation effects has led to the development of research facilities at a number of locations to explore the different phenomena. Those that can expose samples to UV and SXR simultaneously include the Solar Radiation Simulator (SORASI) at the Materials Division of ESTEC and the Integrated Space Environment Factors Simulator (KOBE)[73] at the DLR Institute of Space Sensor Technology and Planetary Exploration. Other laboratories have built specialised facilities for focusing on just one radiation source for their experiments, such as the simulated space vacuum ultraviolet facility[74] at NASA's Glenn Research Centre.

Interest in synergistic effects is not limited to UV, SXR and AO research; there have been simulations of 5-year missions at 0.98AU and the L2 point to examine the effects of concurrent UV, proton and electron exposure on the thermophysical properties of polymeric films[75], and it has been found that exposing Teflon to protons and electrons simultaneously produces less degradation than the sum of the damage caused by these charged particles independently[76].

However, the current research involving STORM focuses on the synergistic effects between UV, SXR and AO as these are the predominant environmental factors in the LEO regime where they will be based. Other environmental factors, such as micrometeoroids, orbital debris, and neutral ambient gas are monitored by other instruments onboard MEDET. Further factors, such as the impact of electrons and other charged particles, have been neglected as being of little importance to degradation mechanisms due to their much lower flux in comparison to AO attack (as described in Section 1.3).

2.1.3 The Role of STORM with respect to MEDET in Materials Exposure Research

To avoid the drawbacks of a lack of discrimination between environmental factors it is imperative to use active monitoring of each specific factor of interest

The trend in space-based materials research, as described above, has been one of growing complexity over the past 25-30 years. STORM, and MEDET as a whole, is intended to continue this trend and further develop on-orbit capabilities.

In deliberate contrast to the great majority of previous exposure experiments, MEDET will endeavour to provide an on-orbit monitoring of the majority of components of the LEO space environment during a flight exposure. Coupled with this will be the ability to actively monitor a selection of materials throughout the duration of the mission. With these two attributes MEDET will represent the state-of-the-art in LEO-based materials exposure experimentation.

To this end STORM plays a vital role within MEDET. With the detection of three environmental factors, SXR, UV and AO, it makes a large contribution to the overall active analysis of the LEO environment. No detector suite has previously been used in such a configuration (as further demonstrated below), so both MEDET and STORM represent novel technological designs for which the pay-off could be a large increase in our understanding of the singular and synergistic effects of environmental factors in the erosion of space-based materials.

As has been noted above, there is some controversy regarding the role of SXR in the degradation of materials on-orbit. The radiation detectors on STORM have been specifically chosen to explore this issue and help determine the difference in the rates of erosion generated by the synergistic effects of AO and SXR, and AO and UV. Further, due to the fluctuations in SXR and Lyman-α produced during solar flares, it is hoped that the measurements made by the detectors will enable the determination of the relationship between flux level and rate of degradation.

Actively monitoring the materials being exposed should enable MEDET to avoid previous analysis problems. Calculating which environmental factors have the greatest effect should be straightforward. Other difficulties that can be overcome are rates of decay – passive exposure cannot demonstrate if degradation is linear, exponential, or of any other form – and orbital effects – passive exposure cannot delineate different rates of degradation at different altitudes, for example.

MEDET's potential advances in our understanding may also provide data that will allow improvements in ground-based testing facilities, as they will shed light on which environmental factors have the greatest impact on various material groups. Such a result, although not revolutionary, would serve to help reduce costs and increase the reliability and active life of spacecraft and space instruments in the future.

2.1.4 Characteristics of Solar Generated UV and Soft X-rays

This thesis concentrates on the contribution to STORM/MEDET provided by the SXR and UV radiation detectors. This section provides a brief description of the current knowledge regarding the source mechanism and characteristics of SXR and UV generation by the Sun.

All the electromagnetic energy radiated by the Sun ultimately comes from the fusion reactions occurring within its core by the proton-proton chain and the CNO cycle. The vast majority is radiated from the surface in the visible and infra-red regions of the electromagnetic spectrum, closely emulating a black-body spectrum for an object at 5780K. However, at the higher energies in the UV and SXR regions, the solar spectrum deviates significantly from this theoretical ideal due to processes in the solar chromosphere, transition region and corona.

The visible 'surface' of the Sun, or photosphere, is regarded as the base of the solar atmosphere. The temperature at this altitude of approximately 6×10^3K is relatively cool and thus the ionised gas at this level only radiates in the visible and infra-red. However, the next atmospheric layer, the chromosphere, reaches temperatures of 2×10^4K and so excites ions to high enough energy states that they begin to emit UV radiation when the electrons transition to lower energy bands. This emission is dominated by characteristic lines that are created by common transitions in the most abundant ions that still retain electrons (at these higher temperatures the lighter elements such as hydrogen, helium, lithium, etc. have been fully ionised).

It is in the region between these two layers that the predominance of UV radiation is generated in the range 100-300nm. The UV and shorter wavelengths (<300nm) comprise ~1% of the Total Solar Irradiance (TSI) [77], but it is this region that has been found to be significant to the degradation of space-based materials, as described above. Below 100nm only ~0.01% of the TSI is generated, including much of the EUV spectrum that is generated at the increasingly higher temperatures within the chromosphere, transition region and corona. Due to this large difference in emitted energy between the 100-300nm and <100nm regimes it is little wonder that the lower-energy portion of the vacuum ultraviolet (VUV: 10-200nm) from 100-200nm and the full range of the near ultraviolet (NUV: 200-380nm) have a greater impact on materials than the higher-energy but low flux region <100nm.

One dominant attribute of the UV spectrum is the hydrogen Lyman-α emission line at 121.567nm, generated over a region from 800-2,300km in altitude above the photosphere with a temperature range of 6,000-25,000K[78] (for the quiet Sun during solar minimum). This one emission feature (with a spectral width of ~0.1nm) contains as much energy, on average 6mW/m^2, as the entire solar spectrum below ~150nm and thus has a greater potential to degrade materials than any other photon energy within this range.

From the above considerations it was decided that the UV detectors onboard STORM must be sensitive to the UV-C (<280nm) spectral region with, if possible, some discrimination for the Lyman-α emission line. This would enable a broad monitoring of the activity in the UV and potentially relate different degradation effects to the action of UV radiation with/without the inclusion of the Lyman-α region.

It has been observed that the maximum, long-term Lyman-α variation is slightly in excess of a factor of 2. This maximum variation of the UV decreases with increasing wavelength until ~300nm where no significant long-term variation above 1-2% is measured.[79] This long-term variation – between solar maximum and minimum, will not necessarily be observed by the AlGaN detectors during the 3-year mission.

However, of greater significance is the variation during solar flares, of which there is mixed observations within the literature. It has been observed by SOLRAD-8 that a flare event has been accompanied by a 20% increase in Lyman-α flux[80], similar to more recent observations by the CORONAS-I and -F satellites[81,82]. Yet other observations have seen clear dips in the Lyman-alpha flux[83] during flare events. This may possibly be due to different geometry of the flare structure and positions on the solar disk during these separate observations, but any short-term variation such as these are potentially significant to the rate of degradation of materials.

The CORONAS instruments in particular provide the best current Lyman-α monitoring with measurements[84] of the solar flux <130nm, during minimum in 1994, of 7.5-8 erg cm^{-2} s^{-1} and Lyman-α intensity of (3.3-3.7)x10^{11} photons cm^{-2} s^{-1}.

It is hoped that the AlGaN detectors used for STORM will be capable of discriminating the changes in the Lyman-α region over these short timescales in order to potentially correlate them with changes to the materials carried onboard MEDET.

As mentioned above, the solar flux below ~120nm is far less than that produced by the Lyman-α region; yet soft X-rays remain of interest to degradation mechanisms due to their observed effects, as reported in Section 2.1.2, above. Passing from the chromosphere, through the transition region and into the corona, the temperature of the solar atmosphere increases markedly to around $2\text{x}10^6$K. This high temperature fully ionises most of the light elements that make up the majority of the atmosphere and highly ionises heavier elements so that electron transitions of high energy, corresponding to the SXR and EUV, become more commonplace. Although the precise mechanism(s) of how the corona is heated to these high temperatures is still under investigation, it is known that a SXR continuum is generated by Bremsstrahlung radiation from thermal electrons being deflected by interactions with ambient protons in the corona. This is distinct from the generation mechanism of hard X-rays (HXR – 10-100keV) by the collision of non-thermal electrons with protons, and the generation of microwaves by synchrotron emission due to the constant acceleration of electrons trapped in helical paths by the 'closed' 1mT magnetic fields in active regions.

Where the magnetic field lines of the Sun are 'open' and extend into the Solar System, charged material is projected away, generating the solar wind – the lack of magnetic confinement leads to a massive drop in density, reducing the frequency of interaction between thermal electrons and protons, thus forming voids in SXR images of the Sun known as coronal holes.

Due to SXR emission being related to the prevalence of active regions on the Sun's surface, the flux level changes markedly over the Solar cycle between maximum and minimum. In the band from 0.1-7nm the flux level can vary by a factor of 11 over the solar cycle, and can vary by as much as 44% over the 27-day cycle of the Sun's equatorial rotation[85], as observed by the Student Nitric Oxygen Explorer (SNOE).

However, such changes are minor compared to those that occur during solar flares that can increase the brightness of the Sun in SXR wavelengths by up to four orders of magnitude. This increase is due to the massive conversion of energy from magnetic to kinetic that accelerates the electron population trapped in active region closed loops to thermal velocities. The consequent increase in frequency of interaction between these thermal electrons and the protons also trapped in the closed loops generates the observed increase in flux of SXR.

The period over which flares emit is proportional to their size. Most M-class flares last for a matter of minutes, while the more powerful X-class can last for hours or even over a day in the most powerful examples that have been observed. Such transient events will be of great importance to the study of the effects of SXR irradiation of space materials – indeed; as the variation is so marked with respect to the UV variation it should be straightforward to delineate the effects of these different radiation bands.

To this end it is important that not only are the STORM SXR detectors sensitive across as much of the energy band from 1-10keV as possible, but that they also have the dynamic range to cope with the changes in SXR flux expected while on-orbit.

For both sets of detectors it will be important that they have a temporal resolution high enough to delineate between the transient events that generate variations in the VUV and SXR ranges. As noted, the ability to delineate between events in these energy ranges will be imperative in correlating different radiations with different materials effects.

Further references that contain information relating to the Sun and solar generation of radiation can be found in the bibliography.

2.2 Historic Spacecraft Usage of UV and SXR Detectors for Direct Solar Observation

The study of solar electromagnetic radiation in space has always been of great importance due to its varied effects on materials, electronics, organisms, and the inability of certain wavelengths to be monitored from the ground. This section aims to comprehensively review the instrumentation used on previous space missions, throughout the history of spaceflight, to monitor the dose rates of UV and SXR radiation from the Sun. Other applications, such as instrumentation designed to study the solar spectrum, the spectra of non-local stars and back-scattered radiation from planetary bodies has not been included for the sake of brevity. This will serve to place the STORM radiation instrumentation into context within the modern space research framework for solar dose monitoring.

The other aim of this section is to demonstrate the lack of previous use of AlGaN photodetectors in the space environment. Silicon photodiodes have been used on a number of missions for soft X-ray study, but it is of importance to this thesis to establish the novelty of the use of AlGaN in an original space-based application.

The section is split into two major parts, first a description of the general detection technologies used for radiation studies in the UV and soft X-ray, and second a tabular listing of all the spacecraft instrumentation that has carried out recordings within these spectral regions.

2.2.1 Radiation Detection Instrumentation

Many methods for detecting radiation have been employed on spacecraft. This section contains a summary of these methods and a discussion of their practicability for use on the STORM module.

2.2.1.1 Photographic Film

A technique used on some early space missions used cameras with films sensitive to UV to capture images in the required wavelength range. While appropriate for initial research due to the relatively low-level technological requirements, such instruments suffer from a variety of drawbacks for the aims of STORM:

- The film must be returned intact for processing – over a 3-year mission period such as that for STORM this would be inappropriate due to cumulative radiation degradation to the recorded images. This would also increase the risk of all data being lost in the event of accident before the return of the flight hardware.
- The amount of data storage is limited by the space available for film. For long duration missions this would also make such a device unacceptably heavy.
- The lenses and winding mechanism are too bulky and power-hungry for the current application.
- STORM only requires radiation flux measurements, not imaging capability – camera equipment would therefore embody over-engineering in its recording capability that has an impact on other constraining factors (such as mass/power).

Although cameras were developed for some soft X-ray photography on manned spaceflight missions, these devices still suffer the same drawbacks as those for UV observation.

2.2.1.2 Ion Chambers

Ion chambers have been used extensively on space-based platforms due to their high reliability and longevity. A target gas is contained within a sealed container that has a filter window at one end to transmit the wavelength range under study. An incident photon ionises some of the gas and, under a potential field, the resulting ions and electrons flow to the electrodes to create a pulse of current. For high flux applications the pulses merge to create a steady, measurable output current proportional to the flux of incident radiation.

Although reliably proven in spaceflight, they would be impractical for the STORM mission for the following reasons:

- The chambers themselves occupy too large a volume to fit within the constraints. Although smaller chambers are available with modern technology, compared to those used on early missions, there is still the problem of the additional space required for mounting brackets and the impact on the internal layout of STORM. Smaller chambers are also more delicate and, therefore, more likely to be damaged by launch vibration loads – even a tiny hairline crack can cause gas loss to make the instrument inoperative over the mission timescale.
- Larger power requirements are needed to produce the potential within the chamber to create the ion/electron flow.

2.2.1.2.1 Proportional Counters

A subset of ion chambers includes proportional counters (also known as avalanche or cascade detectors). These chambers use a higher electric potential to accelerate the ionised electrons from the original photon/gas interaction so that the resulting collisions with other gas atoms generates secondary electron emission. The resulting increase in ionisation creates a larger pulse proportional to the accelerating potential. This increases the energy resolution of the device, which can be extremely important for certain applications.

However, the additional mass and power requirements, compared to ion chambers, would further compound the problems of fitting such devices within the restrictions placed on STORM.

2.2.1.3 Photocathodes

Photocathodes, used in a number of configurations, are very popular for use in spacecraft instrumentation due to the high gain in signal strength they can achieve in conjunction with photomultipliers. Within a sealed vacuum chamber, incident photons eject electrons from the photocathode (via the photoelectric effect) that are attracted to the anode to create a measurable pulse of current.

Usually a photocathode is used in conjunction with a number of dynodes – the emitted electrons are accelerated within a potential and strike a succession of dynodes. The collision with the dynodes ejects more electrons (denoted as secondary electrons) to boost the current pulse and therefore increase the response of the detector. This signal-boosting effect is used, with different configurations, in photomultipliers, channeltrons and micro-channel plates.

However, for the purposes of STORM photocathodes suffer from similar drawbacks to ion chambers:

- A sizable (relative to STORM) volume must be occupied by the vacuum chamber containing the photocathode (plus any associated photomultiplier).
- Power requirements for supplying the acceleration potential are higher.

2.2.1.3.1 Scintillation Detectors

One important sub-group of photocathodes are scintillation detectors where a target material generates a pulse of photons when an incident photon strikes it. This photon pulse is then detected by a photocathode, as described above, which is sensitive to the unique wavelength of light generated by the target material.

While especially useful for high energy photon detection, scintillation detectors further compound the volume and mass limit problems of photocathodes and so were also considered unsuitable for the STORM mission.

2.2.1.4 Solid State Photodetectors

The most advanced forms of detector currently used involve solid state, or semiconductor, photodetectors. Incident photons strike a target semiconductor material and promote electrons from the valence band to the conduction band to create a measurable current. This is the operating principle of photodiodes such as those used on STORM (further detailed in Section 1.7).

The great advantages of photodiodes, that drove the choice for their inclusion on STORM, are:

- Low volume and mass, allowing multiple detectors within the dimensions of STORM to afford active redundancy.
- No additional power requirements when run in the unbiased mode.
- No need for (de)pressurised vessels that are more delicate and can constitute a hazard on-orbit.

Although simple photodiode detectors do suffer from a lack of energy resolution compared to some of the other detector types above, this was not considered a driving factor considering the high count flux rates expected (individual photon energy discrimination would be almost impossible).

2.2.1.4.1 Charge-Coupled Devices (CCDs)

CCDs are an important subset of solid state photodetectors as they are increasingly being used for imaging purposes.

A CCD contains an array of metal-oxide semiconductor (MOS) capacitors that store the charge generated within them by incident photons. Once accumulated, this stored charge is read out and recorded for each individual capacitor (or pixel) to generate an image of the observed target.

While important for space-based observatories, the relatively high power requirements, cooling, and optical focusing structures required for CCDs makes them totally impractical for the STORM system for either UV or SXR monitoring.

2.2.2 Record of Previous Spaceflight Radiation Detectors

Due to the lengthy nature of the record it has been placed in Appendix I, Section 7.1, below, along with the relevant explanatory notes.

Along with references to the literature included in the list, further resources from which this information has been compiled is included in the bibliography and additional resources, Section 8.

As can be seen with reference to this record, no references are found of AlGaN photodiodes ever being used for UV detection on a historic or currently active spacecraft. This demonstrates that not only is the specific application novel, but also that the application of AlGaN detectors to manned spaceflight is novel. All of the qualification testing that went into the construction and delivery of STORM should thus help this new detector material be accepted for future space applications. In a similar vein it has become clear (see below) that no space qualification/characterisation work has been carried out on these detectors which reveals another gap in our knowledge that this research endeavours to fill.

However, there are craft that have flown Si photodiodes, notably TIMED and SORCE, plus many others that have flown silicon based detectors (CCDs especially) and beryllium windows as the filter element. For this reason it is not a similar case that the characterisation of the silicon detector represents knowledge of a novel detector material for this application.

2.3 Aluminium Gallium Nitride Detectors Review

Following on from the above review regarding the lack of previous use of AlGaN for any space-based applications, it is appropriate to search the AlGaN literature to understand why this is the case and what observations from this research will provide additional information in the study of this semiconductor.

Due to their wide band gap there has been considerable interest in III-V Nitride semiconductors over the past three decades for UV applications. For the UV sensitivity that is the concern of this thesis, AlGaN has been found to be the most appropriate material currently available. This section will provide a review of the properties of AlGaN and the applications for the material that includes its usage as a detector. Further information is provided in Appendix II regarding the major developments in AlGaN's discovery and utilisation.

2.3.1 Why use AlGaN Detectors for STORM?

There is a limited variety of different sensing technologies available today for the UV spectrum. Non-solid-state detectors are covered in Section 2.2.1 and ruled out mainly due to their unacceptably large mass, volume and power requirements.

Most of the remaining alternatives to AlGaN are based around Si photodetectors and photomultipliers. This choice was made for the STORM soft X-ray detectors as there was no other viable option (no EUV-blind semiconductor detectors currently exist!). However, they suffer from the considerable drawback of requiring separate filters to remove unwanted, lower energy photons. This has the disadvantages of being more expensive, more complex, heavier, more time-consuming in design, and reducing the field of view (as demonstrated by the beryllium windows for the soft X-ray detectors).

The photomultiplier substitute suffers from the need for a high potential difference supply.[86] This has similar disadvantages of being more expensive, more complex, heavier, requiring greater volume, more power-demanding and time-consuming in design. Such a choice could never be envisaged for STORM with its stringent budgets on volume, mass and power.

The only remaining options are to use diamond-based or other Group III semiconductors with alloys of phosphorus or arsenic. However, both of these groups of semiconductor detectors have, quite simply, not progressed to the current quality and affordability seen in AlGaN devices[87]. (It should be noted, however, that 'current' in this case refers to the year 2000 when the choice of detector was made and frozen in to the ensuing designs – recent advances in diamond detector fabrication have produced some very promising results[88]).

The only commercially available and cost-effective solution was to use off-the-shelf AlGaN photodiodes.

2.3.2 AlGaN Properties

AlGaN is a subset of gallium nitride based semiconductors. These Group III-V compounds have the important property of a band gap of equivalent energy to the ultraviolet region of the electromagnetic spectrum. As a result, they are ideally placed for UV and short-wavelength visible light generation and detection.

The range of sensitive wavelengths can be tuned by altering the mole fractions of the ternary alloys, AlN or InN, with the base GaN[89]. The proportions of the alloys used enable the absorption edge to be tailored over a band-gap range of 1.9-6.2eV, corresponding to a wavelength cut-off from 650nm (InN) to 200nm (AlN)[90], as shown in Figure 14, below.

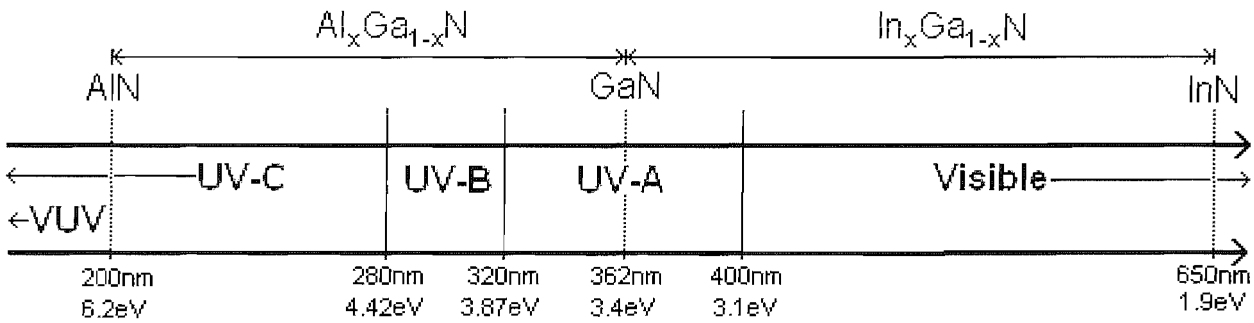

Figure 14: Spectral cut-off range covered by Group III-V nitrogen-alloy-based semiconductors[91]

Thus, the generated alloys can have intrinsic visible-blindness, where the cut-off is at or below 400nm, or even intrinsic Solar-blindness, where the cut-off is at or below 280nm[92]. This is a useful characteristic that eliminates the necessity of an extra filter that would increase the mass, cost and complexity[93,94] and decrease the field of view of a space-based UV-C detector.

Materials based on GaN are tolerant to high temperatures[95,96], thus making them more resilient to the strains of on-orbit thermal variations. Due to their high band-gap they are also generally unreactive and thus more resistant to chemical-based (as opposed to kinetic impact) erosion[97], another useful feature considering the charged particles present in the LEO environment.

The greatest problem that AlGaN (and other GaN based semiconductor devices) has is the high density of structural defects that it contains. The defects invariably arise as a result of the deposition (crystal growth) process or during post-deposition design of the semiconductor device[98]. Their major impact is to interfere with the band gap and thus directly and detrimentally affect the electrical and optical properties of the device[99,100].

Defects arise for a number of reasons:

1. Large lattice mismatch between AlGaN and the substrate (usually sapphire or SiC).
2. Difference in thermal expansion coefficient between AlGaN and the substrate[101].
3. Temperature gradient at the growth interface.
4. Effect of doping materials.
5. Chemical reactions at the interface between the semiconductor and adjacent metal components (e.g. electrode contacts)[102].

For the purposes of UV flux measurements the most important impacts of the defects is to reduce the responsivity in the UV range while increasing the responsivity in the visible range. The UV responsivity can be reduced by physical cracks within the depletion layer of the p-n junction presenting a barrier to free-flow of photoelectrically stimulated electrons from the AlGaN to the Schottky contact. Conversely, defect traps within the depletion layer can introduce unwanted energy levels between the valence and conductance band

and allow photoelectric excitation of electrons by light of a lower energy, thus increasing responsivity in the visible and near-UV spectrum.

Although it is impossible to eliminate these defect problems, it is possible to monitor the detectors by measurement of the dark current before and after system tests when various factors (vibration damage, high intensity radiation exposure, etc.) may cause changes within their structure.

The last property, although perhaps the most important, is the cut-off between the UV-C and the lower energy spectrum. Although AlGaN has a theoretical cut-off range over 200-362nm it is difficult to reach the UV-C as higher mole fractions of Al introduce a greater concentration of defects. This is most probably still due to difficulties in eliminating impurities (typically oxygen) from AlN during the crystal fabrication process. This causes a spreading of the cut-off region in the response curve for a Schottky photodiode detector and a reduction in its responsivity, as observed by Monroy et al.[103]

However, even considering this reduction in performance, it was important to use a commercially available detector with the lowest possible cut-off as the increasing solar flux with wavelength in the region of interest threatens to swamp any signal from the higher energy UV-C and Lyman-α region.

2.3.3 Application of AlGaN Detectors to Space Missions

Due to its inherent visible and solar blindness, AlGaN is suitable for many ground based applications including:

1. UV imaging and cameras[104,105,106]
2. Bragg reflectors for laser diodes[107]

3. Chemical and biological analysis (by monitoring UV absorption lines in ozone, pollutants, organic compounds etc.)
4. Flame detection (fire alarms, missile tracking)
5. Optical communications (especially inter-satellite)
6. UV emission calibration (from UV sources and lithography)
7. Astronomical studies[108]
8. UV dosimetry measurement

The ability to tailor the cut-off wavelength over the entire UV-A and UV-B range allows for applications that require large-ratio rejection of Solar-generated visible or UV light.

However, the application of AlGaN detectors to a space mission has never before been attempted (see Section 2.2.2 for a full review of UV space-based instrumentation to date). There has been growing interest over the past 2-3 years in using these detectors, most notably from the 'Blind to the Optical Light Detectors (BOLD)[109]' European inter-organisation group[110] that is looking toward the development of the ESA Solar Orbiter[111] and the NASA Solar Probe[112].

For low cost missions with stringent mass, volume and power demands, the AlGaN detector appears to be eminently suitable for UV-C monitoring at the present time. Due to its novel use in this application, however, the effects of the space environment on the response of the detector can only be estimated. The discussion in Section 5 endeavours to predict the effects of certain elements of the LEO environment and highlight potential interference generated by further elements that have not undergone ground testing (due to the inherent restrictions in ground-based testing facilities as mentioned in Section 2.1).

2.4 Review Conclusions

It has become apparent that the novelty inherent in the research carried out for this thesis revolves around three main aspects:

1. The STORM instrument suite is part of only the second active materials degradation monitoring experiment to be placed on a spacecraft. Its use of SXR and UV detectors in such an application has not been tried before (SAMMES[50,51], the only other active materials monitoring experiment, notably omits detecting these electromagnetic radiations). The combination of environmental factors observed by STORM and MEDET as a whole will, therefore, provide novel insights into materials degradation in LEO, made more effective with the simultaneous monitoring of material samples in-situ. This is effectively two steps ahead of any other current materials experiment on the ISS, almost all of which just rely on passive exposure and post-retrieval analysis. The research and engineering work carried out to create such a unique instrument suite will be of great potential benefit to future exposure experiment design.
2. The STORM sub-experiment itself is an original engineered structure that brings together four separate detector technologies into a single unit. The novel use of the SXR and UV detectors for this application carries the potential, if successfully validated on the MEDET flight, to become a baseline model for a standard solar electromagnetic radiation monitoring package that can be subsequently flown on many varied payloads.
3. The experimentation carried out on the AlGaN detectors for the purposes of calibration represents new knowledge regarding the sensitivity of these detectors to certain wavelengths of electromagnetic radiation and charged-particle radiation. The qualification of the detectors (as part of the STORM unit) for the launch environment provides further new knowledge concerning the ability of both sets of detectors to withstand the vibration and vacuum environment they will experience.

3 Experimental Apparatus

A number of different experimental locations across Europe were used during the practical research of this thesis. This was required as no single location was available to accurately calibrate the detectors so that their performance could be predicted with as small a margin of error as possible.

The main locations that were used for experimental work were:

- The Physikalisch-Technische Bundesanstalt (PTB) in Berlin
- The Materials and Processes Division at ESTEC in Noordwijk
- The Astronautics laboratories at the University of Southampton

This chapter will describe the different test locations and the facilities available at each.

3.1 The Physikalisch-Technische Bundesanstalt

The Physikalisch-Technische Bundesanstalt (PTB) in Braunschweig and Berlin is the German National Institute for Science and Technology. It contains the BESSY II electron storage ring that has been in operation since 1998[113,114]. This synchrotron system can generate beamlines of monochromatic radiation from 3eV up to 10keV, with undispersed radiation up to a maximum of 200keV.

A synchrotron was required to be able to absolutely calibrate the spectral responsivity of the detectors in order to be able to accurately gauge the magnitude of the signal they would produce on orbit. This knowledge is critical to setting the gain on the detectors' amplifiers so that the output remains within the 0-10V signal range of the MEDET onboard data handling (OBDH) system.

Details are given in the next chapter of the beamlines the detectors were exposed to. Further details regarding the BESSY II storage ring can be found in Richter et al.[115] PTB was chosen to carry out the tests due to their efficient service and past experience in the calibration of detectors for space-based applications.

3.2 The Materials and Processes Division at ESTEC

ESTEC's Materials and Processes Division is primarily concerned with supporting the design, fabrication, and qualification phases of spacecraft missions by analysing the physical properties of the materials chosen for the vehicle. The ability to expose subjects to analogues of the different components of the LEO environment naturally lends itself to an analysis of active instrument behaviour when exposed to these components. This philosophy led to a suite of experiments carried out at the Division, taking advantage of the range of test facilities available at a single location.

The following sections describe the individual apparatus that were used throughout the test campaign.

3.2.1 The Solar Radiation Simulator (SORASI)

The SORASI is an ultra-high vacuum facility used to expose materials and electronic components to radiation and electrons.

The main chamber of SORASI is kept at a constant vacuum that can reach pressures as low as 1.8×10^{-8} mbar. To insert a test sample one must be prepared on the insertion axle in the pre-chamber. The pre-chamber is then sealed and pumped-down. Once at a low enough pressure (approx. 5×10^{-6} mbar) the door dividing the two chambers is opened and the sample is wound into the main chamber using the insertion axle.

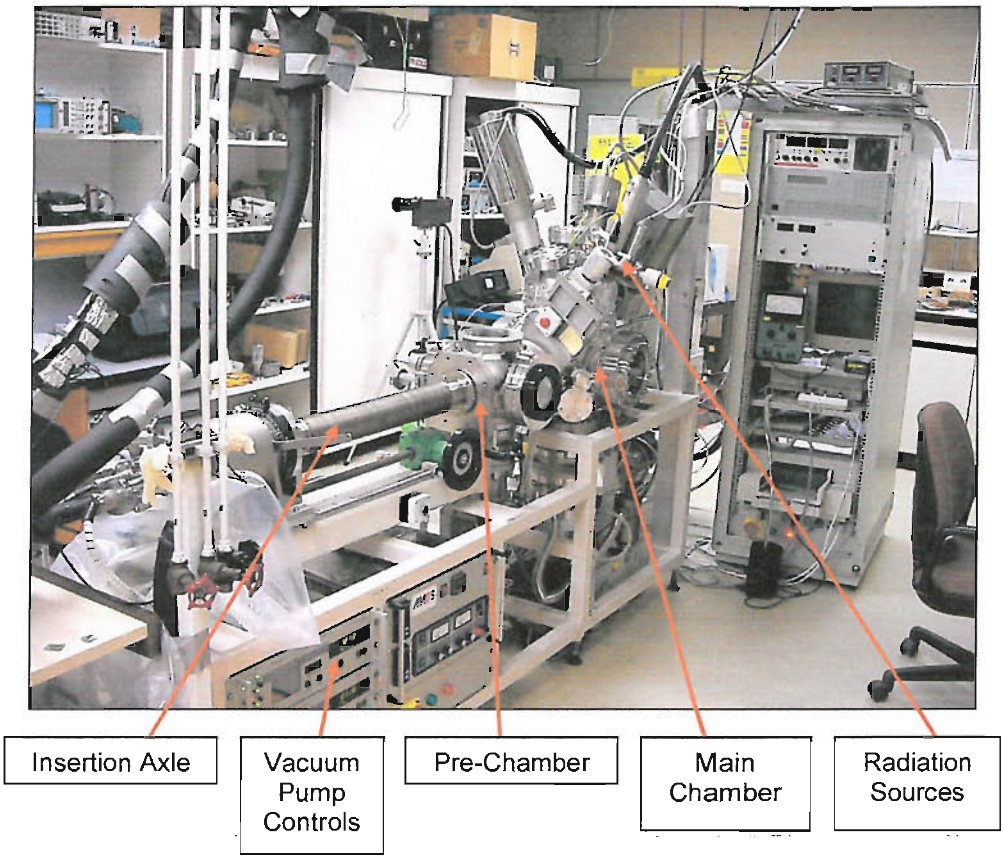

Figure 15: The Solar Radiation Simulator (SORASI)

Once the sample has been prepared and placed in the main chamber it can then be exposed to the required radiation source(s). The sources are mounted on the upper surface of the main chamber and are operated independently of the SORASI, via their own power supplies.

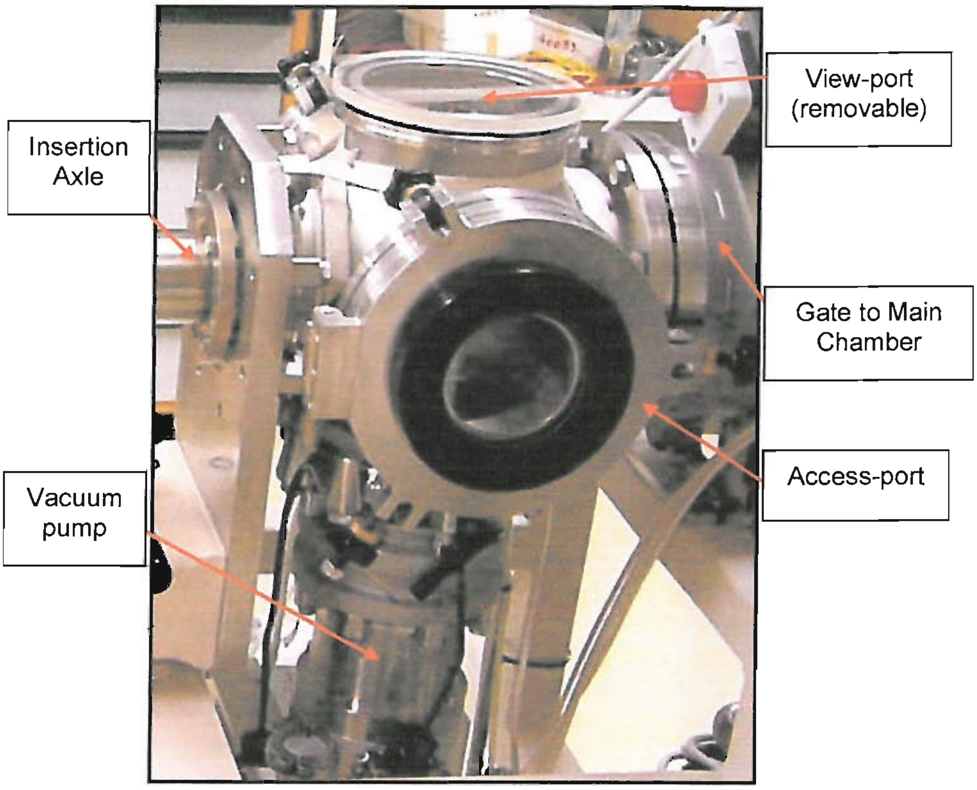

Figure 16: SORASI Pre-Chamber (external)

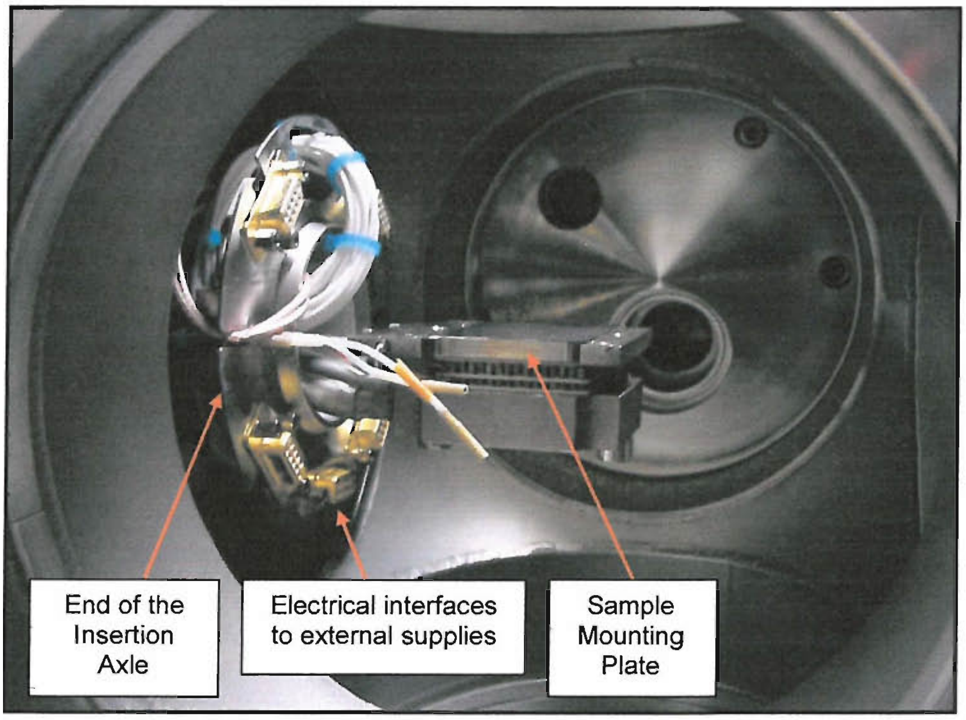

Figure 17: SORASI Pre-Chamber (internal)

The use of a pre-chamber significantly reduces the amount of time between exposures of different samples (or in this case different configurations of the detectors) as only a small portion of the total SORASI volume needs to be pumped down from atmospheric pressure. This method also reduces contamination to the main chamber by removing the bulk of out-gassed material while the pre-chamber is pumping down.

Three types of radiation sources are installed on the SORASI at present and all were used during the detector test campaign.

3.2.1.1 SORASI Deuterium Lamp (UV Source)

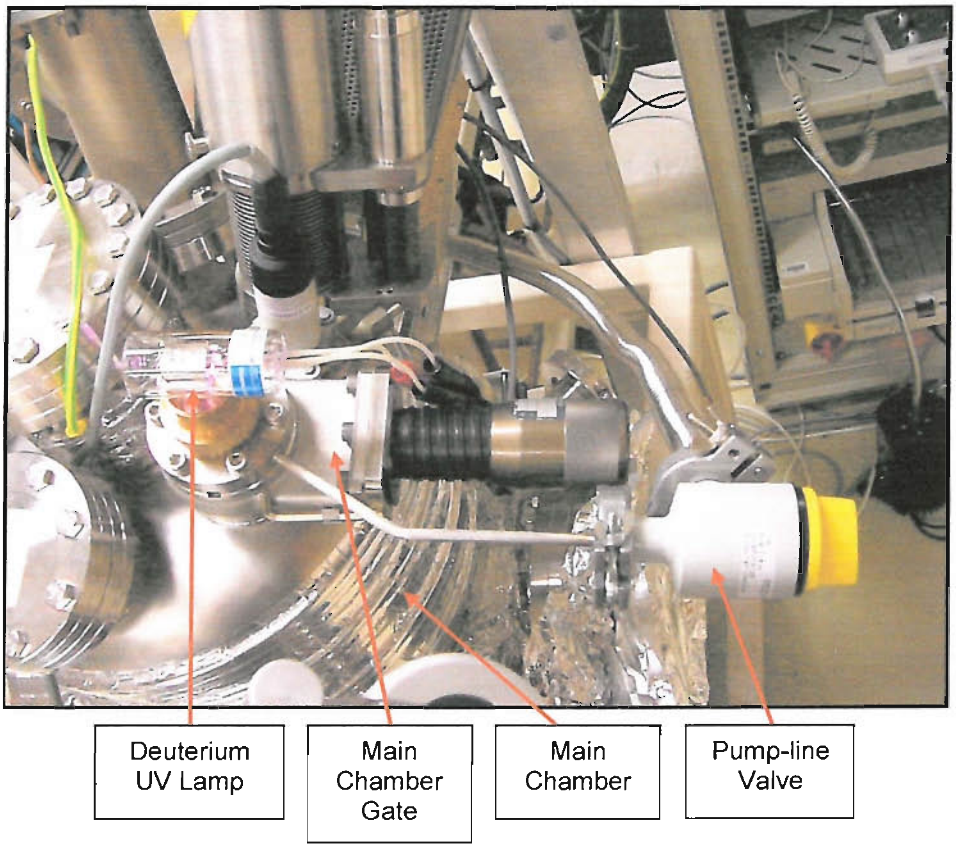

Figure 18: Deuterium Lamp on SORASI

The Deuterium Lamp is a Hamamatsu L7293, long-nose projection type, with a magnesium fluoride transmission window. It is mounted on the top of the main chamber as displayed in the above figure. A separate vacuum pump is used to reduce the pressure between the lamp's transmission window and the main chamber gate before the gate is opened to the ultra-high vacuum of the main chamber. This is to reduce contamination to the main chamber and to avoid rapid changes in pressure that might damage the lamp's transmission window. The separate vacuum pump necessitates the use of a separate pump-line with an associated valve to isolate the pump before opening the main chamber.

The spectrum of the Deuterium lamp is displayed in Figure 19, below, from the manufacturer's data tables[116]. Note, however, that they have not included data from the magnesium fluoride windowed lamp. However, it is unlikely to be very different to the synthetic silica values and a precision measurement of the spectrum is unnecessary as the quantitative measurements carried out with this lamp are only required for relative signal comparison e.g. angle of incidence response.

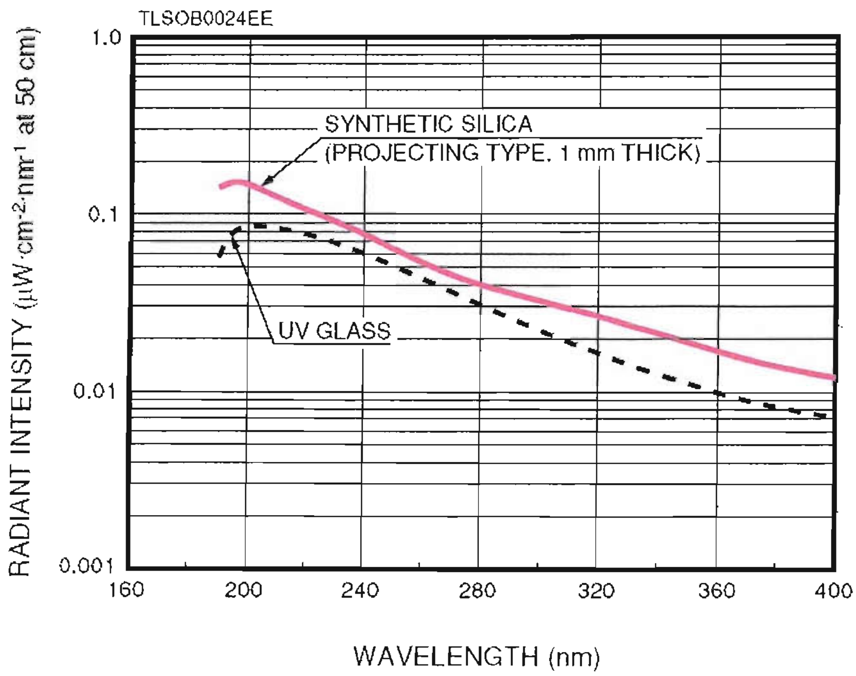

Figure 19: Spectrum for the Hamamatsu L7293 Deuterium Lamp

The manufacturer's data table also describes the spectral distribution of the lamp to be from 115-400nm, even though the lower end of this distribution is not plotted on the above figure. This lower limit is delineated by the cut-off of the magnesium fluoride window, as demonstrated in Figure 20, below.

However, earlier work demonstrates that the power density of the lamp is approximately 1.4W/m^2 in the 100-180nm range[117]. Taking the synthetic silica data above from 180-285nm we have a total irradiance of approximately 1.49W/m^2 within the response range of the AlGaN photodiode.

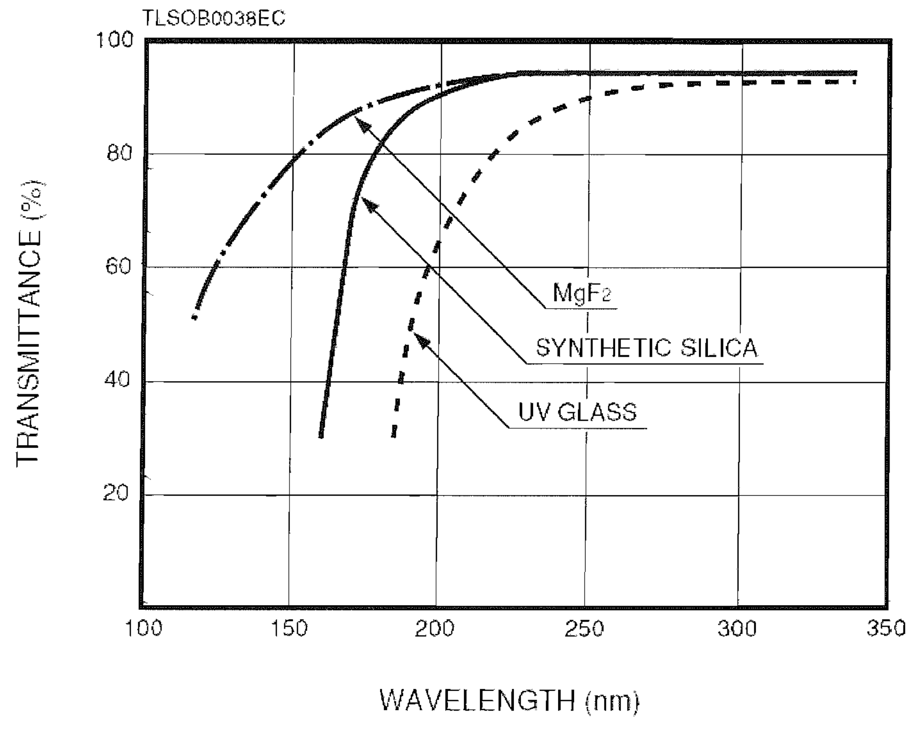

Figure 20: Transmission Spectra for the Hamamatsu L7293 Lamp Windows[116]

Using a Solar UV figure of approximately 8.2W/m^2 (see Figure 71) within this range produces an acceleration factor of 0.18. Therefore, the signal produced by the AlGaN detector when illuminated by the SORASI UV lamp should be approximately one fifth of that generated by the average Solar UV flux in LEO. This is only an approximate calculation due to the change in sensitivity of the

AlGaN detector over this wavelength range, but it produces a ball-park figure within which to interpret the UV detector output.

3.2.1.2 SORASI X-Ray Gun

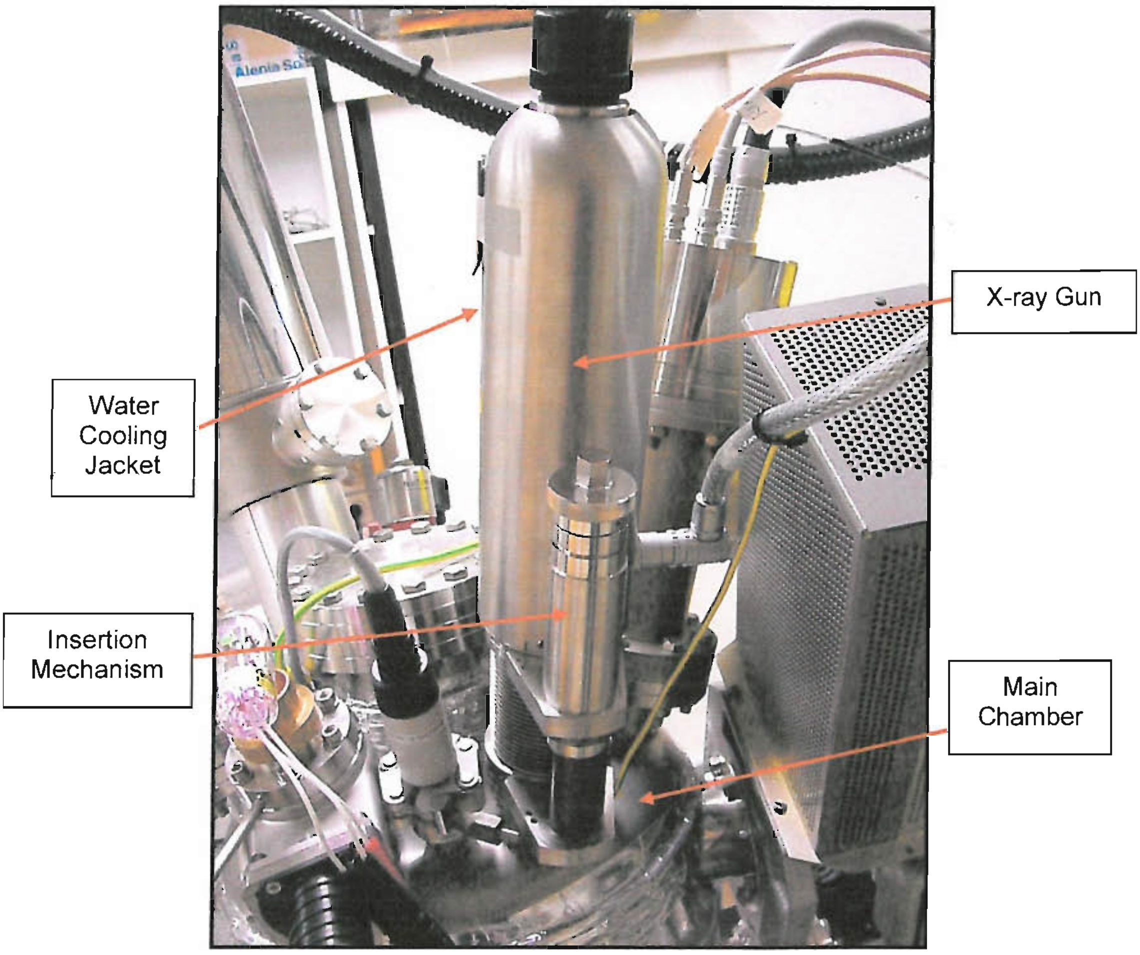

Figure 21: X-ray Gun on SORASI

The X-ray gun on SORASI is a Fisons XR3E2 X-ray source produced by VG Microtech. Although it has dual magnesium and aluminium anodes, only the aluminium anode was used during testing due to its ability to produce K_α photons of higher energy at 1486.6eV (as opposed to magnesium's 1253.6eV)[118]. This allowed the Si detector to be irradiated by a marginally greater range of energies (although quantised) to better fit its expected detection range of 1-10keV.

The gun operates on the principle of accelerating electrons, discharged by a filament, on to the aluminium anode. The collisions between the accelerated electrons and the anode remove the anode's electrons from their shells. As electrons in higher positions cascade down to fill the vacated ones, X-ray photons are produced. The generated X-ray distribution is isotropic, but the barrel of the X-ray gun absorbs those that do not travel directly to the exit window.

A great deal of heat is also produced by the electrons colliding with the anode and this is removed by an outer jacket that circulates water as a coolant.

Photon production can be altered via the power supply by changing two variables of the electron acceleration:

- The High Voltage setting controls the potential over which the electrons are accelerated; the higher the potential, the higher the energy of the incident electrons and the more X-rays can be generated by the resulting greater level of ionisation (although the energy of the X-rays themselves are dictated by the respective quantum energy levels of the anode's electron shells between which electrons cascade). This will thus increase the flux density of the X-ray beam.
- The Beam Sequence setting controls the rate at which electrons are emitted from the filament. By increasing the Beam Sequence, more electrons are produced and accelerated on to the anode. Again, this will increase the flux density of the X-ray beam.

The X-ray gun can also be inserted up to a maximum of 5cm into the SORASI main chamber. This is another method whereby the X-ray flux can be increased on to the target sample.

Using the magnesium anode, a Beam Sequence of 22mA and a High Voltage of 11kV the integrated power of the X-ray beam is approximately 1.5W/m^2 at 0cm insertion into the SORASI main chamber[117]. An assumption has been made that using the aluminium anode at the same settings would produce a similar power output even though the distribution of the various photon energies will be significantly different. This assumption is justified by the fact that at the same power settings, the electron beam on to the anode will generate the same integrated power of X-ray flux, to a close approximation. The integrated flux is all that is monitored by the detector, as it has no spectral resolution apart from its inherent sensitivity range.

The anticipated soft X-ray flux between 1-10keV in Low-Earth Orbit (LEO) is approximately 10^{-8}–2×10^{-3}W/m^2 [119] (ranging from the average background to a powerful X-class flare event). This implies an acceleration factor of between 750-150x10^6 for the X-ray gun. The low end of this range (750) corresponds to an acceleration with respect to a high-energy flare (X20), while the high figure (150x10^6) represents the acceleration with respect to the average Solar X-ray background. Although the acceleration factors imply that the X-ray detector is being exposed to fluxes many orders of magnitude higher than expected, it is important that this is quantified so that the gain of the associated amplifiers can be properly configured.

3.2.1.3 SORASI Electron Gun

The electron gun on SORASI is a STAIB Instruments reflection high energy electron diffraction (RHEED) EK-300, capable of producing electrons over a 1-

25keV range. It is manually operated, allowing control of the position, width and current of the electron beam on the target.

When in the main chamber the beam position and width is monitored by incidence on to a zinc sulphide-covered plate that fluoresces to produce a visual reference. The visible ‘spot’ created on the zinc sulphide is necessary to accurately set the focus between experimental runs (by measurement against a scale inscribed on the plate) to maintain the electron flux at a steady value per unit area.

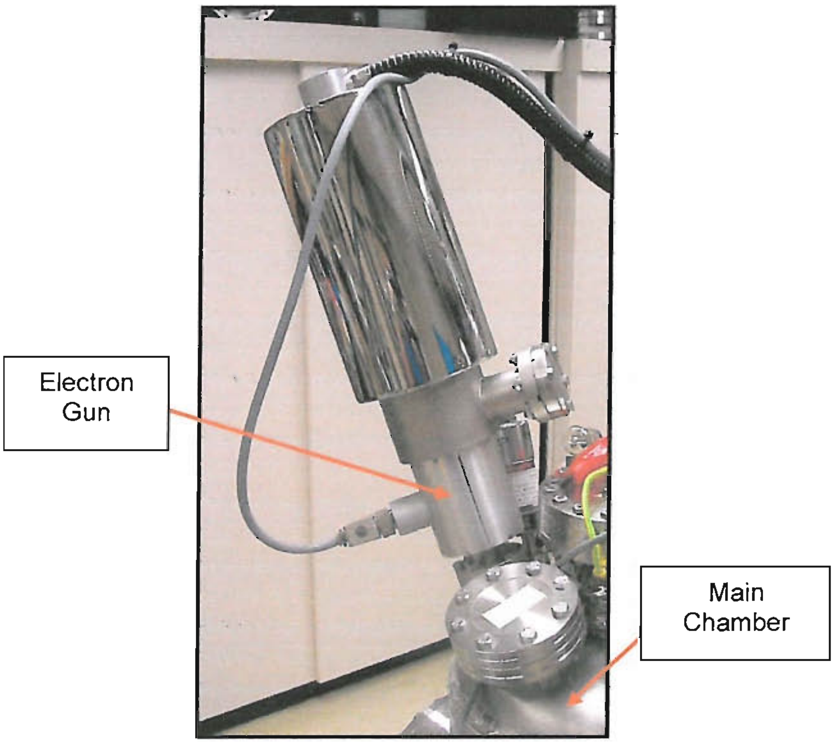

Figure 22: Electron Gun on SORASI

When taking measurements of the response of the detectors to the electron beam it was important to know the flux as well as the electron energy. However, the flux is unknown via the manual controls as small changes in the power supply current have a large effect on the incident power of the beam.

This problem was resolved by measuring the electron beam directly. An aluminium foil target was placed on the circuit shield to act as an electron absorber, a crude Faraday Cup. Connected via a SORASI electrical feed-through to an ammeter and then to ground, the current emitted by the electron gun could be directly monitored when the beam was positioned over the target foil. The drawback of this method is accurately estimating the amount of the electron beam that is effectively converted to a measurable current.

Electrons incident on to a target material are not necessarily absorbed but can be transmitted, backscattered, or scattered before absorption – all will act to reduce the measured current.

Loss of current through transmission of the electrons is minimal due to the 30μm thickness of the aluminium foil. The greatest penetration of electrons will be at the highest energy level: 25keV. A theoretical expression for the depth of penetration of electrons in aluminium is given by[120]:

$$r = \frac{2.76 \times 10^{-2} A\, E_0^{\;1.67}}{\rho\, Z^{0.89}}$$

Equation 4: Theoretical range of penetration of electrons incident on a material

Where: r = depth of penetration (μm)
A = atomic mass (27 for Al)
E_0 = energy of incident electrons (keV)
ρ = density of the material (g/cm^3) (2.7g/cm^3 for Al)
Z = atomic number (13 for Al)

For incident electrons with energy of 25keV this penetration depth will be 6.08μm (3 sig. fig.) – significantly smaller than the thickness of the foil used. Undoubtedly a tiny percentage will be transmitted due to the inverse exponential mechanism of attenuation, but this amount is insignificant when compared to the losses by other means.

Loss of current through interaction with the aluminium atoms takes the form of characteristic x-ray production, bremsstrahlung radiation, phonon excitation (heating) and cathodoluminescence. Unfortunately these factors could not be monitored directly within the main chamber; however, some of their effects can be estimated.

Bremsstrahlung (or braking) radiation is caused by the interaction of the electrons with the electric fields of the aluminium atoms. The acceleration of incident electrons through this interaction produces a continuum X-ray spectrum of photons. The proportion of the beam's energy that is lost during this process is given by:

$$p = (1.1 \times 10^{-6})\, Z\, E_0$$

Equation 5: Proportion of electron beam energy lost as bremsstrahlung radiation

For 25keV electrons incident on aluminium the proportion, p = 0.00036 (5 d.p.) or 0.036% of the beam energy is converted into X-ray continuum radiation.

For characteristic X-ray production the incident electrons collide with and promote aluminium electrons to higher atomic orbitals. These then decay back to their ground state, releasing an X-ray of fixed (or characteristic) wavelength. However, like the production of the X-ray continuum, this process is very inefficient and it can be expected that <1% of the incident electron beam energy will be converted to X-ray photons in this manner.

Cathodoluminescence, or visible light emission, from the target can be ruled out due to aluminium's nature as a conductor. Cathodoluminescence is generally restricted to materials with semiconductor properties where promotion of valence to conductance electrons, by interaction with the incident electrons, results in their later decay back to the ground state, emitting photons of a few eV in the visible light range.

Phonon excitation, or heating, is the same mechanism that occurs in conductors when an electric current is passed through them. Although it could not be measured effectively in the experimental setup used, the low currents generated by the electron gun are too small to lose a large proportion of their energy as radiated heat, due to the high electrical conductivity of aluminium.

Backscattering of the incident electrons and emission of electrons from the target are the remaining sources of lost current.

Auger electrons can be emitted from the aluminium when a characteristic X-ray is generated but immediately reabsorbed by a bound electron. The electron is emitted with a characteristic energy, but only from regions very close to the target surface as their low energy makes them easy to reabsorb. As noted above, X-ray generation is very inefficient and this is also reflected in Auger electron production. As a result, the Auger production mechanism is also very inefficient and losses of <1% of the beam energy are expected.

Secondary electrons can also be emitted from the target surface where an incident electron has ionised an aluminium atom, exciting a bound electron with enough energy that it can escape from the aluminium altogether. However, like Auger electrons, secondary electrons must be emitted from a shallow layer on the target surface or they will just be reabsorbed by the aluminium. This reduces their yield significantly and so, coupled with their low energies, reduces the amount of current loss generated. This energy loss is estimated as <2% of the beam strength, higher than Auger electrons as they can be emitted from slightly deeper within the aluminium target.

The final energy loss mechanism, and the one that has the greatest effect, is that of backscattering of the incident electrons. In this case the incident electron is reflected straight back out of the foil target by interaction with the electric field of an aluminium atom. The proportion of electrons backscattered is highly dependent on the atomic number of the target material. A theoretical approximation of this proportion can be calculated with the following equation[121]:

$$n_b = n_{b20}[1 + a\ln(\tfrac{E_0}{20})]$$

Equation 6: Backscatter proportion of electron beam

Where n_b = proportion of electron beam that is backscattered

$n_{b20} = -5.23791\times10^{-3} + 1.5048371\times10^{-2}Z - 1.67373\times10^{-4}Z^2 + 7.16\times10^{-7}Z^3$

$a = -0.11128 + 3.0289\times10^{-3}Z - 1.5498\times10^{-5}Z^2$

This produces a backscatter proportion for aluminium of 0.161 or 16.1% (3 sig. fig.) at an incident electron energy of 25keV and of 0.200 or 20.0% (3 sig. fig.) at an incident electron energy of 1keV. These values match well to those that have been derived experimentally[122].

So the sum total of electron beam losses we can expect at 25keV is approximately 20% and at 1keV approximately 24%. These estimations are necessarily crude, but they indicate that the values measured for the current are significantly lower than the absolute value for the electron beam itself, so some upward adjustment to the data can be made.

3.2.2 UV Pen in Nitrogen Well

In addition to using the radiation sources on the SORASI, alternative external sources were also used. The first was a small mercury UV lamp, the Pen-Ray lamp (catalogue no. 90-0012-01 (11SC-1L)) produced by UVP International, Inc., hereafter described as the 'UV pen'. It has a spectral range of approximately 200-400nm and thus only the lower end of this was detected by the AlGaN detector. As the pen was used in an open environment, it was important to remove any oxygen from between the pen and the sensor so that as little UV would be absorbed as possible. To accomplish this, the test apparatus was placed in a makeshift nitrogen-well to replace the immediate atmosphere with pure, dry nitrogen.

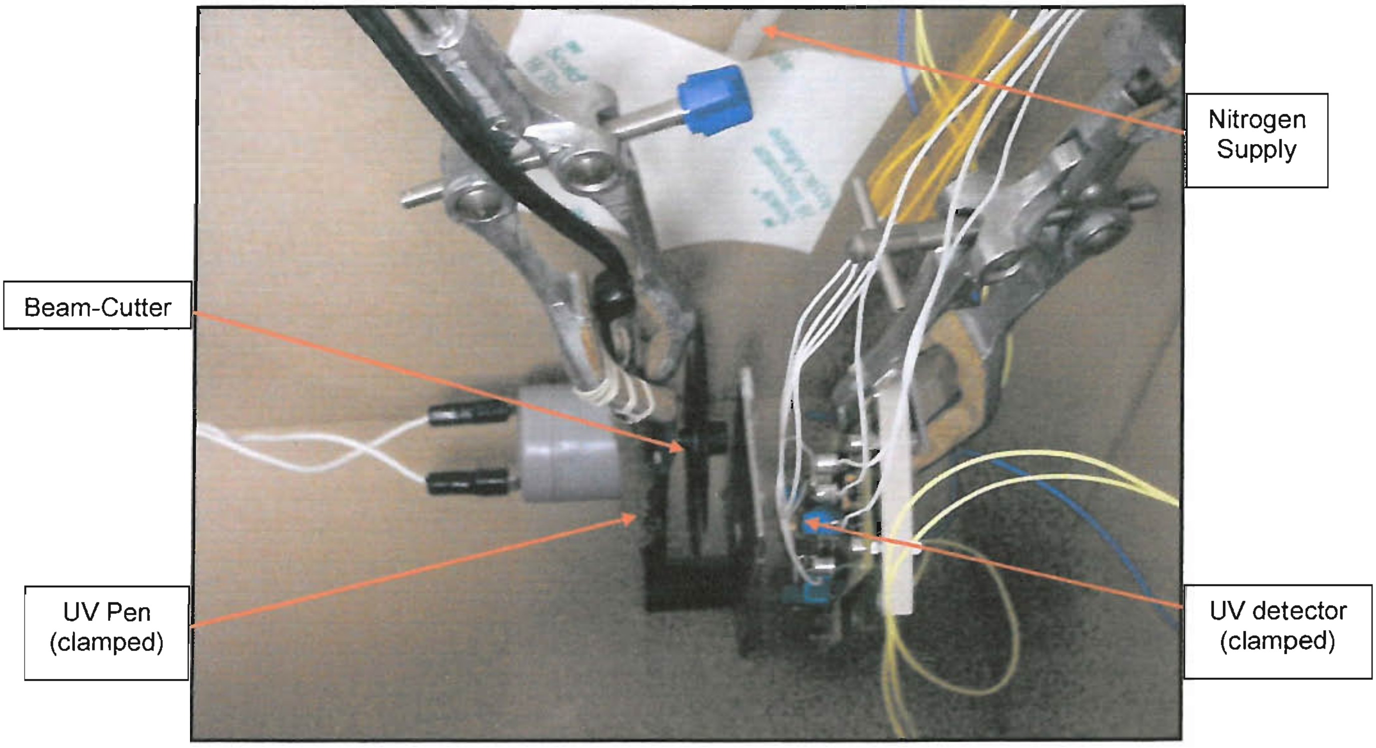

Figure 23: Close-up view of the Nitrogen-Well apparatus

The above figure displays the UV pen during testing within the nitrogen well. With the entire test-apparatus clamped into position it was possible to accurately adjust the distance of the UV pen from the detector using a stand-rail that supported the pen's clamp. A beam-cutter was used to control the UV flux on to the AlGaN detector so that the relative response could be measured without relying on an absolute determination of the lamp's intensity. This ability was not available inside the main chamber of SORASI.

Gautois meshes were also used to cut out known percentages of flux to augment the data gathered by the beam-cutter.

3.2.3 Philips UV Lamp

The second external UV source used was a Philips B2-1 UV lamp. This was used for the calibration of the high wavelength responsivity of the AlGaN detectors (see section 4.2.1 below).

The lamp was water-cooled to maintain its operating temperature and was suspended at a fixed distance above the detectors during the measurements. The lamp was too large to fit within a nitrogen-well. However, as it was used for monitoring the longer UV wavelengths the absorption of the lower wavelengths by oxygen and ozone interaction was not considered important. Coupled with the high power of the lamp, the rapid air circulation due to the cooling systems and the monitoring of the laboratory atmosphere with an ozone meter, the amount of radiation attenuated would be minimal.

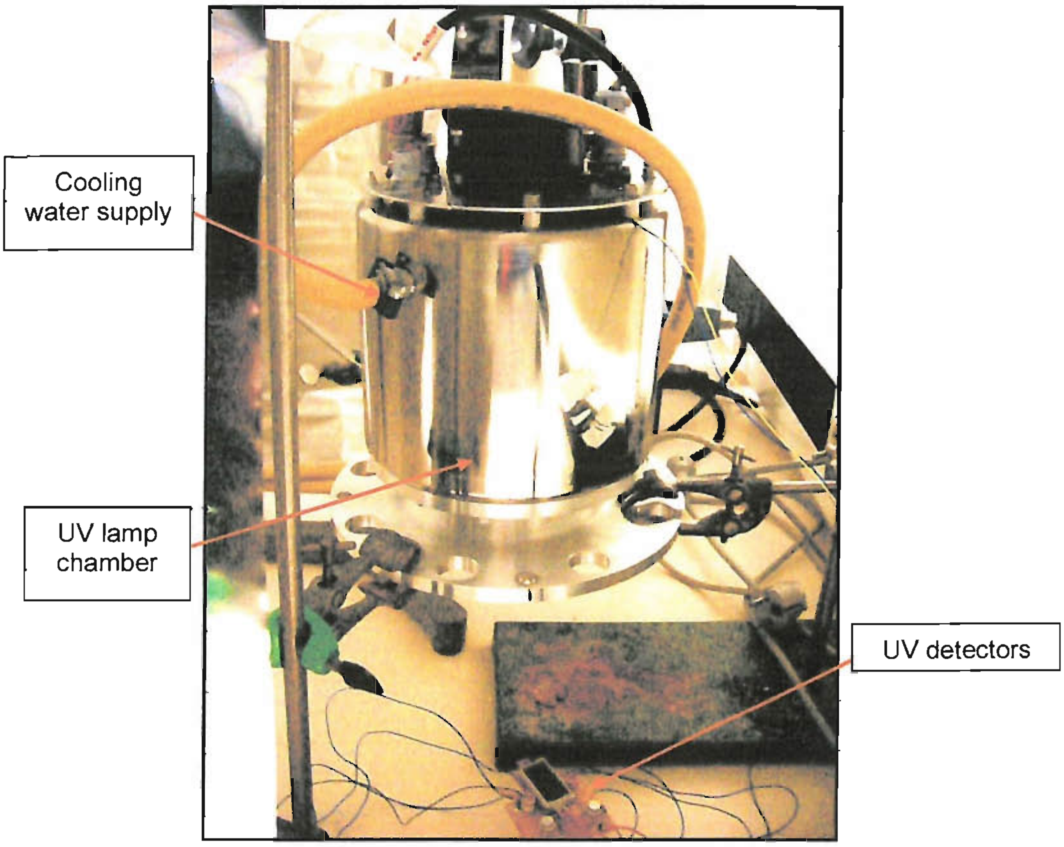

Figure 24: Philips UV lamp

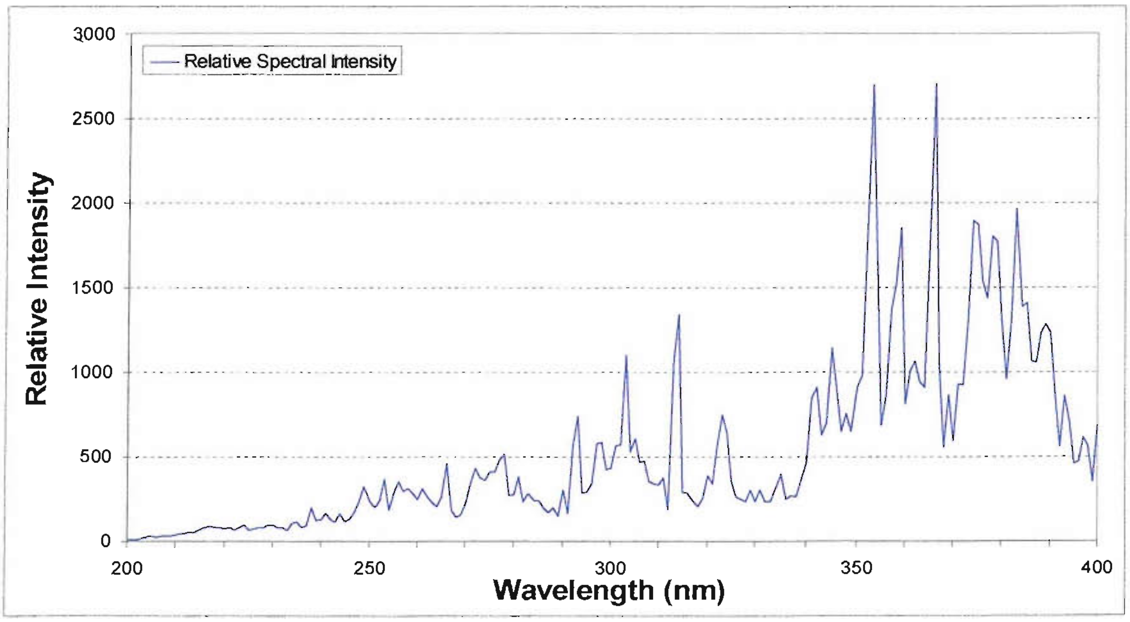

Figure 25: Philips UV lamp output spectrum

The above spectrum for the lamp is that measured by ESTEC in the materials laboratory. Although it extends beyond 400nm, this is the region required to calculate the responsivity of the AlGaN detector around the upper wavelength cut-off.

In addition to the output spectrum, the flux from the lamp was also monitored by the use of three calibrated UV detectors that covered the UV-A, UV-B and UV-C bands respectively. These were UV radiometers produced by Dr. Gröbel UV-Elektronik GmbH (parts 811110, 811120, 811130). Measuring the flux in this way was vital in order to calculate the responsivity of the AlGaN detectors from the output signal they produced under illumination by the Philips UV lamp.

3.2.4 Detector and Amplifier Test Circuits

Throughout the test campaign at ESTEC a number of detectors were exposed to the radiation sources. These were mounted on 'test' circuits that could be attached to the SORASI mounting plate or used to hold the detectors when under external lamp illumination. The test circuits were constructed in-house at the Electronics and Computer Science department of the University of Southampton, but required a number of alterations during the test campaign to allow for different filters to be attached and to replace amplifiers and feedback resistors (to set the gains of the detectors).

The circuits were bolted to an interface plate, required for connection to the SORASI sample plate (see Figure 17, above). The detectors were placed at one end so that they could be inserted into the SORASI by the greatest distance, thus enabling them to be positioned over as great a range of the radiation beams as possible. This required a protective, grounded Kapton covering to be wrapped around the rest of the circuit, to protect it from the radiation, without blocking the detectors' view.

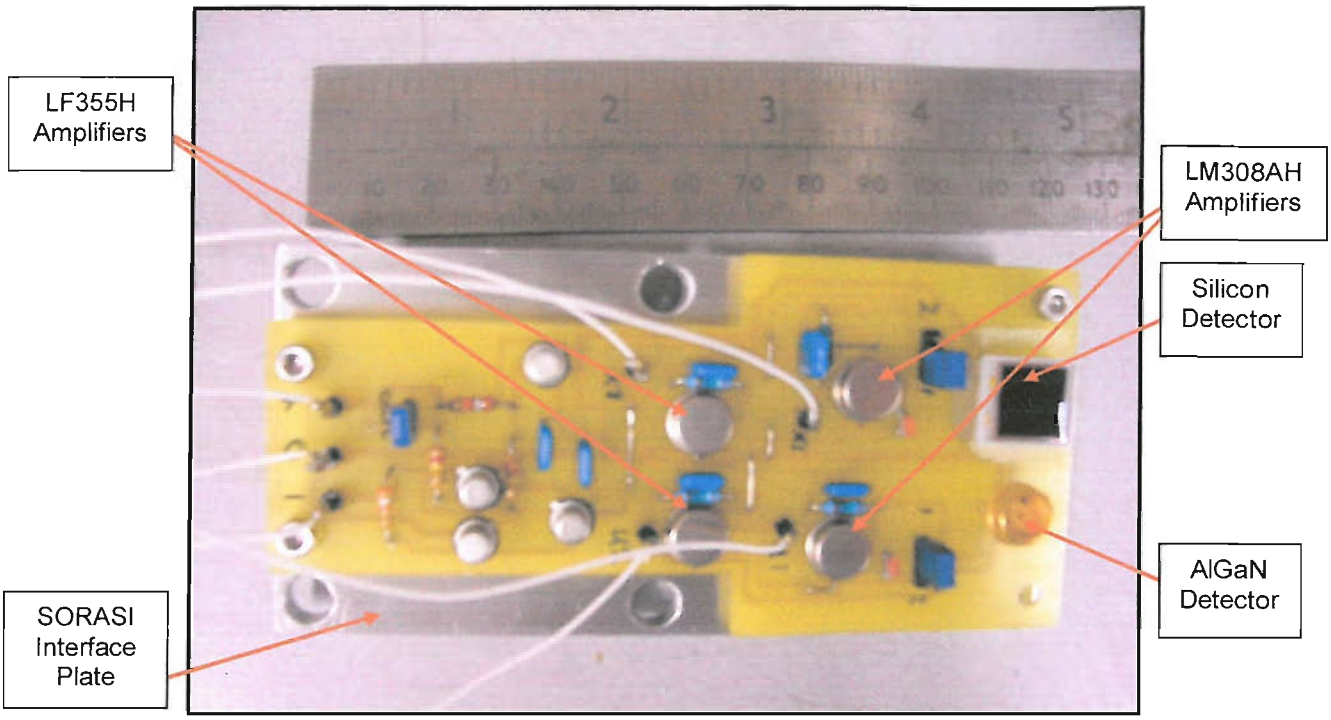

Figure 26: Test Circuit 1 mounted on the Interface Plate

All the components used were commercial-off-the-shelf (COTS) parts, although a number were changed between circuit versions as the final choices for the STORM instrument were made.

In addition to the radiation detectors, temperature sensors were also used on the circuit for direct, in-situ measurements. The temperature sensors were platinum PT100's, rated for use within an ultra-high vacuum environment. Their wide range, stability and small size allowed the detectors and amplifiers to be monitored throughout long experiment cycles.

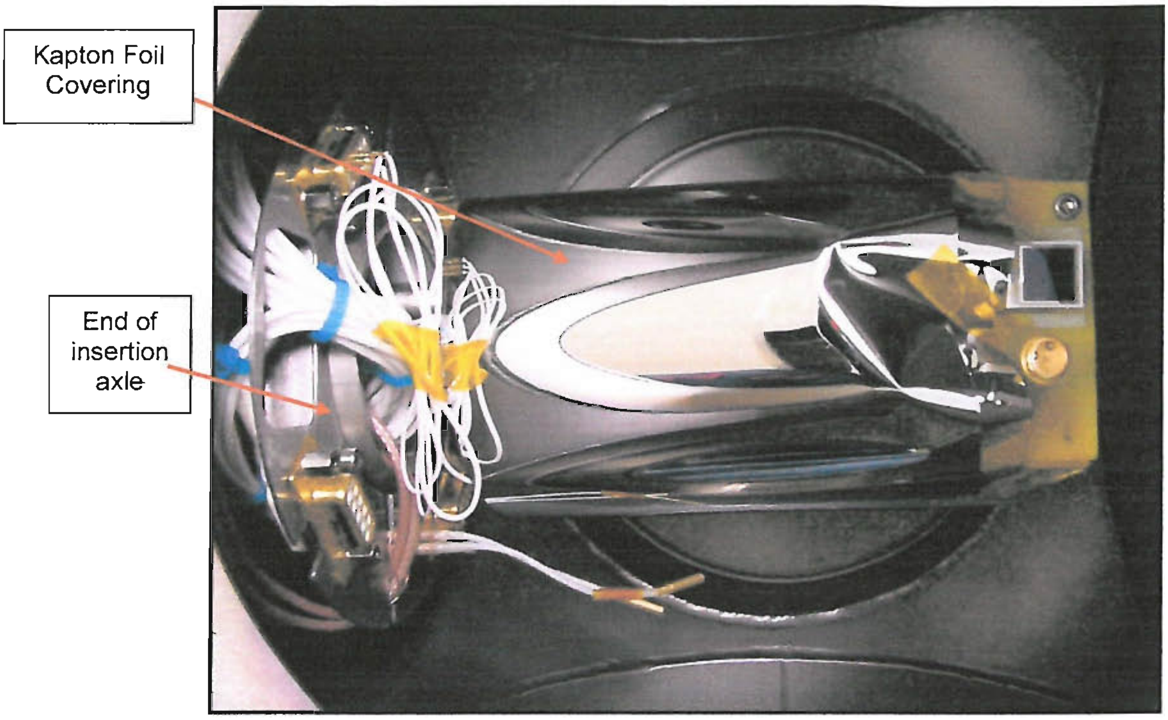

Figure 27: Test Circuit 1 in Pre-chamber

Aluminium and beryllium foil filters were also used on the radiation detectors for a number of the tests. These filters were used to cut out visible and UV light from the silicon detector and UV light from the AlGaN detector to test its sensitivity to X-rays.

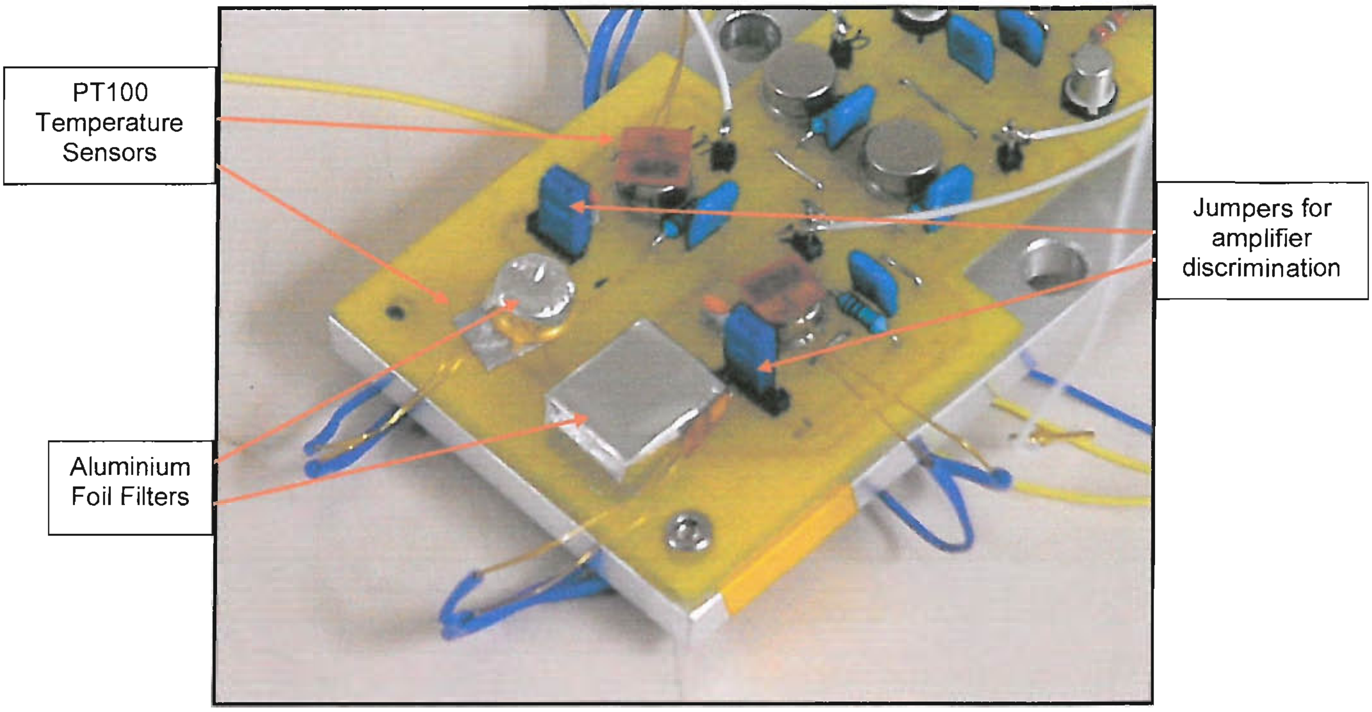

Figure 28: Close-up view of Filtered Radiation Detectors on Test Circuit 1

Jumpers on Test Circuit 1 allowed the signal to be manually switched through two different amplifiers for each channel. This was done to test the amplifiers concerned in the early stages of the campaign in order to aid a decision on the versions to be used in the final design. All the amplifiers on Test Circuit 1 were set to the same gain of 20 (resulting in a sensitivity of 20 V/A) so that their performance could be directly compared.

Test Circuit 2 was of a similar design but incorporated both filtered and bare AlGaN detectors. Due to size restrictions amplifier switching could not be supported, but by this stage the choice for the final design had been made. The ability to monitor both versions of the AlGaN detector within the same environment was very useful for understanding the differences in their responsivity to the radiation sources.

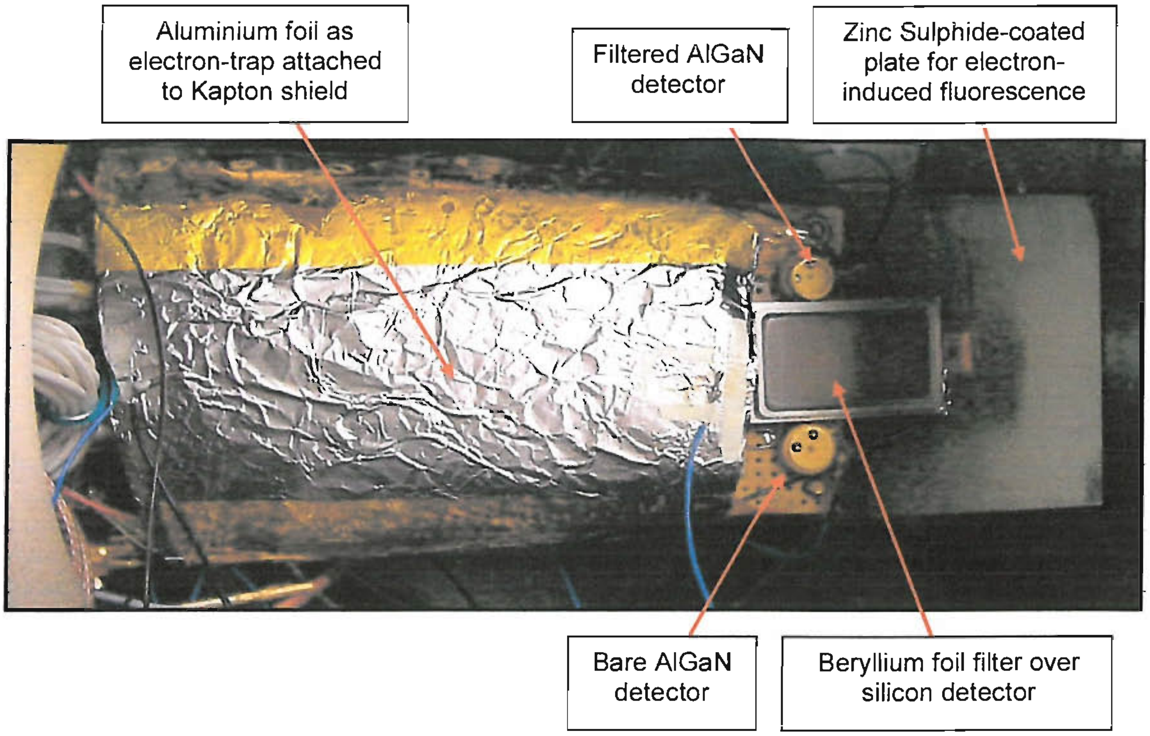

Figure 29: Test Circuit 2 in SORASI Pre-Chamber

At this stage in the campaign the beryllium filters were also available for incorporation into the tests. Another useful addition was the final choice of PT100 sensors – these were sandwiched between the detectors and Macor support spacers, similar to the configuration in the STORM instrument.

The detectors on this test circuit were set with a gain of 470 x 10^6 (sensitivity of 0.47 V/nA), to better analyse the detectors' responses at lower flux levels.

3.3 The Astronautics Laboratories at the University of Southampton

The astronautics laboratories were used for the final tests on the completed STORM models. This involved vibration, depressurisation and thermal shock testing of the engineering/spare and flight models. Although these tests were for the STORM instrument as a whole, as a corollary they are applicable to the onboard detectors.

The vibration tests were carried out on a Ling Dynamic Systems V721 LPT600 shaker table. The STORM instrument was sequentially fixed in each axis by a custom-built mount for the tests. The full qualification levels to which the equipment was subjected were as follows:

Frequency (Hz)	**PSD in X** (g^2/Hz)	**Frequency** (Hz)	**PSD in Y** (g^2/Hz)	**Frequency** (Hz)	**PSD in Z** (g^2/Hz)
20	0.01	20	0.01	20	0.01
50	0.08	50	0.1	50	0.08
100	0.08	110	3	110	0.08
160	0.5	120	3	120	0.13
500	0.5	140	0.13	270	0.13
560	1.4	670	0.13	460	0.8
600	0.3	720	0.024	480	0.8
700	0.3	2000	0.005	600	0.04
800	0.02	-	-	800	0.04
2000	0.005	-	-	1000	0.014
-	-	-	-	2000	0.005
Overall GRMS (g)	18		14		13

Table 2: Vibration Loads for Qualification Testing

These loads were derived from the MEDET finite element model; they are those as calculated for the STORM centre of mass. As a result, they will not perfectly match the frequency-dependent accelerations experienced by the detectors due to the mechanical construction of the STORM instrument – the transmission of the accelerations will be slightly damped or amplified due to the stiffness of the support pins and printed circuit boards. However, such modifications will be small as the instrument has been designed as a rigid unit, so the above figures can be taken as a good approximation for the lower limit of survivability of the detectors.

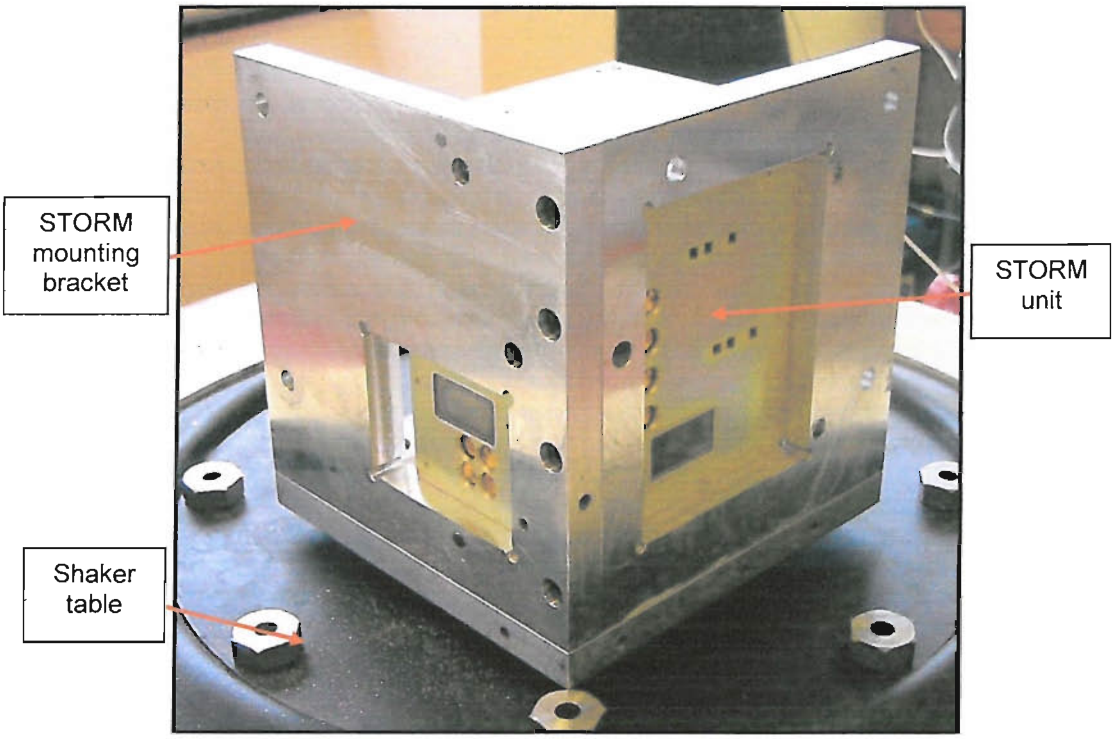

Figure 30: STORM installed on shaker table

The depressurisation test was a simple pump-down of a vacuum chamber while the full STORM unit was inside and operating. This was to simulate launch depressurisation loads as atmospheric gases within the unit evacuated via the instrument and D-connector apertures. Of most concern were the filtered AlGaN detectors and the beryllium mounting frame shroud that surrounds the silicon detector and sits flush against a collar on the circuit board to block all stray light. These were the parts that could potentially crack or burst on depressurisation, but no damage was caused over a 40s cycle down to ~100μbar – far faster than the Shuttle depressurises on ascent.

4 Experimental Tests and Results

This chapter describes the tests carried out with the experimental apparatus and provides the results from those tests. The tests are categorised according to the equipment used: either at PTB, ESTEC or Southampton.

4.1 PTB Tests

The tests carried out at the Physikalisch Technische Bundesanstalt (PTB) were concerned with the absolute calibration of the X-ray and UV detectors' response in the relevant wavelength ranges that they would be monitoring on board STORM.

Knowledge of the response of the detectors, the amount of current generated by a known amount of incident radiation of a certain wavelength, is critical to the prediction of what on-orbit signal range is to be expected and the calculation of the necessary level of amplification to acquire a strong signal. Absolute calibrations were carried out by the beamlines at PTB for both detector types plus transmission measurements of the beryllium filter for the X-ray detector.

Unfortunately, due to cost restrictions on the use of the PTB facilities it was only possible to calibrate a single Si detector and two AlGaN detectors, one with filter and one without. There was thus no way to directly assess the consistency of response of each set of detectors to be used on STORM. As a result it has been necessary to assume that the detectors and their associated amplifiers respond very similarly to each other.

4.1.1 Si Detector Responsivity and Be Transmission

It is essential to know the current-generating capability of the silicon detector across the spectral range of interest. This was analysed by measuring the output current of the detector when illuminated by an absolute radiation source.

The response of the Si detector was compared to that of a cryogenic electrical substitution radiometer by alternately placing both detectors in to the synchrotron beams. For the soft X-ray measurements the soft X-ray radiometry beamline, the four-crystal monochromator beamline and the wavelength-shifter beamline were used from the BESSY II electron storage ring.

The photon beam had diameters of ~1mm x ~1mm (FWHM), the typical radiant power was below 10μW and was linearly polarized to better than 90%. As the photon beam could not cover the entire detector surface the responsivity could be directly measured without the adjustment for detector area required for the AlGaN detector, below. This also allowed a scan of the homogeneity of the spectral responsivity of the detector to be made by sweeping the beam across the detector in the x and y axes.

The measurements were carried out by first observing the radiant power of the photon beam at the monochromator exit with the reference detector. The Si photodiode is then placed within the photon beam and the generated photocurrent measured. During measurement the stored electron current in the synchrotron ring gradually decreases as the monochromatic radiation beam is generated. Thus the output photocurrent from the Si photodiode is normalised against the measured current within the storage ring. After the photodiode measurement has been taken the reference detector is inserted into the beam once more for another reading to check for any possible instabilities that have not been picked up by the storage current monitor.

The measurements for the detector homogeneity for the spectral responsivity are shown below in Figure 31, Figure 32, and Figure 33. In Figure 31 the contours are in 0.5% relative steps with the minimum (darkest) value being 89%. In Figure 32 and Figure 33 the contours are in 0.1% relative steps with the minimum values being 97.8% and 99.3% respectively.

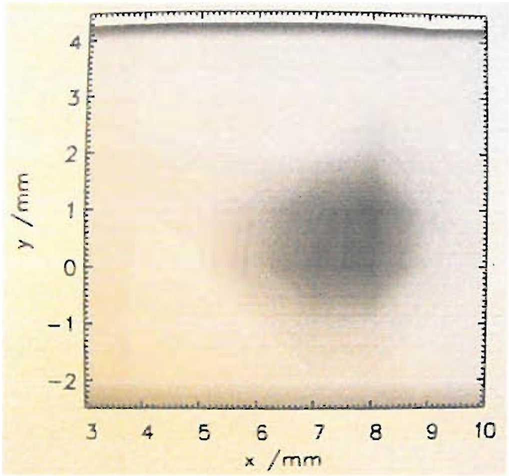

Figure 31: Si Detector Homogeneity at 0.5keV

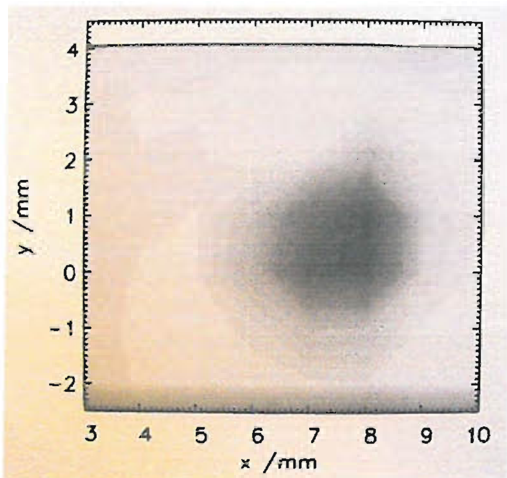

Figure 32: Si Detector Homogeneity at 1keV

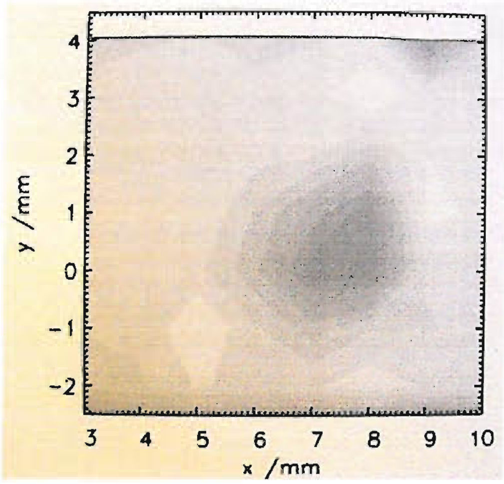

Figure 33: Si Detector Homogeneity at 1.5keV

On all three images the large spot is most likely a result of localised degradation of the detector when it was placed in the high energy photon beam, the magnitude of degradation being a function of the total dose received while in the beam. As a result the main regions of importance are the surrounding areas that were undamaged. At all three energy levels the homogeneity is reasonable: 0.5% at 0.5keV, 0.2% at 1keV and 0.1% at 1.5keV (although there does appear to be a slight defect in the upper right corner visible at the 1keV and 1.5keV levels).

For the integrated spectrum that the detectors will monitor on-orbit such a level of homogeneity is adequate as the incident radiation will itself be homogeneous across the area of the detector. The detector will undoubtedly degrade over its lifetime, but this degradation will apply equally across the detector surfaces.

From the images it is also clear that radiation damage will have a greater effect on the spectral responsivity at lower energies. This is to be expected as the lower energies will be more susceptible to absorption and scattering by induced inhomogeneities in the surface structure of the detector. The degradation of the detectors' signals during the lifetime of the mission will therefore be energy dependent – the detection ability of the detector across the energy range of interest will change non-uniformly. There is, unfortunately, little that can be done to calibrate for this non-uniform degradation without the capability of repeated spectral responsivity calibration.

For the measurement of the transmission of the beryllium window the signal produced by the reference detector was compared before and after insertion of the beryllium window into the photon beam. This allowed for a direct and simple observation of the amount of radiation of the specified energy that was being transmitted.

The transmission curve of soft X-rays through the beryllium window is displayed in Figure 34 below.

As can be clearly seen, there are no absorption discontinuities for the transmission curve over this energy range. The cutoff is therefore as clean as possible for a single material filter. While it was the aim to achieve a cutoff at 1keV the 50% transmission mark is at 2 keV, so the 1-2keV range is not as well represented as hoped. However, the cutoff at 1keV is very good and by 4keV the transmission is over 90%. Greater than 99% transmission occurs at 6.5keV, within the planned 1-10keV range of the detectors.

The transmission of the beryllium window can be multiplied with the responsivity of the detector to provide the sensitive operating range of the detector/filter system, as shown in Figure 35, below. Greater detail of the silicon detector responsivity at lower energies can be seen in Figure 36, below.

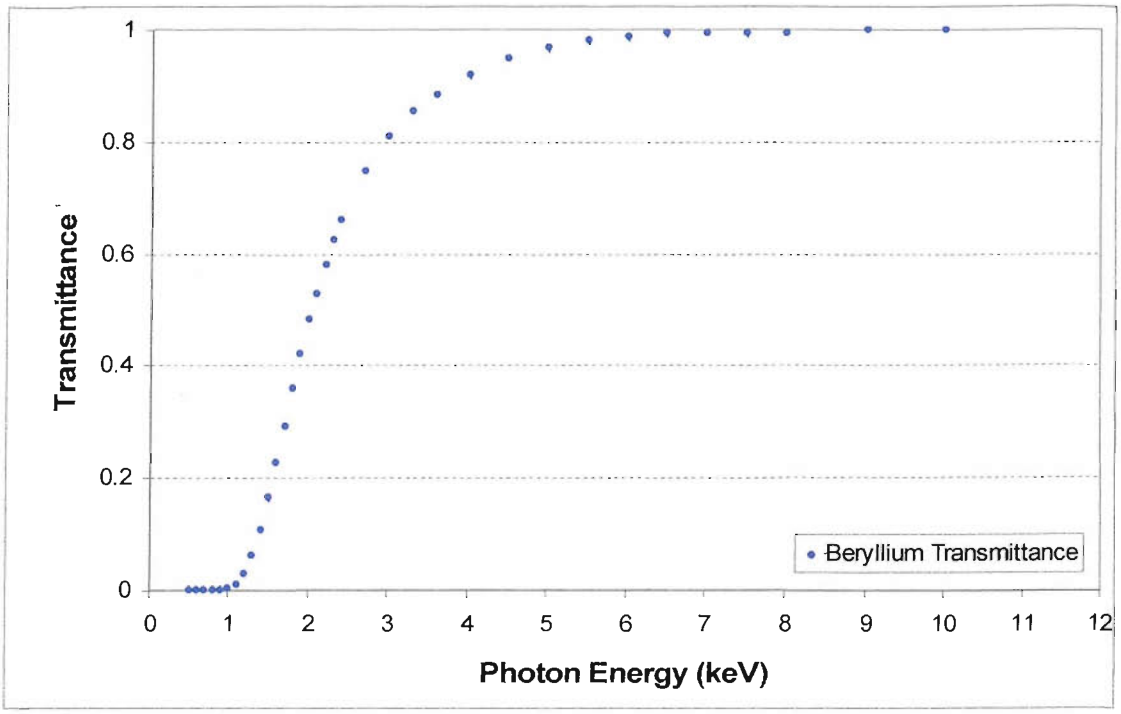

Figure 34: Transmission of Soft X-rays through the Beryllium Window

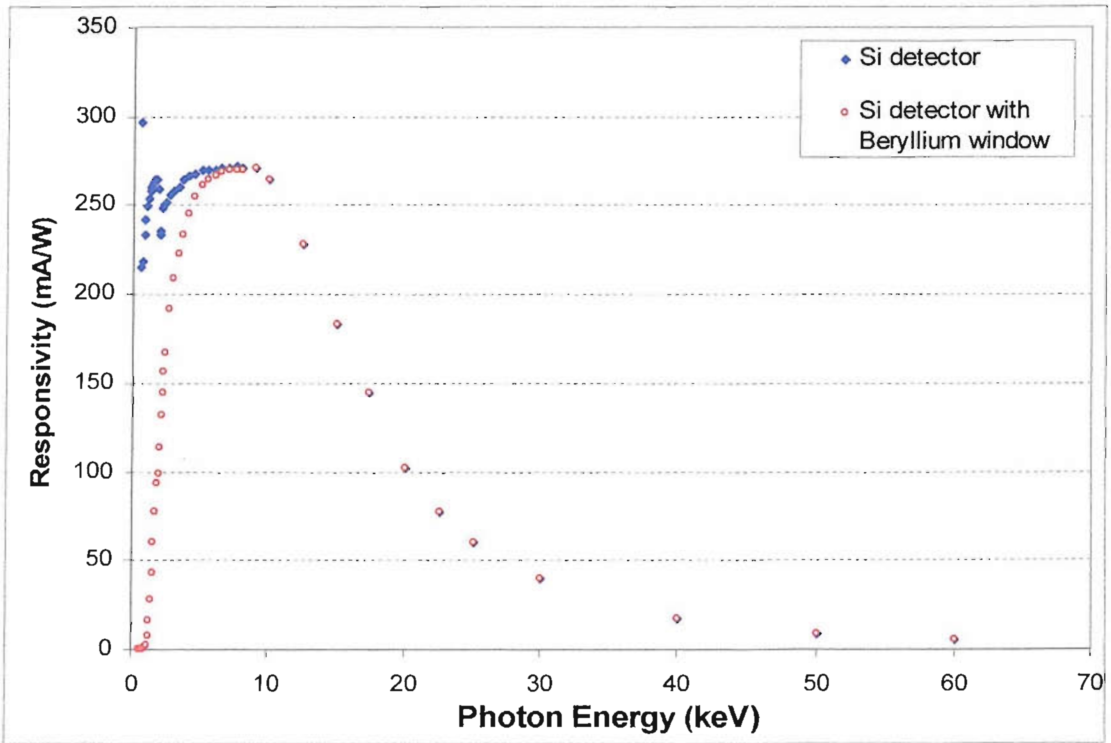

Figure 35: Responsivity of the Silicon detector with and without the Beryllium window

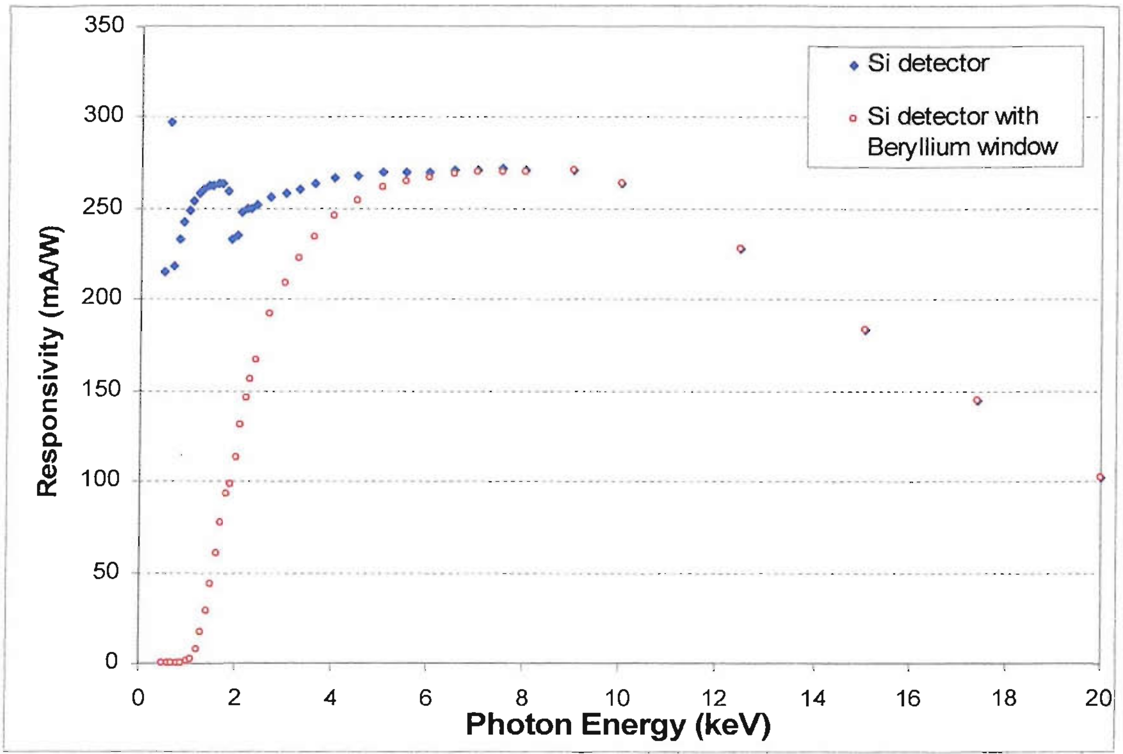

Figure 36: Detail of Silicon detector responsivity at lower energies

Due to the electronic structure of silicon it has a more complex responsivity at the lower energies between 0-2keV. However, these inhomogeneities are neutralised by the beryllium window transmission within this area, resulting in the smooth arch of responsivity of the combined detector/window system.

The silicon detector is more sensitive to higher energies than expected, descending to a 50% (normalised to maximum responsivity) detection rate at approximately 17.9keV. Combined with the sharp cut-off at the lower energies, this provides a FWHM measurement of 15.7keV centred at 10keV.

Although this 'top-heavy' bandwidth includes higher energy photons, their impact on the signal level will be mitigated by their relatively lower flux at these higher energies. This can clearly be seen by comparing the flux at 2-10keV and above 10keV in Figure 37, below[123] (using the black unbroken line as the total expected flux). Over the 2-10keV range the flux levels drop by approximately 2 orders of magnitude, while from 10-60keV (the effective upper limit of detectability of the silicon photodiode) it drops by a further three orders.

Therefore the vast majority of the integrated signal generated by the silicon detector will be composed of the 2-10keV range within the target bandwidth.

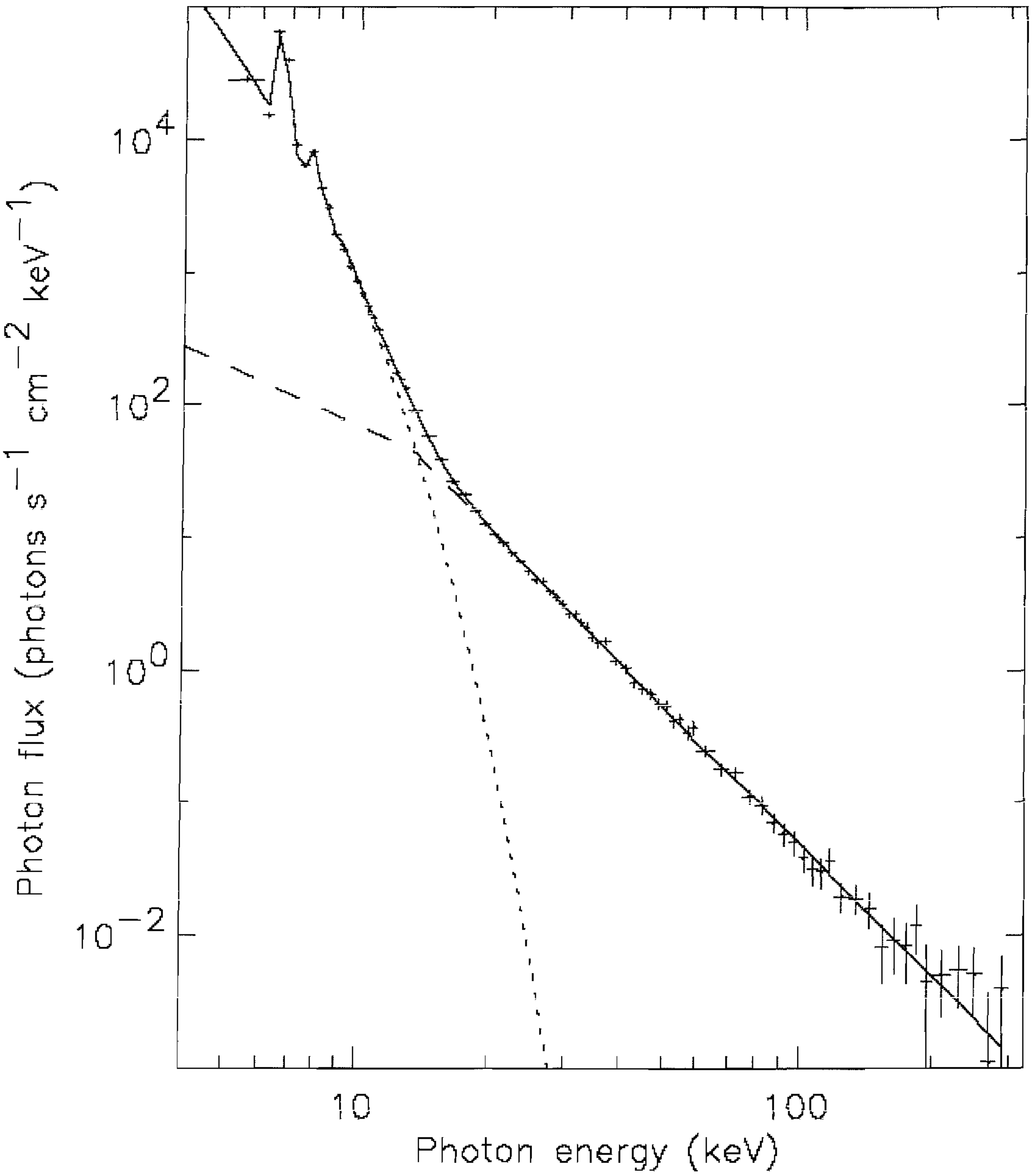

Figure 37: Solar Flare X-ray Spectrum from RHESSI Data

The quantum efficiency of the detectors, as a function of incident photon energy, can be produced from this data as the percentage of the energy of the photons that is converted into current (using the silicon band gap energy of 1.14eV for the amount required to promote an electron into the signal current). This is displayed in Figure 38, below.

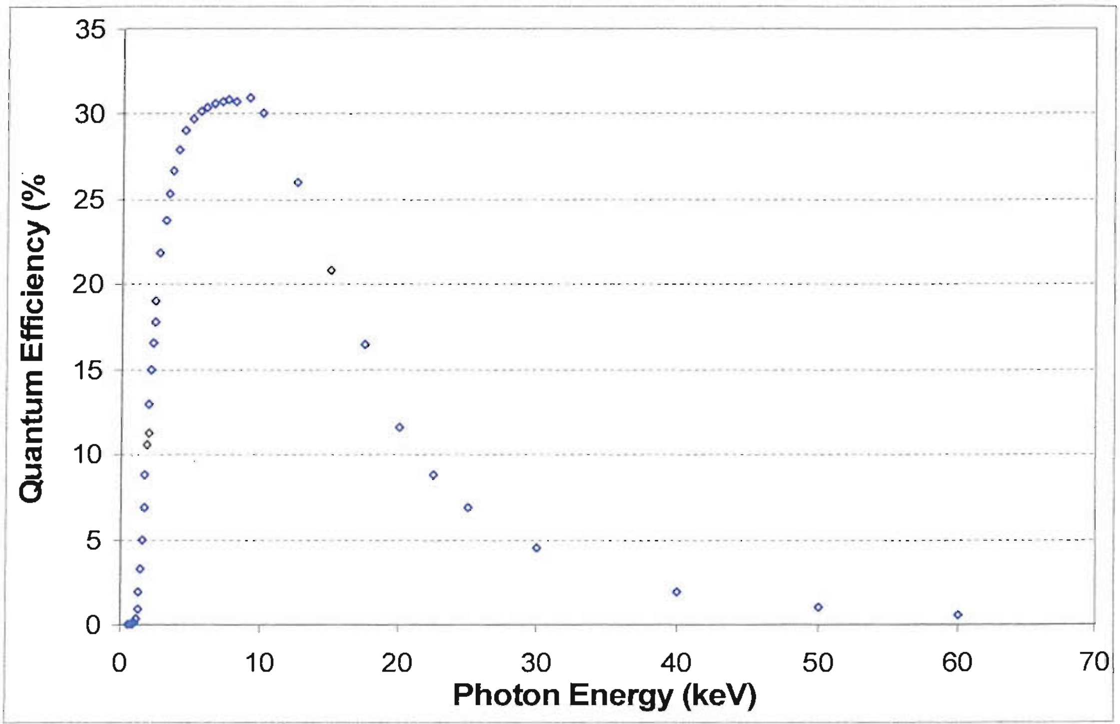

Figure 38: Silicon detector quantum efficiency as a function of photon energy

This plot of the quantum efficiency is for the complete system of the detector plus the beryllium window. As such, it very closely resembles the responsivity plot in Figure 35, above.

4.1.2 AlGaN Detector Spectral Irradiance Responsivity

The most important information concerning the operation of the AlGaN photodiode is the signal generation it is capable of across the spectral range of interest. This can be analysed by the accurate measurement of the output current from the diode during irradiation from an absolute radiation source.

The exposure to the beamlines at PTB achieved this for two diodes; one with and one without a fused silica filter. It is unfortunate that financial restrictions did not allow for testing over a larger sample number of photodiodes, but detector consistency can be estimated with other comparisons between non-absolute UV sources.

The measurement of the sensitivity of the two photodiodes allows an estimate of the signal differential between the filtered and non-filtered versions when exposed to UV on orbit. The differential will then provide a relative response to the Lyman-α region that can be tracked over time.

The detectors were exposed to the Normal-Incidence Monochromator (NIM) beamline at PTB's BESSY II electron storage ring. The calibrations were carried out with and without a circular aperture, 2.5mm in diameter, to isolate the effects of incident radiation on the contact electrodes of the photodiodes. Due to the beam dimensions of ~1mm x ~3mm for selected wavelengths (with aperture: 105, 120, 121.6, 125, 150, 157.6, 180, 200, 230, 260, 280nm; without aperture: 100, 110, 121.6, 125, 130, 140, 150, 180nm; with aperture and filter: 150, 157.6, 180, 200, 260nm; without aperture and with filter: 145, 150, 180nm) the detector was scanned across the beam and then numerical integration applied to produce the responsivity. This was carried out to make sure there were no inhomogeneities in detector response, due to its position in the beam, which could produce systematic errors affecting all of the results. The first measurements on the AlGaN detector with aperture and without fused silica filter contained the highest number of wavelength checks. Fewer checks were needed for the subsequent aperture/filter configurations as only those regions of the response that differed from the initial run required double-checking.

In between these selected wavelengths the detector was placed in the centre of the beam profile and the measurement wavelengths taken at 5nm intervals – the assumption being that as no inhomogeneities were recorded at the above wavelengths then further checks on the interconnecting wavelengths were unnecessary.

Due to the beam of incident radiation being larger than the active detector area the spectral irradiance responsivity is calculated instead of the spectral responsivity directly. This is due to the detector area being of critical importance if the beam is larger – the spectral irradiance responsivity is the current generated at a specific wavelength per unit incident radiant power for each unit area of the beam that is absorbed (i.e. the area of the detector). Conversely the spectral responsivity can be directly monitored if the entire monochromatic beam falls within the detector – the beam has a known power so the output current can be directly associated to this flux of incident radiation.

The spectral radiant power of the spectrally dispersed synchrotron radiation, generated by the electron storage ring, varied between 20nW and 200nW for all the measurements. These temporal variations were corrected for by monitoring the relative changes in the electron current within the storage ring.

In order to generate the absolute values for the spectral irradiance responsivity of the two AlGaN photodiodes, their output signal was referenced against transfer detector standards (the detectors transferred from the primary standard to the test beamline)[124]. The standards used were two semiconductor photodiodes (ETH UVS-100) that were rotated into the beam during each wavelength measurement interval. The transfer standards were previously calibrated against the cryogenic electrical substitution radiometer, SYRES[125], which is used by PTB as the primary detector standard.

The following Figure 39 presents the spectral irradiance responsivities of the two detectors, with and without the aperture. This is the raw data generated by the absolute calibrations.

To correct for the spectral irradiance to generate the responsivity, the data must be divided by the area of the detector (0.196 mm^2). This only affects the scale of the y-axis and results in the similar plot demonstrated in Figure 40.

These data clearly demonstrate a signal disparity between the filtered and non-filtered detectors across the entire wavelength range. Even though the fused silica is transparent at wavelengths above 140nm it still causes significant attenuation of the incoming photons. As we shall see, this creates a considerable problem for measuring the signal differential produced by variations in flux of the Lyman-α region.

Concern over the effect of photoionisation from the electrode contacts of the detectors prompted the shielding of the electrodes for the calibration with the use of an aperture. Some results were also taken without the aperture, as demonstrated in the 'without aperture' and 'with fused silica' legends of Figure 39 and Figure 40.

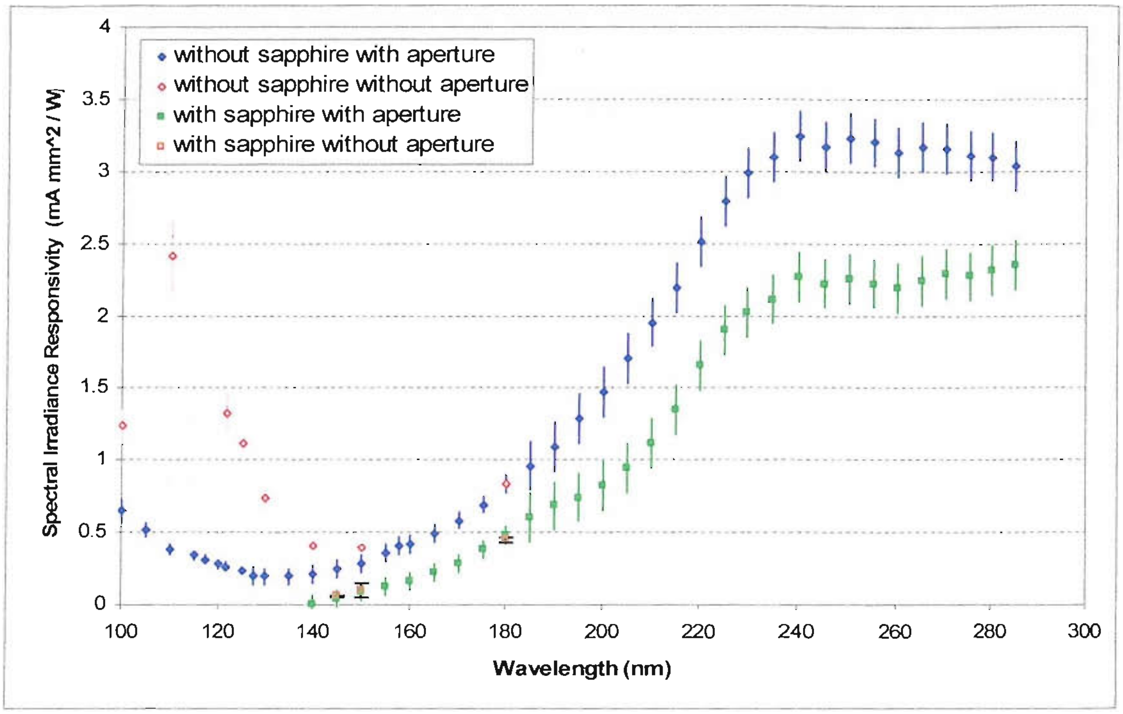

Figure 39: Spectral Irradiance Responsivity of AlGaN detectors

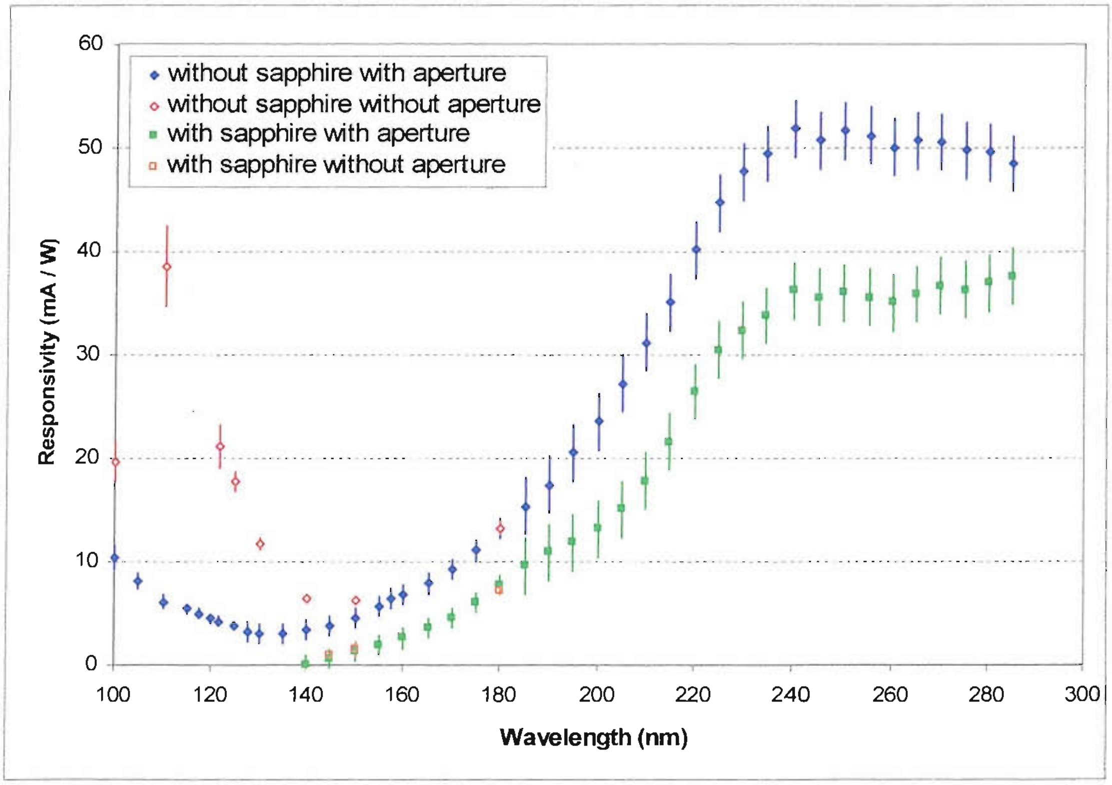

Figure 40: Responsivity of AlGaN detectors

The difference for the fused silica-filtered detector is negligible – this may well be due to the filter itself blocking the higher energy photons that cause the photoionisation.

However, the difference with the unfiltered detector, in the wavelength range of 100-140nm is marked. The detector actually has an increased responsivity in this region. Unfortunately, the signal fluctuated markedly in these regions, making for the large error bars and the lack of data points – the error bars being calculated as the combined absolute standard uncertainty: the combination of the standard deviations of the measurements used to calculate the responsivity. As such, even with the increased sensitivity, this makes it unsuitable for use as a detector of these wavelengths without some form of shielding.

For the STORM module the use of metal apertures placed over the top of the detectors would have severely restricted their field of view and so reduced the amount of data they could capture. As a result an alternative filter on the bare detectors was used by applying araldite over the electrodes themselves. This has the added advantage of increasing the structural support for the delicate gold contact wires leading from the electrodes to the detector itself. Unfortunately the araldite covering was applied after the PTB tests had been completed, so no further absolute calibration of this modified configuration was possible. It is assumed that as araldite is a polymer-based compound it will be opaque to UV wavelengths and thus have an equivalent effect to the metal aperture used during the tests. Unfortunately, due to time constraints during testing it was not possible to verify this assumption – on-orbit analysis of the results will provide further information based on the differences in signal level between the bare and filtered detectors.

An aperture mechanism for the fused silica-filtered detectors was considered unnecessary based on the data produced above.

A comparison with the fabrication company's (APA Optics Inc.) calibration curve for the bare AlGaN detector gives the plot in Figure 41, below. The fit appears poor for the data region provided. However, no information is provided on the calibration equipment used for these measurements at APA Optics – the smaller range that their data cover is most probably a function of the equipment used). The data is, at least, within the correct order of magnitude. There is a danger of oxygen contamination having altered the responsivity of the bare photodiode prior to testing at PTB. However, the fused silica-filtered photodiode is encased, due to the filter, within a dry nitrogen environment – and it responds in a similar (though attenuated) fashion to the bare photodiode.

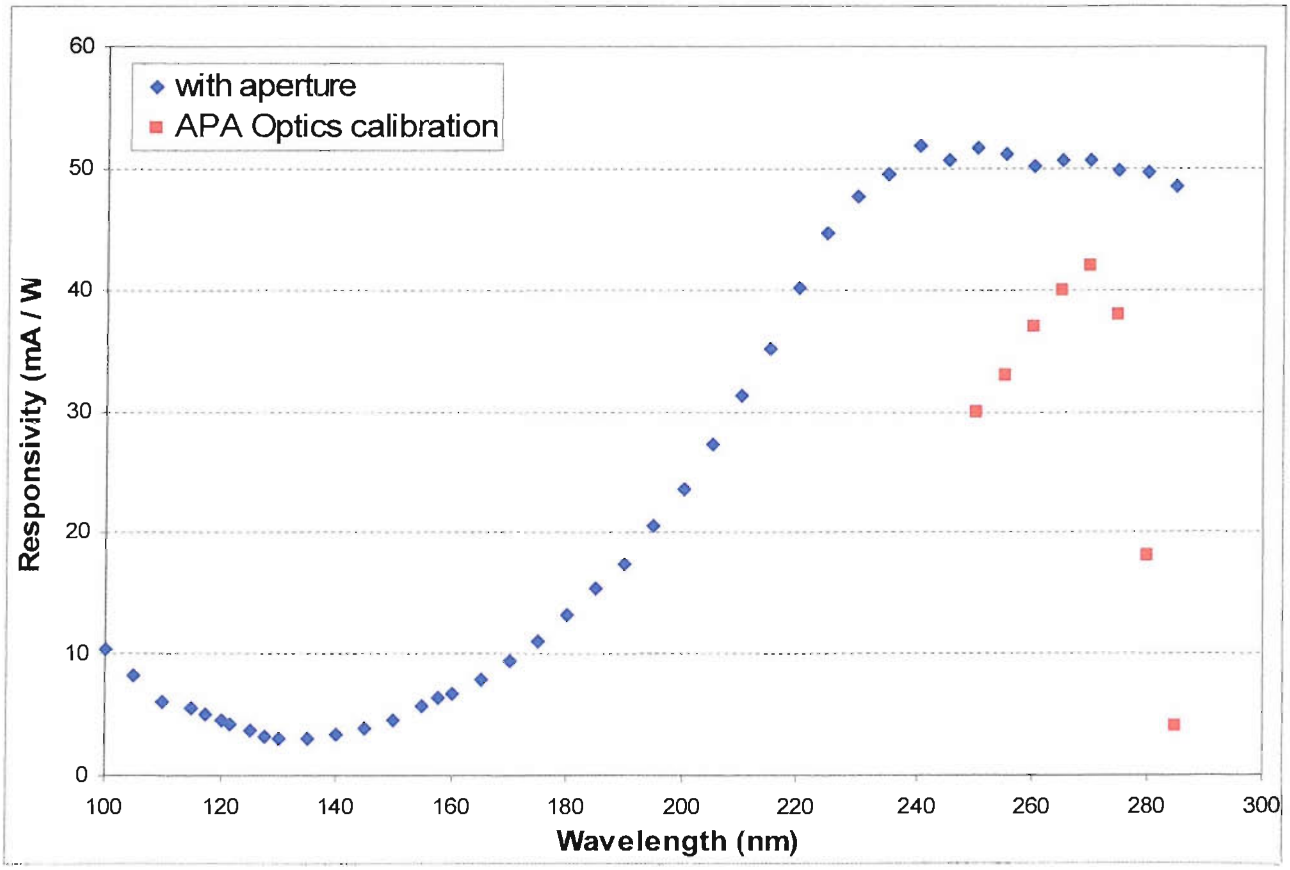

Figure 41: Comparison of bare AlGaN detector responsivity to APA Optics' data

The fact that the PTB tests do not demonstrate the same cut-off at the 285nm region necessitated further calibration tests to be carried out – without the knowledge of the upper-limit for the wavelength cut-off it would be impossible to calculate an accurate ratio between the signal from the Lyman-α region and the rest of the UV spectrum. The determination of the cut-off was carried out at ESTEC (see section 4.2.1, below) as budget restrictions barred further measurements to be made at PTB.

4.2 ESTEC Tests

The tests carried out at the ESTEC Materials Division laboratories have been concerned with the further calibration of the AlGaN detectors, the response of the detectors to changes in flux level, angle of incidence, electron irradiation and the stability of the detectors with constant signal input.

Apart from the further calibration of the AlGaN detectors, these tests are necessarily quantitative as there is no means for precise spectral response measurements to be taken as the detectors integrate a broad-band signal source. However, taken with the absolute qualitative measurements provided by the PTB synchrotron facility, they provide necessary information on how the detectors will operate on orbit.

4.2.1 Further AlGaN Detector Spectral Irradiance Responsivity

Following on from the PTB calibration measurements for the AlGaN detector (see section 4.1.2, above) it was necessary to determine the cut-off in responsivity at the higher wavelength range (around 285nm). Without a monochromatic source a different approach was required for the determination. This necessitated the use of an external UV lamp at the ESTEC materials laboratory (see section 3.2.3, above).

The output signal of the detectors is given by:

$$S_{total} = \int_{\lambda=0}^{\infty} S(\lambda) = \int_{\lambda=0}^{\infty} R(\lambda)I(\lambda) \cong \sum_{\lambda=100}^{400} R(\lambda)I(\lambda)$$

Equation 7: Output signal as a function of integrated response per unit wavelength

Where	S_{total}	Output signal (mA)
	$S(\lambda)$	Output signal for a given incident wavelength (mA)
	$R(\lambda)$	Responsivity of detector to radiation of a given wavelength (mA/W)
	$I(\lambda)$	Intensity of incident radiation of a given wavelength (W/nm)

For any given wavelength of incident radiation the detector will have a specific responsivity, yet when using a non-monochromatic source (as was the case in the ESTEC experiments) it is impossible to isolate a given wavelength from among the continuum covered by the source. An approximation must therefore be made where the intensity of the source is treated as divided into discrete 1nm 'bins' that each has a specific responsivity with respect to the detector output. Thus the approximate transition from the integral to the summation in the above definition is a reflection of the transition from the theoretically 'pure' continuous range of responsivities to the practical limitation of having to treat the changing responsivity with wavelength as divided into discrete bins of 1nm width (the smallest interval that can be accurately measured). In this case only the range from 100-400nm is appropriate as this is the approximate range of wavelengths to which the detector is exposed.

Due to the fact that the AlGaN photodetectors integrate the output signal over the detectable, incident wavelength range, it was important to minimise this range as far as possible in order to gain accurate estimates for the responsivity in the unknown region at and above 285nm. To this end, five long-pass filters (LPFs) were used to remove all light with wavelengths shorter than five set wavelengths over the unknown region. This would allow for the measurement of a step-by-step decrease in the range of the incident UV radiation until the final, highest-wavelength LPF placed in front of the detector resulted in no signal output at all. The LPFs used had their half-maximum cut-offs at 297nm, 303nm, 312nm, 332nm, and 369nm. They are referred to as LPF297, LPF303, LPF312, LPF332 and LPF369, respectively. Their calibrated transmission curves, as measured at ESTEC, are as follows:

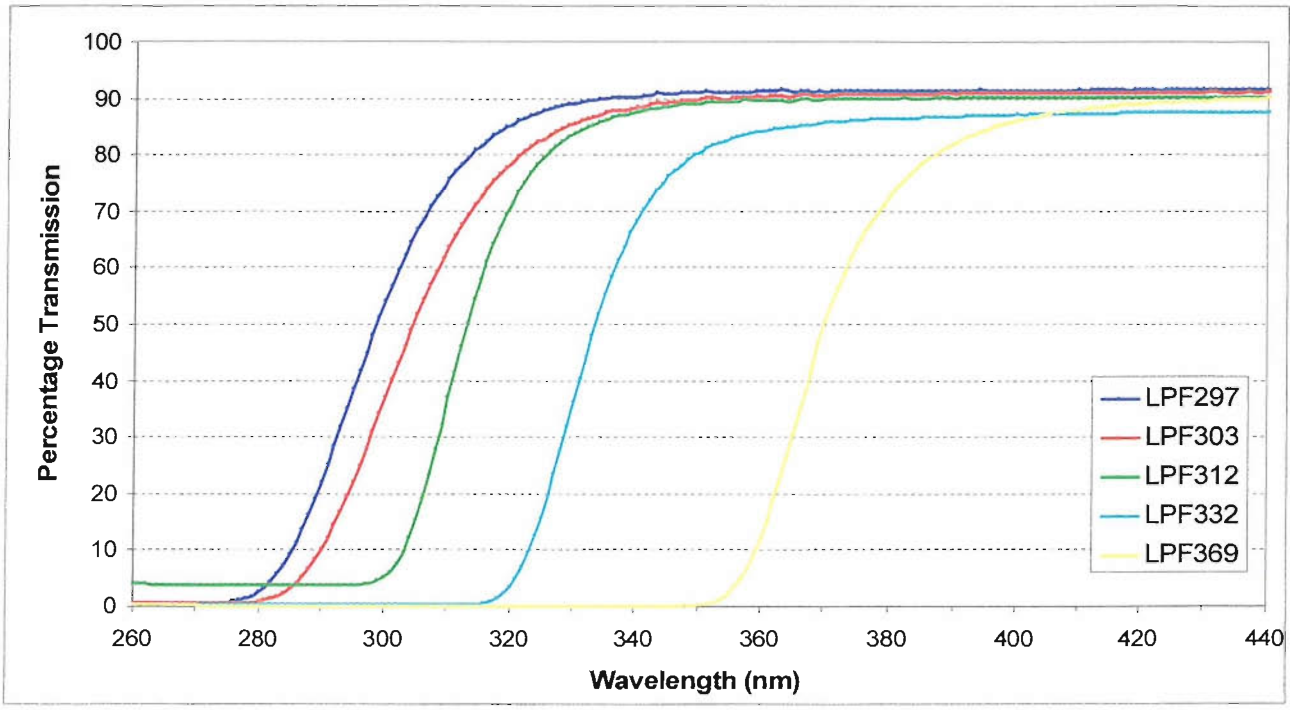

Figure 42: Transmission curves for UV Long Pass Filters

The transmission curves are reasonably consistent, all producing near total cut-off at lower wavelengths and a 90% transmission at higher wavelengths. The difference in cut-off wavelength of each filter is a function of the level of impurities remaining in the glass after curing. The slight deviations being the LPF312 allowing ~4% transmission at wavelengths below ~300nm and LPF332 reaching only ~87% transmission at wavelengths higher than ~410nm. However, such behaviour will be automatically accounted for in the signal calculations.

With an LPF placed in front of the detector the expression for the signal output becomes:

$$S_{total} = \sum_{\lambda=100}^{400} R(\lambda)I(\lambda)T_{LPF}(\lambda)$$

Equation 8: Output signal with Long Pass Filter in place

Where $T_{LPF}(\lambda)$ The percentage of light of a given wavelength transmitted by the specific LPF

Similar to the intensity and responsivity, the value for the transmission must be given as a discrete value for each wavelength range of 1nm, taken from the transmission curves above.

In order to derive a value for the AlGaN responsivity within the range being studied, it is necessary to know the intensity spectrum of the radiation source over the range to which the detector is being exposed (thus providing the values for $I(\lambda)$). This is provided in Figure 25, above (see section 3.2.3).

Given this expression for the output signal as it was measured during the experiment, it is clear that finding $R(\lambda)$ for a given wavelength in the unknown range of interest is still impossible – the output signal is still dependent on a summation of the responsivities from the LPF cutoff to the point at which the responsivity of the detector reaches zero (presently unknown). Ideally it would be best to reduce the summation to as small a wavelength range as possible so that a reasonable estimate for the average responsivity across this range can be established.

In order to achieve this, the approach has been taken to deduct the AlGaN detector output signal while using a higher-wavelength LPF from the output signal while using a lower-wavelength LPF. This will result in an output signal (or rather, a signal difference) that precisely relates to the range of the difference in transmission between the two filters, as given by:

$$S_{x-y} = \sum_{\lambda=100}^{400} R(\lambda)I(\lambda)\left[T_{LPFx}(\lambda) - T_{LPFy}(\lambda)\right]$$

Equation 9: Signal difference between two Long Pass Filters

Where	$S_{x\text{-}y}$	Signal difference between LPFx and LPFy
	$T_{LPFx,y}$	Transmission of Long Pass Filter x or y where these variables refer to 297, 303, 312, 332, or 369nm and obeying y>x

It will be impossible to designate precise responsivities to precise wavelengths of incident radiation, but a mean of the responsivities over the range given by the signal difference will at least enable a good approximation to be made to complete the responsivity curve of the AlGaN detector.

The first stage of this process is to calculate the intensity spectrum that is incident on to the AlGaN detector when each of these filters is in place. This is the product of each of the transmission curves, T(λ) (Figure 42), with the output spectrum of the UV lamp, I(λ) (Figure 25).

$$I_{tr}(\lambda) = I(\lambda)T_{LPF}(\lambda)$$

Equation 10: Intensity of UV Radiation transmitted through a LPF as a function of wavelength

Where $I_{tr}(\lambda)$ Intensity of transmitted radiation of wavelength λ

The resulting spectra are displayed below.

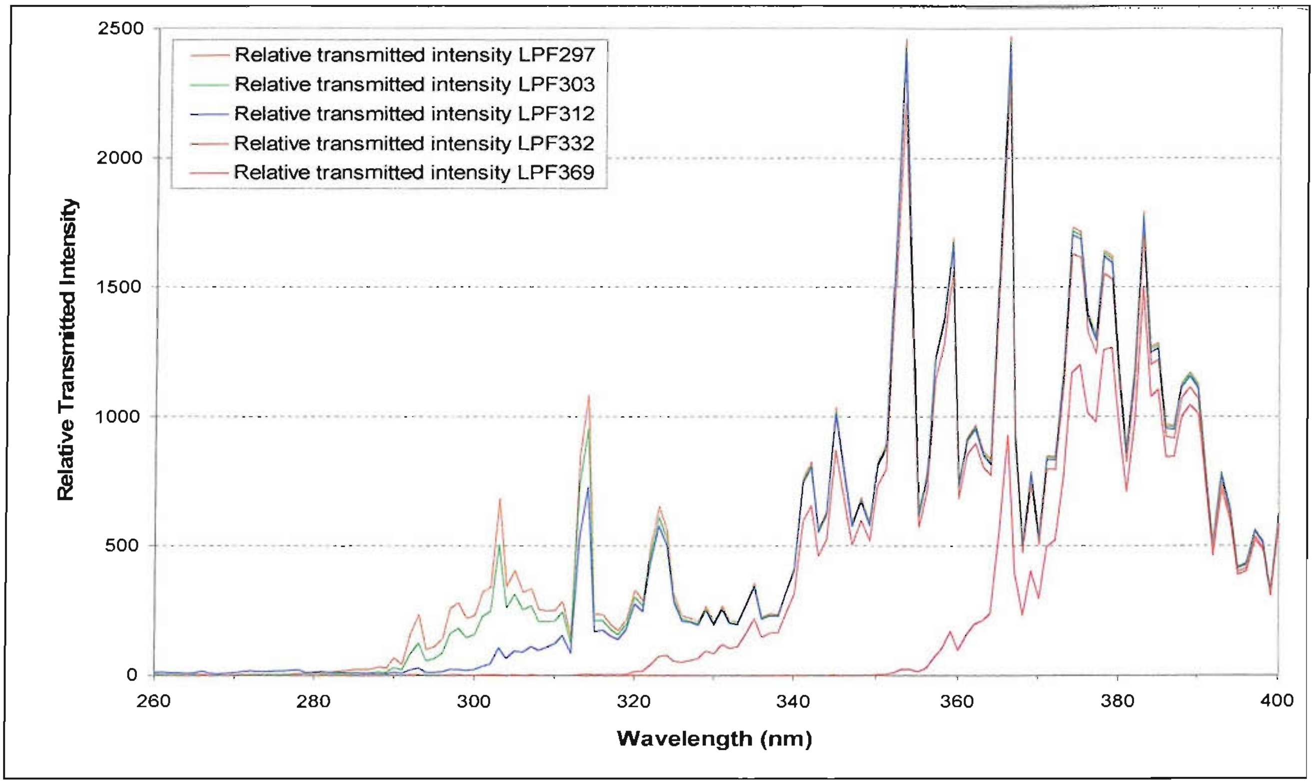

Figure 43: Relative Transmitted Intensity spectra from Philips UV lamp through LPFs

The data are described as 'relative transmitted intensity' because the output spectrum from the lamp is not absolutely calibrated. To achieve an absolute calibration required monitoring the lamp with alternative, calibrated detectors (mentioned in section 3.2.3) and will be discussed further on. It is clear that LPFs 303, 312, 332, and 369 all steadily decrease in the relative area of the output lamp spectrum that is detected. However, the decrease in area between LPF297 and LPF303 is much smaller, notably because these two filters have very close cut-offs. It is also of note that the output spectrum from the lamp decreases between 280nm and 290nm – precisely the region that would hopefully be more pronounced in the LPF297 transmitted spectrum. This has important consequences that are described later.

The next step is to establish the spectral ranges that are responsible for the difference in signal between measurements with different LPFs. As five LPFs were used, four different ranges can be calculated by differencing between adjacent spectra, using the expression given in Equation 11, below. The result of this process is displayed in Figure 44.

$$\begin{aligned} I_{diff.tr(x-y)}(\lambda) &= I(\lambda)T_{LPFx}(\lambda) - I(\lambda)T_{LPFy}(\lambda) \\ &= I_{tr.x}(\lambda) - I_{tr.y}(\lambda) \end{aligned}$$

Equation 11: Difference in Relative Transmitted Intensity between LPFs 'x' and 'y'

Where	$I_{diff.tr(x-y)}(\lambda)$	Difference in transmitted intensity between LPFx and LPFy
	$I_{tr.x}(\lambda)$	Transmitted intensity through LPFx
	$I_{tr.y}(\lambda)$	Transmitted intensity through LPFy obeying y>x

The difference in transmission has an obvious correlation with the distance between the cut-off wavelengths. LPF297-LPF303, with 6nm between cut-off wavelengths, has a differenced transmission of far lower magnitude than LPF332-LPF369, with 37nm between cut-off wavelengths. However, what is vital here, in order to plot points over the wavelength region in which the AlGaN detector responsivity drops to zero, is the range of wavelengths over which these differences measure.

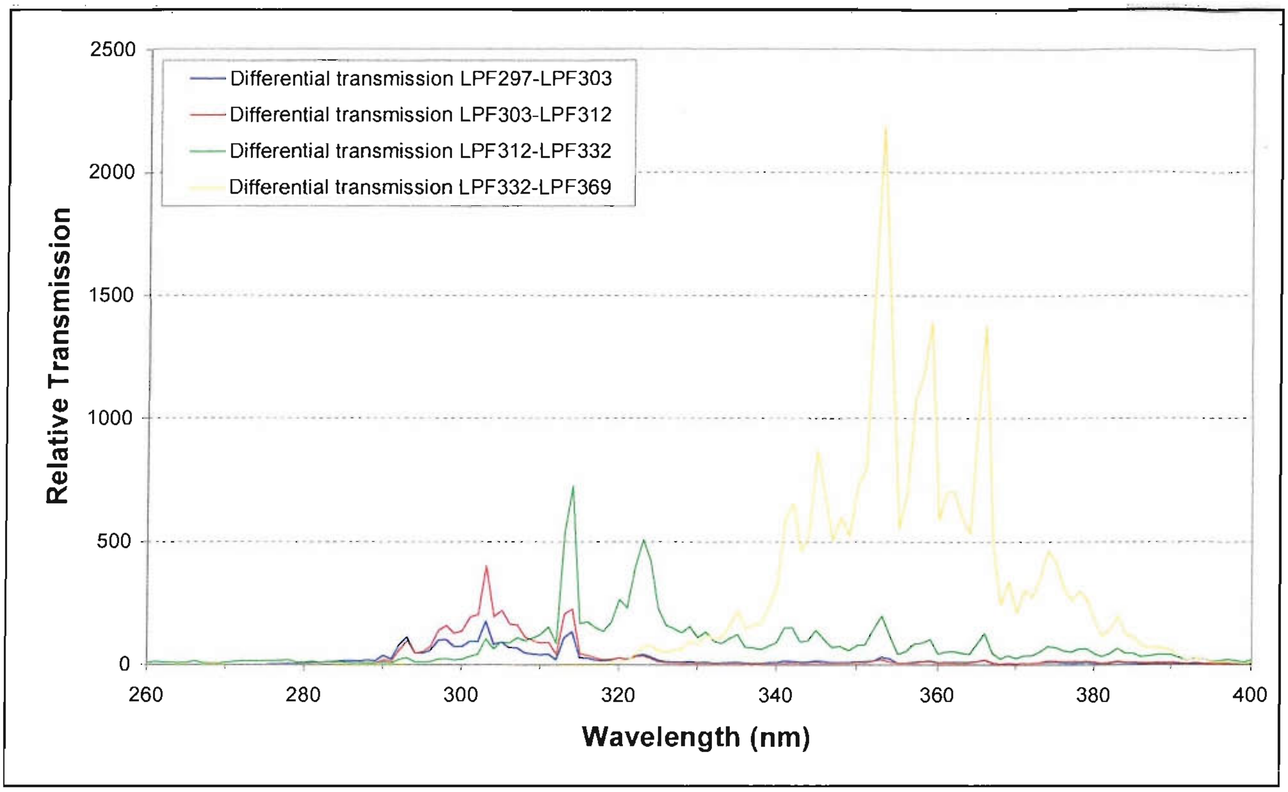

Figure 44: Differential transmission spectra of the LPFs

From the wavelength ranges of the differences it is necessary to find an average wavelength value, weighted with respect to the intensity, given by:

$$\overline{\lambda_{x-y}} = \frac{\sum_{\lambda=m}^{n} \lambda I_{diff.tr(x-y)}(\lambda)}{\sum_{\lambda=m}^{n} I_{diff.tr(x-y)}(\lambda)}$$

Equation 12: Intensity-weighted mean wavelength of the wavelength range covered by the difference in transmitted intensity between LPFx and LPFy

Where $\overline{\lambda_{x-y}}$ Intensity-weighted mean wavelength of the wavelength range covered by the difference in transmitted intensity between LPFx and LPFy

m,n Start and end wavelength for the wavelength range covered by the difference in transmitted intensity

The difference LPF332-LPF369 covers the region from ~320nm to ~390nm and has a mean centred on 356.7nm. The mean value acts as the data point for the responsivity at that wavelength, with error bars in the x-axis delineating the range over which this value may reside. The difference LPF312-LPF332 covers from ~300nm to ~390nm, although it is heavily weighted towards the lower wavelengths and thus has a mean of 331.8nm.

Both remaining differences are almost identical in range from ~290nm to ~325nm, though not in magnitude. This is a direct result of the reduction in output of the UV lamp in the 280-290nm range; if the output had been stronger it would have produced a greater difference between LPF297 and LPF303, extending the range of LPF297-LPF303 into shorter wavelengths. As a result of the similarity, the mean value for the LPF297-LPF303 range is 315.8nm, while the mean for the LPF303-LPF312 range is 317.6nm. While this does place both provisional data points at almost the same position on the x-axis of a responsivity plot (making a poorer spread of data points with which to curve fit), it does allow a comparison of responsivity results for very similar ranges so that the accuracy of the technique can be estimated.

A further incongruity to note here is why the two differences between the filters with the lower wavelength cut-offs have mean values that are outside the range covered by the cut-off wavelengths (e.g. the mean for LPF297-LPF303, 315.8nm, is outside the range 297nm-303nm). This outcome is due to two factors. The first is that the transmission curves for the filters, displayed in Figure 42, do not precisely align at higher wavelengths. Thus, the wavelength range covered by the differenced intensity spectra is extended to these higher wavelengths which then skews the mean as a direct result. The second is the fact that the UV lamp used produces greater intensities of UV radiation at higher wavelengths, thus magnifying the skewing due to the first factor. Such effects are undesirable, but unavoidable given the extreme difficulty of producing filters to the exacting standards required here.

Before going to the experimental data to cross-reference these ranges with the differences between the signals, it is crucial to calculate the actual flux being produced by the lamp instead of just the relative values between the ranges. Without the actual fluxes it would be impossible to generate a meaningful mA/W value for the responsivity of the detector in this range.

The calibrated UV radiometers from Dr. Gröbel UV-Elektronik GmbH (see section 3.2.3) were used to provide a measurement of the UV flux from the Philips lamp in three separate bands. The manufacturers published responsivity data for the detectors are in Figure 45, below.

The responsivity curves have obviously been normalised with respect to their maximum response; it is extremely unlikely that each detector will have a maximum responsivity value that is identical to the others. This is unfortunate as the company involved was unwilling to divulge further information regarding the absolute values of their calibration (that had also been carried out at PTB). As is, it is impossible to know how the maximum values of responsivity vary between the radiometers. This forces a compromise to be made where the responsivity curves must be 'de-normalised' with respect to each other, by looking at the ratios of expected response to the Philips UV lamp and actual signal readout. This process must be done by taking each radiometer in turn and treating it as having the 'true' responsivity figure (to which the others have been normalised). This produces three sets of data from which a mean value can be taken to produce a data point with error-bars along the y-axis to represent the range covered by the averaging process.

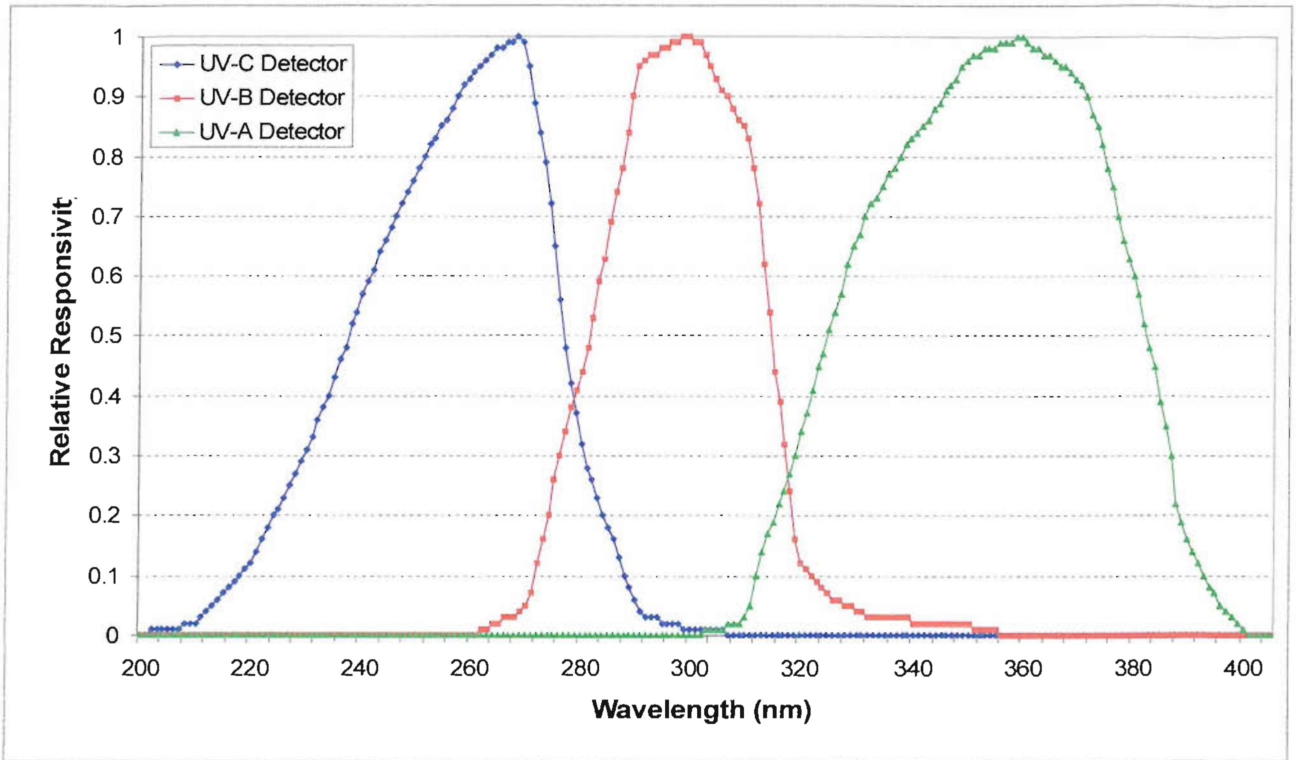

Figure 45: Responsivity curves for Dr. Gröbel UV radiometers

The UV radiometers work in a similar fashion to the Si and AlGaN photodetectors: they integrate a signal over their detection range that is both source-frequency magnitude dependent and response-frequency dependent, then produce a single output value (in W/m^2) in return. Due to this integration and wavelength dependency, a monochromatic source at 240nm incident on the UV-C radiometer would produce only half the reading that it would at 270nm, at the same level of flux.

This being the case, it is necessary to adjust the output values of the UV radiometers to correct for the integration inherent in their operation. The observed output readings taken from the radiometers were:

Radiometer	Output Reading (W/m^2)	Symbol
UV-C	5.81	$S_{(C)}$
UV-B	2.53	$S_{(B)}$
UV-A	52.78	$S_{(A)}$

Table 3: UV radiometer readings for Philips UV lamp

Using the relative output spectrum of the Philips UV lamp, in Figure 25, it is possible to calculate the integrated intensity, a_C, a_B, a_A, of the portions of the lamp spectrum that each UV radiometer is responding to, given by:

$$a_x = \sum_{\lambda=p}^{q} I_L(\lambda)$$

Equation 13: Integrated Intensity of Philips UV Lamp spectrum detected by radiometers

Where a_x Integrated intensity of the spectrum detected by radiometer 'x' where x=C, B, A

p, q Start and end wavelength to the range of sensitivity of the radiometer

$I_L(\lambda)$ Relative intensity of the Philips UV lamp for the 1nm 'bin' centred on wavelength λ

These integrated intensities will be directly proportional to the flux level that the radiometers are monitoring and thus directly proportional to their signal outputs, given above. As noted, the responsivity of the radiometers varies over their range of sensitivity (wavelengths recorded either side of the peak in responsivity will not fully reflect the true flux level). So, by taking the sum, over each nm wavelength, of the products of the relative lamp intensity and radiometer responsivity, relative values, $S_{rel(c)}$, $S_{rel(b)}$, $S_{rel(a)}$, are calculated that are equivalent to the observed absolute readings of the radiometers in Table 3:

$$S_{rel(x)} = \sum_{\lambda=p}^{q} r_x(\lambda) I_L(\lambda)$$

Equation 14: Relative radiometer signal output under Philips UV lamp illumination

Where:	$S_{rel(x)}$	Relative value that is equivalent to observed signal of radiometer 'x' (W/m^2)
	p,q	Start and end wavelength to the range of sensitivity of the radiometer
	$r_x(\lambda)$	Relative responsivity of radiometer 'x'

This is very similar to Equation 7, the same protocol being followed that the responsivities have to be split into 1nm 'bins' in order that a summation can be carried out that accurately reflects the integrated signal. However, the crucial difference is that the responsivities in this case are relative values, a fact that must be adjusted for later.

The observed radiometer readings are corrected by:

$$S_{true(x)} = \frac{S_{(x)} a_x}{S_{rel(x)}} = \frac{S_{(x)} \sum_{\lambda=p}^{q} I_L(\lambda)}{\sum_{\lambda=p}^{q} r_x(\lambda) I_L(\lambda)}$$

Equation 15: Correction of observed radiometer reading to true value

Where $S_{true(x)}$ Corrected signal to give a true value for the incident UV flux (W/m^2) on to radiometer 'x' where x=C, B, A

$S_{(x)}$ Observed radiometer signal (W/m^2)

It can be seen from this correction that if each radiometer was equally responsive across its respective wavelength range, so that $r_x(\lambda) = 1$ for all λ, then $S_{c(x)} = S_{(x)}$ and no correction would be required.

Given the reality of the radiometers' responsivities in Figure 45, the corrected readings for the radiometers are as follows:

Radiometer	**Corrected Reading** (W/m^2)
UV-C	14.51
UV-B	7.78
UV-A	81.71

Table 4: Corrected true UV radiometer readings for Philips UV lamps

These corrected readings are proportional to the plot areas of the Philips UV lamp spectrum that each radiometer is sensitive to. Therefore, using arbitrary units for the area under the spectrum, absolute values for the flux (W/m^2) per unit plot area can be derived for each radiometer. However, because the responsivity curves for the radiometers have all been normalised, different values for the flux per unit integrated intensity are generated.

Unfortunately, it is not known which responsivity curve is the original to which the other two have been normalised. This provides a rather severe problem, as mentioned above. The only possible approximate solution proceeds as follows.

The product of each responsivity spectrum with the relative output of the Philips lamp provides the relative signal output spectrum of each radiometer:

$$S_{rel(x)}(\lambda) = r_x(\lambda) I_L(\lambda)$$

Equation 16: Relative signal output of radiometer 'x' as a function of wavelength

Where $S_{rel(x)}(\lambda)$ Relative signal output of radiometer x as a function of wavelength where x=C, B, A

Note the similarity to Equation 14, although in this case the signal output is the spectrum, not the summation to produce a single value equivalent to the integrated signal. The spectra produced by this equation are displayed in Figure 46 and Figure 47, below – the ones not 'de-normalised'. The integrated intensity of this spectrum is equivalent to the observed signal output, so dividing the integrated intensity of the spectrum by the observed signal gives the flux per unit integrated intensity.

$$F_{rel(x)} = \frac{S_{rel(x)}}{S_{(x)}}$$

Equation 17: Relative flux per arbitrary unit integrated intensity under relative spectrum detected by radiometer 'x'

Where $F_{rel(x)}$ Relative flux per arbitrary unit integrated intensity under the relative spectrum detected by radiometer x where x=C, B, A

There are three values of this relative flux, one for each spectrum detected by each radiometer. In order to 'de-normalise' the spectra with respect to each other a 'de-normalisation' factor must be calculated proportional to the spectrum used as the assumed absolute one:

$$N_{y(x)} = \frac{F_{rel(x)}}{F_{rel(y)}}$$

Equation 18: 'De-normalisation' factor for radiometer 'y' with respect to radiometer 'x'

Where	$N_{y(x)}$	De-normalisation factor for radiometer y with respect to radiometer x
	x, y	C, B, A but where $x \neq y$

This produces six correction factors, two for each relative signal spectrum that will de-normalise it with respect to the other two signal spectra when multiplied:

$$S_{rel\,y(x)}(\lambda) = N_{y(x)} S_{rel(x)}(\lambda)$$

Equation 19: Relative signal output spectrum for radiometer 'y' with respect to radiometer 'x'

Where	$S_{rel\,y(x)}(\lambda)$	Relative signal output of radiometer y with respect to radiometer x as a function of wavelength
	x, y	C, B, A but where $x \neq y$

There are six permutations of this equation, each of which produces a new 'de-normalised' spectrum, also displayed in Figure 46 and Figure 47.

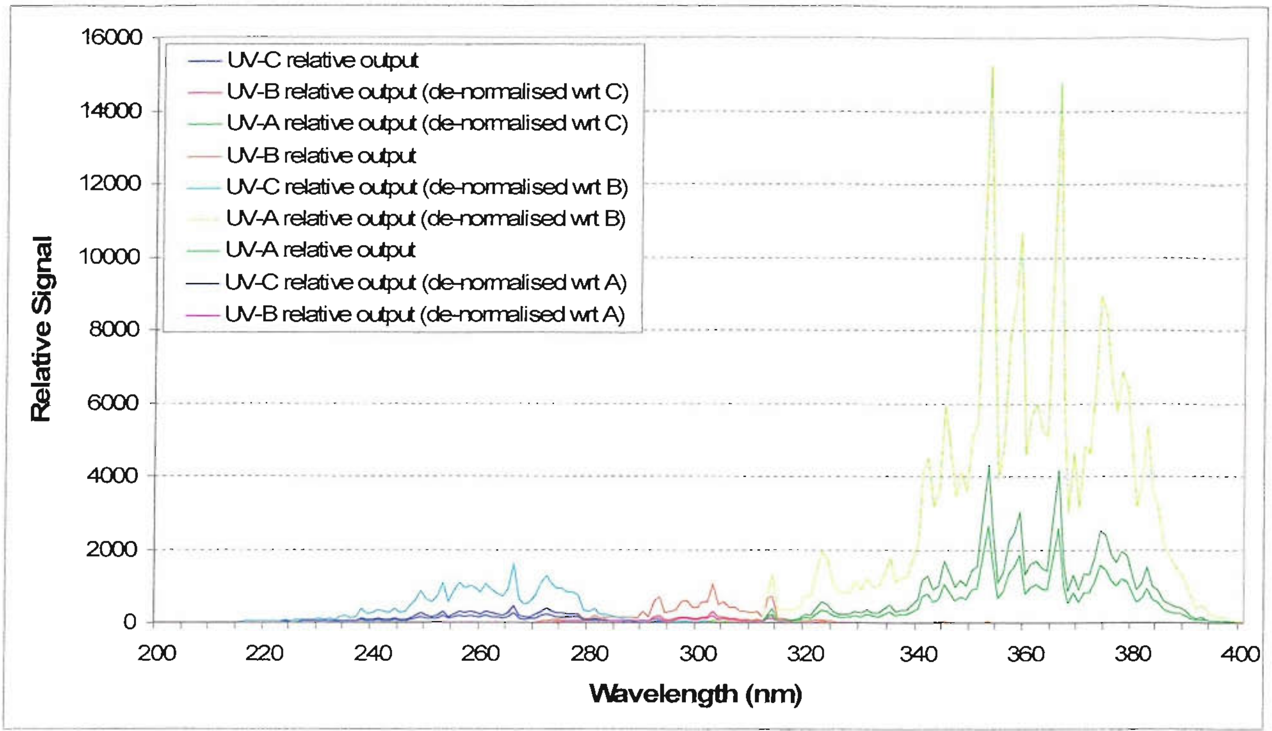

Figure 46: Radiometer relative signal spectra with respective 'de-normalisations'

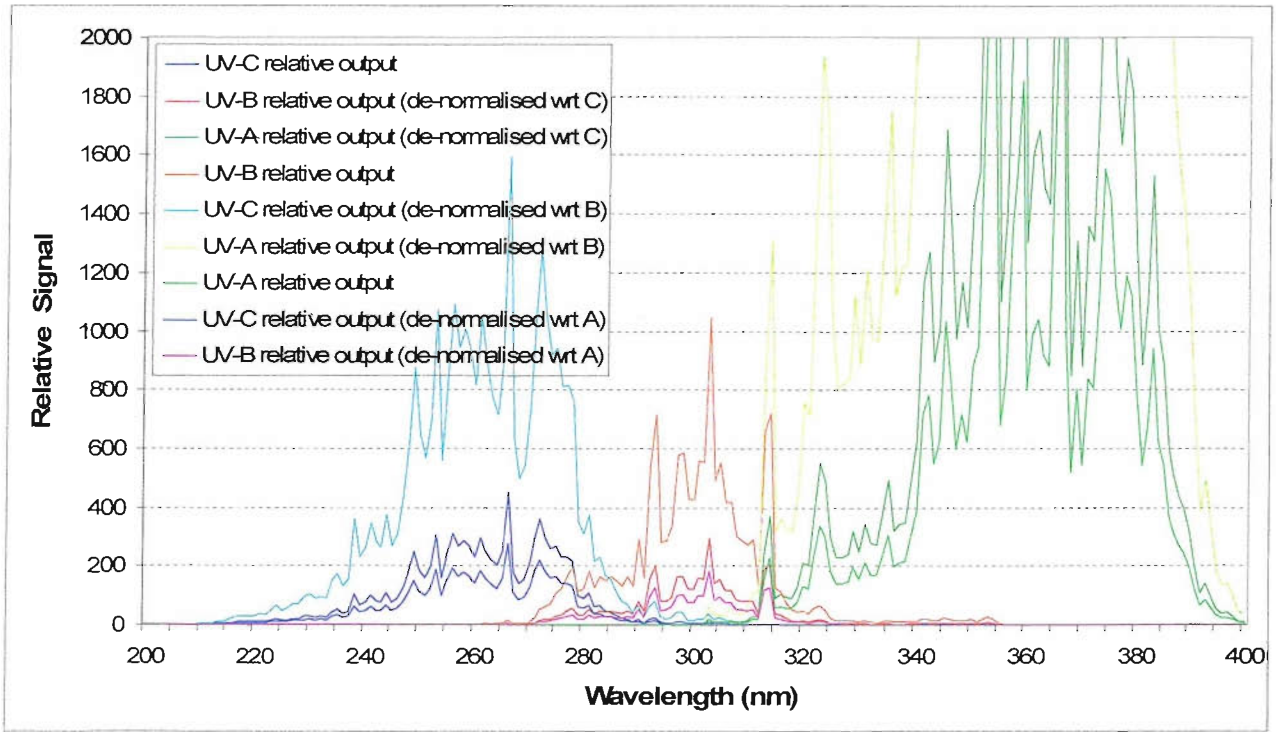

Figure 47: Radiometer relative signal spectra with respective 'de-normalisations' (detail)

Because the UV-B radiometer recorded the highest flux per relative unit integrated intensity then the spectra of the other two radiometers are massively enhanced when 'de-normalised'. Similarly, the UV-A radiometer recorded the lowest flux per relative unit integrated intensity so the other two radiometers are reduced when 'de-normalised'.

One of these sets of signal spectra is correct, depending upon which radiometer was used as the baseline for normalisation by the manufacturers. Without this information a mean of the plots for each radiometer was calculated by:

$$\overline{S_{rel(x)}(\lambda)} = \frac{1}{3}\left[S_{rel(x)}(\lambda) + S_{rel\,y(x)}(\lambda) + S_{rel\,z(x)}(\lambda)\right]$$

Equation 20: Mean relative signal output spectrum for radiometer 'x'

Where	$\overline{S_{rel(x)}(\lambda)}$	Mean relative signal output for radiometer x as a function of wavelength
	x, y, z	C, B, A but where x ≠ y ≠ z

This produces a further three spectra as displayed in Figure 48.

The integrated intensity under each of these spectra is taken to be the best approximation to the absolute values provided by the corrected radiometer readings. Dividing the corrected reading by the integrated intensity thus gives a flux value per unit area of the relative intensity spectrum:

$$I_{rel(x)} = \frac{S_{true(x)}}{\sum_{\lambda=p}^{q} \overline{S_{rel(x)}(\lambda)}}$$

Equation 21: Intensity of incident UV per unit arbitrary area under incident spectrum with respect to radiometer 'x'

Where	$I_{rel(x)}$	Intensity of incident UV light from Philips lamp per unit integrated intensity under the incident spectrum with respect to radiometer x
	x	C, B, A
	p,q	Start and end wavelength to the range of sensitivity of the radiometer

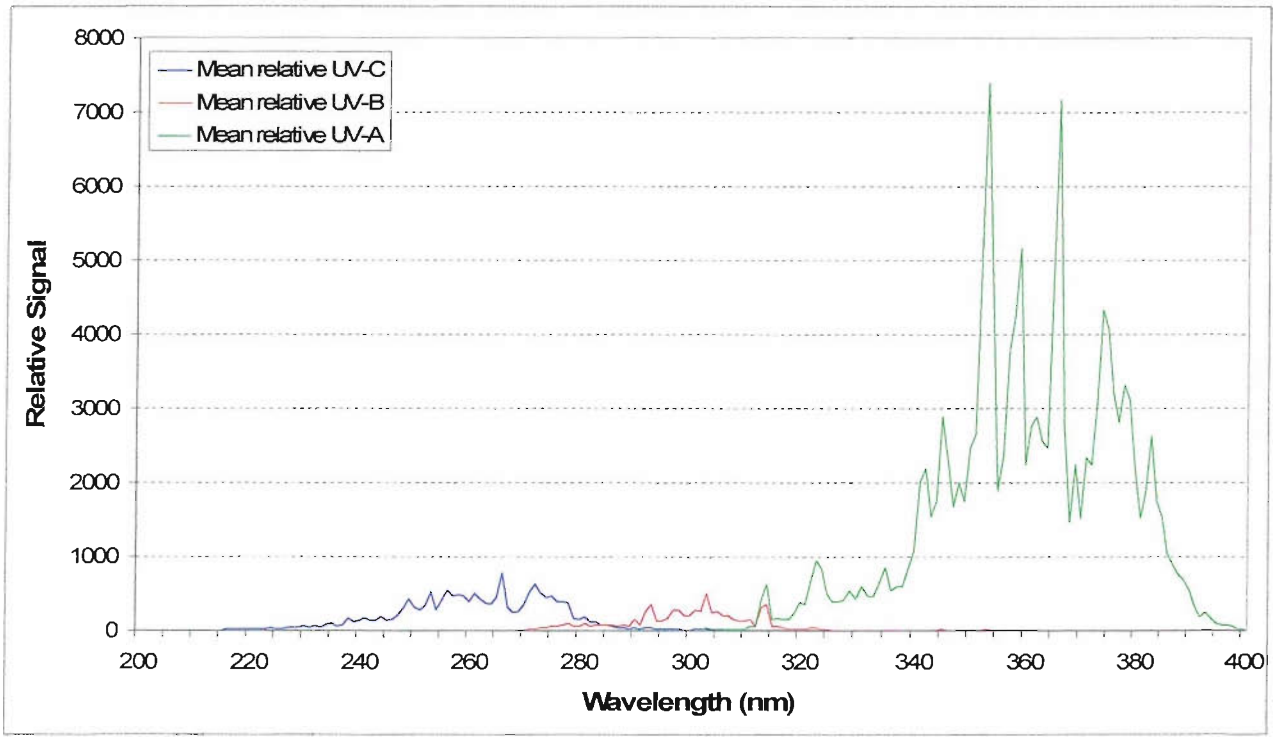

Figure 48: Mean radiometer relative signal output spectra

This produces three values, one for each radiometer, as displayed in Table 5, below. Ideally, if the baseline radiometer were known this would produce three identical values for the flux per unit integrated intensity. Unfortunately, due to the necessity of taking the mean of the 'de-normalised' spectra, three different values are calculated, the mean of which is used as the effective absolute value for the flux per unit plot area of the relative Philips UV lamp spectrum.

Radiometer	**Mean flux per unit integrated intensity** ($W/m^2/[L]^2$)
UV-C	0.000876
UV-B	0.001079
UV-A	0.000543
Mean:	0.000833

Table 5: Mean flux per unit integrated intensity of the UV radiometers' signals

This is an 'effective' absolute value because there is some intrinsic uncertainty due to this process of de-normalisation that endeavours to derive an absolute value from previously manipulated data. It is as close to the true absolute value as is possible using this technique, but the normalisation that has been applied to the radiometer responsivity data and the relative flux values given for the Philips UV lamp impedes a more accurate evaluation.

Now that an effective absolute value has been calculated for the flux per unit integrated intensity this can be applied to the integrated intensity of the differenced plots in Figure 44, above; the product between these values results in the flux produced by the Philips UV lamp over the differenced ranges.

Differenced Spectrum	Spectrum Integrated Intensity	Spectrum flux (W/m^2)
LPF297-LPF303	2899.5	2.41
LPF303-LPF312	3885.1	3.24
LPF312-LPF332	11034.6	9.19
LPF332-LPF369	30342.6	25.27

Table 6: Flux calculated for the differential transmission spectra

The active area of the AlGaN detector is $0.79mm^2$, so the energy deposited on the detector for each differential transmission spectrum is:

Differenced Spectrum	Energy incident on Detector (μW)
LPF297-LPF303	1.90
LPF303-LPF312	2.56
LPF312-LPF332	7.26
LPF332-LPF369	19.96

Table 7: Energy deposited on AlGaN detector for each differenced spectrum

Finally, the experimental data can be matched with the energy that is incident on to the detector within the differenced spectra ranges. This is done by taking the differences of the signal output from the detector when it has each separate LPF in place. This potential difference signal is then converted to a current by dividing by the detector's sensitivity of 0.47V/nA. Dividing this current by the energy deposited on the detector produces the responsivity for that differential spectrum range, as displayed in Table 8, below.

Signal Difference	Signal (V)	Detector Current (nA)	Responsivity (mA/W)	Mean Resp.[y] (mA/W)
LPF297-LPF303 (Mean: 305.7nm)	0.028 0.026 0.028	0.060 0.055 0.060	0.031 0.029 0.031	0.030
LPF303-LPF312 (Mean: 305.8nm)	0.023 0.024 0.025	0.049 0.051 0.053	0.019 0.020 0.021	0.020
LPF312-LPF332 (Mean: 323.9nm)	0.013 0.009	0.028 0.019	0.0038 0.0026	0.003
LPF332-LPF369 (Mean: 355.3nm)	0.004 0.005	0.009 0.011	0.0004 0.0005	0.0005

Table 8: Derived responsivities from the signal differences

The mean responsivities, derived from the repeated experimental measurements, can now be plotted alongside the data produced at PTB, as displayed in Figure 49, below.

The very low values for the responsivities generated by the ESTEC data demonstrate that there must be a very sharp cut-off between the end of the PTB results and the beginning of the ESTEC results, in the range 285nm to 315nm. It is unfortunate that there was not a larger array of LPFs commercially available to be able to study this region in more detail. However, the good result from this test is that the cut-off of the AlGaN detectors has not drifted too far from that quoted by the manufacturers.

The solid lines depict the PTB data and the blue points to the right of the plot depict the ESTEC data. To match the two sets of data, in order to represent the cut-off, projected points have been added by sinusoidal interpolation. A sinusoidal fit has been chosen as both data sets appear discontinuous; a sinusoidal 'join' provides a more realistic, smooth transition curve, in comparison with linear, exponential or logarithmic interpolation that would have generated sharp discontinuities in the responsivity curve.

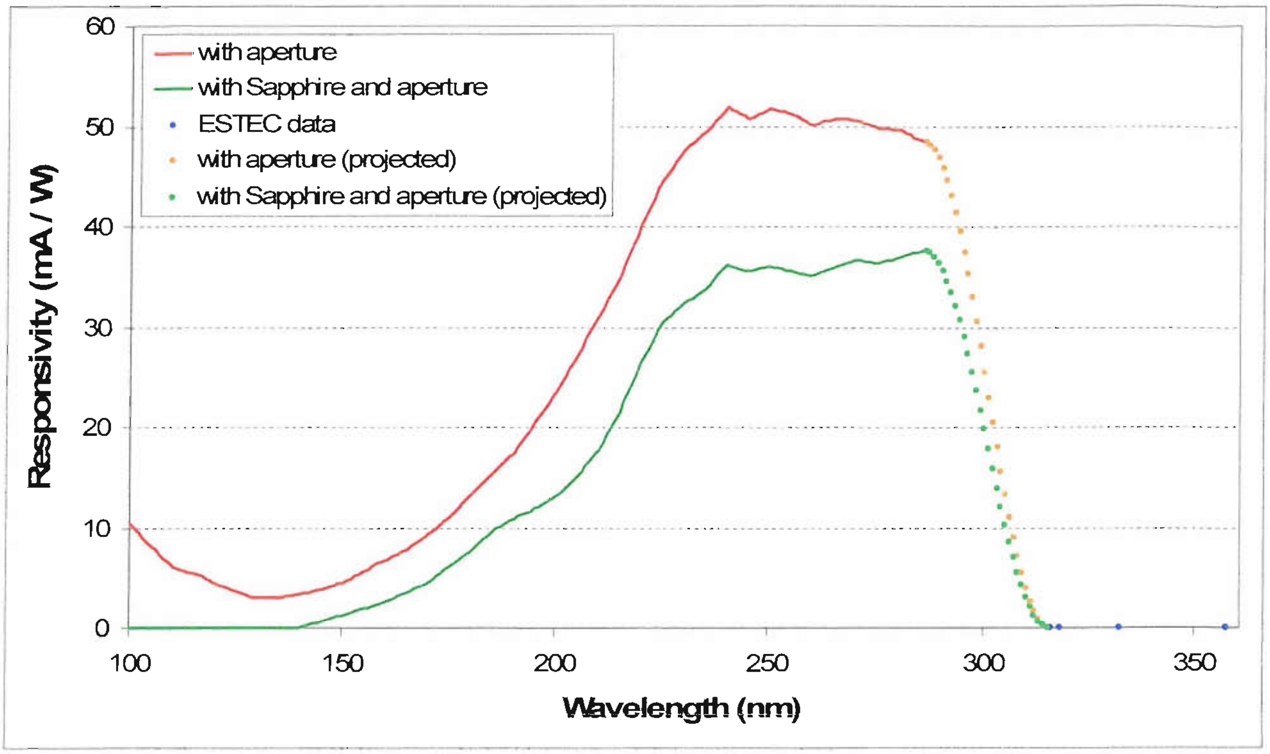

Figure 49: Combined responsivity data of AlGaN detectors

It is disappointing that no data could be generated that produced an overlap between the ESTEC and PTB data as this would assure some confidence that the two sets matched correctly. This failure in the analysis was as a result of the limitations of the available long-pass filters, the lowest wavelength filters commercially accessible were sourced but these could not produce data over the wavelength range covered by PTB.

From these complete responsivity curves the FWHM value for the bare (with aperture) detector can be calculated as 97nm centred on 251.5nm (a range from 203-300nm). Similarly, for the filtered detector (with fused silica and aperture) the FWHM value is 90nm centred on 256nm (a range from 211-301nm). The responsivity of both detectors extends deep into the shorter wavelengths, however, a necessary trait for any possible discrimination of the Lyman-α region.

The quantum efficiency of the detectors can be calculated as the percentage of each incident Joule of energy at a specific wavelength that is converted into a current, where each electron in the detected current absorbs 3.93eV for its promotion to the conductance band. This level of 3.93eV for the band gap is derived from the threshold for detection as found at 315nm in the complete responsivity plot, above. The quantum efficiency plots are similar to the responsivity curves as displayed here:

Figure 50: Quantum efficiency of bare and filtered AlGaN detectors

The finalised responsivity curves for the detectors can now be used to calculate expected on-orbit signal levels for the UV detectors, as described later in the discussion, Section 5.1.

4.2.2 Angle of Incidence Response

Due to the ISS's constantly changing orientation with respect to the Sun and the static positioning of the STORM unit, the angle of incidence of measured radiation from the Sun will change throughout the lifetime of the experiment. Consequently the measurement signal will also vary, independently of any Solar flux variability.

This necessitated the measurement of the response of the detectors at different angles of incidence to a radiation source. From this data it is possible to calibrate for this effect, so that at any given angle the response can be calculated as if the detector was at normal incidence to the incoming solar flux. This is vital as all the measurements for the responsivity of the detectors were taken at normal incidence, so it is only possible to derive values for the solar flux in the wavelength ranges of interest by taking this into account.

The angle of incidence measurements also provided the field of view of the detectors so that the amount of usable data they will be able to collect during the lifetime of the mission could be estimated (see Section 5.4.2, below).

In order to isolate this angular variation and correct for it, it is necessary to know how the response of the detectors change with angle of incidence from a constant radiation flux. This was accomplished in the SORASI facility by rotating the detectors around the insertion axis once they were under vacuum and being irradiated.

4.2.2.1 Silicon Detector Angle of Incidence Response

The silicon detector was monitored with the beryllium window in place, as it was recognised that the window itself will have an effect on the field of view. The results of the silicon detector angle of incidence measurements are shown in Figure 51, below.

The total range of motion of the SORASI insertion axis is limited, due to connectors, to the range covered by the data. The measurement angle is the direct recording from the arbitrarily-aligned chamber scale and is not a representation of the angle of incidence.

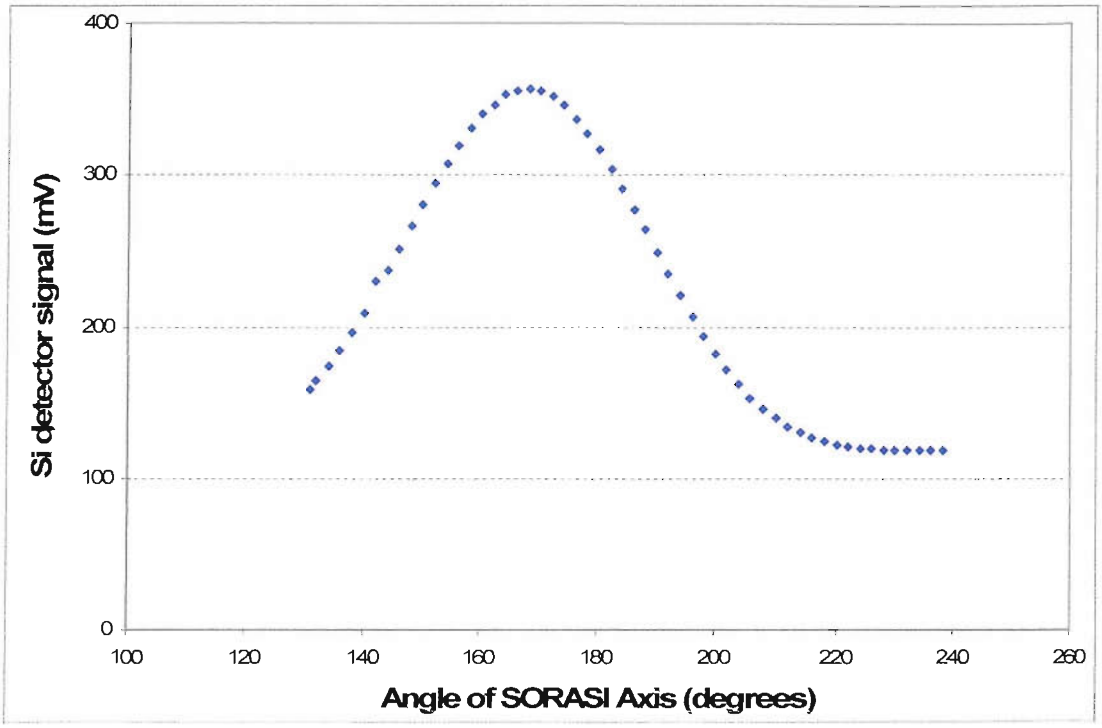

Figure 51: Silicon Detector Angle of Incidence Response

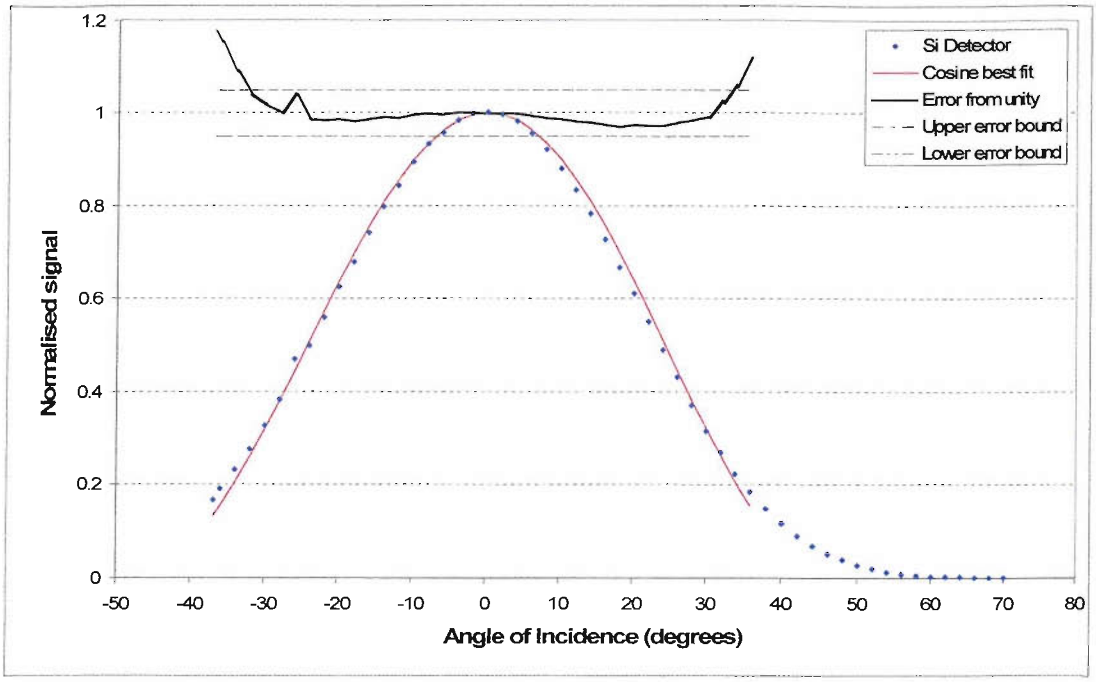

Figure 52: Normalised Silicon Detector Angle of Incidence Response

The peak in the data gives the position where irradiation was normal to the detector surface. It was expected that the data would follow a sinusoidal distribution and this is correct to a high degree.

The data was normalised along the y-axis between the maximum signal value given in the data and the minimum bound given by the detector offset baseline. The angle of incidence was centred so that the maximum value aligned with the normal incidence at 0°. These functions were applied to the data so that a resulting curve of best-fit could be calculated, as displayed in Figure 52, above. The curve of best fit was highly accurate, with a mean residual value per data-point of the least-squares best-fit being 3.29×10^{-4} (3 sig. fig.).

Using the ISS positioning telemetry it should be possible to calculate the angle of incidence of any radiation for a given moment in the signal data stream. Using the above best-fit line it would then be straightforward to calculate the expected signal at that time, if the incidence was normal, by using Equation 22, below.

$$S_c = \frac{2(S_r - S_b)}{\cos(3.706\theta) + 1} + S_b$$

Equation 22: Silicon Detector Signal Correction for Angle of Incidence

Where:

Where:	S_c	Signal corrected to normal incidence (V)
	S_r	Recorded signal (raw data) (V)
	S_b	Baseline signal (offset of the detector's amplifier when no radiation is incident) (V)
	θ	Angle of incidence as generated from ISS telemetry (radians)

By plugging the observed data values from the experiment back into this equation and dividing by the maximum recorded signal, the deviation of the best-fit line from the normalised data can be calculated. This is represented by the 'error from unity' data set in Figure 52, above, a dimensionless value that is plotted against the y-axis values given. Values at or close to '1'/unity represent a good match between the observations and the calculated values, as the error line moves away from '1' it signifies a progressively worse fit to the sinusoidal function. The error deviates more markedly from the function at the higher angles of incidence, demonstrating that there is only a finite range over which the best-fit calibration is valid. This drives the effective operating field of view of the detector – as the error increases above a threshold then the calibration ceases to be accurate. This threshold has been arbitrarily chosen at a 5% level of error, which generates an effective field of view of +/-32° for the silicon detector with the beryllium window in place. The error bounds for this threshold are also displayed in the above plot.

Further calibration beyond this range is made difficult due to the physical restrictions in rotating the SORASI insertion axle (in the negative direction, at least) and from the non-geometric change in signal. Considering that beyond this range the signal levels are so low (<10% of maximum), it is questionable whether any calibration would serve a useful function.

However, the one major drawback to this analysis is the fact that it can only be carried out with rotation around one axis. The rotation, with respect to the Sun, on board the ISS will be around two axes, as displayed:

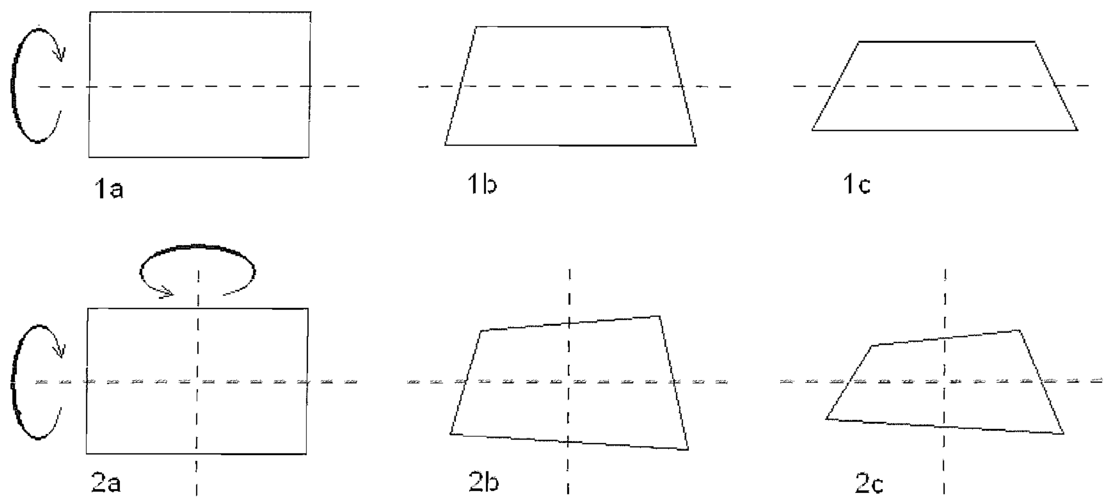

Figure 53: Changes to apparent area of the SXR detectors by rotations about 1 and 2 axes

These projections are made with respect to a point-source observer, such as the human eye, and so the effects of perspective serve to skew the angles of the corners of the detector – this is done to make obvious the difference between rotating around one and two axes. The reality of being illuminated by an extended source, such as the Sun, is that the effects of perspective are negated (as all photons that strike the detector follow parallel tracks, on average), thus an isometric projection is required, as shown in Figure 54.

As is clear from this Figure, the apparent area of the detector changes with respect to the source (or observer) as it is rotated. The apparent area is also different depending on whether the detector is rotated about one axis or two axes. This crucial difference is due to the rectangular shape of the active area of the detector (exaggerated in the image) – an angle of incidence to the normal when the detector has been rotated about one axis will see a different apparent area than the same angle of incidence when the detector has been rotated about two axes.

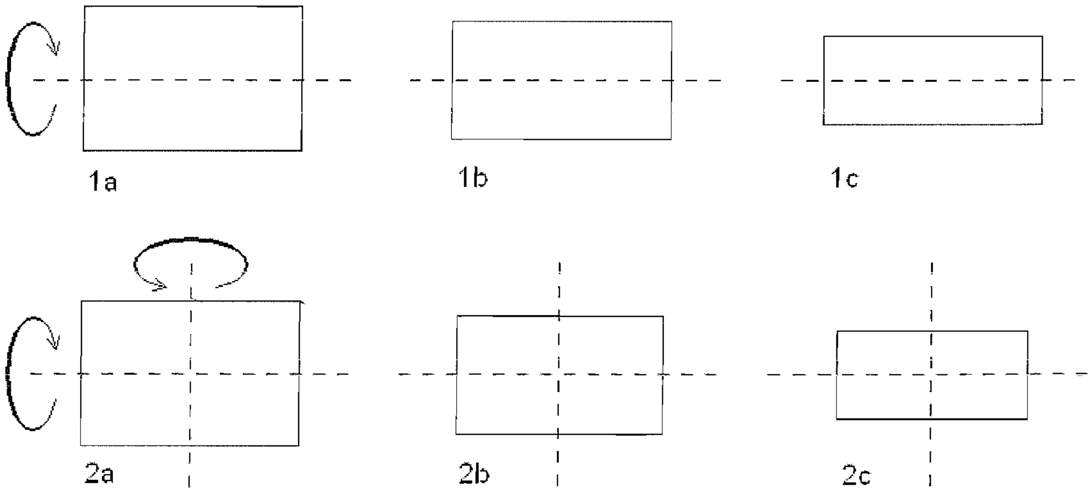

Figure 54: Isometric projection of changes to apparent area of the SXR detectors by rotations about 1 and 2 axes

Note that for a given angle of incidence when the detector has been rotated in two axes, the relationship between the angle of incidence and the angles of rotation is:

$$\theta = \tan^{-1}\left(\sqrt{\tan^2 \alpha + \tan^2 \beta}\right)$$

Equation 23: Angle of incidence as a function of the angles of rotation about two axes

Where	θ	Angle of incidence
	α	Angle of rotation about x-axis
	β	Angle of rotation about y-axis

From this expression it is straightforward to demonstrate that an angle of incidence formed from a rotation about two axes generates a lower apparent isometric area of the detector (i.e. 2b, 2c in the images above) than the same angle of incidence formed from a rotation about a single axis (i.e. 1b, 1c above).

Although it is not possible to rotate the detectors (or position them) for 2 axes rotation within the test facilities, it will be possible to calibrate for this effect on the ISS, using orbits with a Beta Angle of 0°. For these orbits the detector will act as if it is only rotating around the single axis, as calibrated for above, and so this can then be used to compare and calibrate against further orbits at different angles, as displayed in the following Figure:

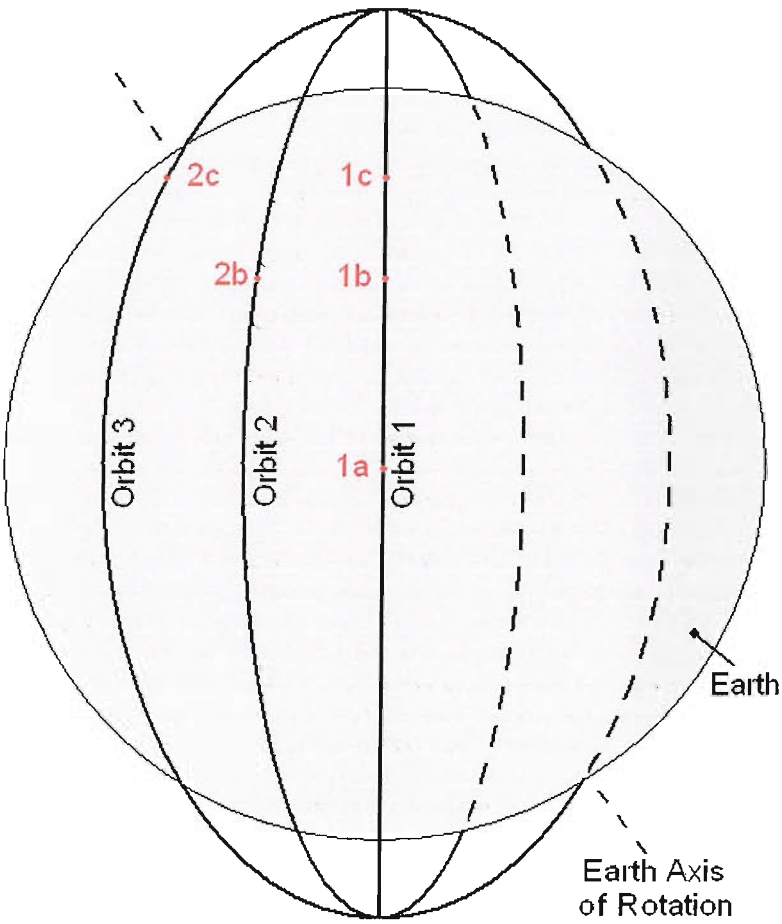

Figure 55: Position of various detector rotations along their separate orbits

This Figure is drawn from the perspective of looking back at the Earth along the Earth-Sun vector (so the Sun is 'behind' the reader). Orbit 1 has a Beta Angle of 0° and so appears as a straight line from this perspective. The positions 1a, 1b and 1c along this orbit refer back to the rotations given in Figure 53 and Figure 54 – they are the positions where the detector will have this appearance at these respective locations, being rotated about a single axis. Similarly, positions 2b and 2c, which lie on orbits with Beta angles of increasing size, denote the positions referring to the images of the detector rotated about 2 axes. Note that the image has been aligned so that Orbit 1 appears vertically to coincide with the axis of rotation for images 1a, 1b, and 1c in Figure 53.

4.2.2.2 AlGaN Detector Angle of Incidence Response

The AlGaN detectors were monitored simultaneously as they were rotated by the SORASI insertion axle. This was carried out under illumination from a Deuterium lamp in the main chamber and under illumination from the UV-pen while in the pre-chamber. It was hoped that illumination by two different sources would enable a check to be made between the two responses to elucidate whether different spectral ranges had similar angle of incidence responses.

The UV-pen, having a long, thin filament, was rotated by ninety degrees (producing measurement data sets where the filament is parallel or perpendicular to the insertion axle – see Figure 56, below) and the measurements repeated in order to distinguish any difference in outcome due to the fact that it was a non-point source of UV radiation. This was in contrast to the Deuterium lamp (and x-ray source for the Si detector angle of incidence response) that was, to a reasonable approximation, a point source in a fixed orientation.

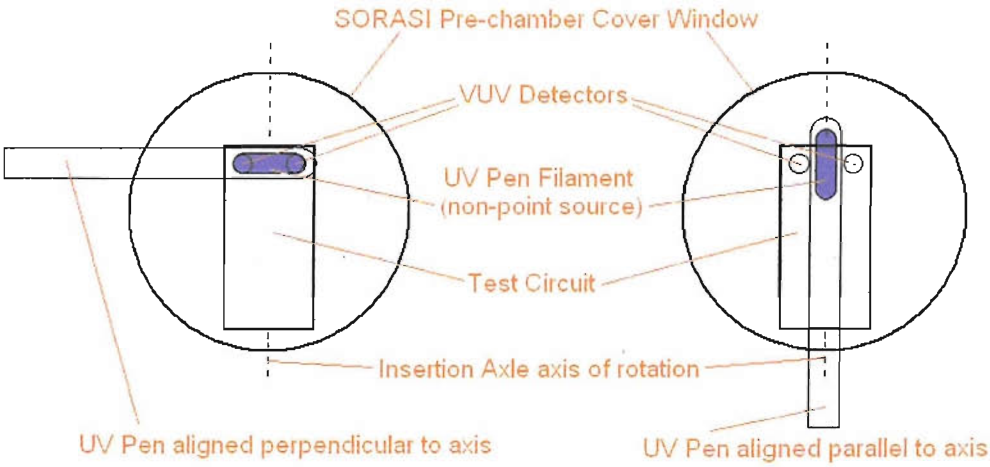

Figure 56: Plan view of the alignment of the UV Pen during VUV detector Angle of Incidence measurements

The raw results from these angle of incidence measurements are displayed in Figure 57, below. The bracketed 'F' and 'B' designators in the legend correspond to the 'filtered' AlGaN detector and 'bare' AlGaN detector, respectively. The bracketed 'Para.', 'Perp.' and 'Deut.' designators refer to 'UV-pen in parallel alignment', 'UV-pen in perpendicular alignment' and 'Deuterium lamp', respectively.

The obvious misfit in the data sets is that for the response of the filtered detector under the Deuterium lamp. Such a major disparity will be caused by a systematic error within the experimental setup – possibly a reflection within the main chamber that gave rise to an intensity maximum at the ~140° SORASI axis position. It certainly appears that the response behaves normally between ~190° and ~260°, reaching what looks like a maximum at ~190°, yet continues to increase as the angle is decreased below ~190°, as if a second source was incident – reaching the combined maximum at ~140°. A reflection could explain this behaviour even though the bare detector does not seem to be affected – the detectors are separated on Test Circuit 2 by a significant margin. Significantly, similar signal levels were observed when the insertion axle was rotated back over the measurement range, signifying that it is unlikely this was a transient error.

It is possible that the reflection affecting the filtered Deuterium signal was generated by the inside surface of the TO5 can that holds the filter itself. However, this appears unlikely as there is no similar effect observed in the two data sets from the filtered detector when illuminated by the UV-pen. As a result of this discrepancy the data set is worthless for carrying out an analysis similar to the silicon detector under x-ray exposure.

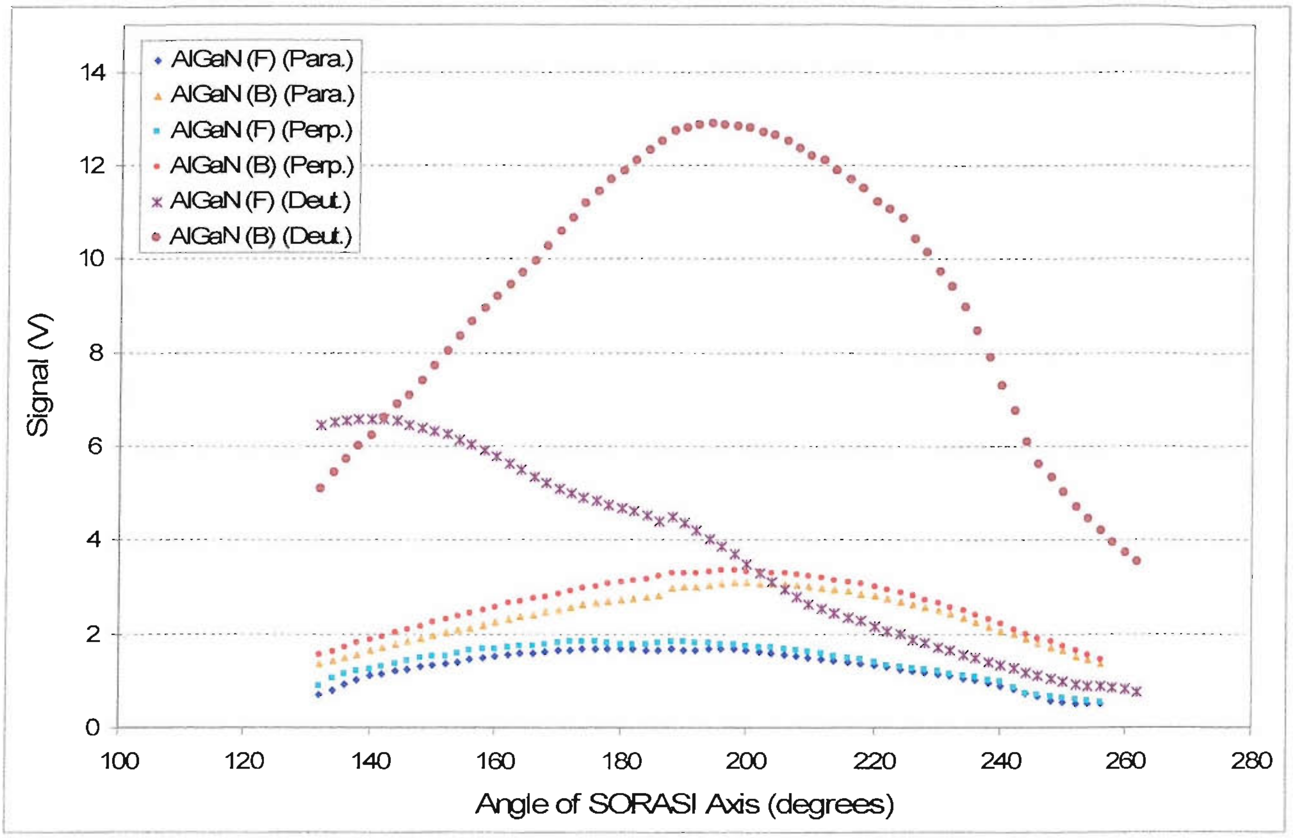

Figure 57: Bare and Filtered AlGaN Detector Angle of Incidence Response under Deuterium Lamp and UV-pen Illumination

In contrast, the bare detector's response to the Deuterium lamp conforms far more closely to the expected result of a sinusoidal relationship, due to the apparent area of the detector from the perspective of the source being a function of the rotation of the detector about the axis. By taking the maximum signal to be the normal incidence measurement angle it is possible to derive a cosine best fit curve, as displayed in Figure 58, below, in a similar operation to that used for the silicon detector angle of incidence response.

It is clear that the fit is not as good as the silicon detector results; the mean residual value per data-point from the least-squares best-fit calculation is 5.00×10^{-4} (3 sig. fig.), comparing unfavourably with the silicon detector's 3.29×10^{-4} result. Again, this is most probably due to the internal reflections within the main chamber which may account for the almost linear response of the detector from ~-60° to ~-15°.

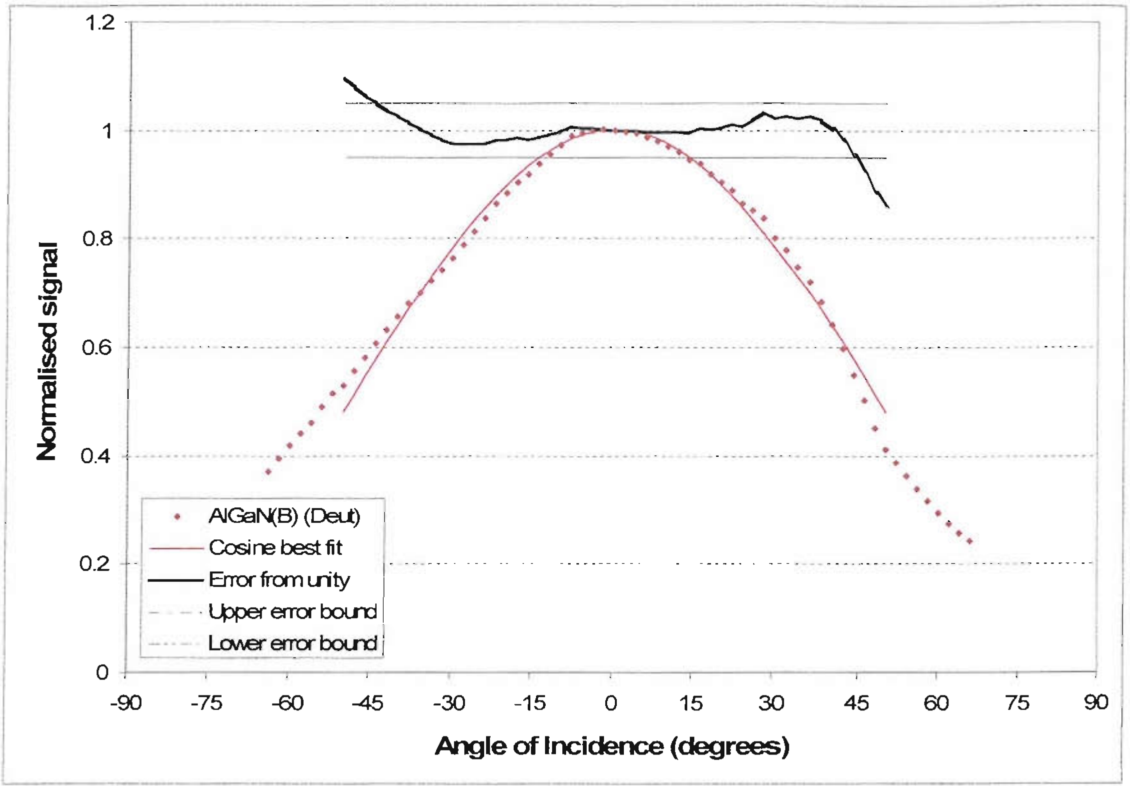

Figure 58: Normalised bare AlGaN detector angle of incidence response to Deuterium lamp

At the ~50° point it was noticed during the measurements that the insertion axle of SORASI was beginning to slip, as a result of trying to return to the horizontal orientation due to the torque generated by the coolant pipes being twisted during large-angle rotations. The effect of this can be clearly seen with a concurrent deflection in the data set at this angle to a shallower gradient. However, by this stage the error from unity had already increased beyond the 5% threshold boundary (as used for the silicon detector), thus this error was not included in the best-fit calculation.

The effective field of view calculated by the error bounds is +/- 44°, significantly wider than the silicon detector but, as will be seen below, not a true representation of the actual field of view that can be achieved.

For comparison with the UV-pen results, the equation for calculating the actual signal representative of the UV flux from the raw data at an angle of incidence is as follows:

$$S_c = \frac{2(S_r - S_b)}{\cos(1.844\theta)+1} + S_b$$

Equation 24: Bare AlGaN Detector Signal Correction for Angle of Incidence under Deuterium lamp exposure

with the same variables as used in Equation 22, above.

The raw data sets produced by the UV-pen results are noticeably smoother than those produced by the Deuterium lamp exposure. They are displayed in greater detail in Figure 59, below.

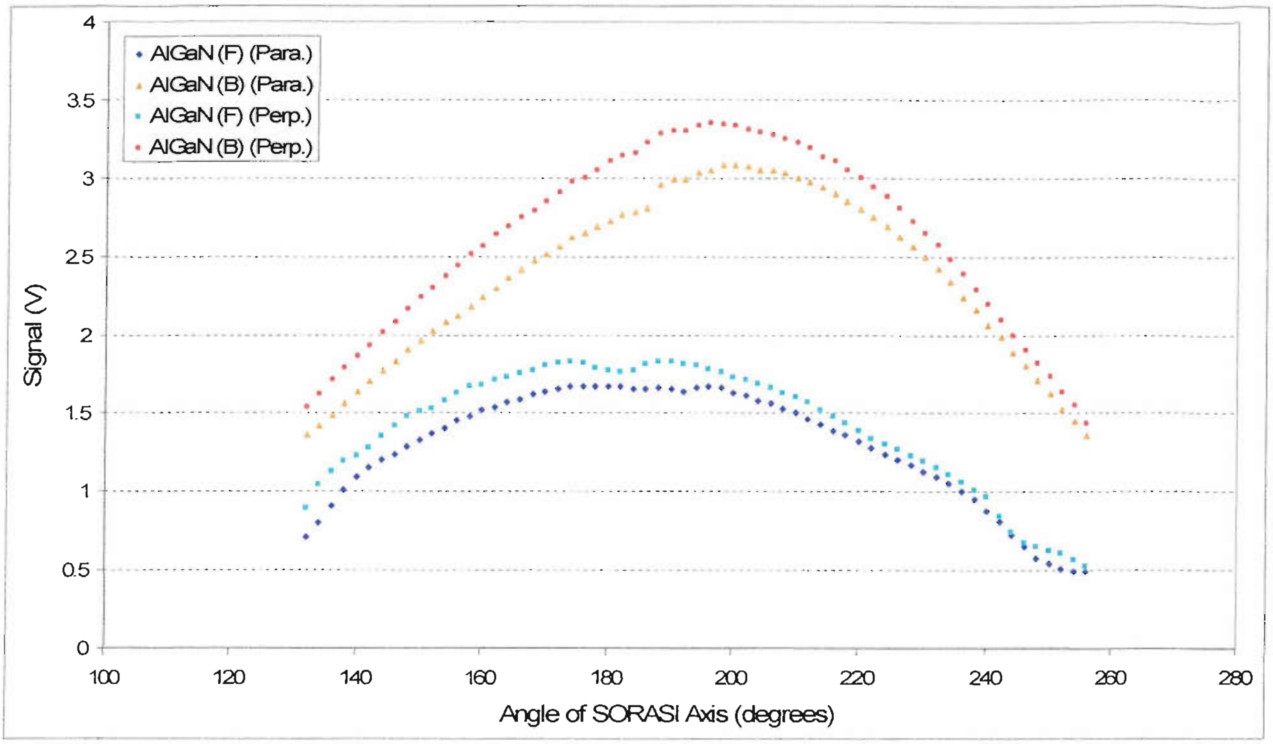

Figure 59: Bare and Filtered AlGaN Detector Angle of Incidence Response under UV-pen Illumination

However, unlike the previous data recorded for the silicon detector and AlGaN detectors under the Deuterium lamp exposure, there are a couple of corrections required to this data to account for the difference in geometry of the experimental setup. This is most obvious by the observation of the separation of maxima between the bare and filtered sets of results, caused by the physical separation of the AlGaN detectors on Test Circuit 2 combined with the closer proximity of the UV source. Whereas the Deuterium lamp is situated in a fixed position within the SORASI main chamber, the UV-pen was not – it had to be positioned above the view-port of the SORASI pre-chamber, over the cover window. As a result it was significantly closer to the detectors to reduce absorption of UV by the atmosphere (between the lamp and top of the view-port) and to produce a maximum signal from the detectors when at normal incidence illumination (which would produce better ranges of results).

This, the more important of the two geometric corrections, caused the measured angle on the intrinsic SORASI scale to underestimate the true angle of incidence as the radius of the circular locus described by the detectors as they were rotated was a significant fraction of the distance between the detectors and source. This error became greater as the angle through which the detectors were moved from the normal was increased.

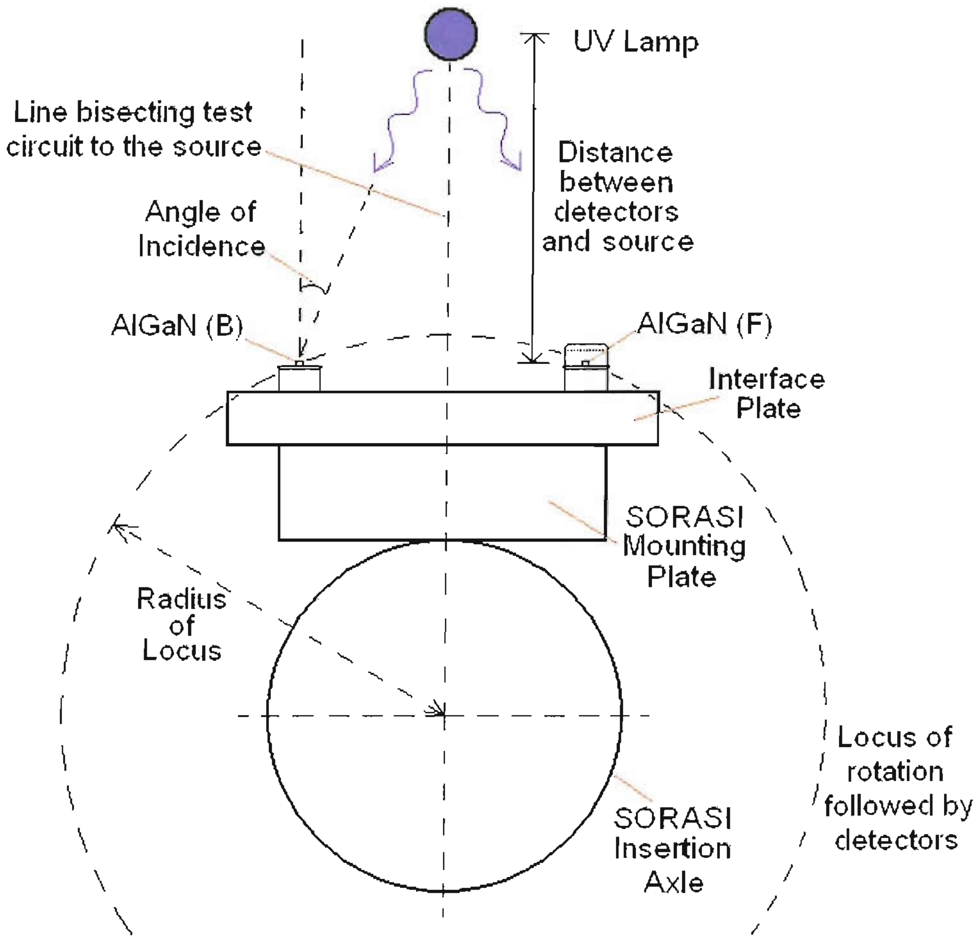

Figure 60: Elevation view along the Insertion Axle axis of detectors and source

This can be seen by taking the above Figure and imagining that the detectors, along with the interface plate and mounting plate are being rotated about the SORASI insertion axle. When the insertion axle is rotated by 90° the detectors will be in a position along the locus where the angle of incidence is *greater* than

90°. Similarly, to achieve an angle of incidence of 90° on to either detector the axle must be rotated by *less* than 90° - and this angle is different for both detectors and which direction the axle is rotated depending on which side of the line bisecting the test circuit to the source the detector is on.

The result of this error is to skew the recorded data away from a cosine distribution – this can clearly be seen in the data in Figure 59 where the modulus of the gradient is greater on one side of the maximum than the other for all the data sets. This skewing is, of course, determined by which side of the line bisecting the test circuit to the source the detector is on, as also can be clearly seen in the results.

The second geometric correction was required as the UV-pen was not aligned above the point exactly between the two detectors. This had a more subtle effect on the data by causing a small angular shift on the normal positions for the two different detectors (the normals being at two different measurement angles due to the detectors' lateral separation from the axis of rotation).

A final correction was required for the drift with time of the intensity of the source. The measurements were taken by rotating away from the SORASI insertion-axle normal position (marked as 186° on the intrinsic scale) in one direction, returning the axle to the normal position, then taking measurements while rotating in the opposite direction.

As the drift from the starting intensity increased (it was noticed that the UV-pen output increased in intensity as it warmed up) then the resulting data set would have a time-dependent error that increased throughout the course of the measurements. Such an error would most strongly manifest by creating a discontinuity in the data set when the insertion-axle was rotated back to the normal position half-way through the recording to measure the response in the second direction of rotation. This can most clearly be seen in the AlGaN (B) (para.) data set in Figure 59, above. The other data sets also contain discontinuities at this position, although they are far less pronounced (the data having been recorded at a later time when the UV-pen was closer to its maximum temperature).

The error was counteracted by measuring the detectors' outputs when they were at the normal position (at the beginning, mid-point and end of each data set – delineating two sections to the set). Unfortunately it was not possible to take an accurate recording of the time at which each incident-angle measurement was taken – recordings had to be carried out by hand while holding the insertion axle steady and monitoring the signal output. Thus, it was assumed that each recording took an equal amount of time and so a linear-interpolated 'smoothing' was applied to the data set proportional to the amount of increase in the signal at the normal position from the beginning to the end of the section.

This is only an approximate correction as it was noted that the increase in intensity of the UV-pen asymptotically approached a maximum value. Although this increase was not itself linear, a linear approximation is the best that can be made considering the lack of timed measurements. The results of this operation on the raw data can be seen in Figure 61, below.

Unfortunately, due to time constraints on the use of the facilities at ESTEC it was not possible to simply wait for the source, detectors and amplifiers to reach thermal equilibrium as this tended to take a few hours. Similarly, an additional measurement run while keeping the detectors in a stationary position would have necessitated a further period of letting the UV Pen, detectors and amplifiers cool to their original temperatures – another lengthy process. Ideally, if these measurements are repeated in future, time should be allotted for the entire system to reach thermal equilibrium before measurements are taken.

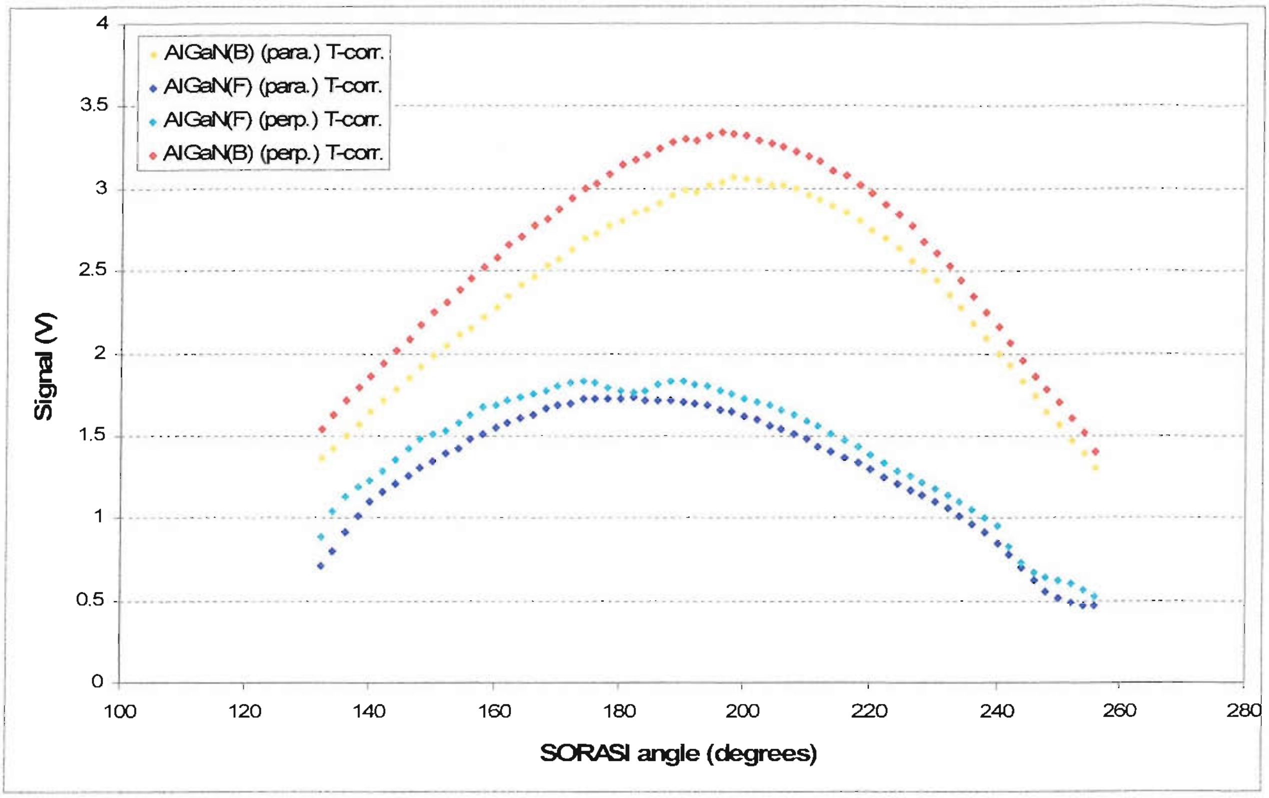

Figure 61: Bare and Filtered AlGaN Detector Angle of Incidence Response Corrected for Intensity Drift of Source

Although the correction is not perfect (slight discrepancies can still be discerned in the AlGaN (B) data) there is no possibility of reaching a better correction without timed measurements.

The two geometric corrections were applied simultaneously through the use of a single expression. The following, Figure 62, displays the relationship between the detectors (only one marked) and the UV-pen source.

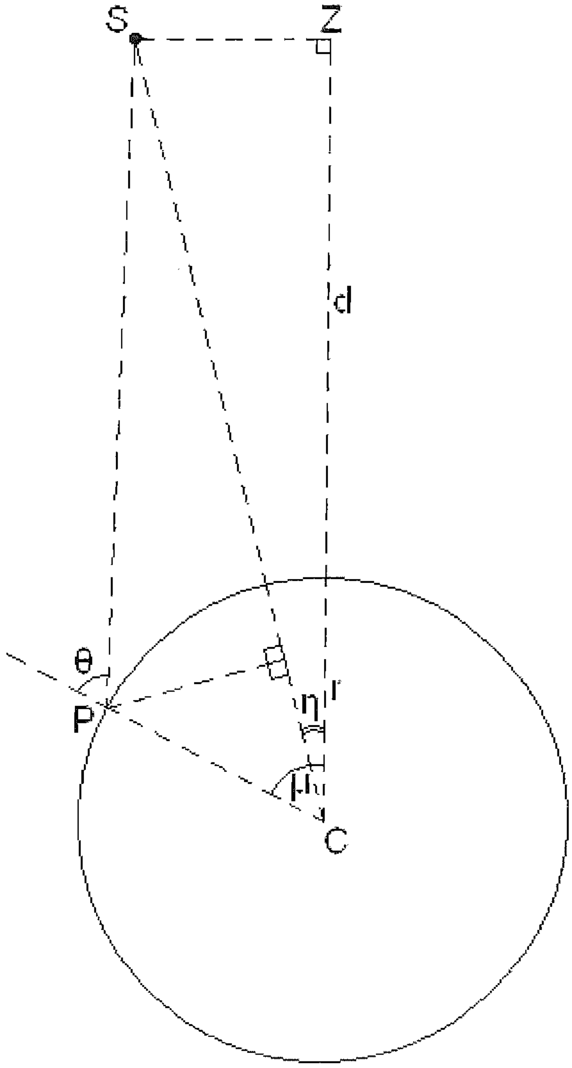

Figure 62: Geometric Relationship of AlGaN Detectors to UV-pen

Where:

	S	Source of UV illumination – the UV-pen (fixed)
	P	Position of AlGaN detector (variable)
	Z	Zenith point directly above
	C	Centre of the locus (solid circle) followed by the detectors
	d	Distance from Z to the top of the locus
	r	Distance from C to the top of the locus
	η	Angle measuring the displacement of S from Z (fixed)
	μ	Modified SORASI measurement angle (variable)
	θ	True incidence value on to a tangent to the locus at P from S

By trigonometry, the expression used to calculate the true incidence angle is:

$$\theta = \frac{\pi}{2} + |\mu - \eta| - \tan^{-1}\left[\frac{\dfrac{d+r}{\cos\eta} - r\cos(|\mu-\eta|)}{r\sin(|\mu-\eta|)}\right]$$

Equation 25: Expression for the True Incidence Angle from UV Source on to Detector

All angular measurements used are in radians and it should be noted that angles μ and η are sign-dependent with respect to their orientation from line ZC – positive if clockwise (up to π radians) negative if anti-clockwise. This results in η being a fixed negative value for the duration of the corrections. Angle θ is not sign-dependent as it is only necessary to treat the angle of incidence on to the detector as a scalar quantity, however the positive and negative values have been kept for the sake of the data plots even though there is no significant physical difference between being at a positive or negative angle of incidence.

The expression is symmetric about the line CS, from the centre of rotation of the SORASI axle with the fixed Test Circuit to the UV source. So, as P, the position of the detector in question, is rotated and follows the circular locus, the expression remains valid over the significant range of positive and negative values of μ between the two positions where line SP becomes a tangent to the circular locus. This range of values corresponds to all angles of incidence from 0° to 90° and the symmetry allows the expression to be used equally for both detectors.

A further value affecting the angle of incidence is the fixed orientation of the detectors with respect to the tangent to the locus at P (32.5°). This is because the detectors on Test Circuit 2 are displaced horizontally on either side of the mid-line of the Test Circuit that runs parallel to the SORASI insertion axle. As a result, when the Test Circuit is in its original, horizontal position on the axle (at 186° on the intrinsic scale) so that it lies normal to line CZ, the filtered AlGaN detector lies on the locus at a point with a negative value of μ (-32.5°) while the bare AlGaN detector lies on the locus at a point with a positive value of μ (+32.5°). When in this position both detectors will have normals that are parallel to line ZC, and these normals will be at the fixed orientation to the respective normals to the tangents at these points as previously mentioned.

The results of the geometrical corrections are displayed below in a separate plot for each data set. The signal has been normalised in an identical manner to the previous angle of incidence data so that 0° corresponds to normal incidence from the source on to the detector and a value of '1' corresponds to the greatest signal recorded for that data set.

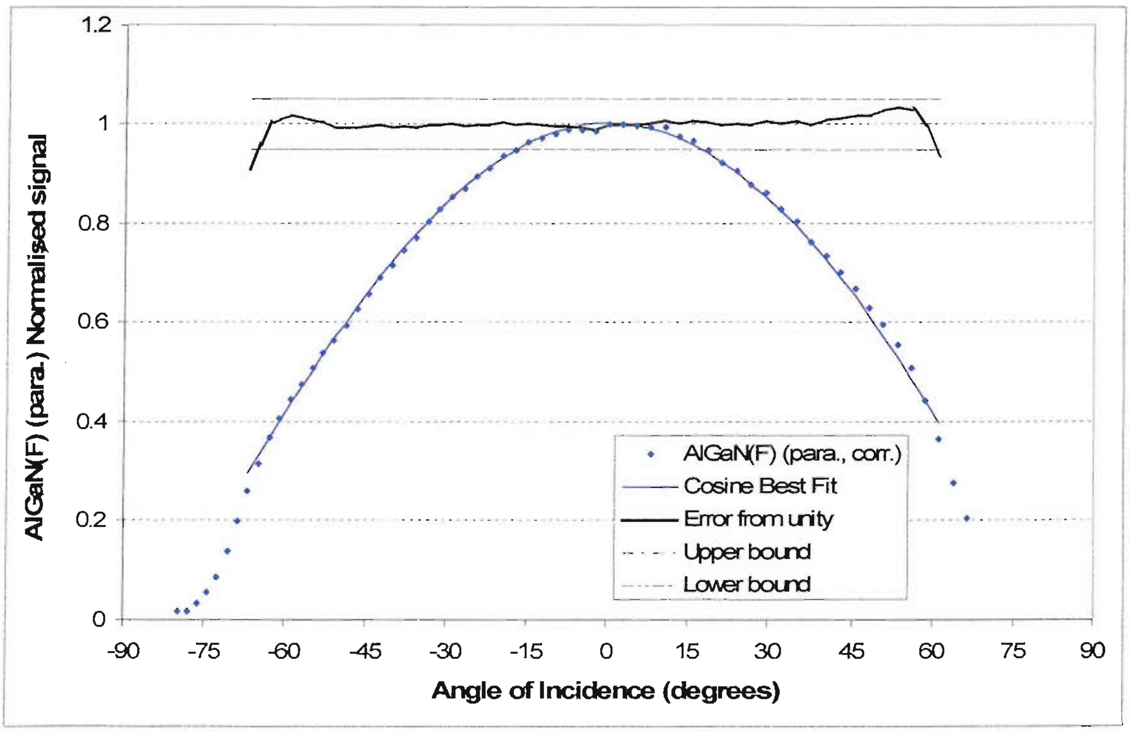

Figure 63: Corrected, Normalised AlGaN(F) (para.) Signal

In the first of the data sets it is clear that the geometric correction has significantly reduced the skewing present in the raw data. The data follows the cosine best fit line:

$$S_c = \frac{S_r - S_b}{\cos(1.091\theta) + 0.002} + S_b$$

Equation 26: Filtered AlGaN Detector Signal Correction for Angle of Incidence under UV-pen exposure in the parallel orientation

with the same variables as used in Equation 22, above.

The mean residual value per data-point from the least-squares best-fit calculation is 1.16×10^{-4} (3 sig. fig.), demonstrating a closeness of fit greater than the previously generated values for the silicon and AlGaN data sets above. From the plot of the error from unity a field of view of +/- 60° is derived, using the same arbitrary error bounds of 5%, as before. This is significantly greater than the field of view calculated for the bare detector when illuminated by the Deuterium lamp within the SORASI main chamber.

At angles greater than this range there is a noticeable change in gradient of the measured data corresponding to the deviation from unity above 5%. This is due to shadowing by the TO5 can that holds the filter in place – as the shadow lengthens up the side of the detector it consequently reduces the active area exposed to the UV source. The gradient of the data set increases, as a result, to reflect this decrease in incident UV.

The following, Figure 64, displays the corrected, normalised data set for the filtered AlGaN detector when the UV-pen is in the perpendicular orientation.

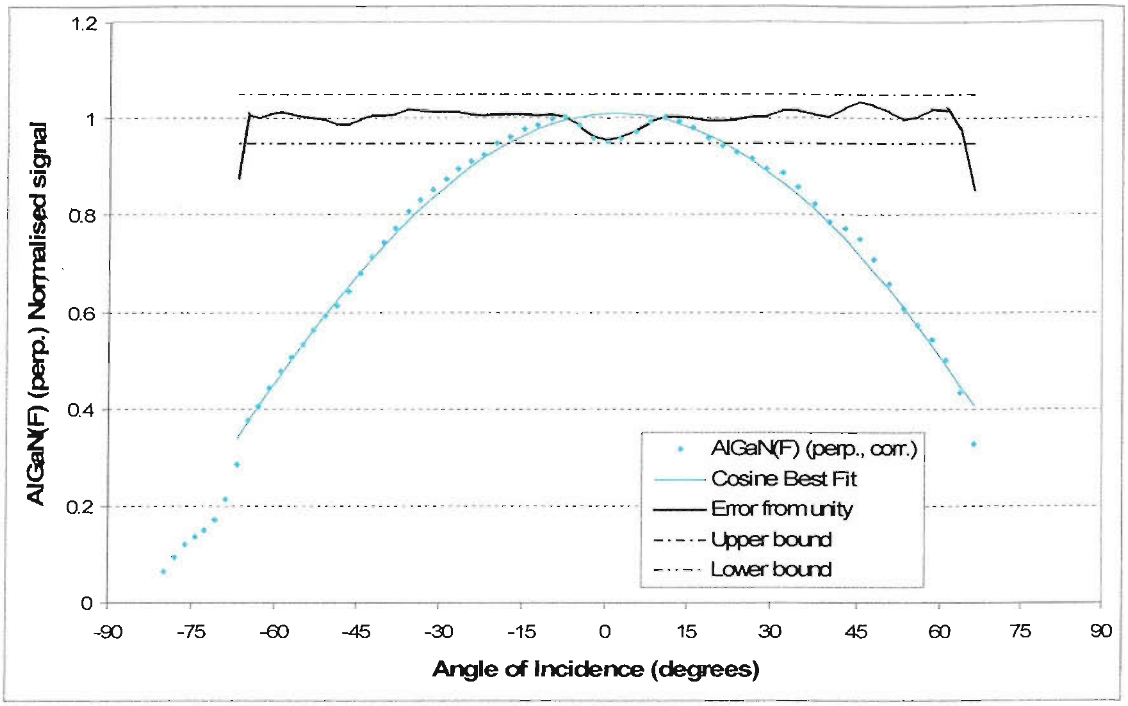

Figure 64: Corrected, Normalised AlGaN(F) (perp.) Signal

Again, the geometric correction has clearly reduced the skewing of the original raw data. However, there is a significant difference between -8° and +8° when compared to the filtered detector illuminated by the UV-pen in the parallel orientation. There is a 'dip' in the data corresponding to a relative reduction in incident UV to the detector. As can be seen above and below, none of the other data sets suffer from such an anomaly. A potential cause may be due to the filter itself generating some increased reflection of the incident UV light at small angles of incidence, yet this is not noticed when the UV-pen is in the parallel orientation. It appears unlikely that any polarisation effect could cause the decrease as the rotation of the filter is not in the plane of polarisation – so any reduction in incident UV caused by absorption through polarisation would affect all the data similarly. Of course, the anomaly could be generated by an inconsistent electrical or mechanical error that only affected this data set, yet this seems unlikely due to the symmetry of the 'dip' itself around the normal incidence position.

With no clear cause for the anomaly it would be prudent to monitor the 'live' data while on-orbit for any similar discrepancies for certain orientations to the Sun – any polarisation or angular-dependent reflective effects will be apparent as the detectors move through their full range of orientations during the course of a few months. Regardless, the anomaly is not considered serious as it does not increase the error from unity above the 5% threshold level.

The data follows the cosine best fit line:

$$S_c = \frac{S_r - S_b}{\cos(1.032\theta) + 0.009} + S_b$$

Equation 27: Filtered AlGaN Detector Signal Correction for Angle of Incidence under UV-pen exposure in the perpendicular orientation

with the same variables as used in Equation 22, above.

The best fit is very similar to that for the UV-pen in the parallel orientation, providing confidence that the orientation does not have a significant impact on the response of the detector. The mean residual value per data-point from the least-squares best-fit calculation is 4.58 x 10^{-4} (3 sig. fig.), a higher value than the parallel orientation, although the central anomaly is no doubt responsible for a majority of the increase.

The error from unity plot provides a field of view measurement of +/- 64°, similar to the parallel orientation. Even though this value is improved, it must be noted that when in the perpendicular orientation the UV-pen source changes the geometry of S in Figure 62, above, from a point to a horizontal line. This will serve to exaggerate the field of view of the detector as the source will be partially visible over a wider range at the extreme angles of incidence as it is being eclipsed by the TO5 can.

In a similar fashion to the parallel orientation, the data increases in gradient significantly due to shadowing of the detector by the TO5 can at higher angles of incidence.

Displayed in Figure 65, below, is the first of the bare AlGaN detector data sets:

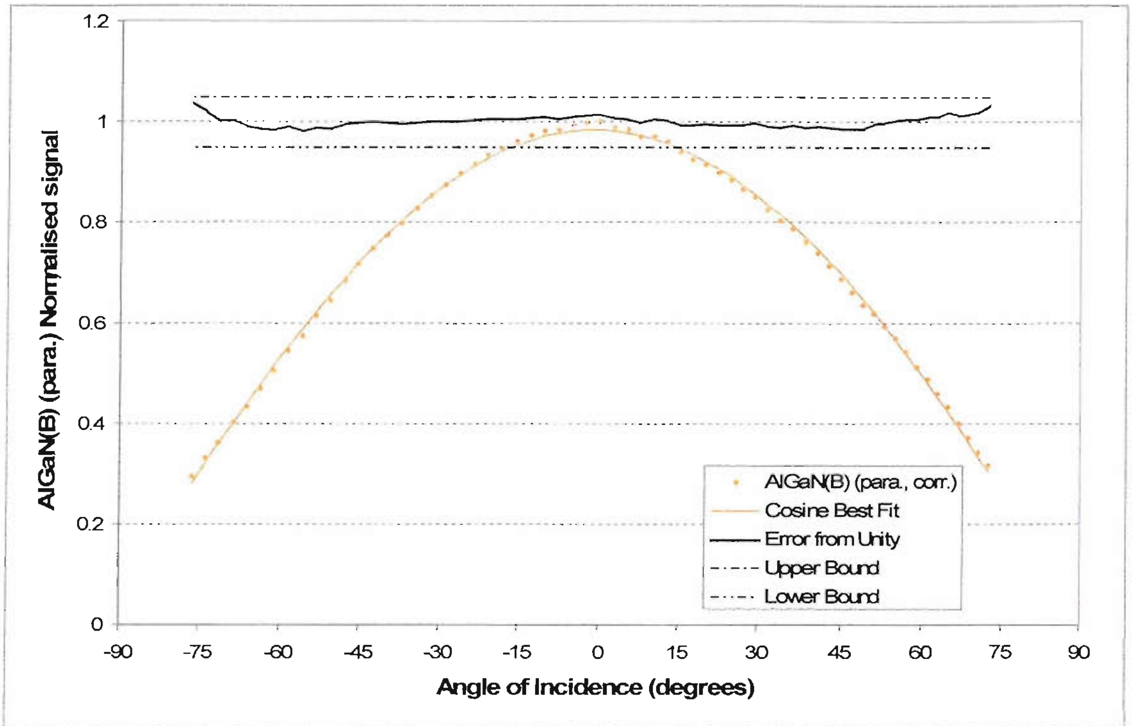

Figure 65: Corrected, Normalised AlGaN(B) (para.) Signal

Once more, the geometric correction has effectively eradicated the skewing in the data. This is even more significant considering that the deviation from a cosine distribution is more apparent in the data from the bare detector than from the filtered one, as displayed in Figure 61, above.

There is only a slight deviation from the cosine best fit around the normal angle of incidence, where it appears the detector is generating a stronger signal than expected. However, this deviation is so slight that it is of little practical significance – registering only a 1-2% error in deviation from unity. Indeed, at no point in the entire range of the data does the error from unity exceed the 5% bounds. The field of view is +/-75°, the largest yet calculated for any of the detectors, but this is a measurement based on the restricted angle of rotation of the SORASI insertion angle – the complete field of view may well be larger (though it should be noted that the bevelled apertures on the outer faces of the ram and zenith STORM panels, through which the UV detectors point, create a limit on the achievable field of view in this application).

The data follows the cosine best fit line:

$$S_c = \frac{S_r - S_b}{\cos(0.967\theta) - 0.017} + S_b$$

Equation 28: Bare AlGaN Detector Signal Correction for Angle of Incidence under UV-pen exposure in the parallel orientation

The equation is, again, very close to those generated by the Filtered AlGaN best-fit curves from the UV-pen. With a mean residual value per data-point from the least-squares best-fit calculation of 6.25×10^{-5} (3 sig. fig.), it is also the best fit by almost a factor of 2. This figure is no doubt improved due to the experimental limits of the angular measurements; all other angle of incidence measurements were affected by shadowing from the surrounding filters that impacted on the 'outermost' measurements.

Apart, of course, from the previous bare AlGaN detector exposure under the Deuterium lamp that compares unfavourably with the apparently more precise measurements described here. The results from the bare AlGaN detector illuminated by the UV-pen provide confidence that the deviations from a cosine best-fit in the Deuterium lamp measurements are artefacts of the environment within the main chamber (e.g. reflections), rather than an accurate record of the detector's angular response.

The last data set for the angle of incident measurements was for the bare detector illuminated by the UV-pen in the perpendicular orientation, as displayed in Figure 66, below.

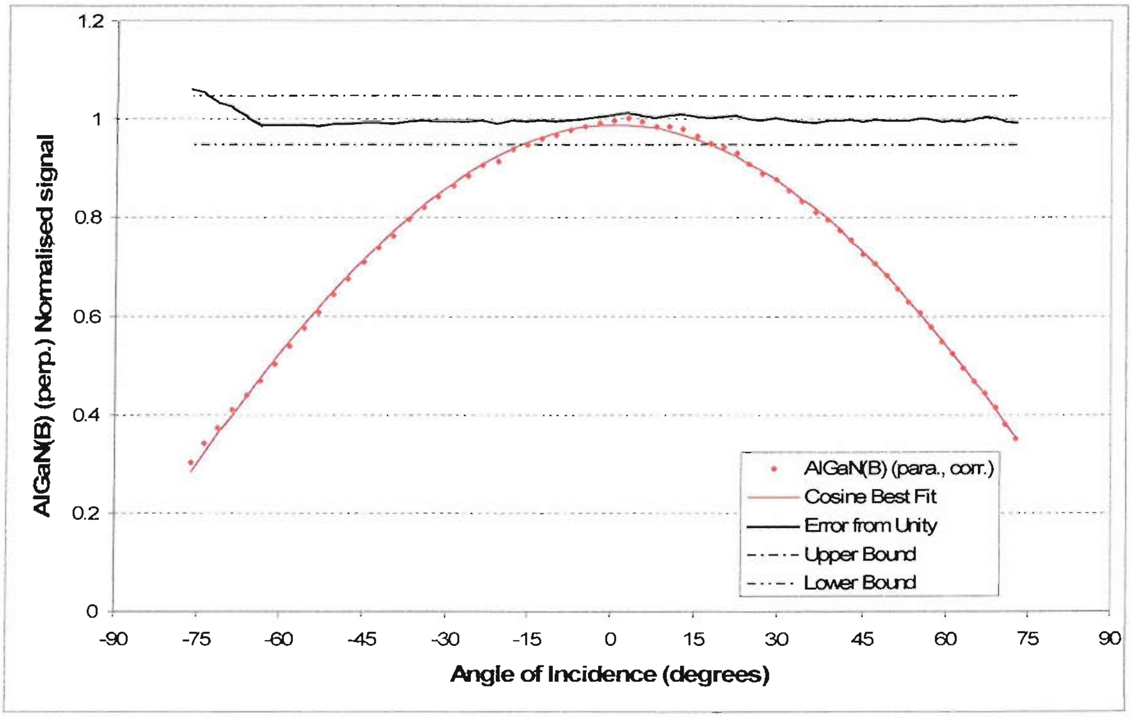

Figure 66: Corrected, Normalised AlGaN(B) (perp.) Signal

As previously, the skewing inherent in the raw data has been almost entirely removed by the geometric correction. Similar to the results for the bare detector with the UV-pen in the parallel orientation, there is a slight deviation from the cosine best-fit around the normal angle of incidence where the detector appears to be generating a stronger signal. However, as before, the error is small and practically insignificant, being well within the proposed bounds.

An anomaly is observed in the -67° to -75° region where the error from unity increases rapidly to pass beyond the +5% bound. This may well be due to slippage of the SORASI insertion axle occurring again at high angular rotations. Indeed, the signal levels recorded in this region are higher than expected by the cosine best-fit, as would be expected if the axle was rotating back to the central position.

Apart from this discrepancy, the error from unity is exceptionally low. Again, like the previous bare detector measurements, the bounds are not broken when rotating in the positive direction. The observed field of view is +/-72°, not quite as good as before, although this is entirely down to the anomaly at high negative angles.

The data follows the cosine best fit line:

$$S_c = \frac{S_r - S_b}{\cos(0.95\theta) - 0.013} + S_b$$

Equation 29: Bare AlGaN Detector Signal Correction for Angle of Incidence under UV-pen exposure in the perpendicular orientation

This is extremely close to the previously calculated angle of incidence correction for the bare detector in Equation 28, above, improving confidence that the UV-pen results are more significant than those measured under the Deuterium lamp. The mean residual value per data-point from the least-squares best-fit calculation is 4.87×10^{-5} (3 sig. fig.), the most precise of all the data sets, even with the anomaly included.

The angle of incidence results are some of the most important measurements with respect to the STORM instrument as the majority of all data generated on-orbit will be taken while the detectors are not at normal incidence to the Sun. The fact that the correction equations for the angle of incidence are so close to 'perfect' cosine relationships, as would be expected from changes in incidence angle, provides assurance that it will be possible to gather a far greater volume of accurate data over the full fields of view of the detectors.

4.2.3 Electron Response

The third radiation source on the SORASI main chamber (see section 3.2.1.3), the STAIB Instruments electron gun, was used to irradiate the detectors with electrons at energies between 2keV and 25keV25keV in order to analyse the detectors' sensitivity to an incident electron flux, as will be experienced on-orbit (see Section 5.3.2, below).

The electron exposures were carried out on test circuit 2 so that each of the different detectors could be monitored. After setting the beam to a 3mm diameter circle (judged against the scale by eye from the fluorescence of the zinc sulphide), it would be positioned over the detector using the manual controls. Fine adjustment was required to produce the maximum output signal and this position setting was used for every reading. The same process was carried out when positioning the beam over the Faraday cup; maximum electron flux output from the gun was found by searching for the point on the cup that generated the largest current throughput and the same setting used subsequently for every direct current measurement. The fine positioning of the manual controls was of critical importance to producing consistent results, especially when the beam is difficult to focus and control within the main chamber.

Measurements were taken at six energy levels: 2keV, 5keV, 10keV, 15keV, 20keV and 25keV. This covered the maximum range of the instrument. For each energy level the current would be gradually increased from 1nA up to a maximum of 25nA, although usually the amplifiers would become saturated before this level was reached. Thus the sensitivity of the detectors over the energy range and the linearity of response to increased electron flux could be measured.

However, the results for the silicon detector (with beryllium filter) and the filtered AlGaN detector signified zero response. Even pushing to higher currents, the electron energy was insufficient to penetrate either of the filters. The bare AlGaN detector, though, did respond well.

Figure 67, below, is a plot of the data recorded from the electron exposures. There are six data sets corresponding to each of the energy levels that were incident on the detector. For each data set there is a best-fit line with the associated linear equation and residual sum of the squares. As can be seen, the detector responds in a linear fashion to increasing current over all the different energies, with no evidence of the breakdown limit being approached. It should also be noted that the gradient of the best-fit slopes increase with increasing energy up to 10keV before decreasing again. This is symptomatic of a maximum in sensitivity being reached over this range.

There were enough data points across the energy range at two current levels for this feature of the detector to be explored. Figure 68, below, displays the response curves across the energy range at 3nA and 5nA current levels.

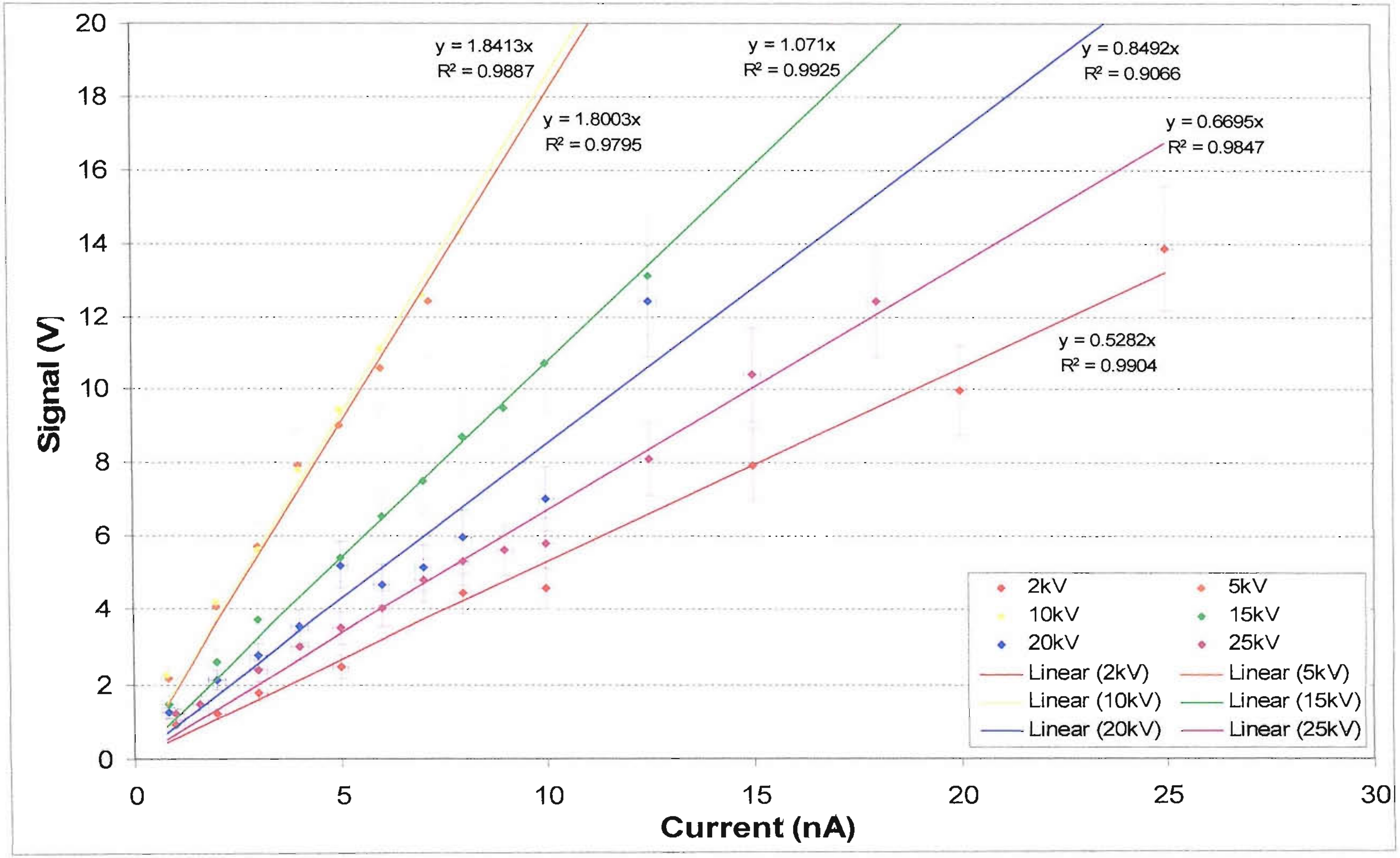

Figure 67: Bare AlGaN detector signal response to electron fluxes

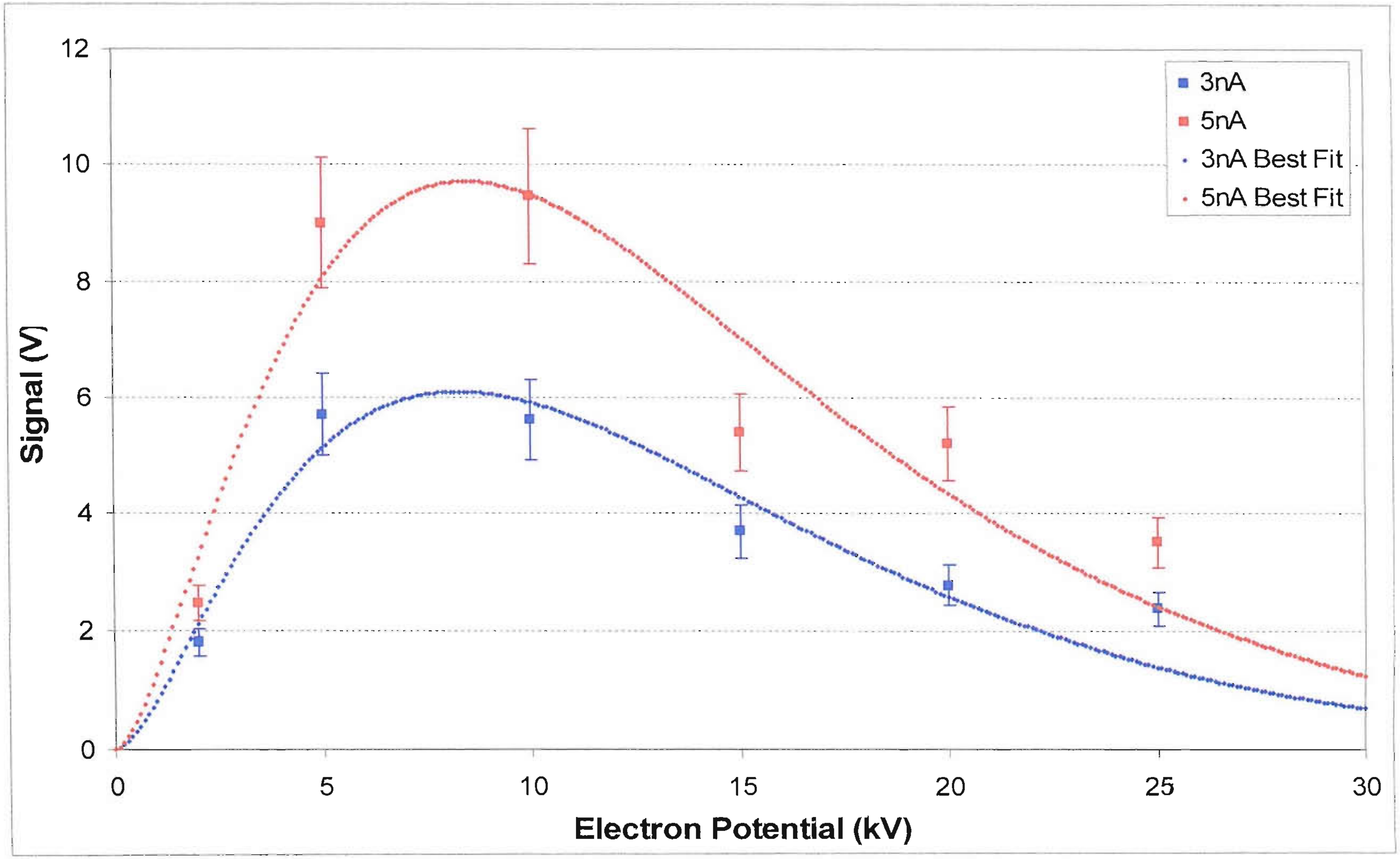

Figure 68: Bare AlGaN detector response curves to fixed fluxes

The best-fit curves are of the form:

$$f(x) = a\left[\frac{\left(\frac{2}{b}\right)^{c}}{e^{\frac{2}{d}}}\right]$$

Equation 30: Form of AlGaN electron exposure best-fit

Where a, b, c, and d are all constants. The curves are a reasonable fit and demonstrate their consistency by producing similar maxima: 8.3keV for 3nA and 8.5keV for 5nA. The FWHM ranges are very similar too: for 3nA the FWHM is 15.7keV between 2.8keV and 18.5keV, for 5nA the FWHM is 16keV between 2.9keV and 18.9keV. By extrapolating the curves to greater energies the signal drops below 0.1V at ~43keV for 3nA and ~47keV for 5nA.

4.2.4 Proportional response of the AlGaN detector

The calibration carried out between PTB and ESTEC was vital for determining the responsivity of the AlGaN detector as a function of wavelength. However, equally important is the determination of the response of the detector as a function of the intensity of the incident radiation flux. To this end the beam-cutter and Gautois meshes were used (see section 3.2.2) to vary the flux directed at the detector from a fixed, constant UV source (the UV-pen).

Figure 69, below, displays a close fit to a linear, proportional response from the UV detector (R^2=0.9872). The main central group of data points was predominantly obtained from the Gautois meshes and contains the greatest divergence from the linear fit. At either end of the fit, the outlying points were predominantly produced by the beam-cutter. These points lie almost perfectly along the linear fit calculated so this may be evidence that the beam cutter is a more consistent item of apparatus to use to reduce flux levels by an accurate, relative amount.

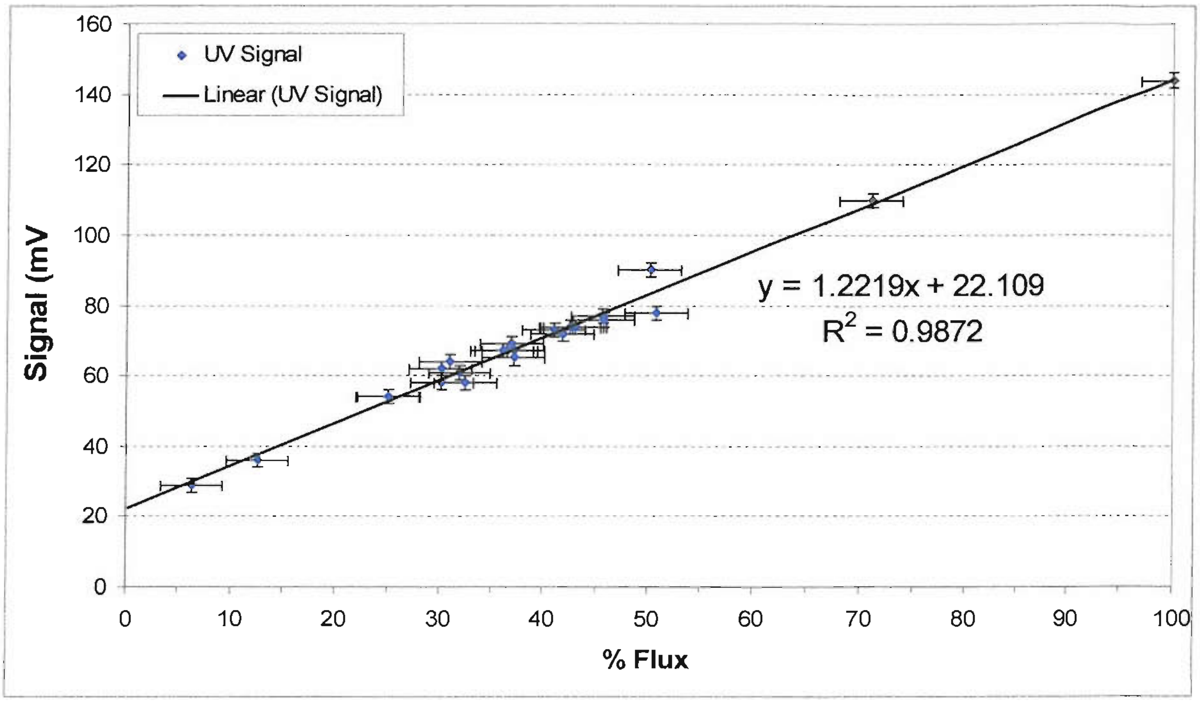

Figure 69: Response of AlGaN detector to known UV flux change

This is a straightforward demonstration of the linearity of response of the AlGaN detector. Although this is a relative measurement, it is an important result as it forgoes the need for complex determination of non-linear responses. There is little reason to expect fluxes at both low and high thresholds of detection to deviate from this linear response, considering such signal limits are predominantly set by the associated amplifiers and MEDET on-board data-handling (OBDH) system.

At the low threshold the signal output will be dominated by the offset from the associated amplifiers, shown in the above Figure as the intercept on the y-axis.

As can be seen, the response appears to be linear with intensity right down to ~7% of the flux level used. At the distance the UV Pen was placed from the detector the flux level, while not absolutely known, would be reasonably close to that expected on-orbit. This is due to the Pen being a similar distance from the detector as that used in the angle of incidence response, where the signal levels were similar to those used in the further responsivity measurements at ESTEC at a similar flux to a single solar constant, according to the absolute radiometers. Thus, if there is non-linear behaviour at very low flux levels it will only affect a small proportion of the detectors' signal range. However, considering the physical process of the signal generation it is unclear how non-linear behaviour could arise at low flux levels – the incident energy will promote electrons to the conductance band in a manner proportionate to the intensity.

At the high threshold, however, it is clear that non-linear behaviour could arise due to the rate of replenishment of electrons to the valence band failing to keep up with the rate of promotion of electrons to the conduction band. Alternatively, interference due to increased thermal excitation at high flux levels could impede the motion of electrons through the detector crystal. Both of these effects would serve to reduce the signal output disproportionately with increasing intensity. Yet no non-linear behaviour was observed, even at flux levels similar to what will be found on-orbit (as described above).

Throughout the tests at ESTEC it was noted that the detectors reached a maximum signal level when the associated amplifiers saturated, *not* when the above effects were observed to limit the detectors' outputs. Considering that the saturation level, for the second test circuit at least, was above 10V, then the range of the MEDET OBDH system up to 10V will place its own limit on the detectable range of flux intensity that will be far lower than the point at which non-linear effects are noticeable (if they arise at all).

4.3 University of Southampton Tests

The tests carried out at the University of Southampton were primarily concerned with the survivability of the STORM instrument unit with the detectors incorporated. Environmental extremes were generated by vibrational loads, thermal shock, and rapid depressurisation in order to assure that the instrument would survive the rigours of launch and insertion into the vacuum environment in LEO. In addition, standard house-keeping measurements of the amplifier offsets for the detectors were taken at various stages of construction and delivery in order to monitor any degradation of the detector systems (only the data from the Si and AlGaN detectors will be reproduced here as they are the most relevant).

Only the vibration testing and detector offset measurements are reproduced here. The thermal and depressurisation tests were mainly concerned with a coarse quantitative measure of the survivability of the detectors and the STORM module as a whole and are of little relevance suffice to say that the detectors were capable of handling the environmental loads applied.

4.3.1 Vibration Tests

The details of the shaker table used and the qualification vibration loads to which the STORM unit was submitted can be found in Section 3.3, above. The flight spare was tested to these qualification levels, whereas the flight model itself was tested to slightly lower acceptance levels so as to avoid over-stressing the structure.

In addition to the flight and flight spare models a number of other configurations were tested. These included:

1. A structural model consisting of the outer metal panels, the internal pins and unoccupied PCBs.
2. An electrical model similar to the structural model except for the inclusion of all internal electrical connectors and some populating of the boards.
3. An engineering model that comprised a fully operational version of STORM apart from the use of dummy-resistors for the detectors and a commercial level of soldering assembly.

All of these other configurations were tested to the qualification vibration levels. The only problem that was discovered during the vibration test campaign was the shearing of electrical connectors between the main PCB stack and the perpendicular main board for the zenith detectors on the electrical model. This problem was fixed by the addition of a fillet of epoxy resin between the connectors and their anchor point on the PCB – supplying the required level of mechanical support to resist the shearing forces.

Considering the only problem found was with an electrical connection with the STORM unit, it is clear that the detectors chosen are well capable of withstanding the vibration environment expected on launch by the Shuttle.

4.3.2 Detector Offset Measurements

When there is no incident radiation of the appropriate wavelengths on to the detectors, they produce a positive zero-offset reading that is capable of being read by the MEDET OBDH system. This is important as it provides a baseline signal level that can be easily identified as the point at which no radiation, or other interference, is affecting the output signal. If this baseline signal was too close to zero there would be the possibility that it could drift and become negative. If this were the case then the MEDET OBDH would not be able to recognise when the zero signal level had been reached – a zero reading could still be registering a small signal, yet this would be unknown. This situation would be very bad for the recording system as it would introduce a systematic error into all readings taken with the detector in question.

The following table notes the offsets recorded for the SXR and UV detectors on the Flight Spare and Flight Model of the STORM instrument suite, before and after the final stage of vibration testing.

Detector	Pre qualification test output signal on Flight Spare (UoS)	Post qualification test output signal on Flight Spare (UoS)	Pre acceptance test output signal on Flight Model (UoS)	Post acceptance test output signal on Flight Model (ESTEC)
	19/11/03	**24/11/03**	**26/11/03**	**11/12/03**
X-ray1	0.144V	0.132V	0.120V	0.1187V
X-ray2	1.30V	1.30V	1.17V	1.15V
X-ray3	0.044V	0.035V	0.031V	0.0304V
X-ray4	1.22V	1.26V	1.13V	1.09V
X-ray5	0.139V	0.131V	0.100V	0.0974V
X-ray6	1.25V	1.24V	0.99V	0.97V
X-ray7	0.041V	0.035V	0.035V	0.0352V
X-ray8	1.00V	1.02V	1.08V	1.07V
UV1	0.584V	0.579V	0.569V	0.571V
UV2	0.635V	0.635V	0.617V	0.617V
UV3	0.497V	0.499V	0.508V	0.509V
UV4	0.581V	0.586V	0.514V	0.514V
UV5	0.554V	0.554V	0.624V	0.625V
UV6	0.640V	0.639V	0.573V	0.572V
UV7	0.533V	0.532V	0.579V	0.580V
UV8	0.531V	0.529V	0.468V	0.464V

Table 9: Zero-offset level for each SXR and UV detector output line on the Flight Spare and Flight Model of STORM

There is the same number of SXR channels as UV channels because each SXR detector has two output channels, as described in Section 1.7.1. The most important point to note is the general consistency of the offset readings that demonstrate that the amplifiers and the detectors themselves are relatively stable (although these readings were taken a relatively short time apart).

These values will be required during the angle of incidence correction carried out on the flight data, as described in Section 4.2.2.

Unfortunately, it was not possible to carry out any further tests on long-term changes to the flight equipment – the instrument housing was too large and unwieldy for vacuum chamber insertion for SXR exposure and restrictions on the clean-room facilities used to store the flight model precluded the in-situ use of UV lamps.

As mentioned in Section 4.1, the lack of data on the consistency of response of the detectors has resulted in the assumption that each group will behave in a similar manner. It is recommended that when (if) the flight model is returned to ground a post-flight comparison between the flight model and flight spare model is conducted with the dual role of accurately assessing the degradation to the flight detectors and also assessing the similarity of response within each detector grouping.

5 Discussion

The broad investigation into the operation of the AlGaN and Si detectors described above allows for conjectures to be made into the ability of the STORM module to fulfil its role within the MEDET instrument suite. This section provides analyses of the results in the context of the STORM mission and its position on the ISS at its CEPF location.

Included are discussions concerning the ability of the radiation detectors to accomplish their goals; sources of interference that are expected on-orbit; and the expected operations if STORM reaches orbit and operates successfully.

Throughout the discussion there are many points where reference needs to be made to the orientation of the ISS throughout its orbit, as this will have a large impact on the expected data return from all of the radiation detectors and on the sources of interference they are likely to experience. To complement this analysis a geometric model of the variations in the ISS orbit over a period of one year was developed in an Excel spreadsheet to calculate, to a good approximation, how the attitude of the ram and zenith faces change with respect to the Sun vector. A brief overview of a single orbit is described here, with more detailed reference made to the model later on.

Figure 70, below, provides a plan representation of the orbit of the ISS when the orbital plane is parallel to the Earth-Sun vector (at a Beta angle of 0°). The orbit of the ISS is thus 'edge-on' with respect to a viewpoint from the Sun looking towards Earth. The orbital plane of the ISS does precess around the Earth, so this depiction is only valid at certain times, but it stands as a good example for now. Precession will be dealt with later in more detail as it affects data-return most specifically.

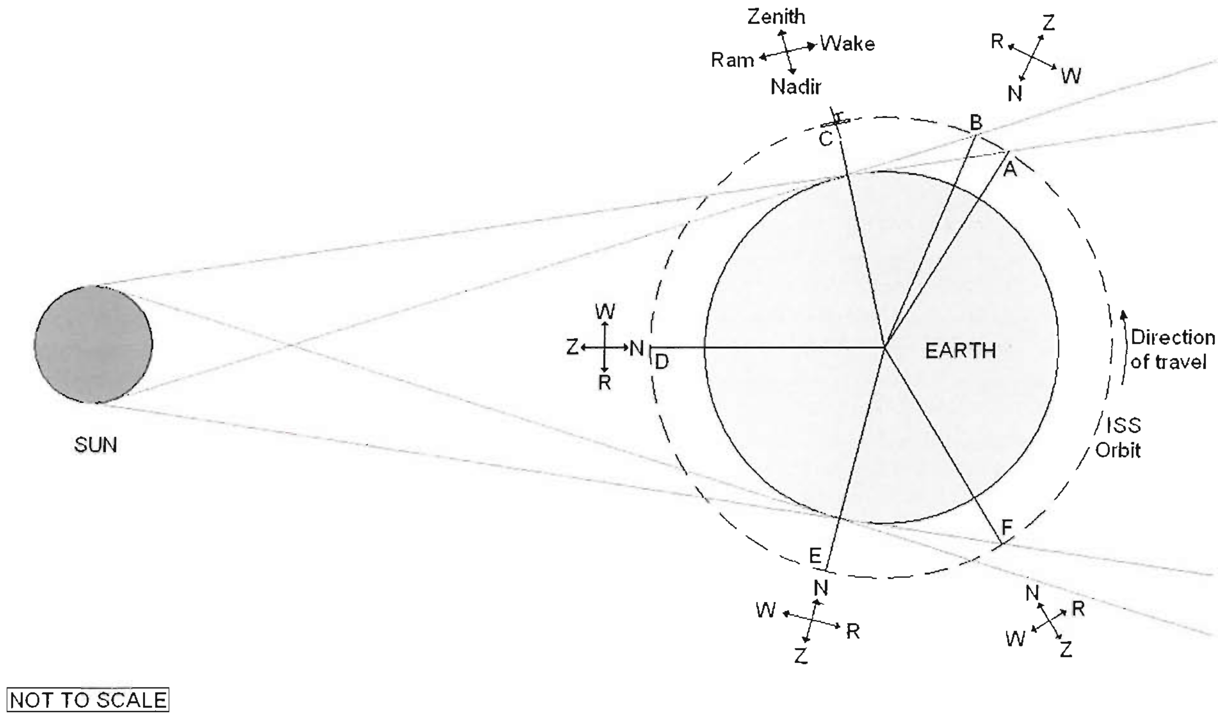

Figure 70: Plan representation of ISS attitude during an orbit

There are a number of important points (labelled A – F) during the orbit that need to be highlighted for their relevance to the operation of the detectors. At each of these points the orientation of the ISS is depicted with respect to the Ram, Wake, Zenith and Nadir directions – the Nadir being the side of the ISS that is constantly locked with respect to the Earth. Note that the lack of scale and proportion of the diagram is merely for convenience for this geometrical representation – a far more accurate geometry (i.e. where the lines from the limbs of the Sun passing the limbs of the Earth converge beyond the Earth due to the greater size of the Sun) has been used in the Excel model.

At point ‘A’ the ISS passes out of the full shadow, or umbra, of the Earth and the Ram face is immediately illuminated. It is expected for the Ram face detectors to begin registering a solar-dominated signal at this point. The Zenith detectors will remain in shadow for a few minutes further. At point 'B' the ISS passes out of the partial shadow, or penumbra, of the Earth and the full disk of the Sun comes into view of the Ram face. In the above diagram the distance of the transition crossing the penumbra from 'A' to 'B' is larger than in reality due to the distortion of the incorrect scale and proportions. The transition should take approximately fifteen seconds, so it is expected there will be a handful of readings taken during this time that show a sharp increase in signal level from the Ram face detectors as the penumbra is traversed.

At point 'C' the Ram face becomes perpendicular to the Sun vector; this is the point of maximum signal level for the Ram face detectors. It is also the point where the Zenith face begins to be illuminated, although the illumination of the Zenith detectors comes shortly afterwards due to their limited fields of view. Similarly, at point 'D' the Ram face becomes shadowed as it turns away from the Sun, while the Zenith face becomes perpendicular to the Sun vector and the detectors on that side reach their maximum signal level. Between points 'C' and 'D' are six further critical points relating to the fields of view of the Ram and Zenith sets of filtered UV, non-filtered UV and SXR detectors. These points are where all sets on the Ram face become shadowed as the Sun moves out of their field of view and where all sets on the Zenith face become illuminated as the Sun moves into their field of view. These will be described in more detail below under the discussion concerning fields of view for each detector type.

At point 'E' the Zenith face becomes shadowed as it turns away from the Sun, although there will be three points between 'D' and 'E' when the filtered UV, non-filtered UV and SXR detector sets each become shadowed as the Sun moves out of their fields of view. Lastly, point 'F' is where the ISS passes back into the umbra of the Earth. Although this has no effect on the readings of solar flux taken by the detectors (all of them now being shadowed), it will have a significant impact on potential sources of interference, such as backscattered atmospheric UV and charged particles, which will be reduced on the dark-side of the Earth.

Note that there is no corresponding point for when the ISS passes back into the penumbra as it is not thought that this will have a significant effect on the readings of the detectors considering they will all be shadowed by this stage.

It is also worth appreciating here that there are periods when the ISS does not enter the Earth's umbra during an orbit. Due to the ISS' inclination of ~51.6° with respect to the Earth's equatorial plane and the Earth's rotational inclination of ~23.5° with respect to the plane of the ecliptic there are periods during the year where these values sum to give a value of ~75.1° for the inclination of the ISS' orbital plane with respect to the ecliptic. At such times, and assuming a nominal altitude of 450km, the ISS will not pass into the umbra of the Earth for a number of consecutive orbits. Thus, for this special case, there will be certain orbits throughout the mission where points 'A', 'B', and 'F' do not arise.

These variations in the detection environment for both faces while on-orbit, while complicating matters compared to a Sun-pointing system, do have their uses as will be explained in the following discussion.

5.1 UV Detection

In Sections 4.1.2 and 4.2.1 the analysis of the AlGaN spectral response demonstrates that it is well suited to detection of VUV and NUV in the 120-315nm range. However, it is apparent that the sensitivity is far greater over the 230-290nm interval and that this, coupled with a corresponding larger solar flux, will serve to dominate the signal received by these detectors.

With the complete responsivity curves of the AlGaN detectors it is now possible to make an estimate of the expected on-orbit signal output by calculating the current produced per unit wavelength (nm), with respect to the incident flux from the Sun.

In order to generate an expectation value for the on-orbit signal the responsivity plots for the bare and filtered detectors must be multiplied, at each unit wavelength, by the UV irradiance of the Sun to generate the signal spectrum:

$$S(\lambda) = R(\lambda) I_{sol}(\lambda)$$

Equation 31: Expected signal from either AlGaN detector by solar illumination

Where	$S(\lambda)$	Signal induced in detector as a function of wavelength (mA)
	$R(\lambda)$	Responsivity of AlGaN detector (either bare or filtered) (mA/W)
	$I_{sol}(\lambda)$	Solar irradiance as a function of wavelength (mW/m^2/nm)

The solar irradiance data needed for the $I_{sol}(\lambda)$ values is displayed in Figure 71, below.

This irradiance data is an amalgamation of recordings taken by the EUV Grating Spectrograph (EGS), part of the Solar EUV Experiment (SEE) on NASA's Thermosphere, Ionosphere, Mesosphere Energetics and Dynamics (TIMED) spacecraft[126] (100-170nm at 0.4nm resolution), and the Solar Backscatter Ultraviolet 2 (SBUV/2) instrument on the National Oceanic and Atmospheric Administration 9 (NOAA-9) spacecraft[127] (170-360nm at 1.1nm resolution) during a period of solar maximum.

This data closely resembles that provided by the ASTM International Standard regarding zero air mass solar irradiance spectra[128]. However, the amalgamated data provided here is used in preference as it covers the Solar spectrum down to 100nm (providing information on the Lyman-α region), rather than the ASTM Standard coverage that ends at 200nm.

It should be noted that the solar UV irradiance varies markedly throughout the solar cycle. At the higher wavelength range >200nm this difference can be up to ~10%, at the lower range, including Lyman-α, it can be up to ~100%. This range of irradiances can be introduced to the expected signal level to produce an expected signal range.

Note the logarithmic scale used to denote the irradiance levels. Although the Lyman-α region dominates the low wavelength scale, once ~200nm is reached the higher wavelengths begin to dominate. The vast majority of the output signal is then expected to be generated by the 220-300nm range.

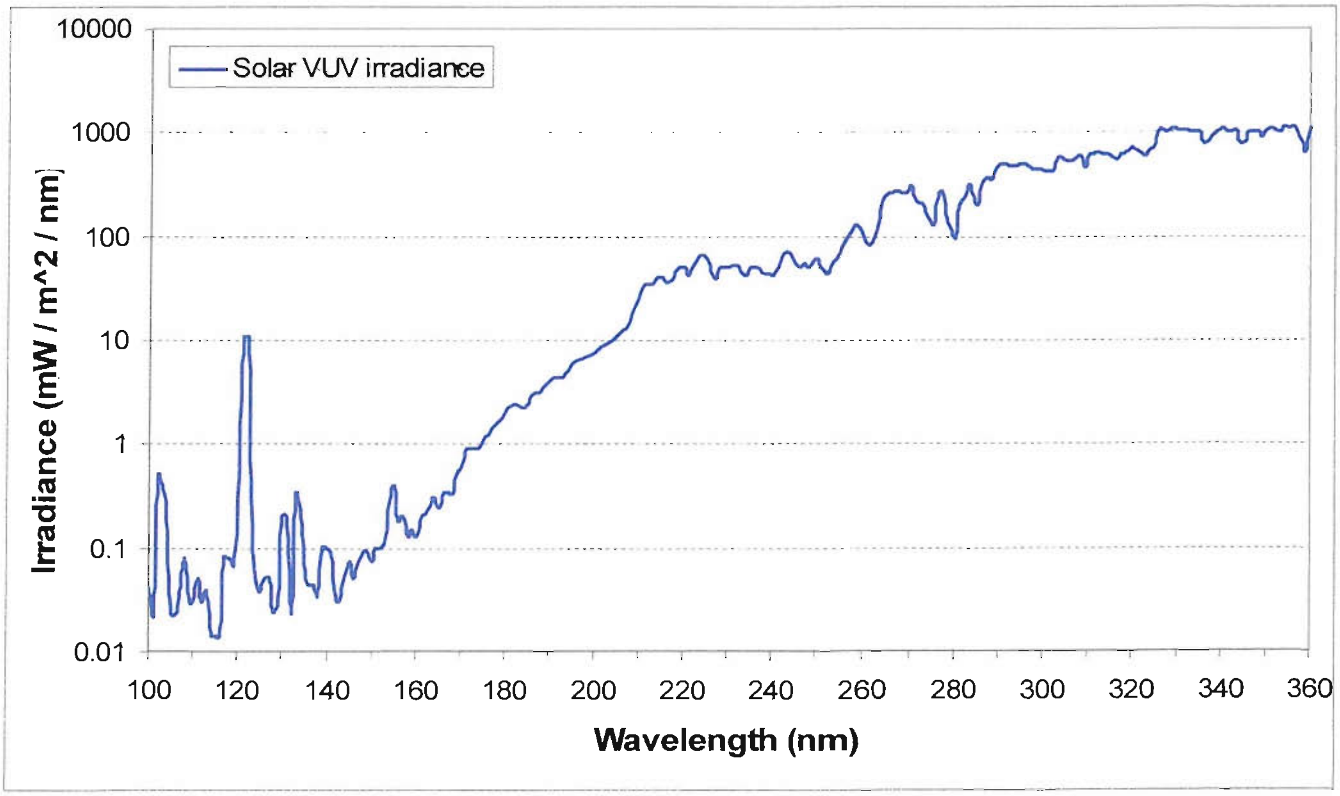

Figure 71: Solar VUV Irradiance from 100nm-360nm

The data in Figure 49 (the R(λ) values) and Figure 71 (the $I_{sol}(\lambda)$ values) are used, via Equation 31, to produce the expected signal per unit wavelength, as displayed in Figure 72, below.

The major effect of the multiplication by the responsivity is to further extend the logarithmic signal axis by more orders of magnitude. The effect of the lower wavelength region is thus further reduced in overall effect. The range from 260-310nm will totally dominate the output signal of the detectors.

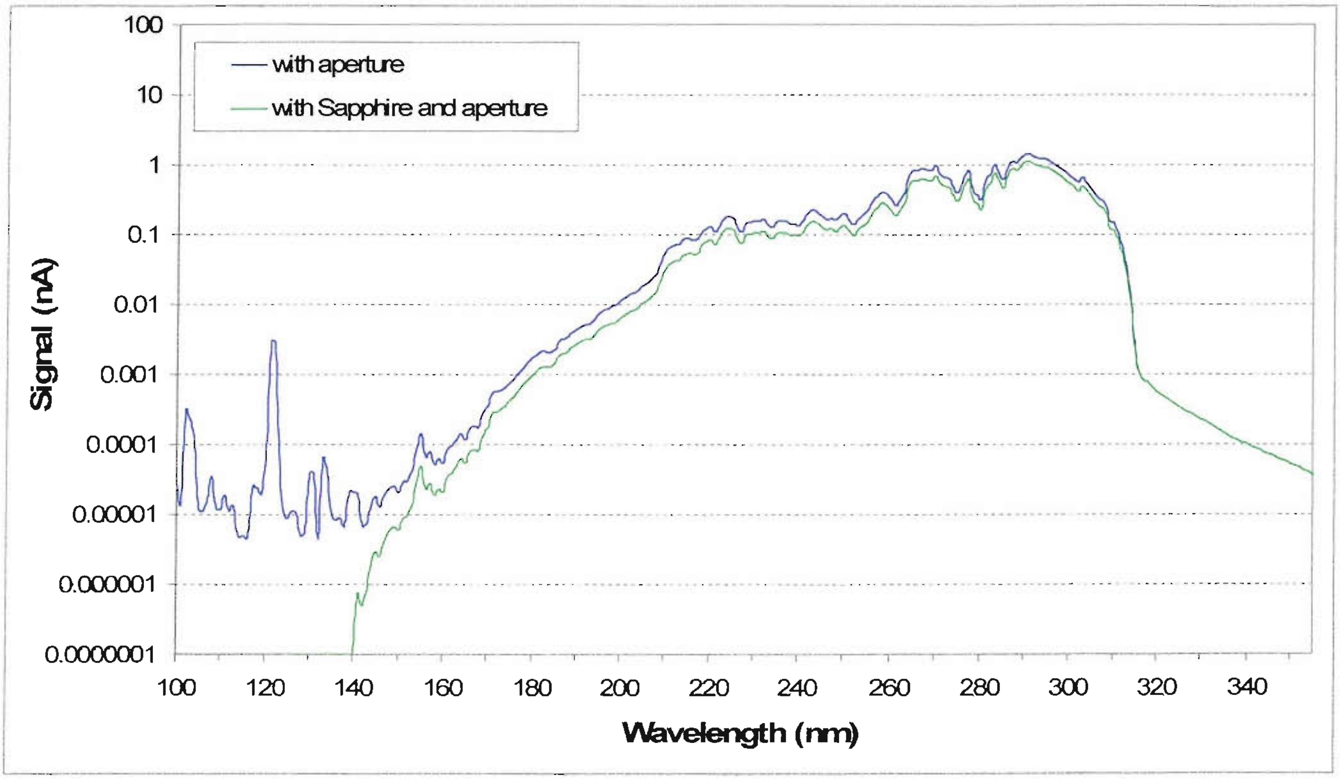

Figure 72: Expected on-orbit output signal of AlGaN detectors per unit wavelength

In order to ascertain the effect of the Lyman-α region on the signal output of the detectors it is necessary to look at the signal difference between the filtered and unfiltered signal values. This is done by deducting the 'with fused silica and aperture' signal from the 'with aperture' signal in Figure 72 to produce the signal difference, as displayed in Figure 73, below.

The signal difference closely represents the solar UV flux due to the logarithmic scale being the primary driver of the signal output. However, the detector systems will only measure an integrated response proportional to the total incident flux. In order to accurately calculate the signal component of each separate wavelength region in the spectrum, the signal difference needs to be converted to a linear scale, as shown in Figure 74, below.

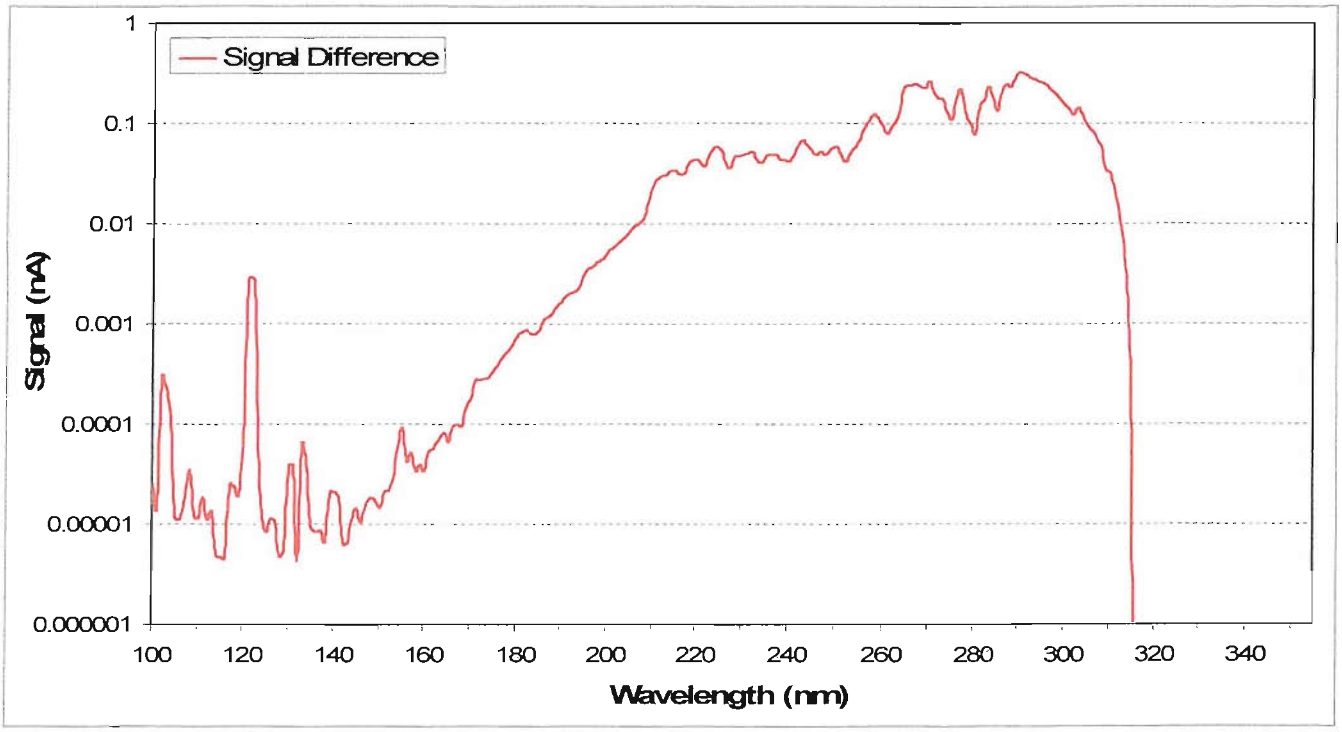

Figure 73: Logarithmic signal difference between bare and filtered AlGaN detectors

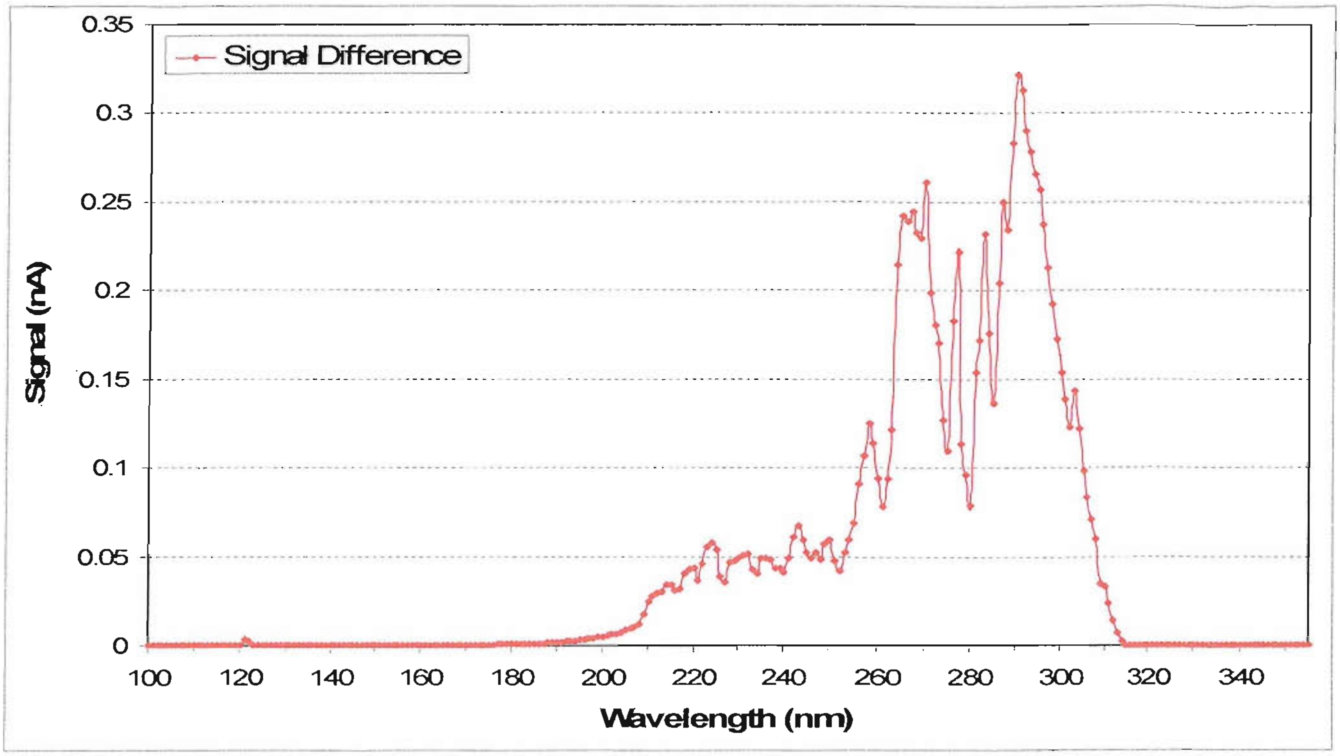

Figure 74: Linear signal differential between bare and filtered AlGaN detectors

From the linear scale it is clear, as noted previously, that the higher wavelength range (above ~200nm) totally dominates the differenced signal produced between the bare and filtered AlGaN photodiodes. The Lyman-α region has only a negligible contribution to this differenced signal, calculated from the integrated flux estimates of the data as 0.049%.

The estimated total integrated signal for the bare detector is: 37.1nA (3 sig. fig.)
The estimated total integrated signal for the fused silica-filtered detector is: 27.2nA (3 sig. fig.)

For a signal difference of 9.9nA the contribution to this of 0.049% from the Lyman-α spectral region will only just be detectable at the 12-bit resolution of the STORM instrumentation. 12-bit resolution gives a lower threshold limit of

0.0244% (3 sig. fig.). However, this assumes that the signal variation will cover the full 0-10V range of the detection electronics.

Taking these figures for the expected output current of the detectors, expected potential difference signals can be calculated by substituting them into Equation 3:

$$\begin{aligned} &Bare: && V_0 = I_d R_f = 37.1nA \times 470M\Omega = 17.4V \\ &Filtered: && V_0 = I_d R_f = 27.2nA \times 470M\Omega = 12.8V \end{aligned}$$

Equation 32: Expected on-orbit signals of bare and filtered UV detectors at Solar Maximum

It appears that the on-orbit expected signals will be larger than the desired range for the MEDET OBDH system. However, this is for the signal generated when the detectors are at normal incidence to the UV source, in addition to it being an approximation for solar maximum.

To correct for solar minimum an approximation is made whereby the flux for wavelengths >200nm is treated as being 10% lower and a linear reduction in flux from 120nm – 200nm[129] is made starting at 50% lower at 120nm[130] and ending with 10% lower at 200nm[131], in approximate accordance with the solar flux data as mentioned above. As a result the expected signal currents are 33.4nA and 24.5nA for the bare and filtered detectors respectively. The expected signals are therefore:

$$\begin{aligned} &Bare: && V_0 = I_d R_f = 33.4nA \times 470M\Omega = 15.7V \\ &Filtered: && V_0 = I_d R_f = 24.5nA \times 470M\Omega = 11.5V \end{aligned}$$

Equation 33: Expected on-orbit signals of bare and filtered UV detectors at Solar Minimum

So, the expected ranges of signal that can be expected at normal incidence are 15.7V – 17.4V for the bare UV detector and 11.5V – 12.8V for the filtered detector.

Whereas at normal incidence the detector will saturate the signal level, at a certain angle of incidence the signal produced by the detector will fall below the 10V threshold set by the MEDET OBDH system. For example, for the bare detector at solar maximum this angle can be calculated by using Equation 28 and assuming the recorded signal is 10V, rearranging (assuming a baseline signal of 0V for the example – each separate detector has its own baseline signal as given in Table 9):

$$\theta = \frac{\cos^{-1}\left(\dfrac{10V}{17.4V} + 0.017\right)}{0.967} = 55.6°$$

Equation 34: Minimum angle of incidence at which the estimated UV signal at solar maximum becomes detectable by the bare UV detector

Taking the minimum field of view measured for a bare detector of +/-72°, it will still be possible to take measurements when the Sun is incident between 55.6° and 72°. This may appear to be a narrow margin, but considering the lower rate of change of the UV irradiance as compared with the SXR irradiance, this will still allow for flux measurements to be made every orbit by detectors on both faces without missing important variations.

This case, the bare detector at solar maximum, is the worst – by comparison the filtered detector produces a result, from Equation 26, of:

$$\theta = \frac{\cos^{-1}\left(\frac{10V}{12.8V} - 0.002\right)}{1.091} = 35.6^{\circ}$$

Equation 35: Minimum angle of incidence at which the estimated UV signal at solar maximum becomes detectable by the filtered UV detector

For the minimum measured field of view of the filtered detector of +/-60°, this still allows measurements to be taken when the Sun is incident between 35.6° and 60° – a larger margin than for the bare detector.

For solar minimum when the expected signal values at normal incidence are lower (Equation 33), the minimum angles will be lower still, allowing for more measurements per orbit.

As mentioned previously, the difference in sensitivity between the filtered and non-filtered detectors, at all wavelengths (as shown in Figure 40, Figure 73 and Figure 74), means that there will always be a difference between the signals regardless of the fluctuations of the Lyman-α region.

The only way to monitor changes to the Lyman-α flux will be by temporal comparison of the data. If the filtered detector signal remains steady while the unfiltered signal changes, then the change can be attributed to the Lyman-α region. This method will severely limit the amount of data on the Lyman-α region because any fluctuation at other wavelengths (which will occur frequently) is likely to swamp the changes in Lyman-α.

Even when the filtered signal doesn't change it will be impossible to tell that this isn't due to one region of the spectrum increasing in flux while another region decreases – such undetectable simultaneous changes on the filtered detector will generate an apparent change in the non-filtered signal (due to the differences in responsivity at each wavelength region) and thus a false positive for Lyman-α region activity. However, such simultaneous and perfectly balancing flux changes are unlikely. The energy drivers for the Solar spectrum work across the spectral range – so an increase in one region of the UV spectrum will be accompanied by a corresponding increase across all wavelengths. But this fact also demonstrates the difficulty in isolating the Lyman-α region using the above method.

This is a disappointing conclusion, but one that is unavoidable given the properties of the detector and the Solar flux. A better configuration would have been to use a ~130nm short-pass filter over a selection of the detectors that would then only be sensitive to the Lyman-α region – providing a direct measurement rather than relying on a differenced signal analysis. This was not done for two reasons: 1) no short-pass filter with such characteristics was available, pre-integrated, from the supplier; and 2) such filters would limit the redundancy of the detectors as the filtered detectors would become insensitive to all longer wavelengths – in the current configuration redundancy is maintained due to the over-lapping sensitive regions of the filtered and non-filtered detectors. With design-decisions being required prior to the comprehensive calibration, the above reasons took precedence over delaying detector choice to a later date.

But even without the ability to detect the Lyman-α region, the inclusion of filters still has some potentially useful applications, as described in further detail below.

The proportional response of the detectors, as described in Section 4.2.4, indicates a straightforward linear translation of the recorded signals on-orbit to the incident flux. This is positive as it does not necessitate any complex signal processing to elucidate the magnitude of the relative flux changes. However, the fact that the response is linear is not particularly surprising as each incident unit of flux of a certain wavelength should promote equal numbers of charge carriers from the valence to the conductance band within the semiconductor. There was potentially a danger that at high flux levels the detector itself (as opposed to the amplifier) would saturate – the rate of charge carrier promotion being greater than the rate at which the valence band could be replenished from the circuit. Fortunately, this does not appear to be the case as it was always noted throughout the experiments on the detectors that the limits to the detectable flux were introduced by the amplifiers and not the detectors – easily verified by changing the gain on the amplifiers and noting a new saturation level.

In contrast, the most important factor to take into account for the on-orbit data will be the angle of incidence of the detector with respect to the Sun vector. As previously noted, this will change markedly throughout the mission over short timescales on every orbit. In Section 4.2.2.2, values for the field of view of the bare UV detector were measured as +/-72° and +/-75°, using the data from the UV pen that is, apparently, less affected by errors due to reflection than the data from the SORASI-mounted deuterium lamp. Similarly, for the filtered UV detector values of +/-60° and +/-64° were measured for the field of view. Taking the lower of these values as a conservative measure it is possible to see how the UV detectors on both Ram and Zenith face will interact during an orbit.

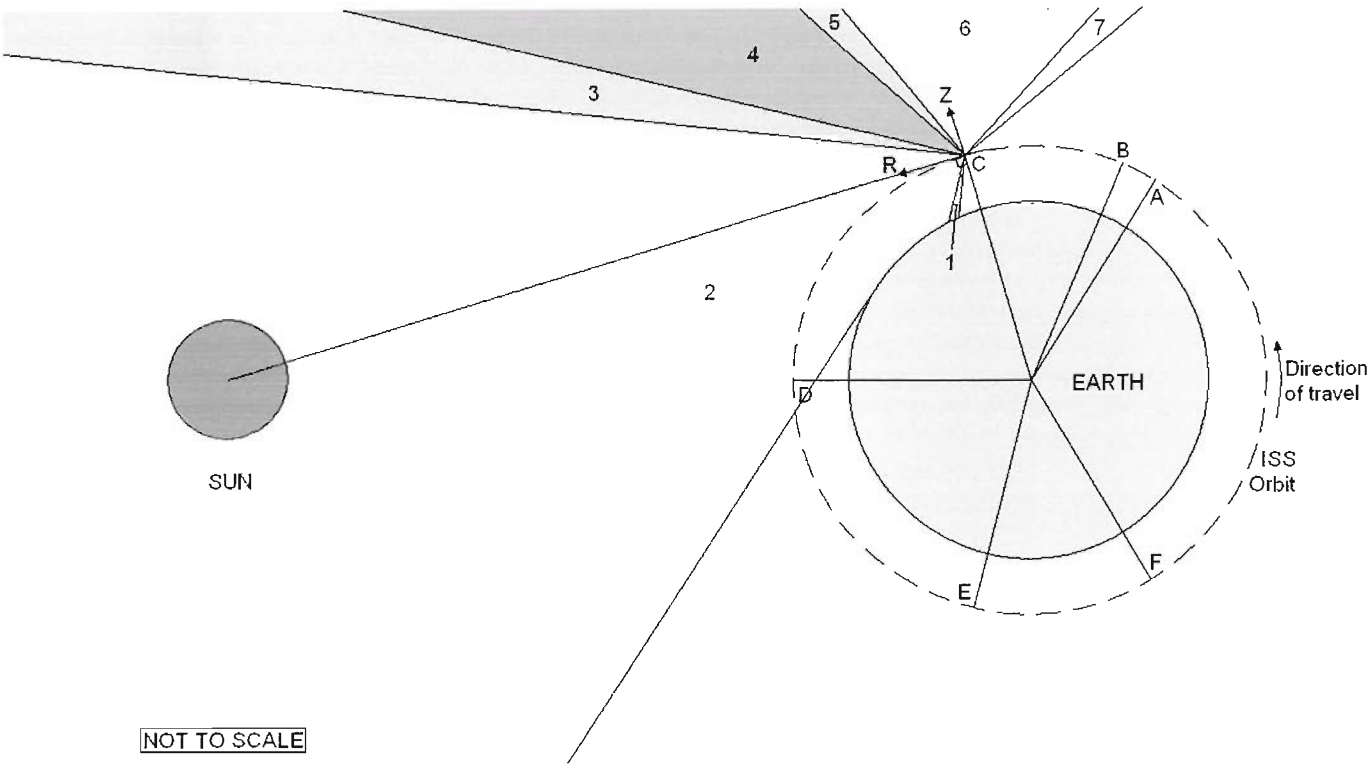

Figure 75: Plan representation of the fields of view of Ram and Zenith VUV detectors

Figure 75, above, is an altered version of Figure 70 to depict how the fields of view of both filtered and bare sets of UV detectors on the Ram and Zenith faces overlap when the ISS is at position 'C' with the Ram face perpendicular to the Sun vector. The shaded areas between the Earth and the Sun represent regions that are within the line of sight of one or more sets of detectors. These areas are split into 7 numbered zones that correspond to the detector sets as described in the following Table.

As the ISS continues in its orbit the Zones will remain fixed with respect to the Ram and Zenith vectors (depicted as R and Z in the above Figure) and so will sweep through 360° as the ISS rotates with respect to the Sun, as shown in Figure 70. The transitions between Zones 2 & 3, 3 & 4, 4 & 5, and 5 & 6 are four of the six previously mentioned critical points that occur between points 'C' and 'D' (the other two being for the SXR detectors).

Zone	Ram, Bare	Ram, Filtered	Zenith, Bare	Zenith, Filtered
1	✓	X	X	X
2	✓	✓	X	X
3	✓	✓	✓	X
4	✓	✓	✓	✓
5	✓	X	✓	✓
6	X	X	✓	✓
7	X	X	✓	X

Table 10: VUV detector fields of view with respect to Zones in Figure 75

Where: ✓ Sun is within the detectors' field of view

X Sun is not within the detectors' field of view

Zone 1 appears to be always and only oriented towards the Earth. Yet this is only the case for this special condition when the plane of the ISS' orbit is parallel with the Sun vector. As the orbital plane precesses there will be times when the Sun does enter Zone 1, more on this below.

Zones 2 and 6 have the common property of being the two regions where the respective bare and filtered UV detectors on both faces are in view of the Sun simultaneously. They also contain the periods of maximum signal value. Both of these properties will allow a comparison between the readings taken on the Ram and Zenith faces that will elucidate any divergence of response, for example due to higher atomic oxygen erosion affecting the sensitivity of the bare Ram UV detectors and the transmission of UV through the filters.

These will also be the most advantageous times to compare the filtered and bare detector signals for any differences due to changes in the Lyman-α region. Although it appears unlikely that any changes to the Lyman-α flux will be able to be determined from the difference between the separate signals, the best time to check this will be when the detector readings are at their highest level.

Zones 3, 4, and 5 are periods when the difference between the Ram and Zenith signals can be compared using simultaneous data (although comparing signal levels from Zones 2 and 6 are unlikely to be greatly in error as the Solar UV flux does not change that rapidly on the order of minutes). Zone 4 is especially useful in this regard as it contains the point where both faces are simultaneously inclined at 45^{o} so the data from all UV detectors at this point will be produced by equal flux levels.

Zone 7 merely delineates the maximum field of view of the bare Zenith detectors.

When each of the lines separating the Zones sweeps across the Sun as the ISS rotates, there will be a period of ~15 seconds when the Sun is in partial view. This is analogous to when the Sun initially becomes visible to the Ram detectors as the ISS passes through the penumbra. It should be expected that a handful of readings covering this time-span will be produced that rise (or fall) rapidly as the Sun comes into (or moves out of) the detectors' field of view.

The investigation done to determine the fields of view of the UV detectors and provide equations from which the true value of the Solar UV flux can be determined has covered essential ground in the characterisation of the detectors that will be of great use to interpreting the data when the instrument is on orbit.

As a final point regarding the AlGaN detectors, it was previously mentioned that the precise ratio of AlN:GaN was not made available (see Section 1.7.2). However, from the determination of the cut-off wavelength at which the responsivity of the detector effectively reaches zero (315nm – see Figure 72) it is possible to estimate that the amount of AlN present is ~28%, using data from

Shan et al.[132], far different than the 35-40% provided by the manufacturer. However, this apparently smaller level of AlN may well be due to contamination by oxygen, as noted below in Section 5.3.5.2.

5.2 SXR Detection

In Section 4.1.1 the analysis of the SXR detector's sensitivity demonstrates that it will be suitable for the proposed purpose. The FWHM of 15.7keV centred at 10keV is slightly wider than for the proposed range of 1-10keV and similarly the lower energy cut-off at ~2keV (50% of maximum sensitivity) will miss the 1-2keV region (although this will still be detected at sensitivity levels <50% of maximum). However, it is recognised that these deviations from the proposed range are inherent to the properties of the materials used.

To reduce the lower energy cut-off would have required a thinner beryllium filter. While this would have been possible it would have necessitated a non-standard thickness that would have driven up costs. It would also have made the filters more delicate and therefore more susceptible to damage, either through accident or through micrometeoroid impact. Lastly, the thinning of the filter would have projected the 'tail' of the low energy sensitivity into the region below 1keV. This could have had a disproportionate impact due to the rapid increase in Solar flux levels over energies lower than 1keV. The 50μm thickness used for the filters proved to be the best trade-off between these factors, producing a sharp cut-off at an acceptably close proximity to the 1keV proposal while retaining the maximum thickness to ensure as much strength and longevity as possible.

It is far more difficult to estimate an expected on-orbit signal level for the SXR detectors than for the UV detectors. This is because the available data in the literature for the SXR energies of interest does not have a spectral energy resolution equivalent to that given for the SXR detector sensitivity in Figure 35 and Figure 36. For example, a good review on the variability of the Sun's output (Lean J. 1997[131]) only provides the background SXR flux as a band from 1-8Å (1.5-12.4keV) with an integrated value ranging over 0.1-5μW/m^2, derived from GOES satellite data. Almost all spectral irradiance data for the Sun is provided with a resolution of 1nm, so for the range of interest from 1-10keV this corresponds to 0.1-1.2nm – so it is only to be expected that only a single integrated value for the Solar flux over this band is currently available.

This being the case, the expected signal output for the SXR detectors when flare events are not occurring will be somewhat approximate. Taking the range given above the average responsivity for the SXR detector (from Figure 35) is 260mA/W. With an active area of 0.81cm^2 the expected output current range will be:

$$\begin{aligned} &SXR\ background\,\mathrm{min.}: && 260mA/W \times 0.1\mu W/m^2 \times 0.81cm^2 = 2.1pA \\ &SXR\ background\,\mathrm{max.}: && 260mA/W \times 5\mu W/m^2 \times 0.81cm^2 = 105pA \end{aligned}$$

Equation 36: Expected SXR detector signal currents for maximum and minimum levels of the solar background

These background signal levels are tiny, but will be magnified by the amplification stages to produce potential difference readings that can be estimated using Equation 1 and Equation 2 and that are reproduced in Equation 37, below.

Given the 12-bit resolution of the MEDET OBDH system over the 0-10V output range, it will be able to discriminate down to ~0.002V increments. As it is now expected that STORM will be operational as the next solar maximum is approached then it is clear that the V_{O1}(3.3kΩ) channel will be capable of detecting the background SXR flux from the Sun.

$$
\begin{aligned}
V_{O1}(3.3k\Omega) &= 2.1pA \times 10M\Omega\left(1+\frac{1M\Omega}{3.3k\Omega}\right) = 0.006V \quad (Solar\,\text{min.}) \\
&= 105pA \times 10M\Omega\left(1+\frac{1M\Omega}{3.3k\Omega}\right) = 0.319V \quad (Solar\,\text{max.}) \\
V_{O1}(10k\Omega) &= 2.1pA \times 10M\Omega\left(1+\frac{1M\Omega}{10k\Omega}\right) = 0.002V \quad (Solar\,\text{min.}) \\
&= 105pA \times 10M\Omega\left(1+\frac{1M\Omega}{10k\Omega}\right) = 0.106V \quad (Solar\,\text{max.}) \\
V_{O2} &= 2.1pA \times 10M\Omega\left(1+\frac{1M\Omega}{100k\Omega}\right) = 0.0002V \quad (Solar\,\text{min.}) \\
&= 105pA \times 10M\Omega\left(1+\frac{1M\Omega}{100k\Omega}\right) = 0.012V \quad (Solar\,\text{max.})
\end{aligned}
$$

Equation 37: SXR Detector expected signal ranges for solar background on all channels

During low-intensity solar activity it will be the same channel that is used for detailed monitoring. However, once the SXR flux increases in magnitude by 2-3 orders then this channel will saturate and $V_{O1}(10k\Omega)$ will take over as the most detailed monitor. The same will occur again for the largest events where the two remaining V_{O2} channels will monitor the largest solar flare events while the other two channels are saturated.

In all, the detectors cover a dynamic range with a factor of ~300 (given the solar max. levels). However, the largest solar flare events can increase the background flux level by four or even more orders of magnitude. It will probably not be possible to capture the peak levels of the very largest events, but almost an extra order of magnitude in the detectors' dynamic range can be found due to the angle of incidence response, as displayed in Figure 52. At angles of incidence at or just greater than +/-32°, the detected flux will be five times lower than at normal incidence, allowing the V_{O2} channels to monitor flare events of five times greater magnitude than if they only monitored the Sun at normal incidence.

It was, unfortunately, not possible to carry out any proportional response tests for the SXR detector due to no appropriate SXR source being available. That used in the SORASI tests was not collimated and the internal geometry of the chamber itself was not known to a high enough degree to ensure accurate results. However, it is well known that silicon detectors respond linearly in response to linear changes in signal level at other wavelengths (e.g. power production calculations for silicon solar cells for missions throughout the Solar System at different ranges from the Sun), thus it stands to reason that the response at SXR energies will also be linear. Similarly to the UV detectors, it was found that the saturation levels of the SXR detectors was determined by the gain level of the associated amplifier – this demonstrates that no effects at the quantum level, such as the rate of repopulation of charge carriers being less than the rate of promotion to the conductance band, will affect the signal produced while on orbit.

The angle of incidence measurements taken of the SXR detector differ quite markedly from the bare and filtered VUV detectors due to a much narrower field of view of +/- 32°. This is undoubtedly due to the beryllium filter placed over the detector. However, it also means that there is no overlap between the fields of view of detectors on the Ram and Zenith faces, as illustrated in Figure 76, below.

As a result, there is no period when the SXR detectors on the Ram and Zenith faces will be taking measurements simultaneously. A comparison of the detectors' performance can therefore only be made when they are at similar attitudes to the incoming solar flux – changes in the solar flux in the meantime must be anticipated, which will undoubtedly prove problematic. Care must be taken to compare the Ram and Zenith detector sets when the solar SXR flux is at a relatively constant level, usually when the Sun is not active.

Zones 1 and 2 in Figure 76 are just representative of the regions covered by the Ram and Zenith SXR detectors, respectively. It must be noted that the Earth appears to be outside of the field of view of the Ram detectors (Zone 1). This will not be the case in reality, but is merely a figment of the scale contortions used in the Figure for the sake of clarity (indeed, for a nominal altitude of 450km a ram-facing detector would require a field of view of less than ~+/-20.9° in order for the Earth to be outside of this field).

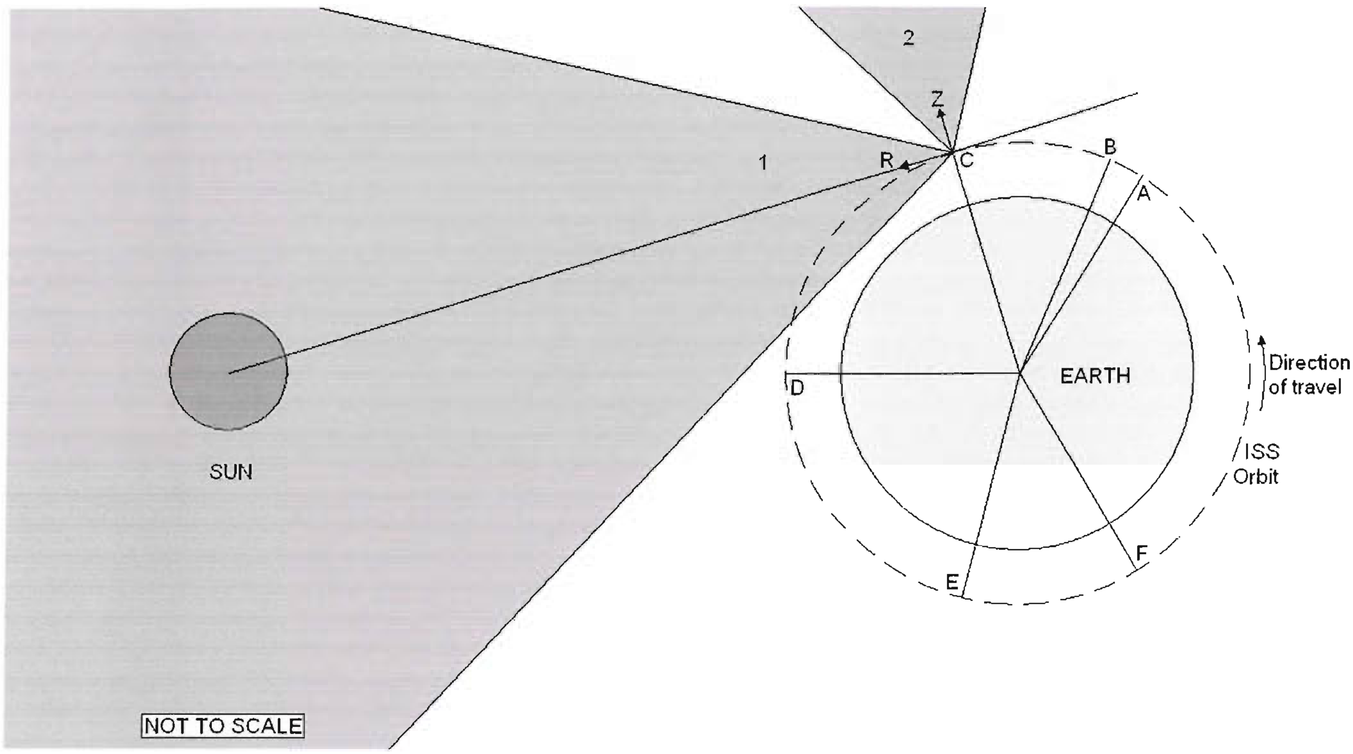

Figure 76: Plan representation of the fields of view of Ram and Zenith SXR detectors

As noted for the UV detectors, when the boundaries of the Zones move across the Sun there will be a short period when the detectors are only looking at the partial solar disk. Therefore, there will be brief periods of rapid signal increase and decrease at the beginning and end of each observation period.

The points at which the Ram and Zenith sets of SXR detectors become illuminated and then occulted make up the further two critical points between 'C' and 'D' and the further critical point between 'D' and 'E', as mentioned in Section 5.

It is obvious that the coverage of the sky by the SXR detectors is inferior to that provided by the UV detectors. This will have an impact on the amount of data recovered by each detector proportionate to their percentage cover of the celestial sphere. This concern was the major reason underlying the decision to use unfiltered VUV detectors where possible, unfortunately the same could not be accomplished for the SXR detectors. Whereas such a limitation in their field of view is disappointing, it is a necessary sacrifice in order to achieve the desired sensitivity range.

5.3 Sources of Interference

While on orbit the radiation detectors of STORM will be exposed to every element of the LEO space environment. Although chosen to be sensitive to the target radiation range, it is nevertheless important to appreciate further influences that will affect the signal output level and endeavour to account for these sources of interference in the data analysis during and after flight.

Of greatest concern will be the bare UV detectors. With no filters present the AlGaN crystal that comprises the active detector element will be fully exposed to the environment and will be acted upon by any incident particles and radiation. The filtered UV detectors and SXR detectors are of less risk of direct interference and degrading effects, yet the filters themselves will still be directly affected that could generate indirect influences on the signal levels.

This section will deal with all the sources of interference expected for the detectors and highlight which will be the most important and any possible methods of mitigating their impact.

5.3.1 Thermal Noise

Of significant importance to space operations is the effect that changes in temperature have on various systems. This is no less true of instrumentation, where different thermal regimes can affect the sensitivity of detectors by introducing forms of noise that can swamp the desired signal.

For the radiation detectors on STORM there are two major factors affecting the local thermal environment. The first is the low altitude of the orbit that will necessitate some period of eclipse (usually of about 30 minutes duration) in the vast majority of orbits during a year's operation. This will generate thermal cycling with a ~90 minute period with lowest temperatures seen just before sunrise (when MEDET has cooled over the entire eclipse period) and highest temperatures when the Sun is above the zenith plate (when MEDET has been heated for the longest period – beyond the zenith the wake face of MEDET will begin to be shadowed by the other experiments onboard EuTEF and the incident solar flux will correspondingly reduce).

The second major factor is the rotation of the ISS throughout its orbit. This will illuminate and occult the ram and zenith faces of STORM (and MEDET) for different periods and at different inclinations in each orbit, thus depositing varying amounts of solar radiation on to STORM (and MEDET) that will directly impact the rates of change of temperature and the limits of the temperature range experienced.

There are further factors that will affect the thermal input to STORM including: the changing view-factors to other components of the ISS (for example, the main port and starboard solar panels that rotate to track the Sun will, at varying times, provide surfaces that will reflect solar radiation back on to the surfaces of STORM and MEDET - the fact that the panels rotate to track the Sun makes the modelling of their variable input to the STORM/MEDET thermal environment extremely difficult); the power output of the other instruments within MEDET, some of which operate transiently, which will affect STORM both by their radiated component within MEDET and their conducted component through the MEDET superstructure; the power output of other experiments onboard EuTEF that will also have radiated and conducted components; and reflected and emitted radiation from the Earth that will vary according to albedo and illuminated/eclipse conditions.

Such complex and comprehensive thermal modelling has been outside the scope of the STORM and even the MEDET project, mainly due to continuing uncertainties in power outputs of surrounding equipment and the lack of configuration information regarding the state of the ISS when EuTEF will be attached (various configurations have been mooted ranging from 'core complete' to full construction and the effects of these differences are dependent on factors, such as launch manifests of the US Shuttle and Russian Soyuz, that are outside the control of the MEDET and EuTEF projects). However, it is possible to appreciate the potential effects of the thermal environment on the detector systems and some capability for on-orbit monitoring has been built into the STORM hardware.

There are two major points in the detector circuits where thermal changes will most dramatically affect the signal output. These are the detectors themselves and the associated transimpedance amplifiers that boost the received signal current and convert it to a potential difference output for the MEDET OBDH system.

For the detectors the greatest source of thermal noise will be in the form of shot noise, where quantum-scale temperature fluctuations cause the random generation of electron-hole pairs, generating an intrinsic current within the detector even when no light of the appropriate frequency is incident. Such a current is known as the dark current due to the fact that it is generated even when the detector is not illuminated. The greater the temperature, the greater the likelihood of thermal fluctuations generating electron-hole pairs and thus the dark current generally increases with increasing temperature.

For PIN photodiodes, that do not have an inbuilt process for increasing the gain of the signal (as opposed to avalanche photodiodes), the dark current is not as debilitating – one of the main reasons for choosing such types of detectors for STORM. This is because any gain in the circuit treats all currents, whether generated by photons or due to noise, as the same and thus the noise is unavoidably magnified as well.

Reproduced below is a plot of the dark current as recorded by APA Optics for one of their GaN detectors.

It can be expected that the AlGaN detectors used for STORM will have somewhat similar dark current characteristics. Whereas the introduction of aluminium creates a larger band-gap that will restrict the number of electron-hole pairs generated by thermal fluctuations, there is the converse problem that a mixture of the two crystal types leads to a higher number of lattice discontinuities that can increase the number of electron-hole pairs thermally generated. Such an investigation into the thermal properties of AlGaN was beyond the scope of the experimental work with the difficulty of separating the thermal effects from the crystal of the detector itself and the rest of the amplification circuit.

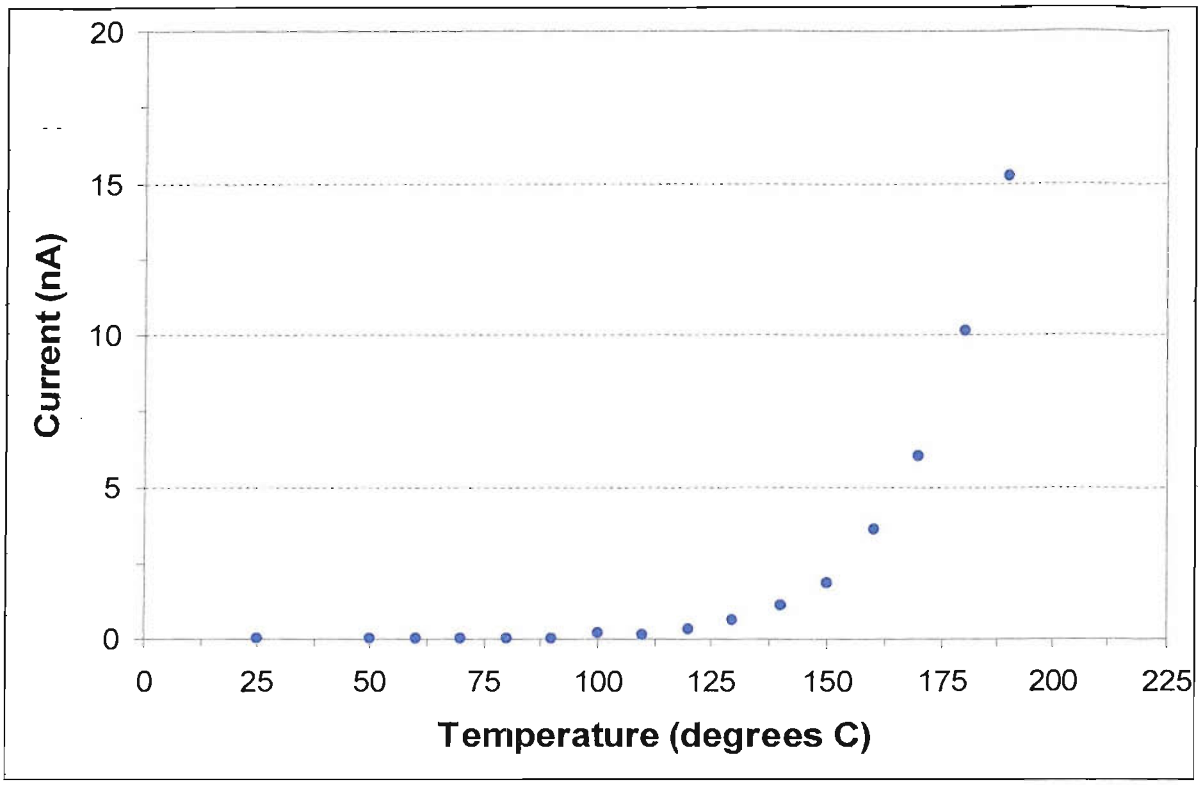

Figure 77: Dark current vs. temperature for an APA Optics GaN detector

Assuming that the AlGaN detectors do have similar dark current characteristics to those plotted for GaN then there should be little interference with the expected signal. MEDET is planned to operate with a maximum temperature of 40°C, whereas the dark current for the detector becomes significant at ~90°C. The planned operating temperature is for a mean level across MEDET – when the ram and zenith panels become illuminated by the Sun they will certainly reach higher temperature levels due to the direct solar flux and delay in conducting this heat away from the faces into the rest of the MEDET structure. This will undoubtedly affect the detectors in a similar manner (especially the bare UV ones) and the maximum temperature that will be experienced is unknown.

However, the STORM unit is fitted with PT100 detectors on six of the eight UV detector cans in order to monitor the temperature of the detectors, as closely as possible, throughout the mission. The large changes in temperature that will be experienced when the detectors are illuminated and occulted can be accurately monitored and correlated with changes in signal level. This will usually coincide with periods when the detectors are collecting data on the solar flux, which will make extrapolation of the thermal effects difficult. However, there will be orbits when the Sun is outside of the detectors' field of view, yet will still be warming the surrounding material on each respective panel. At these times, without the interference of an active Sun-monitoring signal, it should be far easier to correlate changes in temperature with the recorded signal level and from there extrapolate the effects of temperature on the recorded signals in Sun-detecting orbits.

For the SXR detectors the dark current characteristics are known directly from the Hamamatsu catalogue[133]. They are displayed below for convenience.

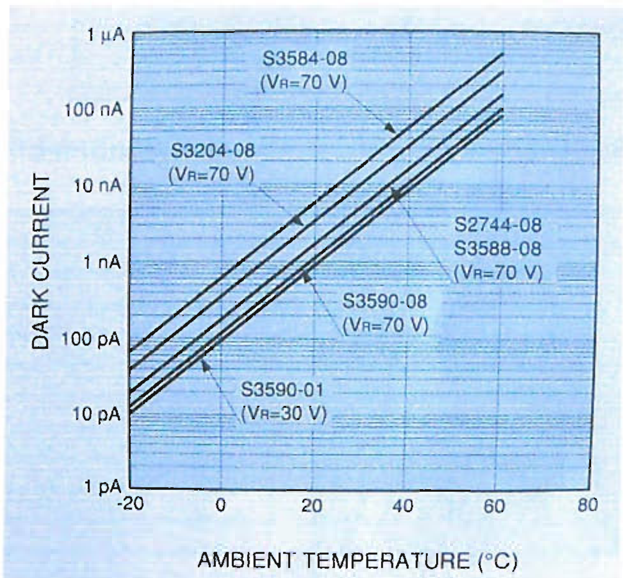

Figure 78: SXR detector dark current vs. temperature

The detector in question is the S3590-08 with the penultimate lowest dark current production of this detector family. It is apparent that as the dark current increases it begins to reach a level equivalent to that expected to be generated by the incident SXR flux. This apparently would appear to pose a problem for the on-orbit recording of the flux signal as the temperature of the detectors rose.

However, during integration of the flight model of STORM a number of baseline measurements of the SXR detector outputs was made (effectively measuring the offset of the amplifiers plus any amplified dark current that was being generated) at temperatures between 20-30°C. No significant deviation from the amplifier offset was observed, leading to the tentative conclusion that the dark current is not greatly affecting the signal output at present.

However, as with the UV detectors, PT100 temperature sensors have been placed against the ceramic housing of the silicon SXR detectors to monitor their operating temperature throughout the mission. It is expected that they will encounter far lower changes to their thermal environment due to the insulation provided by the beryllium filters. This will serve to reduce the extremes of maximum temperature due to direct solar illumination that will affect the UV detectors.

Apart from the detectors the second important component within the circuit that will be affected thermally will be the amplifiers themselves. The amplifiers, being situated within the STORM unit itself, are unlikely to experience large, or rapid, changes in temperature as they will not be directly exposed to sunlight. In addition, due to the decision to operate the radiation detectors constantly the amplifiers will always be active. On being activated they will heat themselves to a nominal operating temperature that will be higher than the surrounding ambient temperature. It may well be possible to discern the rise in signal at the beginning of operations as the amplifiers reach their maximum operating temperature – a process observed to take roughly 40 minutes in vacuum.

For the UV detector amplification and the first stage of SXR detector amplification the LM108A operational amplifier is used. It has an average drift to the input offset current of 2.0pA/°C[11]. For the second stage of SXR detector amplification the dual LM158 operational amplifier is used, where the signal from the first stage is split and increased by different gains across each of the LM158 channels. The typical drift of the input offset current is 10pA/°C[12], although larger than the LM108A this will have a lesser impact on the signal as it is already much larger after the initial stage of amplification.

5.3.2 Charged Particle Noise

One of the most conspicuous elements of the space environment is the abundance of charged particles, mostly electrons and protons of varying energies, which are incident on to spacecraft. For the LEO environment at the ISS' altitude there is also a large component of O^+ ions due to the relatively high density of the neutral atmosphere. The space plasma environment around Earth tends to have low temperature, high density plasma near the thicker layers of the Earth's outer atmosphere which changes with increasing altitude to high temperature, low density as the magnetopause is approached (including such regions as geostationary orbits). Thus the ISS will be situated in the high density plasma region near the atmosphere's outer layers.

From the perspective of spacecraft charging and large local potentials being generated this is of some benefit, as the high density leads to a relatively short Debye length (of the order of a few centimetres) that serves to neutralise large potential differences due to the high flux of particles on to ISS surfaces. Certainly, the STORM and MEDET units are extremely unlikely to be affected by problems concerning arcing and electromagnetic discharge due to the quasi-neutral state of the ISS.

However, it is possible that incident electrons on to the detectors will join the generated current and cause an increase in observed signal level. In order to reach an estimate of this effect the expected on-orbit electron flux must be compared to the electron fluxes that the detectors were exposed to in the ground testing within the SORASI chamber, as described in Section 4.2.3.

The on-orbit electron flux can be estimated from the AE8MAX environment model results as produced in NASA document SSP 30512[134] for the ISS. The data provided therein is represented as the integral flux – for any given electron energy value the integral flux is the number of electrons of that energy or higher incident on to the unit area per unit time. To calculate any signal that might be generated in the detectors it is necessary to know the flux of electrons within specific energy bands, so the integrated flux must be converted into this format, as displayed in Table 11, below.

It is clear from the results of the electron exposure in Section 4.2.3 that the bare UV detector is most sensitive to incident electrons. The results for the best fit of the signal generated by an incident electron beam of constant current against electron energy, displayed in Figure 68, are divided into 0.1keV points or bins.

Energy Range (MeV)	**Electron Flux** (10^9 electrons/cm^2/day)
0.01 – 0.04	4.51
0.04 – 0.07	3.45
0.07 – 0.1	2.65
0.1 – 0.2	5.67
0.2 – 0.3	1.95
0.3 – 0.5	1.07
0.5 – 0.7	2.06
0.7 – 0.9	8.39
0.9 – 1.0	2.68

Table 11: Electron flux per energy band in LEO converted from integrated flux values

A similar division of the electron flux into 0.1keV bins was calculated over the range 0-1MeV using an exponential best fit curve calculated from the data in Table 11. The product of the electron sensitivity per 0.1keV bin with the expected flux per 0.1keV bin thus produced an expected signal for each bin (once corrections had been made for the active area of the detector and time period). The sum of the expected signal for each of the 10,000 bins then produced a final cumulative signal, as expected to be read off by the MEDET OBDH system.

Both the 3nA and 5nA best fit equations were used from Figure 68, correcting the expected signal for the difference in incident current. The expected signal output for each, respectively, is 4.54nV and 4.44nV. Such a signal level is negligible – it is nowhere near high enough to even be registered by the MEDET 12-bit level of resolution.

Considering that these expected flux levels were taken from the AE8MAX model, where the maximum expected electron fluxes were used, and that the model does not take into account the reduced electron flux due to the repulsion by negative charging of the ISS as a result of the higher electron mobility in LEO, it can be concluded that the electron flux on-orbit will have no impact on the signal level of the bare UV detectors. Further, as the electron exposure to both filtered UV and SXR detectors provided negligible signals during testing in comparison to the bare UV detector, then it can also be assumed that the electron flux will have zero effect on the signal from these detectors, too.

The effect of the incident ion flux on to the detectors is unknown. There are two possible significant effects it could have: inducing a current in the detectors, contributing to the level of background noise; and degrading the detectors' performance by directly interfering with the atomic structure of the crystal lattice.

For the first case of inducing a signal current it may well be possible to differentiate this by differences in signal level between the ram and zenith face detectors. The motion of the ISS through the ionosphere will be mesosonic – it will travel at supersonic speed with regards to the ion population and at subsonic speed with regard to the electron population. In such a case the plasma wake created by the ISS will be predominantly free of ions and a bow-shock will be generated by the ram face. As a result the ram face will receive a far greater ion flux than the zenith face on MEDET, while the respective electron fluxes will be comparable (as the speed of electrons is much greater than the speed of the ISS).

The second case regarding the degradation of the detectors by ion impact is covered in Section 5.3.5.1, below.

5.3.3 Orbital Debris Impacts

There is a significant amount of debris in the LEO environment, a great deal of it man-made, which has the potential to affect the radiation detectors. It is accepted that any impact by particles of appreciable size (>1mm) will have enough kinetic energy to destroy any of the detectors with a direct hit. This situation is unavoidable as protective shielding would block the incident radiation that is required to be measured, or, at the least, severely reduce the field of view, which would have an unacceptable impact on the amount of data that will be gathered. This discussion therefore concentrates on the far more likely scenario of impacts by micrometeoroids and man-made debris of a similar scale.

For the bare UV detectors an impact may result in damage to the exposed contact wires, which will cut the detector circuit and cease operation, or chipping and fragmentation of the detector crystal and electrode surfaces, which will severely and permanently affect the performance.

For the filtered UV detectors impacts will most likely be absorbed by the fused silica filter itself – degrading the attenuation of the Lyman-α region, but otherwise leaving the detector intact. Any puncturing of the filter will most likely destroy the detector as a cloud of high-speed fragments from the impact will then be incident on to the detector and contact wires.

For the SXR detectors their larger size will increase their ability to withstand micrometeoroid impacts as compared with the UV detectors. However, this attribute is severely hampered by the fact that any damage to the detectors themselves must have already punctured the beryllium filter above. In this case, the pinhole formed will allow visible and infrared wavelengths of light to be incident on to the detector and into the detector cavity. This will undoubtedly saturate the amplifiers due to the far greater sensitivity of the detectors to visible wavelengths as opposed to SXR wavelengths of light, rendering the detector effectively inoperable, especially when illuminated by the Sun at the times when SXR readings need to be made.

For the LEO environment where the ISS will operate the average collision velocity is ~10km/s with a maximum collision velocity of ~14km/s. Taking the worst case scenario of a maximum velocity strike there will be a threshold size of particle that will be just large enough to puncture the beryllium window and render that detector inoperable.

Observations from the Long Duration Exposure Facility (LDEF) generate a relationship for a given penetration thickness of[135]:

$$t = K_1 m_p^{\;0.352} \rho_t^{\;1/6} v_\perp^{\;0.875}$$

Equation 38: Thickness of material that an impacting particle can penetrate

where t penetration thickness of the target material (cm)

K_1 material constant

m_p mass of the impacting particle (g)

ρ_t density of the target material (g/cm^3)

$v_\perp$ normal component of the velocity of the impacting particle (km/s)

The material constant for beryllium in this scenario is currently unknown, so an assumption has been made to use that given for aluminium of 0.72. With its far lower tensile strength this should produce a conservative figure for the thickness penetrated that is relatively higher than that for an impact on beryllium. Similarly, for $v_\perp$ the most conservative value of 14 km/s has been assumed.

Rearranging Equation 38 for the mass of particle required to penetrate 50μm of beryllium gives:

$$m_p = \left[\frac{5 \times 10^{-3} cm}{0.72 \left(1.822 g / cm^3\right)^{1/6} \left(14 km / s\right)^{0.875}} \right]^{2.841}$$

Equation 39: Mass of impacting particle required to penetrate 50μm of beryllium

This generates a value for the mass required for penetration of 31ng, a tiny fleck of dust. Assuming that the particle is spherical and has a density of $4g/cm^3$ (an average value for a metallic piece of space debris) it will have a diameter of 0.0025cm.

Using this as the threshold size of particle that poses a danger to the SXR detectors, the estimated flux of particles of this size or larger[136] is ~50$m^{-2}yr^{-1}$ for an object orbiting at the ISS' altitude. The area of the beryllium window that covers one SXR detector is 2.13cm^2 and for a mission life of 3 years we can expect, on average, 0.032 particles to strike each detector window. (For the sake of this calculation we count each beryllium filter as two windows as they each cover two detectors – damage to one side will not affect the other due to the baffles put in place for exactly this purpose.)

Taking such an impact to be a rare event with a Poisson distribution then the probability of an impact to a specific window during the mission[137] is 0.032 or 3.2%. The probability of losing at least one detector during the course of the mission is thus 12.2%. But the probability of losing both detectors from one face is only 0.20%, an acceptable level of risk (especially considering the conservative nature of the calculation and that the zenith face detectors will see a significantly lower debris flux than the ram face detectors).

There is the possibility that smaller particles than the threshold calculated above will impact the detector and generate spalling from the reverse side of the window, potentially contaminating the surface of the SXR detectors with beryllium. However, considering the low mass involved in a spalling event of this kind and the relatively large area of the SXR detectors it is unlikely that serious deterioration of performance would result.

For the filtered UV detectors the greater thickness of the fused silica filter makes the risk of micrometeoroid or debris impact virtually negligible, considering that a penetration of the filter would not automatically affect the performance and that the detector area itself is so much smaller.

For the unfiltered UV detectors their small size ensures a low risk of impact. Taking a particle size of 0.1mm diameter (large enough to shear a connecting wire or disrupt an electrode on the detector surface) then the approximate flux of $5m^{-2}yr^{-1}$ would have only a 0.0024% probability of striking the $1.96x10^{-7}m^2$ area of a detector – a negligible possibility.

So, as far as the possibility of micrometeoroids and orbital debris affecting the operation of the detectors by a direct strike goes, it is apparent that there is a significant risk of losing one SXR detector at some point during the mission but that the likelihood of damage to either the UV detectors or to both SXR detectors on a single face is negligible. Other than this potential effect, micrometeoroids and orbital degree will pose no further source of noise for the operation of the detectors.

5.3.4 Non-Solar Electromagnetic Radiation Sources

The last source of interference considered here is the effect on the detectors from sources of radiation in the ranges of interest other than the Sun. Such sources will be capable of directly affecting the signal level recorded by the detectors if they come within the detectors' field of view.

Non-solar sources of SXRs include the diffuse SXR background and point astronomical sources, the two most powerful being Scorpio X-1 and the Crab Nebula. All of these sources are likely to be in the SXR detectors' fields of view on numerous occasions throughout the mission. However, their impact is likely to be small.

The diffuse SXR background dominates the quiet Sun signal at energies greater than ~3.5keV, Scorpio X-1 dominates at energies greater than ~3.8keV[138]. But due to the rapid decrease in flux across the SXR spectrum from 1keV to higher energy levels the Sun still dominates disproportionately in the 1-3.5keV range to which the SXR detectors are sensitive. Coupled with the fact that these comparisons are only for the quiet Sun, it is apparent that solar SXR activity will render the SXR diffuse background as having a negligible impact on the signal level.

There will also be times when the SXR detectors are pointing at non-solar SXR sources when the Sun is not within the field of view. If these sources have an impact on the signal level distinct from the SXR diffuse background then this will be apparent in the data output and should be expected.

The diffuse SXR background, the sum of all extra-solar SXR sources, is predominantly generated by objects within our galaxy and therefore concentrated in the galactic plane. Due to the reasonably narrow +/-32° field of view of the SXR detectors, if the diffuse SXR background has an impact on the signal level then this impact will vary depending on whether the galactic plane is within the SXR detectors' fields of view. Such variations may be observable, especially in the more sensitive signal channel from each SXR detector, when solar SXR is not incident.

For the VUV detectors the most significant source of interference will be from back-scattered VUV radiation reflecting off the upper layers of the Earth's atmosphere. The zenith-facing detectors will not be affected by this, but it must be taken into account for the ram-facing ones.

However, due to the sensitivity cut-off at around 315nm for the UV detectors, the impact of backscattered UV should be small. At 310nm the proportion of solar UV reflected is ~4% for a clear sky and ~7% for a cloudy sky[139]. At wavelengths lower than this the reflected proportion decreases rapidly. Below ~300nm almost all incident radiation is absorbed and reemitted at longer wavelengths. Thus, considering that the range from 300-315nm will only make up a small proportion of the UV detector signal and that only a small proportion of this range will be affected by backscattered UV, the effect on the signal level will be close to negligible.

Nevertheless, it will be possible to discriminate this signal for the ram detectors when the ISS crosses the Earth-Sun vector in its orbit and the ram face becomes shadowed. At this time the illuminated Earth will still be visible without the Sun being in the field of view. If there is a detectable signal from the backscattered UV then as the terminator approaches this signal should decrease – reaching the offset minimum as the ISS passes into the umbra. Although at this stage there may well be a reduction in noise due to lower charged particle flux, this change can be alternatively discriminated between the filtered and bare UV detectors. In this manner these potential sources of interference should be able to be isolated and corrected for separately.

Other potential sources of UV interference may come from reflections off spacecraft surfaces – either on the ISS (i.e. solar arrays) or on the Shuttle when one visits. However, the view-factors to these objects will be small for ISS-based surfaces or obvious from the timing for Shuttle and other spacecraft arrival. In either case the amount of UV reflected will most probably be negligible, but such a situation must be borne in mind as a possible explanation for anomalous readings.

5.3.5 Signal Degradation

Further to the short-term or short-period temporal variations described above, there are a number of factors that may well lead, over the course of the mission, to deterioration in the signal level. The deterioration may manifest by either a permanent increase or decrease in signal level, depending on the physical effect. Ultimately, the cumulative long-term impact of such processes may lead to the disabling of one or more of the detectors through either saturation of the amplifiers or complete eradication of the detector's ability to generate a signal current. Unfortunately, due to the number of different factors present that may have an impact on the signal degradation, it was not possible to quantify the extent of degradation, and thus change in the detectors' sensitivity, that can be expected throughout the mission.

5.3.5.1 Ion Impact

Following on from the discussion in Section 5.3.2, the impact of ions being absorbed into the crystal structure of the detectors is of some concern, especially as regards the bare UV detectors that will be under the greatest incident flux. Deposited protons and heavier ions are likely to generate inhomogeneities within the crystal structure of AlGaN and introduce intermediate energy levels that will increase the sensitivity of the detector to longer wavelengths. Over time, this may well degrade the detectors' ability to discriminate the UV region – although the flux in longer wavelength domains is so proportionately great that the amplifier will almost certainly saturate if it becomes sensitive to them.

However, there is likely to be a significant difference between the bare and filtered UV detectors on the ram face due to the attenuation of ions by the fused silica filter. In addition, as pointed out previously, the difference in ion flux levels to the ram and zenith faces due to the mesosonic regime will also introduce a significant disparity between the degradation to the ram and zenith detector sets. This flux differential between the faces should also be apparent in the SXR detectors, if a significant number of ions are capable of penetrating the beryllium filters.

The ion population in the ionosphere will also change markedly between the day and night sides of the orbit and with solar activity. These variations will also be useful in carrying out necessary on-orbit calibration of the signals received.

Considering that the impact of the orbital electron flux will be negligible to the signal generated by the detectors, as described above, it is unlikely that the incident ion flux will generate any perceptible short-period variations in signal level. The long-term damage caused by ion implantation will be the most important factor.

The impact of O^+ ions and of atomic oxygen itself is of special significance and covered in the following section.

5.3.5.2 Atomic Oxygen Erosion

As mentioned in Section 1.3.2, atomic oxygen is the most abundant particulate species in LEO. It is therefore the most likely environmental species to affect the radiation detectors during the mission.

For the SXR detectors and the filtered UV detectors there will likely be little, if any, impact – the respective filters will shield the underlying detectors from any incident AO. It is unlikely that the SXR transmission properties of the beryllium filters will be significantly affected, the only possible impact being a thin layer of beryllium oxide forming on the outer surface. For the fused silica filters on the UV detectors it is expected that next to no difference will be discerned – fused silica is silicon dioxide and so will be unreactive to further exposure to oxygen.

However, for the bare UV detectors there is the important consideration of the reactivity of aluminium. As the detector is an amorphous conglomerate of aluminium nitride and gallium nitride there may well be substitution of the nitrogen atoms with oxygen due to oxygen's greater reactivity. The resulting formation of aluminium oxide and gallium oxide will be liable to change the electronic properties of the detector crystal, most probably by introducing new energy levels within the band gap between the valence and conduction bands of AlGaN. This, in turn, will allow easier promotion of electrons from the valence to conduction band under illumination by wavelengths of light of lower energy. The result may well be drift of the responsivity of the detectors so that they become more responsive to the wavelengths of interest but, detrimentally, also more responsive to longer wavelength radiation. Considering that the solar spectral irradiance increases markedly when approaching the visible wavelengths from the UV, this may have a severe impact on the detectors' performance – making them too sensitive to longer wavelengths and saturating the amplifiers as a result with the associated increase in signal.

Indeed, this process may well already have occurred to some extent on the ground. When looking at Figure 41 it is clear that the PTB results demonstrate the AlGaN detector being more sensitive, over a larger wavelength range, than the data provided by APA Optics. However, one argument against this is the fact that the responsivity of the filtered AlGaN detector tracks that of the bare detector to a great extent (see Figure 40). The filtered detectors allegedly have the volume within the TO5 can's cap back-filled with dry nitrogen, so they should not demonstrate any drift away from the manufacturer's data. Unfortunately, there is no way to verify the integrity of the nitrogen environment within the filtered detectors now – faults in the seal could easily have allowed oxygen to slowly diffuse in over time and render any comparison with the bare detectors meaningless.

Regardless, the effect of AO attack on the bare detectors on-orbit is a subject of concern. Attempts were made to expose the detectors to AO in the ATOX facility at ESTEC. However, limitations of time, number of available detectors and the vagaries of the ATOX operation itself did not allow for any significant results to be gained. This is unfortunate and highlights a significant path for further research if future instruments are planned around AlGaN detectors. Whereas, apparently, no exposures to atomic oxygen have been made using AlGaN, there are examples of the effect that oxygen can have on the semiconductor[140,141].

However, as with the other forms of interference, it is to be expected that the ram and zenith face detectors will receive different AO fluence levels due to the mesosonic environment. Thus, if AO erosion significantly affects the responsivity of the AlGaN detectors this should become apparent through the difference in signal levels between the two faces. Indeed, it may well be possible to correlate the drift in signal (if detectable) against the results from the AO detectors onboard STORM that will monitor the AO flux and fluence every 24 hours.

5.3.5.3 Contamination

The last source of long-term degradation is man-made – the effects of deposition of contamination from the out-gassing, venting, and exhaust of surrounding structures and docked spacecraft. It is unfortunate that, due to the great size of the ISS and the large number of different materials that has and will go into its construction, it is impossible to accurately predict the likely impact of any and all contaminants.

For example, some recent results[142,143] demonstrate how silicon dioxide has coated some external instruments on the ISS on the Russian segment, the source being from out-gassing of the main solar panel. This contamination has been exacerbated due to the position of the instruments 'down-stream' of the flow of contaminants. The different location of the radiation detectors on STORM may reduce the impact of contamination from that source, but may expose it to others, such as the out-gassing of the Kevlar shroud of the Columbus module that will include a large amount of water (approximately 3-4%, by mass[144,145]).

As with the other types of degradation, however, there is the possibility that the difference in deposition across the ram and zenith faces will lead to a differential effect on the signal level of the detectors on each panel. The ram face will most likely receive the greatest amount of contamination as it is facing the direction of travel – any volatiles driven off the ram side of the ISS will likely be slowed by the ambient atmosphere and find themselves driven back on to the ram surfaces.

Potential sources of contamination include: SiO_2 driven off from the solar panels, this has been an observed source for the MISSE and MPAC/SEEDS exposure experiments although it should not be as great a problem for STORM considering its position at the front of the ISS; the Kevlar micrometeoroid shields surrounding the Columbus module; water out-gassed from the docked Shuttle; and exhaust discharge from the Shuttle Orbital Manoeuvring System.

The most likely effect of any contamination will be the attenuation of the photon flux within the ranges of interest, decreasing the observed signal level. For the SXR detectors it is highly unlikely that any significant degradation of the signal will be possible due to the ability of SXRs to penetrate through thin films. The UV detectors may well be affected, especially the bare ones that could undergo changes in sensitivity due to the binding of contaminants to the surface of the AlGaN crystal in addition to attenuation of UV. A reduced sensitivity may, in turn, reduce the predicted angle at which saturation occurs for the bare UV detectors, actually allowing more data to be acquired during later stages of the mission.

In order to correct for any contamination effects it may be possible to correlate decreasing signal levels on the STORM radiation detectors with changing signal levels on other MEDET instruments, most notably the microcalorimeters that will be observing the contamination levels directly and the spectrometer that will monitor the increased attenuation of solar radiation through material samples caused by the deposition of contaminants. Rapid bursts of deposition, from thruster firings, for example, may be obvious from the timing of any impact on to the detected signal and can be accounted for accordingly. Long-term deposition will be altogether more difficult to divine and may have to wait for post-flight analysis in order to produce final correction factors for the complete mission data set.

5.4 On-Orbit Operations

This final section of the discussion concentrates on the operation of the upcoming mission and the expected data return. The orbit of the ISS around the Earth is critical in assessing the periods within which data can be acquired so a further look at these implications is undertaken here, following on from Sections 5, 5.1, and 5.2. Finally there is a description of the different combinations of measurements that will be taken throughout the mission that will be used for data collection, on-orbit calibration and interference mitigation through comparison analysis.

5.4.1 Further Effects of the ISS Orbit on Detection

As mentioned previously, the precession of the orbit of the ISS around the Earth directly affects at what times the detectors will have the Sun in their respective fields of view. The model generated for plotting the ISS orbit calculated the precession as a change in the beta angle: the angle between the Earth-Sun vector and the orbital plane of the ISS.

Plotting changes in the beta angle over the course of a year yields the following figure:

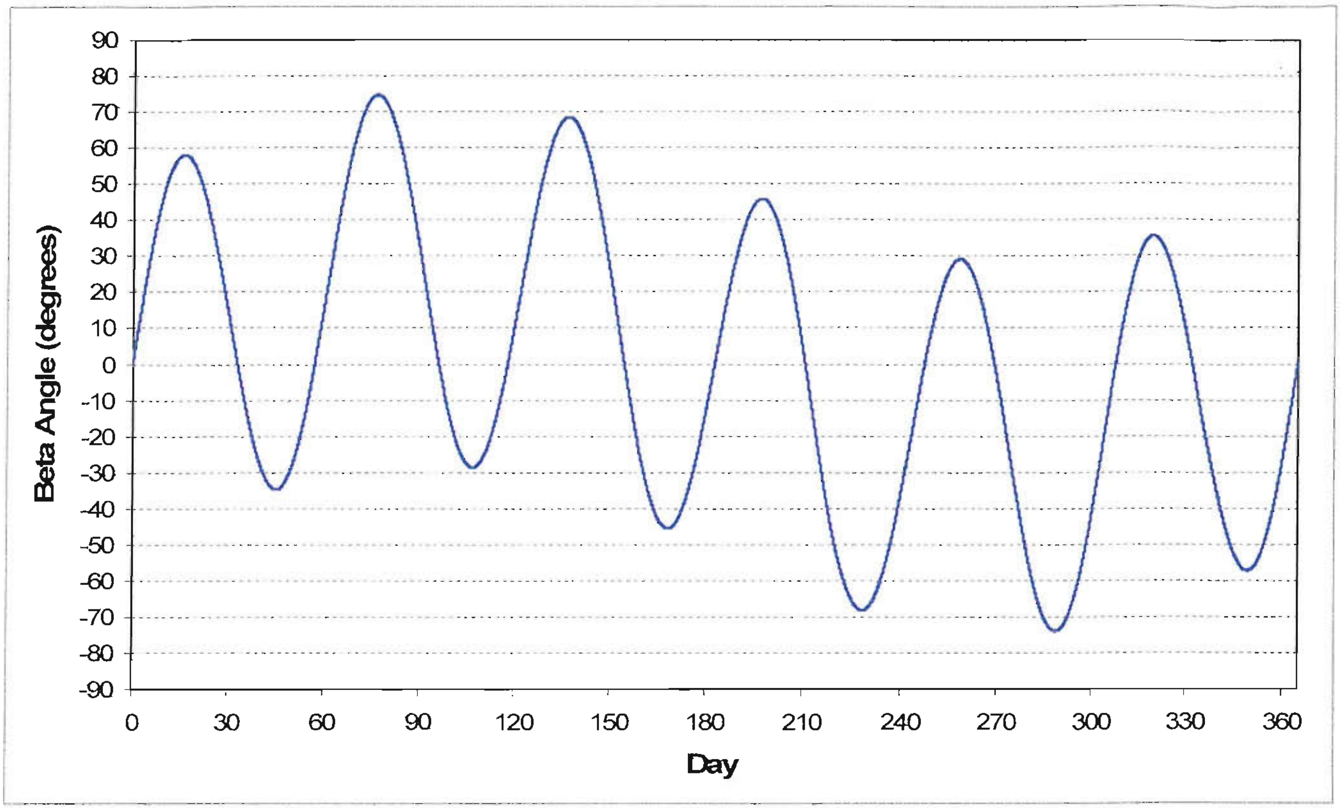

Figure 79: Variation in Beta Angle of ISS Orbit over 1 Year

This calculation of the variation in ISS orbit beta angle agrees very closely with that produced by the Japanese Aerospace Exploration Agency[146]. With a ~91 minute orbital period, each point on this plot represents ~16 orbits/day. The plot is composed of two sinusoidal elements, the short period of ~60 days relating to the precession of the ISS' orbit around the Earth and the long period of 365 days relating to the diurnal changes experienced as the Earth orbits the Sun. As can be clearly seen, the sum of the ISS' inclination to the Earth's equatorial plane and the inclination of the Earth's axis of rotation to the ecliptic can produce beta angles of over 70° at certain times.

In addition, as also noted earlier, at these times when the beta angle is so high there are some orbits where the ISS remains illuminated by the Sun throughout the entirety of its orbit. To illustrate this, the following figure depicts the change in length of eclipse period over the course of a year.

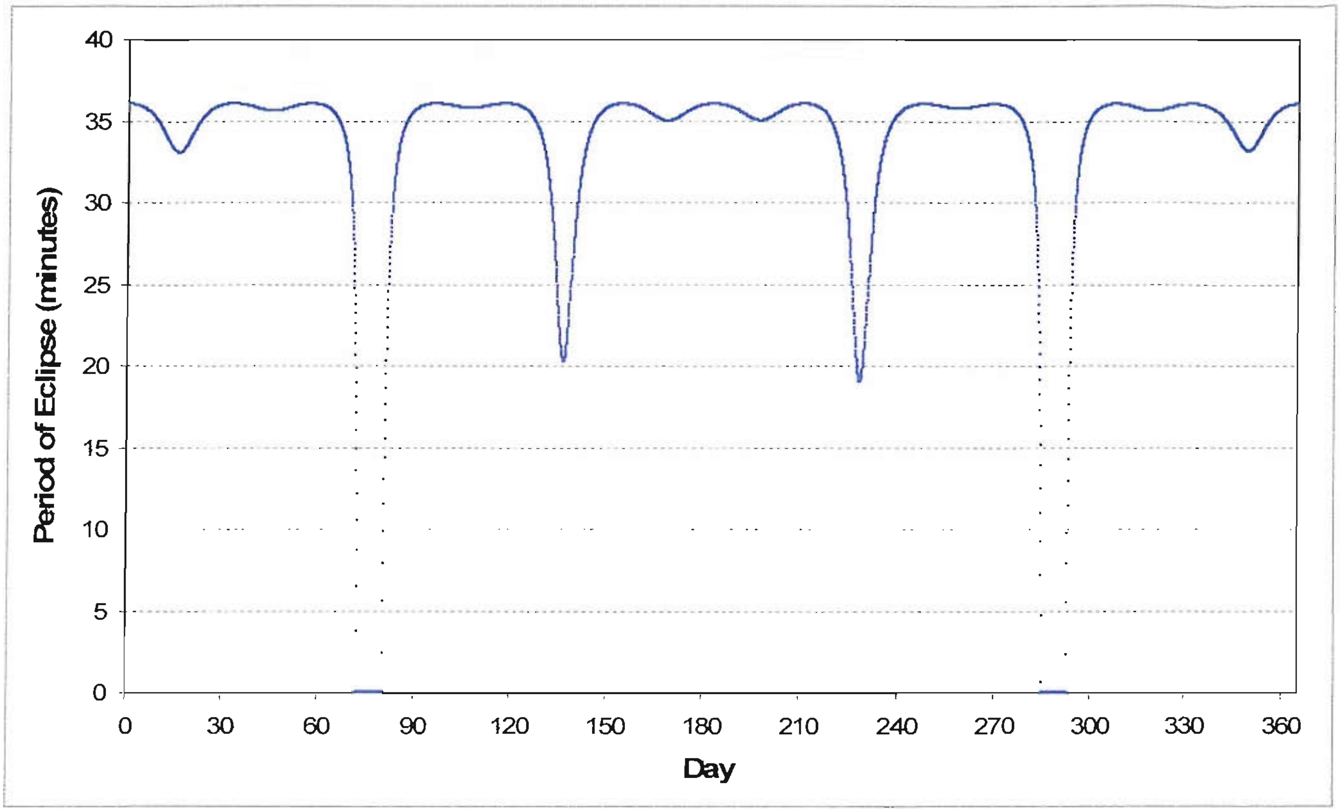

Figure 80: Change in Eclipse Period over 1 Year

As can clearly be seen, there are two periods when, for a number of days, the ISS remains constantly illuminated. This will have no direct impact on the data return, but will be necessary to take into account for interference mitigation as the thermal regime will change and the ISS will remain in permanently illuminated ionosphere where the concentration of charged and neutral particles will stay high.

For any given orbit the number of recordings that each detector set will make depends on the beta angle. When the beta angle is greater than the field of view of the detector then no data will be recorded (that concerns solar illumination, at least – the detectors will still be operating and recording sources of noise and interference). When the beta angle is just below the field of view then the Sun will only illuminate the detectors for short periods during an orbit. The best viewing times will occur when the beta angle is at or near zero as the Sun will remain within the detectors' fields of view for longest. This is depicted graphically in Figure 81, below.

Figure 81 is a Mercator projection of the fields of view of all the radiation detectors as they would appear against the 'celestial sphere'. The conversion from a sphere to a rectangular plane by a Mercator projection treats all angles of right ascension and declination as equal distances on the plane. However, this does introduce some distortion at high beta angles. For narrow fields of view about the 0° beta angle, like the SXR detectors, the projection remains similar to the circle projected on to the 'celestial sphere'. But for large fields of view, as for those of the UV detectors, the projection becomes distorted towards a square with a proportion dependent on the magnitude of the field of view. In the limit of a field of view of +/-90° the projection would become precisely square as this would cover half of the Mercator diagram – the same as half of the 'celestial sphere'.

The shaded regions of the diagram represent the fields of view of all sets of detectors on both faces. The overlapping regions where the detectors from each face can detect the Sun in the same region of sky are clearly discerned. Also included is an outline of the Earth's umbra that impinges on the Ram detectors fields of view. It is the umbra that is important in this application as during the times when the Sun is within this region, the Earth will be blocking its light and so no signal will be received – the outline could equally well serve as a Mercator projection for the sphere of the Earth as viewed from the ISS.

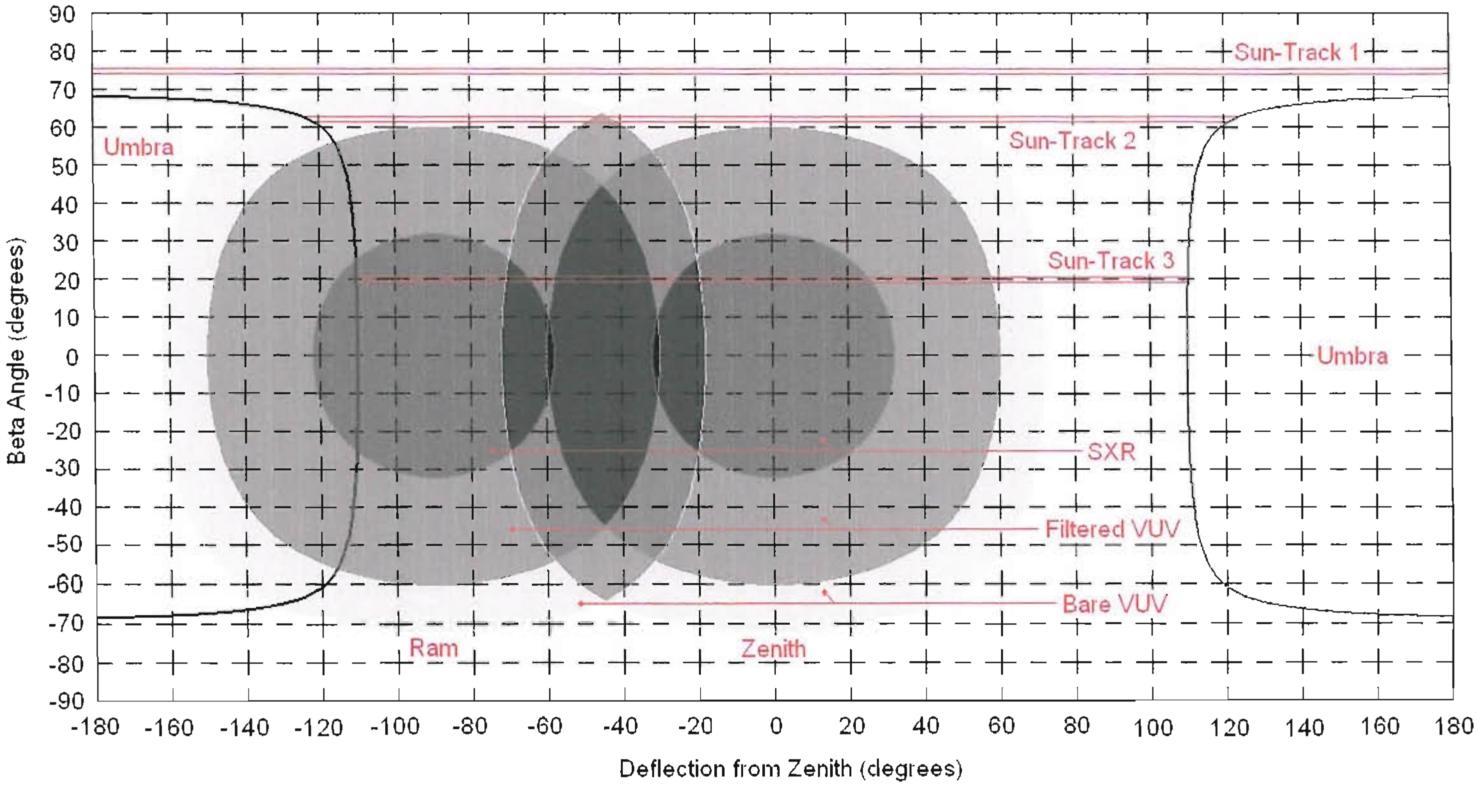

Figure 81: Fields of View of Detectors against the Full Sky

The Sun will move across the fields of view in a horizontal trajectory, in the perspective of the diagram, and three Sun-tracks have been added as examples of the Sun's motion for three different beta angles. The Sun subtends an angle of ~1.5° against the sky and this determines the width of the tracks in the diagram. In this application the advantage of a Mercator projection is that distance along the x-axis is directly proportional to the time-of-flight across that distance by an object, in this case the Sun, against the background. Thus, it is easy to approximate, by eye, the proportion of each orbit, at a specific beta angle, that the Sun will be viewed by a set of detectors.

Taking the Sun-track examples: number 1 demonstrates the Sun's motion at the maximum beta angle of 75.1°. At this great a beta angle the Sun does not pass within the fields of view at all and so no measurements will be acquired for this orbit. It can also be seen that the Sun-track misses the umbra of the Earth too, so this means the ISS will remain illuminated for the entirety of the orbit – directly analogous to the orbits with no eclipse period as displayed in Figure 80.

Sun-track 2 demonstrates a motion across the fields of view that is not directly obvious in Figure 75. At a beta angle of 62° the Sun passes within the field of view of both sets of bare UV detector, but not within the fields of view of the other radiation detectors. A similar situation arises for the filtered UV detectors at lower beta angles that are just outside of the field of view of the SXR detectors.

Sun-track 3 is an example of one beta angle where the Sun passes through an assortment of different detector combinations during an orbit. The Sun appears direct from the umbra into the fields of view of all the Ram detectors, before passing into the important region at 45° from both Ram and Zenith faces where the signals of all UV detectors can be compared at the same incident flux level.

In this analysis of the effect of the orbit of the ISS on the observations that will be possible with the radiation detectors it is important to keep in mind that ideal models have been used for the calculations involved. The Earth has been treated as a sphere with a radius of 6378km and inclination of 23.5°, the orbit of the ISS as precisely 400km in altitude with an inclination of 51.6°. In reality all of these properties differ somewhat from these idealised figures. The most influential will be changes in the ISS' orbital altitude and attitude. The altitude will decay gradually over time and requires periodic re-boosts by visiting supply craft – such changes can affect the area of the sky covered by the Earth and therefore the length of time of eclipse periods.

The attitude of the ISS is also assumed to be constant, with the Ram face always facing precisely in the direction of travel. Unfortunately, this is unlikely to be the case as the true attitude can be slewed by a number of degrees (up to as much as ~10°) in any direction. Such changes are usually due to power and thermal requirements to either orient the solar arrays to collect the maximum amount of sunlight possible, or to keep the thermal panels shadowed to avoid the ISS over-heating.

It is effectively impossible to take such changes into account in any model of the orbit due to the ever-changing nature of re-boost schedules and construction manifests. However, such details must be taken into account in any ground analysis of the data. The orbital analysis thus serves as a benchmark against which the on-orbit performance can be measured – it is an estimate of the performance that can be expected and a rough magnitude calculation for the amount of data expected.

5.4.2 Expected Data Return

Given the rates at which measurements are taken, one recording per radiation detector every 3 seconds, it is expected that throughout the nominal 3 year mission each detector will make 31,557,600 recordings, assuming that all detectors survive for the full duration. For the bare and filtered UV detector groups, each will have 126,230,400 separate readings respectively. For the SXR detector group, with the dual output lines, there will be a total of 252,460,800 separate measurements.

These are obviously large data sets, but not all of these readings will occur when the Sun is within the field of view, of course. In order to calculate the percentage of readings from each detector group that are made when the Sun is within line-of-sight it is necessary to find the product of the length of time the Sun is visible during an orbit of specific beta angle, as given by the calculations for Figure 81, and the number of times that the ISS traverses an orbit with that specific beta angle during the mission, as given by the calculations for Figure 79. For this calculation it is assumed that the 1-year analysis of the changes to beta angle are sufficiently representative of an average year on-orbit to be used for all three years of the proposed mission length.

There will be a significant difference in illuminated time between detector groups on the ram and zenith faces due to the Earth blocking the line-of-sight to the Sun for a period of time on most orbits for the ram detectors (although this is dependent not just on beta angle but also detector field of view – see Figure 81. As such, each detector group on each face is represented separately in the following figure: an enhanced version of Figure 79 with the illuminated periods against the day for an annual cycle, with reference to the beta angle.

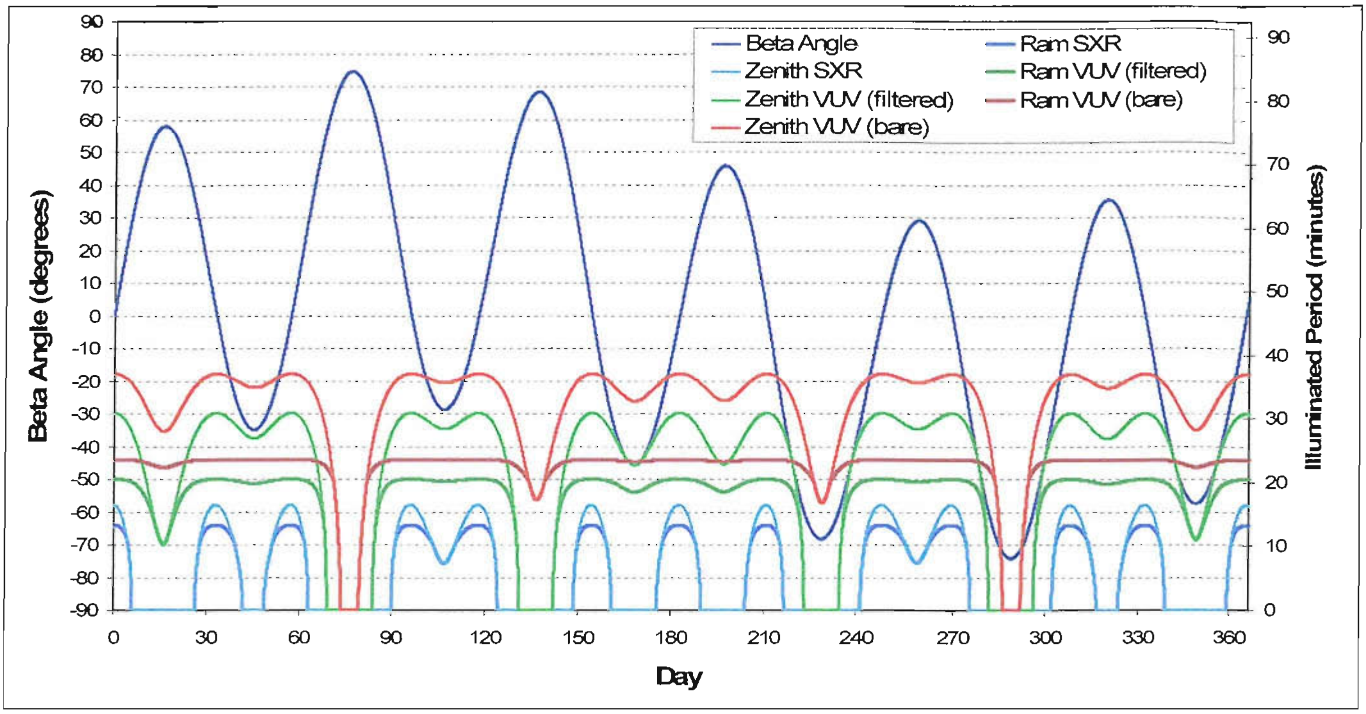

Figure 82: Period of Illumination for each Detector Group for a given Orbit over the course of a Year

It is obvious that field of view is the most important factor in the length of time that the detector remains illuminated. The comparison with the beta angle makes it clear how the measurements are also highly dependent on low beta angle values. This is especially true for the SXR detectors where long periods of time (almost 30 days in some cases) can elapse on-orbit when no illumination occurs while the ISS' orbit precesses through the high beta angles.

The following table denotes the proportion of the mission time that will be spent illuminated and in the umbra by each detector group during the mission lifetime, with the proportionate number of recordings that will be taken under the different conditions.

	% time illuminated	No. of measurements during illumination (millions)	% time in eclipse	No. of measurements during eclipse (millions)	% time not illuminated	No. of measurements without illumination (millions)	Total no. of measur-ements (millions)
Ram SXR	5.99	7.56	35.57	44.90	58.44	73.77	126.23
Zenith SXR	6.75	8.52	35.57	44.90	57.68	72.81	126.23
Ram UV filtered	17.73	11.19	35.57	22.45	46.7	29.47	63.11
Zenith UV filtered	24.36	15.37	35.57	22.45	40.07	25.29	63.11
Ram UV bare	23.92	15.10	35.57	22.45	40.51	25.56	63.11
Zenith UV bare	34.54	21.80	35.57	22.45	29.89	18.86	63.11

Table 12: Percentage Time and Measurements Taken under different conditions for each Detector Group for the 3 Year Mission

Note that the 'no. of measurements without illumination' refers to times when the ISS is in sunlight but the respective detectors are not illuminated. The sum of the '% time illuminated' for each detector group does not equal the total percentage of time on-orbit that the detectors are recording data, except for the SXR detectors. This is due to the overlap in the field of view of the UV detectors – a proportion of time is given over to simultaneous measurements. The proportion of time on orbit that UV recordings are being taken (i.e. the proportion of time when any/all UV detectors are illuminated) is of little use and has not been calculated here – more relevant are the proportion of orbits in which UV measurements of the Sun are taken, as displayed in Figure 82. I addition, the data does not take into account those periods during illumination when the detectors may be saturated. If saturation does occur this will obviously impact the amount of usable data from the 'no. of measurements during illumination' column.

5.4.3 Measurement Combination Analysis

To conclude this discussion is a summary of the different measurement combinations that will be undertaken while on-orbit and their relevance to analysing the signals, both in terms of calculating the solar radiation flux levels and minimising the noise and interference expected while on orbit.

This summary has been tabulated as follows:

Situation	Beta Angle	Position around orbit	Observation
1.	Zero	-90°	Solar photons at normal incidence to Ram face – can take maximum signal measurements from Ram detectors without correction for angle of incidence.
2.	Zero	0°	Solar photons at normal incidence to Zenith face – can take maximum signal measurements from Zenith detectors without correction for angle of incidence. Additionally, can also compare SXR detector readings with Situation 1. in order to correct for different output levels (assuming no change in solar flux level, i.e. during a solar-quiet period).
3.	Zero	Dawn - 90°	SXR detector is rotated about 1-axis – measurements during this orbit can be used to calibrate for rotation about two axes during orbits with non-zero beta angles.
4.	Within illumination range	-45°	Flux incident on all VUV detectors is equal – can correct for different output levels of each detector without having to correct for possible changes to solar flux levels.
5.	Within illumination range	Dawn to -18°	Ram face detectors exposed to sunlight. Measurements taken that are required to be adjusted for angle of incidence.
6.	Within illumination range	-72° to 72°	Zenith face detectors exposed to sunlight. Measurements taken that are required to be adjusted for angle of incidence.

7.	Within illumination range	-18° to terminator	Ram face detectors exposed to charged particle flux through denser, sun-lit portion of ionosphere without solar illumination. Can be used to correct for charged particle interference in Situation 5.
8.	Within illumination range	72° to terminator	Zenith face detectors exposed to charged particle flux through denser, sun-lit portion of ionosphere without solar illumination. Can be used to correct for charged particle interference in Situation 6.
9.	Within illumination range	Terminator to dawn	All detectors in eclipse, exposed to reduced charged particle flux in less dense ionosphere that can be compared to Situations 6. and 7. to monitor impact of charged particles on signal level.
10.	>72°	All	No illumination and reasonably constant charged particle flux. Variations in signal level can be correlated with readings from PT100 sensors to correct for thermal fluctuations at all other times. However, possible interference from non-solar SXR sources depending on position of Earth around Sun.

6 Conclusions

The work carried out for the calibration of the radiation detectors for the STORM module has demonstrated that they should be able to fulfil the requirements of the MEDET mission.

The AlGaN detectors provide a reasonable UV response although this decreases towards the Lyman-α. The calculations made to calibrate the impact of the Lyman-α region indicate that during active solar periods the raised flux will be at the threshold of what is detectable for a differenced signal between the filtered and bare detectors. Such calibrations for the responsivity of the Lyman-α are the first that have been attempted for AlGaN photodiodes.

Due to the unfortunate failure to observe the long-wavelength cut-off of the AlGaN detectors with the PTB results, further experimentation was required to delineate this. However, it should be noted that the method used to calculate the long-wavelength cut-off is not optimal due to the limitations inherent in attempting to derive responsivity values at precise wavelengths from data based on integrated signals. The approximate AlGaN responsivity values generated by the ESTEC data were so close to zero, though, that the inherent errors are somewhat minimised – a large percentage error would not significantly alter the responsivity curve.

The final responsivity curve of the AlGaN detectors made it clear that the responsivity has drifted from the manufacturer's specification. It is speculated that this is due to oxygen substituting for nitrogen in the aluminium and gallium compounds of the detector crystal and contaminating the active region as a result.

Due to this drift, the expected on-orbit signal values are greater than the proposed range for the MEDET OBDH system when the detectors are at normal incidence to the incoming solar UV flux. However, the angle of incidence calibration makes it clear that UV data can still be acquired at greater angles of incidence for every orbit where the Sun enters the detectors' fields of view.

The calibration of the responsivity of the detectors to an incident electron beam was also the first to be carried out for AlGaN detectors. The result that the bare detectors will generate a negligible signal due to the on-orbit electron flux is an important indication as to the low impact of this potential source of signal interference.

The Si detectors appear amply suited to the task of soft X-ray flux detection. Such technology has been used numerous times before, even in very similar configurations. With a FWHM detection bandwidth of 17.9keV centred at 10keV it is sensitive to an energy range larger than that required for the mission parameters. However, the reduction in solar flux level towards the higher end of this energy range will result in a negligible contribution to the output signal.

Field of view analysis has been carried out for the Si detectors too, revealing a straightforward sine-based conversion to be used on the raw data with the complementary attitude data for the ISS. This calibration, along with the varied gain on the output channels, will enable the detectors to cover almost four orders of magnitude of solar SXR variation – an important capability in delineating the power of individual solar flare events.

Overall, the outlook for the operation of the radiation detectors is positive, especially considering the tight budget available for design, test and development. The incorporation of these detectors into the STORM package constitutes the first design and production of an electromagnetic radiation monitor to be used alongside materials exposure instrumentation for the purpose of active monitoring and correlation of results. Furthermore, the instrument suite has been flight qualification-tested and approved for use on a manned spaceflight mission. It can now be considered as a low cost, low power, and low mass solar electromagnetic radiation dose monitoring system for SXR and UV wavelengths available for applications on all spacecraft platforms.

The volume of data that is expected to be generated is also significant – with readings taken every three seconds the temporal resolution of the detectors is extremely good. It should be possible to resolve the smallest transient fluctuations in solar activity. Whether this will be able to shed any light on connections between solar SXR and UV production mechanisms remains to be seen, but the potential remains.

With their inclusion on the zenith face, the detectors have the potential to calibrate for almost all other sources of interference during the course of the mission. This provides the prospect of further novel data concerning the erosion of the detector systems (especially AlGaN) during their operation.

6.1 Proposals for Future Work

Over the course of the development and testing of the STORM radiation detectors it has become apparent that a number of alterations to the design of the detection systems could be made to increase performance. Such alterations are proposed here for use in future development cycles, to provide advice for future solar observation instrumentation into these wavelength bands and to be a source of modifications for the flight spare model if a future carrier becomes available that it could be adapted to.

First, it would probably be of benefit to use diamond detectors to replace the AlGaN ones for VUV detection, as has been proposed for the LYRA[147] instrument on Proba2. At present there is no knowledge of how well AlGaN detectors resist AO attack, whereas diamond detectors are far more stable against erosion and the consequent drift in sensitivity. At the time that the design and development decisions had to be made for the STORM unit such detectors were not available. However, as detector technology is an extremely fast-paced area of technological development it is no surprise that potentially superior detectors have arrived on to the market during the test, delivery and integration phases of the mission where such upgrades would be impossible.

However, switching detectors would necessitate a repeated calibration test campaign, although for new equipment this will be unavoidable as it appears that APA Optics has discontinued the production of their AlGaN detectors at present.

A connected issue with the lack of knowledge regarding oxygen-induced drift in sensitivity would be to install a broader amplification range on the UV detectors to compensate for their increased responsivity from the manufacturer's specifications. This would reduce the expected signal level on-orbit to within a 0-10V range, but could have an impact on redundancy, however, and thus a trade-off would need to be calculated between ensuring increased data-return and the reliability of the system.

Regarding the detection of Lyman-α it would be prudent to use short-pass filters around 130nm to completely isolate the region – trying to delineate the Lyman-α from the full UV spectrum up to 315nm by comparison with a long-pass filtered signal is too difficult at the MEDET signal resolution levels. Of course, this does nullify the justification of using bare solar-blind detectors with their wide field-of-view, but filters could be used on dedicated Lyman-α channels, leaving unfiltered detectors to monitor the rest of the UV. Such short-pass filters were not available built-in to the TO5 design of the detector housing. Modifications to the existing detectors of the flight-spare, for example, would have to be customised 'in-house' to change the filters used. This would involve delicate mechanical operations to remove the existing filters and precision milling of any replacement filter to fit within a TO5 can – a non-trivial exercise.

One limitation of the STORM electronics system was that there was only enough room and track space to place PT100 temperature sensors on a majority of the radiation detectors. Future designs should allocate some PT100's to sit against the associated amplifiers to monitor them for thermal fluctuations. Even though the amplifiers, if operated continuously, reach a steady operational temperature they will still be subject to fluctuations due to changing solar incidence and the power output of surrounding electronics units. Such information would help in the accounting of thermal noise introduced into the system during the amplification stages and delineate this from the noise introduced by the detectors themselves.

The field of view of the SXR detectors could be improved by depositing a metal filter directly on to the detector surface and thus removing the need for a separate filter mounted in its own frame. However, such an arrangement may well necessitate the use of active cooling of the detector as it would now be directly heated by incident solar radiation without the insulating layer of a physically-separated filter overhead. Precise thermal modelling would thus be required and significant alterations to the electronics would be needed if it was found that cooling would be essential.

There are a number of more radical proposals presented here that would be best suited for a new production cycle.

The inclusion of different filters (either by thickness or material) over the silicon photodiodes would enable the detectors to discriminate between different SXR bands. This may make it possible to tell which photon energies are most conducive to degradation for certain materials – possibly shedding light on to the underlying chemical degradation process itself by highlighting the excitation frequency that is most important. With the use of different detector thickness, too, greater energy ranges that extended into the hard x-ray and EUV could be monitored for their impact on degradation processes.

Similarly, the inclusion of a wider range of filters over the UV detectors would enable the discrimination of individual emission lines that could be useful for investigating the effects of EUV on materials. Very little is known regarding EUV effects on materials. Even though its irradiance is much less than the longer-wavelength UV levels, it would be rash to assume it has no effects considering that SXR is allegedly involved in degradation processes at even lower flux levels.

The amount of data recorded could be further increased by mounting the detectors on a Sun-pointing, 3-axis stabilised craft so that normal incidence recordings could be made during all periods when the spacecraft is in sunlight. However, this would probably necessitate the use of reference detectors or a reference source that would not be exposed to the environment in order to calibrate for on-orbit degradation of the active detectors.

The use of such reference sources could also be incorporated without the Sun-pointing in order to improve the monitoring of degradation effects on the detectors. This would be a major revision of the design, though, necessitating changes to the power systems as well as having an impact on the volume and mass of the system. If STORM were to be flown again on another Earth-locked platform (like the ISS) then a more simple solution may be to have detectors pointing in the wake direction (opposite to ram) where they would not be impacted by any atomic oxygen, proton, or other neutral particle species.

The size and mass of the detector electronics could be further reduced by the use of surface-mount electronic components instead of the through-hole components used on all the STORM PCBs. While such savings may be significant, such a substitution may introduce quality control issues, such as vibration-load survivability, that would necessitate a new qualification campaign.

The spectrometer wheel on MEDET eclipses one of STORM's AO detectors during its operation by use of open and closed apertures. A similar system could be used to rotate material samples over the UV/SXR detectors to monitor changes in absorptance of those materials in those energy ranges. The thickness of the samples would have to be very thin to allow for significant transmission and thus would be affected by erosion very quickly. They would therefore only be suitable for very short mission durations. However, during long missions this technique could still be useful if it was expected that the samples would fully erode and thus their end-of-life properties could still be examined (assuming uniform erosion). In addition to material samples, further filters could be incorporated along with open apertures to allow one detector to monitor a number of different energy ranges.

There are many possible configurations of the detector system that would expand its capabilities, whether alongside future materials degradation instrumentation or just as a stand-alone radiation dose measurement device. Regardless, it is hoped that future developments along these lines will be able to build on the knowledge gained throughout this work.

7 Appendices

Included in this section are various supplementary details that are relevant to, but not essential for, the descriptions and explanations included elsewhere in the thesis. They are provided here for completeness.

7.1 Appendix I: Previous Radiation Instrumentation

The solar UV spectrum has always been of interest to space science due to the inability to directly monitor it from the ground due to its absorption at higher wavelengths by the Earth's atmosphere (mainly due to atomic oxygen at altitudes beyond 160km within the thermosphere). Even balloon measurements were not sufficient as their maximum measurement height (40-50km) was still far below the absorption layers. Only with the advent of rocket propulsion could the high altitudes be explored and the first UV data obtained.

The following table lists, in chronological order, every successful spacecraft instrument designed to observe the full-disk irradiance / radiation dose from the Sun within the ranges of SXRs from 1-10keV or UV from 120-285nm. Instrumentation was not included that was either cancelled in design, failed to achieve orbit due to some malfunction of the launcher, failed to collect any scientific data due to incorrect orbit/attitude control or is planned for the future. Some instruments that are sensitive to radiation just outside the ranges of interest are included due to the cut-off in detection range being non-discrete due to the dependency on filter/detector attenuation.

The list does not include all radiation detection instrumentation that use the same energy bands as STORM, but rather the focus has been on all instruments that are used for direct Solar dose monitoring across those bands. This is to keep the list concise as there are many alternative space-based applications for radiation detectors in the energy ranges of interest (some further missions are presented in Appendix I, Section 7.1). As a result, it should not be assumed that the instruments listed for a spacecraft are the full complement of the onboard scientific payload; rather this is just a very specific cross-section of instruments closely correlated to the STORM radiation detectors.

For example, there are a number of solar radiation detectors that use back-scattering from the Earth's upper atmosphere (and even from other Solar System bodies) to make UV and soft X-ray measurements. However, the processing of such reflected signals is necessarily complex as it depends on knowledge of the atmosphere/surface in question (indeed, it is a well known atmospheric/surface composition analysis technique) and this delineates these type of detectors from direct observing systems. As such, these detectors have been omitted as their application, though similar, is significantly different from that of STORM.

For the sake of brevity additional instrumentation that disperses, collimates or polarises the incoming radiation is not listed, even though these are usually described as separate detector systems within the literature. Such instrumentation are usually for imaging applications that still rely on the same detector elements used for broad-band solar flux irradiance measurements. As such, they are not truly 'stand-alone' instruments and have thus been ignored.

Furthermore, the focus of this review has been on long-term observations using orbital spacecraft. Sub-orbital sounding rocket flights have not been included due to their limited application to long-period solar measurements. However, references to previous sounding rocket flights prior to 2000 that have investigated solar VUV emissions can be found in Wilhelm 2003[148].

The table lists in order:

- The name of the spacecraft.
- The general orbital parameters of the spacecraft (stabilisation, perigee x apogee, inclination). The orbit is assumed to be geocentric unless otherwise stated.
- The year of launch and, where known, the year that operations ended. The re-entry date is not included as it is of no importance to the timescale over which data from that spacecraft was collected.
- The name of the instrument(s) on board which detect within the radiation ranges of interest. Only these specific instruments are noted, all other instrumentation on the spacecraft is ignored. Some instruments are generically described (e.g. just as a 'spectrometer') so some further details in parentheses are provided as to the specific type (e.g. Rowland, Ebert-Fastie etc.).
- The range of detection of the instrumentation, provided in units of keV (and sometimes MeV for large upper limits) for the soft X-ray instruments and nm for the UV instruments. Some instruments have many ranges for different detector elements, these ranges are listed in ascending energy order or ascending wavelength order respectively.
- The filters used, where known, for the specific range band. Note that this also includes filter coatings on mirror and detector surfaces.
- The detector element used, where known, for the specific range band, including any active/passive cooling that the detector is subjected to.
- The references where further details of the instrumentation can be found. Where papers are unavailable the name of the Principal Investigator for the instrument has been listed, where known.

For this review the most important information is contained in the 'Detector' column that describes the actual element that converts the incoming radiation to a measurable signal. In many cases, especially with older instruments, this is difficult to ascertain as the detector can be referred to as just a 'photomultiplier' or simply 'photodetector' within the literature. It is this information that leads to the conclusion that AlGaN has not been previously incorporated in a spaceflight scientific instrument.

Wherever possible the detector element has been listed. However, some of the detection technologies listed above would not use a solid state detector such as AlGaN and so, if details are unavailable, the detection technology has been listed instead.

Spacecraft	**Orbit**	**Year**	**Instrumentation**				**Reference**
			Name	**Range**	**Filter**	**Detector**	
Sputnik 2	212x1660km	1957 – 1958	Spectrophotometer	121.6nm 0.1-12keV	Filter wheel	2 photomultiplier tubes	Prof. S.N. Vernov
Explorer 7	Spin-stabilised 573x1073km 50.27° inclination	1959 – 1961	Lyman-α photometer	105-135nm	LiF_2	2 NO_2 ion chambers	Dr. Herbert D. Friedman
			X-ray photometer	2-8 Angstrom	Be	2 Ar ion chambers	Dr. Herbert D. Friedman
Vanguard 3	512x3744km 33.3° inclination	1959	X-ray experiment	1.5-6keV		2 ionisation chambers	Dr. Herbert D. Friedman
Solar Radiation (SOLRAD) Satellite 1 / Grab 1	Spin-stabilised 614x1061km 66.69° inclination	1960	Lyman-α photometer	104-134nm	LiF_2	2 N_2O ion chambers	Dr. Herbert D. Friedman
			X-ray photometer	1.5-6keV	Be	Ar ion chamber	Dr. Herbert D. Friedman
Ariel 1 / UK1	Spin-stabilised 389x1214km 53.85° inclination	1962 – 1964	X-ray detector	0.9-3keV		Proportional counter	Sir Robert L.F. Boyd
			Lyman-α detector				Dr. J.A. Bowles [149]
Orbiting Solar Observatory (OSO) 1	Spin-stabilised with Sun-pointing expt.s 510x539km 32.8° inclination	1962 – 1964	Solar X-ray Flux	1.5-12keV	Be	2 Xe ion chambers	Mr. William A. White
			Solar Hydrogen Lyman-α Flux Monitor	105-123nm	LiF_2	CS_2 ion chamber	Dr. Kenneth L. Hallam [150]
Elektron A & B	9470x58952km 66.7° inclination	1964	Solar X-ray Counter	2-18 Angstrom			
SOLRAD 7A / Grab 5 / 1964-01-D	Spin-stabilised 903x926km 69.9° inclination	1964 – 1965	5 ion chamber photometers	0.2-6keV	Be, Al, mylar	Ar & N_2 ion chambers	[151,152]
			4 UV photometers	122.5-135nm	CaF_2	No gas filler	
Environmental Research Satellite (ERS) 17 / Octahedral Research	Spin-stabilised 153x112694km 34.4° inclination	1965	X-ray detectors	0.9-12keV		3 EON 6213 Geiger tubes	Dr. James I. Vette

Satellite (ORS) 3							
[Polar] Orbiting Geophysical Observatory OGO 2 / POGO 1	3-axis stabilised followed by spin-stabilisation 414x1510km 87.4° inclination	1965 – 1968	Solar UV spectrometer Solar X-rays	17-170nm 0.8-25keV	 6 filters	 4 ion chambers	Dr. H.E. Hinteregger Mr. Robert W. Kreplin [153]
OSO 2	435x466km 32.9° inclination	1965 – 1966	Solar X-ray Bursts Solar UV Spectrometer	0.6-6keV 0.2-0.3keV		5 Geiger tubes	Dr. Talbot A. Chubb Dr. Kenneth L. Hallam
SOLRAD 7B / Grab 6 / 1965-16-D	903x931km 70.1° inclination	1965	Solar X-ray Monitoring Experiment	0.4-25keV		6 ion chambers & Geiger counters	[154,155]
SOLRAD 8 / Explorer 30	Spin-stabilised 704x891km 59.7° inclination	1965 – 1967	Solar X-ray & UV monitor	0.2-25keV 108-135nm		8 ion chambers 2 Geiger counters	Mr. Robert W. Kreplin
IMP-D / Explorer 33	Spin-stabilised 265680x 480763km 24.4° inclination	1966 – 1971	Electron and Proton (& X-ray) Detectors	1-6keV		3 EON 6213 Geiger tubes	[156]
ERS 27 / ORS 3(F)		1967	Solar X-ray Monitor	0.9-6keV 0.9-1.5keV	Mica Mica + aluminium	3 EON 6213 Geiger tubes 3 EON 6213 Geiger tubes	Dr. James B. Gardner
Imp-E / Explorer 35	Spin-stabilised	1967 – 1973	As for Imp-D				
OGO 4 / POGO 2	3-axis and spin-stabilised 412x908km 86° inclination	1967 – 1970	Lyman-α and UV Airglow Solar X-ray emissions Solar UV emissions	123-135nm 105-135nm 135-155nm 0.5-20 Angstroms 17-170nm	Calcium fluoride Lithium fluoride Barium fluoride Sapphire + 7 interference filters	Nitric oxide ion chamber Nitric oxide ion chamber Dimethyl hydrazine ion chamber 4 ion chambers 6 photocathodes	Dr. Phillip w. Mange [157] Dr. Hans E. Hinteregger
OSO-3	3-axis and spin-stabilised 534x564km 32.87° inclination	1967 – 1969	UCSD X-ray telescope Solar EUV Spectrometer	7.7-210keV 4-9.5keV 0.5-2keV 2-6keV	CsI anti-coincidence shield + Be filter	NaI scintillation crystal + phototube Lithium fluoride crystal spectrometer Potassium acid phthalate crystal spectrometer Crystal	[158] [159]

				0.03-0.6keV 1.5-25keV		spectrometer Grating spectrometer	
			Solar X-ray Ion Chamber	1-1.5keV	Al	Nitrogen ion chamber	[160]
			EUV Spectrometer (Rowland)	25-130nm		Magnetic photomultiplier	Dr. Hans E. Hinteregger
OSO-4	3-axis and spin-stabilised 546x560km 33.04° inclination	1967 – 1971	Broadband Solar X-ray Emission Measurement	0.7-10keV	Be, Al, Melinex	7 Proportional counters (Ne/Ar + CO_2) and 8-channel differential analysers	[161,162]
			Solar X-ray Detectors	0.01-1.6nm		Ion chambers	Dr. Talbot A. Chubb
			Solar EUV Spectrometer	30-140nm	Filter wheel	Scanning spectrometer	[163,164]
			Solar X-ray telescope	3-20 Angstroms	Al-coated mylar, Mica	Anthracene crystal scintillator	Dr. Riccardo Giacconi
			X-ray Spectrometer (Bragg)	3.7-19.7keV		2 Ar ion chambers	[165]
Weapons Research Establishment Satellite (WRESAT)	193x1259km 83.2° inclination	1967	Solar UV monitor	105-166, 250nm			
			Solar X-ray monitor	1.5keV			
ESRO 2 / IRIS	Spin-stabilised 334x1085km 97.2° inclination	1968	Solar X-ray Detectors	0.6-12keV		5 proportional counters	Mr. E.A. Stewardson
OGO 5	3-axis & spin-stabilised 272x148228km 31.1° inclination	1968 – 1972	NRL Solar X-ray detector	~3-30keV	Be, Mylar	Xe + CO_2 proportional counter	[166]
			Energetic Radiations from Solar Flares	9.6->128keV		NaI(Tl) scintillation counter	[167]
OV1-15	Spin-stabilised 154x1818km 89.88° inclination	1968	Solar UV monitor	30-200nm	Silicon dioxide, barium fluoride, strontium fluoride, magnesium fluoride	5 photodiodes (one bare) 2 Gas counters	Dr. Fred A. Morse
			Solar X-ray monitor	0.2-12keV		2 ion chambers	Dr. Arthur B.C. Walker Jr.
SOLRAD 9 / Explorer 37	Spin-stabilised 448x638km 59.4° inclination	1968 – 1974	Solar radiation detectors	20-80keV 0.2-25keV 108-135nm		14 standardised photometers similar to SOLRAD 8	[168]
Nimbus 3	3-axis stabilised 1075x1135km	1969 – 1972	Monitor of Ultraviolet Solar	115-300nm	Al_2O_3, MgF_2,	5 vacuum photodiodes	Dr. Donald F. Heath

	99.91° inclination		Energy (MUSE)		CaF_2		[169]
OSO-5	3-axis & spin-stabilised 536x561km 32.95° inclination	1969 – 1984	Solar EUV Monitor (Rowland spectrometer)	28-103nm		Bendix photomultipliers	[170]
			X-ray spectroheliograph	0.7-4keV		Proportional counters	Sir Robert L.F. Boyd Dr. James D. Purcell
			EUV spectroheliograph	28.4-121.6nm			
			Solar Spectrum Studies	0.5-12keV 0.03-0.5keV 1.5-25keV		3 Bragg spectrometers Grating spectrometer 2 ion chambers	[171]
			Self-reversal of Lyman-α	Lyman-α		H_2 & D_2 ion chambers	[172]
			Solar X-ray radiation ion chamber photometer	0.2-25keV	Be, Al, Mylar	Kr, Ar, N_2 ion chambers	[173]
OSO-6	Spin-stabilised 465x516km 32.9° inclination	1969 – 1972	Solar flare X-ray detector	23-82keV		NaI scintillator	
			X-ray Spectrometer	0.3-0.8keV		Bendix M310 photomultipliers + photoelectric counters	[174]
			NRL X-ray Spectrometer (Bragg)	0.5-20keV 2-9keV 0.6-12keV 0.5-0.7keV 1.5-6keV		Bragg crystal spectrometers Pulse-height spectrometer 3 detectors Geiger counter Geiger counter	[175,176,177]
			Study of Solar He1, He2, Oxygen, Nitrogen radiation	18-121.6nm		Channel photomultipliers	[178]
			Solar UV Spectrometer	28-138nm		Grating spectrometer	[179] [180]
OV5-9		1969 – 1972	Solar X-ray flux monitor	0.8-40keV		2 proportional counters	Dr. Arthur B.C. Walker Jr.
Vela 5A & B	Spin-stabilised 110900x112210km 32.8° inclination	1969	Solar X-ray monitor	0.2-40keV	Be, Al, Mylar	NaI(Tl) scintillator + photomultiplier, Ar-He & 2 N_2 ion chambers	Dr. W.H. Chambers
Cosmos 381	985x1023km 74° inclination	1970	Solar UV Detector	0.3-150nm			

Intercosmos 4	263x668km 48.5° inclination	1970	Solar X-ray Polarimeter X-ray spectroheliograph UV photometer X-ray photometer	~15keV 121.6nm		Thomson scattering polarimeter	[181]
Nimbus 4	3-axis stabilised 1092x1108km 80.114° inclination	1970 – 1980	As for Nimbus 3				
Vela 6A & B	Spin-stabilised 111210x112160km 32.41° inclination	1970	As for Vela 5A & B				
OSO-7	Spin-stabilised 321x572km 33.1° inclination	1971 – 1974	X-ray & EUV spectroheliograph Hard Solar X-ray monitoring	0.8-7keV 2-15keV 10-300keV	 Be Pb + CsI/Al anticoincidence shield	 Xe-CO_2 proportional counter NaI(Tl) scintillator + RCA photomultiplier tube	Dr. Werner M. Neupert [182,183]
SOLRAD 10 / Explorer 44	Spin-stabilised 436x630km 51° inclination	1971 – 1979	Solar Radiation Detectors	15-150keV 0.2-120keV 108-160nm	 Be, Al, mylar LiF_2, CaF_2, SiO_2	Caesium iodide scintillation crystal with photomultiplier Kr, Ar, N_2, CCl_4, Xe ion chambers Nitric oxide, triethylamine-8 ion chambers	Mr. Robert W. Kreplin [184]
Atmospheric Explorer-C (AE-C) / Explorer 51	Spin-stabilised 149x4294km 68.1° inclination	1973 – 1978	Extreme Solar UV Monitor (ESUM) Extreme Ultraviolet Spectrometer (EUVS)	20-121.6nm 14-185nm	Filter wheel aluminium, tin, indium	Aluminium oxide photocathodes 24 grazing-incidence grating monochromators	[185,186] [187]
Aeros-B	Spin-stabilised 217x879km 97.4° inclination	1974	Solar EUV Radiation	15-107nm		Photomultiplier	See Aeros-A
Helios 1 (Helios-A)	Spin-stabilised Heliocentric orbit 0.3095x0.985 AU 0.02° inclination	1974	Galactic and Solar Cosmic Rays E7 (+ solar SXR)	2-8keV		Proportional counter	[188,189]

AE-E / Explorer 55	Spin-stabilised 156x2983km 19.7° inclination	1975 – 1981	Extreme Ultraviolet Spectrometer (EUVS) Extreme Solar UV Monitor (ESUM)	14-185nm 20-121.6nm	 Filter wheel aluminium, tin, indium	24 grazing-incidence grating monochromators Aluminium oxide photocathodes	See AE-C See AE-C
D2B	Spin-stabilised 477x707km 37.1° inclination	1975 – 1976	Solar Activity Study Solar Flux Monitor, Flare Evolution	17.4-131.5nm 121.6-310nm		2 spectrometers	Mr. Jean-Pierre Delaboud-iniere Mr. P. Cruvelier
Geosynchronous Operational Environmental Satellite (GOES) 1	Spin-stabilised 34165x36458km 9.9° inclination	1975 – 1985	Solar X-ray Monitor	1.5-12keV Sensitivity 1×10^{-12} J/cm^2/s 4-25keV Sensitivity 1×10^{-13} J/cm^2/s	Be Be	Ar ion chamber Xe ion chamber Dynamic range: 1×10^4	Dr. Harold Leinbach
Prognoz 4	634x199000km 65° inclination	1975	Solar X-ray monitor	2-511keV		NaI scintillator	Dr. G. Ye. Kacharov
Solar Radiation and Thermospheric Satellite (SRATS) / Taiyo	Spin-stabilised 249x3129km 31.54° inclination	1975	Solar X-ray monitor Solar Lyman-α monitor	6-12keV Lyman-α		Proportional counters Lithium fluoride oxide ionisation chamber	[190] [191] [192]
Synchronous Meteorological Satellite 2 (SMS 2)	Spin-stabilised 35778x35799km 1° inclination	1975	Solar X-ray Monitor	1.5-25keV	Be	Ar & Xe ion chambers	Dr. Donald J. Williams
Helios 2 (Helios-B)	Spin-stabilised Heliocentric orbit 0.289x0.983AU 0° inclination	1976	As for Helios 1				
Prognoz 5	510x199000km 65° inclination	1976	Solar X-ray monitor Solar X-ray Spectrometer	2-511keV 2.2-7keV 6-98keV	 Beryllium -	NaI scintillator Gas proportional counter NaI(Tl) scintillation detector	Dr. G. Ye. Kacharov [193]
SOLRAD 11A & 11B/ SESP P74 1c & d	118383x119180km 25.7° inclination 115720x116645km 25.6° inclination	1976	Solar X-ray monitor X-ray monitor Solar X-ray monitor	15-150keV 4-100keV 0.8-12keV 0.2-	 Be (+Al as required)	CsI scintillator 4 gas proportional counters 2 sets of ion chambers	Dr. Gilbert G. Fritz Dr. Herbert W. Smathers Mr. Robert W. Kreplin

				0.3keV			
			Solar EUV monitor	17-50nm 45-85nm 72.5-105nm	Be, Tin, In	3 LiF_2 surface detectors	Mr. Robert W. Kreplin
			Solar UV monitor	108-135nm		Nitric oxide, triethylamine-8 ion chambers + LiF_2 surface detector with evacuated ion chamber	Mr. Robert W. Kreplin
			Solar UV Spectrometer	117.5-180nm	Li, LiH, Be	Photomultiplier tube	Dr. Paul D. Feldman
			Thomson X-ray polarimeter	2-50keV		2 proportional counters	Dr. George A. Doschek
			Continuum & magnesium line monitor	1.4, 1.5, 1.3 keV		3 SHA crystals + proportional counters	Dr. John F. Meekins
			Solar X-ray monitor	0.4-25keV		3 ionisation chambers	Mr. Robert W. Kreplin
GOES 2	Spin-stabilised 35266x36304km 8.3° inclination	1977	As for GOES 1				
Prognoz 6	498x197900km 65° inclination	1977	As for Prognoz 5				
GOES 3	Spin-stabilised 35469x36679km 7.1° inclination	1978	As for GOES 1				
Prognoz 7	Spin-stabilised 483x202965km 65° inclination	1978	X-ray spectrometer	2-200keV		NaI scintillator	Dr. G. Ye. Kacharov
			Solar X-ray spectrometer	2.2-98keV	Be	NaI(Tl) scintillator + gas proportional counter	Mr. O.B. Lickin
			UV Detector	10-130nm			Dr. Yu. M. Kulagin
GOES 4	Spin-stabilised 35776x35800km 0.2° inclination	1980	As for GOES 1				
Prognoz 8	980x197390km 65.8° inclination	1980	As for Prognoz 7 (alleged)				
GOES 5	Spin-stabilised 35715x35769km 0.32° inclination	1981 – 1984	Solar X-ray Monitor	0.03-25keV $1x10^{-13}$ $J/cm^2/s$	Beryllium	Xe, He ion chamber	Mr. Howard A. Garcia
				1.5-12keV $1x10^{-12}$ $J/cm^2/s$	Beryllium	Ar, He ion chamber Range: 10^4	
Solar Mesosphere Explorer (SME) /	Spin-stabilised 535x551km 97.5° inclination	1981 – 1988	Solar UV Monitor	Lyman-α 160-310nm		Ebert-Fastie Spectrometer	Dr. Charles A. Barth

Explorer 64							
Office of Space Science (OSS) 1 (on STS 3)	3-axis stabilised 240x240km 38° inclination	1982	Solar Flare X-ray Polarimeter (SFXP) Solar UV Spectral Irradiance Monitor (SUSIM)	5-30keV 120-400nm	4 lithium scattering blocks	3 sets of 4 photocounters 5 photodiodes + 2 other detectors	Dr. Robert Novick Dr. Guenter E. Brueckner
GOES 6	Spin-stabilised 35775x35796km 0.27° inclination	1983 – 1994	As for GOES 5				
Prognoz 10	Spin-stabilised 421x200520km 64.99° inclination	1985	Solar X-ray Burst Photometer (RF-2P)	2.1-8.2keV 10.5-175keV	Be	Gas proportional counter NaI scintillation detector	Mr. O.B.Lickin [194]
Spacelab 2 (on STS 51F)	3-axis stabilised 312x321km 49.5° inclination	1985	Solar Coronal Helium Abundance High Resolution Telescope and Spectrograph (HRTS) Solar UV spectral Irradiance Monitor	121.6 & 30.4 nm 117.6-170nm 120-400nm		Grazing incidence spectrometer Spectroheliograms + camera with type-101 film 5 photodiodes + 2 photon counters	Dr. Guenter E. Brueckner Dr. Guenter E. Brueckner Dr. Guenter E. Brueckner
GOES G	Spin-stabilised 35788x35788km 0° inclination	1986	As for GOES 1				
GOES 7	Spin-stabilised 35788x35788km 0° inclination	1987	As for GOES 5				
Phobos 1	3-axis stabilised Earth-Mars trajectory	1988 – 1989	X-ray photometer (RF-15) Solar UV telescope (TEREK)				[195]
Phobos 2	3-axis stabilised Earth-Mars trajec.	1988 – 1989	X-ray photometer (RF-15)				As for Phobos 1
Ulysses / International Solar Polar Mission	Spin-stabilised Heliocentric orbit 1.35x5.4AU -78.93° inclination	1991 – Present	Solar X-rays & cosmic gamma-ray bursts (HUS/GRB)	5-15keV 15-150keV		2 solid state detectors 2 CsI(Na) scintillators + photomultipliers	Dr. Kevin C. Hurley [196]
Atmospheric Laboratory for Applications and Science (ATLAS 1 on STS 45)	3-axis stabilised 292x304km 57° inclination	1992	Solar Spectrum Measurement (SOLSPEC) Solar UV Spectral Irradiance Monitor (SUSIM)	180-370nm 120-400nm	MgF_2	EMR G 641 F photomultiplier tube with CsTe photocathode + dual-grating spectrometer 5 photodiodes and 2 photon counters	[197] Dr. Guenter E. Brueckner

ATLAS 2 (on STS 56)	3-axis stabilised 300x300km 57° inclination	1993	As for ATLAS 1				
Shuttle Pointed Autonomous Research Tool for Astronomy (Spartan) 201-01 (on STS 56)	3-axis stabilised 295x311km 57° inclination	1993	Ultraviolet Coronal Spectrograph (UVCS)	Lyman-α	MgF_2	CsI photocathode dual array	Mr. John L. Kohl
ATLAS 3 (on STS 66)	3-axis stabilised 296x310km 57° inclination	1994	As for ATLAS 1				
Coronas-I	501x541km 82.5° inclination	1994	Solar X-ray Spectrometer (RES-C)	1.85-205 Angstrom		Cooled CCD	Dr. I.A. Zhitnik
			High Resolution Spectrometer (DIOGENESS)	2.835-3.356Å 2-160keV		(Bragg) Spectrophotometer	Dr. Janusz Sylwester
			X and Gamma ray Spectrometer (HELIKON)	10keV-8MeV		Calcium sulphate thermoluminescence on to photomultiplier	Dr. E. P. Mazets
			Solar Burst Spectrometer (IRIS)	2-20keV 30-120keV Sensitivity 10 erg/cm^2/s			Dr. G Kocharov
			Solar Ultraviolet Radiometer (SUFR)	0.5-4keV 0.1-4keV Lyman-α	MgF_2, Al, mylar		84
GOES 8 (GOES I)	3-axis stabilised 35783x35799km 0.4° inclination	1994 – 2003	As for GOES 5				
WIND	Spin-stabilised L1 halo orbit 1.5x10^{6}km sunward	1994	Transient gamma ray spectrometer (TGRS)	20keV-10MeV		n-type Ge detector, passive cooling to 85K	Dr. Bonnard J. Teegarden
			Gamma ray burst detector (KONUS)	10keV-10MeV	Pb, Sn	2 NaI scintillators	Dr. E.P. Mazets
Spartan 201-02 (on STS-64)	3-axis stabilised 259x269km 56.9° inclination	1994	As for Spartan 201-01				
GOES 9 (GOES J)	3-axis stabilised 35775x35805km 0.07° inclination	1995 – 2003	As for GOES 5				
Interball Tail Probe / Prognoz 11	Spin-stabilised 192000 x 776km 63° inclination	1995 – 2000	Solar UV Radiation RKI-2				Dr. Tamara V. Kazachev-Skaya
			Dosimeter SOSNA-3	(UV)			Dr. V. Bengin
			Solar X-ray	2-8keV	150μm Be	Ar +10%CO_2	Dr. O.

			Bursts RF-15I	10-240keV	Al	proportional counter 8mm NaI(Tl) scintillation detector	Likin[198]
Solar and Heliospheric Observatory (SOHO)	L1 Halo Orbit 1.5x10^{6}km sunward	1995 – Present	Solar Ultraviolet Measurements of Emitted Radiation (SUMER)	50-161nm		2D-MCP + magnesium fluoride & potassium bromide solid state detectors	[199,200,201]
			Ultraviolet Coronagraph Spectrometer (UVCS)	114.8-128.3nm			[202]
Spartan 201-03 (on STS 69)	3-axis stabilised 370x370km 28.4° inclination	1995	As for Spartan 201-01				
GOES 10 (GOES K)	3-axis stabilised 35590x36310km 0.5° inclination	1997	As for GOES 5				
Spartan 201-05 (on STS-95)	3-axis stabilised 551x561km 28.5° inclination	1998	As for Spartan 201-01				
Student Nitric Oxide Explorer (SNOE)	Spin-stabilised 530x580km 97.7° inclination	1998 – 2002	Solar X-ray Photometer	0.2-3.5 Angstrom	Sn, Ti, Zr/Ti, Al/C	5 Si photodiodes	Dr. Charles A. Barth [85]
GOES 11 (GOES L)	3-axis stabilised 35764x35810km 0.1° inclination	2000	As for GOES 5				
Coronas-F	499x540km 82.5° inclination	2001	UV Radiometer (SUFR)	0.1-130nm (dynamic range 0.1-30 erg/cm^2/s)			Dr. Tamara V. Kazachev-skaya
			UV Spectrometer (VUSS-L)	119.1-124.1nm			Dr. Anatoliy A. Nusinov
			X-ray Spectrometer/ Photometer (DIOGENESS)	2-8keV 10-160keV			Dr. Janusz Sylwester
			Flare X-ray Specrometer (IRIS)	2-200keV sensitivity 10 nanoergs/ cm^2/s			Dr. G. Kocharov
			X and Gamma ray Spectrometer (HELIKON)	10keV-8MeV			Dr. E. P. Mazets
			X-ray spectrometer (RPS)	3-30keV			Dr. Vladislav M. Pankov
			X-ray Polarimeter (SPR-N)	20-100keV	Various metals	Cooled CCD array	Dr. Igor I. Sobelman
			XUV Telescope	0.84-			[203]

			(SPIRIT)	30.4nm			
GOES 12 (GOES M)	3-axis stabilised 35779x35798km 0.2° inclination	2001	As for GOES 5 Solar X-ray Imager (SXI)	0.6-6nm	Various metals	TH7895A-(H) CCD with MCP	204
Thermosphere Ionosphere Mesosphere Energetics and Dynamics (TIMED)	627x628km 74.1° inclination	2001 – Present	Solar EUV experiment (SEE)	0.1-35nm (0.04-12keV) 25-200nm	Various metal films	12 silicon photodiodes Rowland circle grating spectrometer with CODACON array detector	205,206
Shenzhou 2	3-axis stabilised 330x346km 42.6° inclination	2001	Super Soft X-ray Detector	0.2-2keV		Proportional Counter	207
Solar Radiation and Climate Experiment (SORCE)	3-axis stabilised 613x653km 40° inclination	2003 – Present	Spectral Irradiance Monitor (SIM)	200-2000nm		Nickel phosphorus-coated diamond bolometer + n-on-p & p-on-n silicon photodiodes + indium gallium arsenide photodiode	208,209
			Solar Stellar Irradiance Comparison Experiment (SOLSTICE)	115-180nm 170-320nm		CsI photomultiplier CsTe photomultiplier	77,210
			XUV Photometer System (XPS)	0.1-34nm (0.04-10keV) Lyman-α	Fused Si, Ti/C, Ti/Mo/Au, Ti/Mo/Si/C, Al/Nb/C, Al/Sc/C, Al/Mn, Al/Cr, Acton Lyman interference filter	12 Si photodiodes	77,211

Table 13: Previous Spaceflight Solar Radiation Dose Detectors

In addition to these missions and detectors there is an additional record in a similar format of further instrumentation that has been used to detect solar radiations of similar wavelengths, though not primarily for full-disk dose measurements. Also included are the names of various missions for which it is known that solar SXR and UV detection equipment was designed but for which the details are not easily available in the literature (usually because the spacecraft were foreign and their scientific results never translated into English, or due to the design documentation not being published for a wider audience).

Spacecraft	Orbit	Year	Instrumentation				Reference
			Name	**Range**	**Filter**	**Detector**	
SOLRAD 6A	170x869km 69.9° inclination	1963					
SOLRAD 6B / Ferret-12 / Ops-4988	896x931km 70.1° inclination	1965					
Lambda 4S-1		1966					
Lambda 4S-2		1966					
OV1-10	641x769km 93.43° inclination	1966	Solar X-ray crystal scanning spectrometer (Bragg)	1-100 Angstrom	Al-coated formvar	CsI photocathode + Bendix M306 photomultiplier	Dr. Hugh R. Rugge
Cosmos 166	281x553km 48.4° inclination	1967					
Lambda 4S-3		1967					
Cosmos 215	255x403km 48.5° inclination	1968					
Cosmos 230	285x543km 48.5° inclination	1968					
Cosmos 262	259x798km 48.5° inclination	1968					
Lambda 4S-3		1969					
OGO 6 / POGO 3	3-axis stabilised 413x1077km 82° inclination	1969 – 1972	Solar X-ray Emissions Solar UV Emissions Solar UV Survey	2-83keV 16-160nm 180-320nm	 6 gratings Four diffuser disks	Scintillating crystal photomultiplier + proportional counter Photomultiplier Quartz prism spectrograph	Mr. Robert W. Kreplin Dr. Donald E. Bedo Dr. Victor H. Regener
Cosmos 484	203x236km 81.3° inclination	1972					
Intercosmos 7	267x568km 48.4° inclination	1972					
Prognoz 1	950x200000km 65° inclination	1972					
Intercosmos 9	202x1552km 48.5° inclination	1973					
Skylab	3-axis stabilised 434x442km 50° inclination	1973 – 1974	SO20 XUV Solar Photography SO54 X-ray Spectrographic Telescope S055 UV Scanning Polychromator/ Spectroheliometer	0.06-1.2keV (1-20nm) 0.2-6keV 28-134nm 0.6-4nm	In, Be Filter wheel - Fused	Spectrometer + photographic film Scintillator crystal + photocathode Channeltron + 7 solar-blind photomultipliers Kodak SO-212 photographic film	[212] [213] [214] [215]

			SO56 X-ray Telescope (X-ray event analyser X-REA) NRL/S082B EUV Spectrograph	(1.7-5keV) (0.6-2keV) 97-394nm	silica, Be, Al, Ti (Beryllium) (Aluminium) Al, MgF_2, ZnS	(Proportional count'r) (Proportional count'r) Kodak 104 & 101 photographic film	216
Intercosmos 11	484x526km 50.7° inclination	1974					
S3-1 / SESP P73-5	Spin-stabilised 152x3795km 97° inclination	1974	Solar UV Experiment	30-180nm			Mr. A.B. Prag
AE-D / Explorer 54	Spin-stabilised 154x3816km 90.1° inclination	1975 – 1976	Extreme Ultraviolet Spectrometer (EUVS)	14-185nm		24 grazing-incidence grating monochromators	See AE-C
OSO-8	3-axis & spin-stabilised 544x559km 32.9° inclination	1975 – 1978	High-resolution UV spectrometer (Ebert) Chromosphere fine-structure study Mapping X-ray heliometer	115-220nm 100-400nm 2-30keV	-	Photomultiplier tube Grating spectrometer Proportional counters	217 Dr. Roger Maurice Bonnet 218,219 220
Intercosmos 16	465x523km 50.6° inclination	1976					
Solar Interplanetary Gamma-Neutron Experiment 3 (SIGNE 3)	Spin-stabilised 457.33x522.54km 50.67° inclination	1977 – 1978	Solar Monitoring	180-195nm 205-220nm		Spectrometer	Dr. Gerard O. Thuillier
Space Test Program (STP) P78-1 / SOLWIND	Spin-stabilised 560x600km 97.9° inclination	1979	Solar X-ray spectrometer (SOLEX, SOLFLEX, MONEX, & MAGMAP)	0.1-25 angstrom	Be, Mylar	4-channel Bragg crystal spectrometer with Ar/Xe + CO_2 gas proportional detectors	221
Solar Maximum Mission (SMM)	3-axis stabilised 508x512km 28.5° inclination	1980 – 1989	Ultraviolet spectrometer and polarimeter (Ebert) Hard X-ray burst spectrometer (HXRBS) Gamma-Ray Spectrometer Hard X-ray Imaging spectrometer (HXRIS) Soft X-ray	115-360nm 20-260keV 10keV-100MeV 3.5-30keV 0.6-9keV	Al, MgF_2 coat. LiF LiF Al Al (for lower energies) Be, Al -	4 CsI scintillator CsTe scintillator CsI(Na) scintillator NaI scintillation detector (for lower energies) 900 mini-proportional gas counters (95% Xe + 5% CO_2) Scintillators	222,223 224 225 226 227

			Polychromator (XRP)		Be Polypropelene	(KAP, Beryl, ADP, Quartz, Ge) 3 Xe-CO_2 prop. c'nt'r Propane prop. coun'r	[228,229]
Astro A / Hinotori	Spin-stabilised 548x603km 31.3° inclination	1981 – 1991	Rotating Modulation Collimator Bragg Spectroscopy Time Profile Spectroscopy	5-40keV 6-7keV 2-20keV		Gas scintillation proportional counter	Prof. Tatsuo Takakura Mr. Katsuo Tanaka Dr. Masaru Matsuoka
Prognoz 9	Spin-stabilised 380x720000km 65.5° inclination	1983	Solar X-ray Spectrometer	2-8keV 10-160keV	Beryllium	Gas proportional counter NaI scintillation detector	
Spacelab 1 (on STS 9)	3-axis stabilised 242x254km 57° inclination	1983	Solar spectrum observation	170-3200nm		3 grating spectrometers	Dr. Gerard O. Thuillier
Upper Atmosphere Research Satellite (UARS)	3-axis stabilised 574x575km 56.98° inclination	1991	Solar Stellar Irradiance Comparison Experiment (SOLSTICE) Solar UV Spectral Irradiance Monitor (SUSIM)	115-650nm 115-410nm		Ebert-Fastie spectrometer Dual dispersion spectrometer	[230] [79]
Yohkoh / Solar A	3-axis stabilised 517.9x792.6km 31.3° inclination	1991 – 2001	Hard X-ray Telescope (HXT) Soft X-ray Telescope (SXT) Bragg Crystal Spectrometer (BCS) Wide Band Spectrometer (WBS)	15-100keV 0.3-4keV 2.4-7keV 2-30keV 20-600keV 0.2-100MeV		NaI(Tl) scintillator + photomultiplier CCD Ar-Xe ion chamber + 4 germanium (111) scintillators Xe-CO_2 proportional counter NaI scintillator 2 BGO scintillators	Dr. Kazuo Makishima Dr. Tadashi Hirayama Dr. George A. Doschek Dr. Jun Nishimura
European Retrievable Carrier (EURECA) 1	3-axis stabilised 438x447km 28.5° inclination	1992 – 1993	Solar Spectrum Instrument (SOSP)	170-3200nm			Dr. Gerard O. Thuillier [231]
Transition Region and Coronal Explorer/	3-axis stabilised Sun-synchronous 520x547.2km 97.84° inclination	1998 – Present	Imaging telescope	17.1, 19.5, 28.4, 121.6, 155nm +	Al, MgF_2	Phosphor coated Metachrome 2 CCD Passively cooled <218K	[232,233,234,235]

Small Explorer 4 (TRACE / SMEX 4)				132.5-190nm			
Reuven-Ramaty High Energy Solar Spectroscopic Imager / Small Explorer 6 (RHESSI/SMEX 6)	Spin-stabilised 586x600km 38° inclination	2002 – Present	Imaging spectrometer	3keV-20MeV	Be (centre), Al (surround)	9 biased, hyper-pure, n-type, Ge detectors, cryogenically cooled to ≤ 75K	236
GSAT-2	3-axis stabilised 34000x36000km 0.3° inclination	2003 –	Solar X-ray spectrometer (SOXS)	4-25keV 4-56keV		Si PIN photodiode CdZnTe photodiode	237

Table 14: Further Radiation Instrumentation

7.2 Appendix II: AlGaN Detector Development History

The study of AlGaN arose from investigation into the properties of the III-V nitride compounds GaN and AlN.

The formation of GaN is initially recorded in 1928 by Johnson et al.[238] Their analysis revealed GaN's chemical stability and thus ear-marked it for further development as a material for use in high-temperature and caustic environments.

Not until more sophisticated measurement and fabrication apparatus was available could more detailed investigation be carried out. In 1969 Maruska and Tietjen accurately measured the 3.39eV direct band gap of GaN for the first time[239] after successfully growing the first single crystal of sufficient purity. Further study of the photoconductive properties of GaN was carried out by Pankove and Berkeyheiser in 1974[240].

Research continued to focus on better fabrication techniques, with groups in Europe, the US and Japan tackling the problems of matching the Wurzite structure of GaN to suitable substrate material. Much emphasis was made on producing blue light-emitting diodes (LEDs) with the aim of commercialising this technology to take advantage of opportunities in the full-colour outdoor display, traffic signal, and vehicle interior and exterior lighting markets[241].

The study of the second alloy in AlGaN, AlN, suffered from difficulties of synthesis due to the much more reactive Al content – requiring high purity source material and an oxygen-free environment during crystal growth. Investigation into its Wurzite structure was first carried out by Ott[242] in 1924. However, most groups preferred investigating GaN due to its less-stringent fabrication requirements.

It was Yim et al.[243], in 1973, who characterised AlN's optical absorption and determined the room-temperature bandgap to be 6.2eV. Further investigation into AlN's properties was slow and plagued with false results due to the interference of oxygen contamination during synthesis.

Once the bandgaps of GaN and AlN had been identified then AlGaN became the focus of research into III-V nitride alloys due its potential for use in GaN/AlGaN heterostructure devices and to the possibility of tuning the alloy bandgap over the high-frequency visible and UV spectrum. Lyutaya and Bartnitskaya[244], in 1976, were the first to report a GaN-AlN solid solution. Many groups followed with progressively greater enrichment of the crystal structure with Al.

A thorough review of the discovery and analysis of GaN, AlN, and AlGaN has been produced by Strite and Morkoç[245].

The development of complex GaN/AlGaN semiconductor devices was hindered due to GaN's inherent n-type behaviour, the poor crystal quality due to the high density of dislocations and the difficulty of constructing a p-type counterpart. The first step to overcoming these difficulties was made in 1985 by Amano et al.[246]

when they produced the first extremely high-quality GaN crystal with a specular surface free from cracks.

With the advantage of such high quality crystals the same group went on to synthesise the first distinct p-type GaN in 1989 and from there manufactured the first p-n junction blue LED[247].

These two breakthrough developments reinvigorated research into III-V nitride semiconductor devices, leading to massive research growth and device manufacture throughout the 1990s.

In 1991 Nakamura[248] also developed p-type GaN by a different deposition method while Akasaki and Amano[249,250] went on to develop the first p-type AlGaN. Rapid advances followed with the first GaN UV photodetectors being reported by Khan et al. in 1992[251]. The same group[252] went on to construct the first Schottky barrier GaN photodiode in 1993.

The first AlGaN photodetectors, based on the photoconductive principle, were created shortly afterwards[253,254] followed in swift succession by the fabrication of the first AlGaN Schottky photodiodes in 1998[255,256]. Since then the photodiodes have been improved and commercialised by a number of companies, including APA Optics Inc.

8 Bibliography and Additional Resources

In addition to printed reference work, listed here are a number of internet-based resources that were also used to source various material for this thesis. Due to the nature of the internet (especially its unproven long-term stability as a rigorous reference medium) these resources are produced here, and not in the reference list, with the proviso that their locations/existence may change unpredictably in the future.

"The Many Faces of the Sun" Eds. Strong K.T., Saba J.L.R., Haisch B.M., Schmelz J.T., Springer-Verlag New York Inc., 1999, ISBN 0-387-98481-X

"The Sun" 2nd Ed., Stix M., Springer-Verlag Berlin Heidelberg New York, 2002, ISBN 3-540-53796-0

"The Sun from Space" Lang K.R., Springer-Verlag Berlin Heidelberg New York, 2000, ISBN 3-540-66944-2

"Guide to the Sun" Phillips K.J.H., Cambridge University Press, 1992, ISBN 0-521-39788-X

"The Standard handbook for Aeronautical and Astronautical Engineers" Davies M. (Ed.), McGraw-Hill Companies Inc., 2002, ISBN 0-07-136229-0 (MH)

"Spacecraft-Environment Interactions" Hastings D., Garrett H., Cambridge University Press, 1996, ISBN 0-521-47128-1

"The Space Environment – Implications for Spacecraft Design" Tribble A.C., Princeton University Press, 2003, ISBN 0-691-10299-6

"USA in Space (Vols. 1-3)" Eds. Magill F.N., Tobias R.R., Salem Press Inc., 1996, ISBN 0-98356-924-0

"Physics for Scientists and Engineers (Extended Version)" Tipler P.A., Worth Publishers, 1991, ISBN 0-87901-432-6

"Introduction to Space Physics" Eds. Kivelson M.G., Russell C.T., Cambridge University Press, 1995, ISBN 0-521-45714-9

"Space Mission Analysis and Design" Eds. Larson W.J., Wertz J.R., Microcosm Press and Kluwer Academic Publishers, 1999, ISBN 1-881883-10-8

"Spacecraft Systems Engineering" Eds. Fortescue P., Stark J., John Wiley and Sons, 1995, ISBN 0-471-95220-6

"Introduction to the Physics of Electrons in Solids" Tanner B.K., Cambridge University Press, 1995, ISBN 0-521-28358-2

"Theory of Defects in Solids – electronic structure of defects in insulators and semiconductors" Stoneham A.M., Clarendon Press, 1975, ISBN 0-19-850780-1

National Space Science Data Centre (http://nssdc.gsfc.nasa.gov/)

Encyclopaedia Astronautica (http://www.astronautix.com/)

JPL Mission and Spacecraft Library (http://msl.jpl.nasa.gov/home.html)

David Darling's encyclopaedia of astrobiology, astronomy and spaceflight (http://www.daviddarling.info/encyclopedia/ETEmain.html)

Russian Space Web (http://www.russianspaceweb.com/index.html)

Gunter's Space Page (http://www.skyrocket.de/space/space.html)

9 References

[1] Milintchouk A., Eesbeek M.v., Levadou F. "Soft x-ray radiation as a factor in the degradation of spacecraft materials" ICPMSE-3, Toronto, 1996

[2] Yokota K., Seikyu S., Tagawa M., Ohmae N. "A quantitative study in synergistic effects of atomic oxygen and ultraviolet regarding polymer erosion in LEO space environment" 9th International Symposium on Materials in a Space Environment, ESTEC, 2003

[3] Milintchouk A., Eesbeek M.v., Levadou F., Harper T. "Influence of X-ray solar flare radiation on degradation of Teflon in space" Journal of Spacecraft and Rockets, **34**/4, pp. 542-548, 1997

[4] Harris I.L., Chambers A.R., Roberts G.T. "Results from the Space Technology Research Vehicle 1A Atomic Oxygen Experiment" Journal of Spacecraft and Rockets, 0022-4650, **35**/5, pp. 647-652, 1998

[5] Ed. Wilson A. "The International Space Station: A Guide for European Users" ESA Publications Division, BR-137 (ISBN 92-9092-609-0)

[6] Svalgaard L., Kamide Y., Cliver E.W. "Will sunspot cycle 24 be the smallest in 100 years?" Geophysical Research Letters paper 10.1029/2004GL021664, 2005

[7] Hedin A.E. "MSIS Model 1986" MSSDC-ID: MN-61C, NASA Goddard Space Flight Center (Data available at: modelweb.gsfc.nasa.gov/atmos/miss.html

[8] Holmes-Siedle A., Adams L. "Handbook of Radiation Effects" Oxford University Press, 1994

[9] Image courtesy of Atelier Guarniero, Sassenheim. Available online at http://www.guarniero.nl/iss/colombus/EUTEF/EUTEF.htm

[10] Dinguirard M., Mandeville J.C., Eesbeek M.v., Tighe A.P., Durin C., Chambers A., Gabriel S., Goulty D., Roberts G. "Materials Exposure and Degradation Experiment (MEDET)" Conference and Exhibit on International Space Station Utilization, Cape Canaveral, 2001, AIAA-2001-5070

[11] "LM108A/LM208A/LM308A Operational Amplifiers" National Semiconductor Corp. Data-sheet, 1989

[12] "LM158/LM258/LM358/LM2904 Low Power Dual Operational Amplifiers" National Semiconductor Corp. Data-sheet, 1994

[13] Lorenz R.D. "Solar array degradation by dust impacts during cometary encounters" J. Spacecr. & Rockets, **35**/4, pp. 579-582, 1998

[14] "Data requirements for materials flight test" Aerospace Corp., TOR-0091 (6068-02)-1, El Segundo, CA, 1991

[15] Tribble A.C., Haffner J.W. "Estimates of photochemically deposited contamination on GPS satellite" J. Spacecr. & Rockets, **28**/2, p. 222, 1991

[16] Hemenway C.L., Hallgren D.S., Kerridge J.F. "Technical description of the Gemini S-10 and S-12 micrometeorite experiments" Space Research, **8**, pp. 521-535, 1968

[17] Nagel K., Fechtig H., Schneider E., Neukum G. "Micrometeorite craters on Skylab experiment S-149" Interplanetary Dust and Zodiacal Light: Proc. Of the IAU Colloquium No. 31, Lecture Notes in Physics No. 48, pp. 275-278, 1976

[18] Lehn W., Hurley C. "Skylab DO-24 thermal control coatings and polymeric films experiment" AIAA 74-1228, 1974

[19] Harvey G.A., Humes D. H., Kinard W.H. "MIR environmental effects payload and returned MIR solar panel cleanliness" SAMPE, California, 1999

[20] Mandeville J.C. "Aragatz mission dust collection experiment" Adv. Space Res., **10**, pp. 397-401, 1990

[21] Bethoud L., Mandeville J.C. "Material damage in space from microparticle impact" J. Materials Science, **32**, pp. 3043-3048, 1997

[22] Cour-Palais B.G., Brown M.L., McKay D.S. "Apollo window meteoroid experiment" NASA SP-315, pp. 26-1 – 26-10, 1972

[23] Mandeville J.C., Lem H.Y. "Scanning electron microscope analysis and energy dispersive X-ray analysis of the surface features of Surveyor III television mirror" Proc. 3rd Lunar Science Conference, **3**, pp. 3201-3212, 1972

[24] Paul K.G., Rott M., Dirr B. "Post-flight impacts on HST solar cells" HST Solar Array Workshop, ESA WPP-77, Noordwijk, The Netherlands, 1995

[25] Visentine J., Kinard W., Brinker D., Banks B., Albyn K. "Mir solar-array return experiment: power performance measurements and molecular contamination analysis results" J. Spacecr. & Rockets, **39**/2, pp. 187-193, 2002

[26] Townsend J.A., Hansen P.A., McClendon M.W., de Groh K.K., Banks B.A. "Hubble Space Telescope metallized Teflon FEP thermal control materials : on-orbit degradation and post-retrieval analysis" High Performance Polymers, **11**/1, pp. 81-99, 1999

[27] Westphal A.J., Afanasyev V.G., Gunn N.A.C., Price P.B., Akimov V.V., Rodin V.G., Baryshnikov K., Gorshkov L.A., Shvets N.I., Tsigankov O.S. "First results from Large Trek [detectors on Mir for galactic cosmic ray composition measurement" Adv. Space. Res., **19**/5, pp. 743-746, 1997

[28] Visentine J.T., Leger L.J., Kuminecz J.F., Spiker I.K. "STS-8 atomic oxygen effects experiment" AIAA 85-0415, 1985

[29] Synowicki R.A., Hale J.S., Spady B., Reiser M., Nafis S., Woollam J.A. "Thin film materials exposure to low Earth orbit aboard Space Shuttle" J. Spacecr. & Rockets, **32**/1, pp. 97-102, 1995

[30] Koontz S.L., Leger L.J., Rickman S.L., Cross J.B., Hakes C.L., Bui D.T. "Evaluation of oxygen interactions with materials III – mission and induced environments" Long Duration Exposure Flight (LDEF) Symposium, Williamsburg, VA, 1993

[31] Kratz F., Ringel G., Schmitt D.-R. "Material science investigations of superpolished surfaces after exposure in space aboard the SESAM monitors mounted on the ASTRO-SPAS satellite [Surface Effects Sample Monitor]" Deutsche Forschungsanstalt fuer Luft und Raumfahrt (DLR-Forschungsbericht 97-01), 1997

[32] Zimcik D.G. "Advanced composite materials exposure to space experiment (ACOMEX) on STS 41-G" Canadian Aeronautics and Space Journal, **31**, pp. 249-255, 1985

[33] Visentine J.T. "Atomic oxygen effects measurements for Shuttle missions STS-8 and STS-41G" NASA TM-100459, **1**, 1998

[34] Zimcik D.G. "Materials Exposure in Low Earth Orbit (MELEO) experiment" Protection of Materials and Surface Finishes from the Low Earth Orbit Space Environment Forum, Toronto, SEE N93-20810 07-25, p. 18, 1992

[35] Ferguson D.C., Hillard G.B. "Preliminary results from the flight of the Solar Array Module Plasma Interactions Experiment (SAMPIE)" Proc. 13th Space Photovoltaic Research and Technology Conference (SPRAT 13), SEE N95-20502 06-33, pp. 247-256

[36] Warren J., Zook H., Alton J.H., Clanton U.S., Dardano C.B., Holder J.A., Marlow R.R., Schultz R.A., Watts L.A., Wenworth S.J. "The detection and observation of meteoroid and space debris impact features on the Solar Max satellite" Proc. 19th Lunar and Planetary Science Conference, **1**, pp. 641-657, 1989

[37] McKay D.S. "Microparticle impacts in space: results from Solar Max satellite and Shuttle witness plate inspections" NASA/SDIO Space Environment Effects and Materials Workshop, NASA CP-3035, Pt. 1, pp. 301-316, 1989

[38] Hamacher H., Richter H.E. "German space experiments on Spacelab D-2 and EURECA-1 to investigate atomic oxygen interaction with materials" 5th European Symposium on Materials in a Space Environment, pp. 323-330, 1991

[39] Eesbeek M.v., Froggatt M., Gourmelon G., Rieck U., Kersting H., Schwartz B., Rosik H.J. "Post-flight material investigation of EURECA: preliminary findings and recommendations" EURECA – The European Retrievable Carrier, ESA WPP-069, pp. 513-527, 1994

[40] "LDEF – 69 months in space (First post-retrieval symposium)" Proceedings of a symposium held in Kissimmee, Florida, June 1991, NASA Conference Publication 3134

[41] de Groh K.K., Banks B.A., Hammerstrom A.M., Youngstrom E.E., Kaminski C., Marx L.M., Fine E.S., Gummow J.D., Wright D. "MISSE PEACE polymers: an International Space Station environmental exposure experiment" Conf. and Exhibit on International Space Station Utilization-2001, NASA/TM-2001-211311, AIAA-2001-4923

[42] Dever J., Miller S., Messer R., Sechkar E., Tollis G. "Exposure of polymer film thermal control materials on the Materials International Space Station Experiment (MISSE)" Conf. and Exhibit on International Space Station Utilization-2001, NASA/TM-2002-211363, AIAA-2001-4924

[43] Kitazawa Y., Fukasawa K., Kawachi K., Yamaura Y., Miyadera T., Nakamura R., Imagawa K., Kamakura C., Nakayama Y., Yoshiaki T. "MPAC – passive measurement experiment of dust particles on ISS" International Symposium on Space Technology and Science, Morioka, Japan, pp. 2077-2082, 2000

[44] Fumikazu I., Imagawa K. "NASDA's space environment exposure experiment on ISS – first retrieval of SM/MPAC&SEED" Proc. 9th International Symposium on Materials in a Space Environment, Noordwijk, The Netherlands, ESA SP-540, pp. 589-594, 2003

[45] Soares C.E., Mikatarian R.R., Schmidl D., Finckenor M., Neish M., Imagawa K., Dinguirard M., Eesbeek M.v., Naumov S.F., Krylov A.N., Mishina L.V., Gerasimov Y.I., Sokolova S.P., Kurilyonok A.O., Alexandrov N.G., Smirnova T.N. "Overview of International Space Station orbital environments exposure flight experiments" Proc. SPIE, **5526**, pp. 1-14, 2004

[46] Roussel J.-F., Alet I., Faye D., Pereira A. "Effect of space environment on spacecraft surfaces in sun-synchronous orbits" J. Spacecr. & Rockets, **41**/5, pp. 812-820, 2004

[47] Harris I.L., Chambers A.R., Roberts G.T. "A low cost microsatellite instrument for the in situ measurement of orbital atomic oxygen effects" Review of Scientific Instruments, **68**/8, pp. 3220-3228, 1997

[48] Harris I.L., Chambers A.R., Roberts G.T. "Results from the Space Technology Research Vehicle 1a atomic oxygen experiment" J. Spacecr. & Rockets, **35**/5, pp. 647-652, 1998

[49] Osborne J.J., Roberts G.T., Chambers A.R., Gabriel S.B. "Initial results from ground-based testing of an atomic oxygen sensor designed for use in earth orbit" Rev. of Scientific Instruments, **70**/5, pp. 2500-2506, 1999

[50] "Space Active Modular Material Experiments (SAMMES) Technical Requirements Document" Physical Sciences, Inc., PSI-TR-1130, Andover, MA, 1994

[51] Joshi P.B., Malonson M.R., Green B.D., McKay J., Brinza D., Arnold G. "Spacecraft environment and effects monitoring instrumentation for small satellites" J. Spacecr. & Rockets, **35**/6, pp. 821-829, 1998

[52] Uy O.M., Benson R.C., Erlandson R.E., Boies M.T., Lesho J.F., Galica G.E., Green B.D., Wood B.E., Hall D.F. "Contamination experiments in the Midcourse Space Experiment" J. Spacecr. & Rockets, **34**/2, pp. 218-225, 1997

[53] Mill J.D., O'Neil R.R., Price S., Romick G.J., Uy O.M., Gaposchkin E.M., Light G.C., Moore W.W., Murdock T.L., Stair A.T. "Midcourse Space Experiment: introduction to the spacecraft, instruments and scientific objectives" J. Spacecr. & Rockets, **31**/5, pp. 900-907, 1994

[54] de Groh K.K., Banks B.A., Sechkar E.A., Scheiman D.A. "Simulated solar flare x-ray and thermal cycling durability evaluation of Hubble Space Telescope thermal control candidate replacement materials" Proc. International Conference on Protection of Materials from the Space Environment (ICPMSE) 4 (1998), Kluwer Acad. Pub., pp. 253-279, 2001

[55] Brinza D.E., Liang R.T., Stiegman A.E. "VUV-induced degradation of FEP Teflon aboard LDEF" LDEF – 69 Months in Space: Proc. 1st LDEF Post-Retrieval Symposium, NASA CP-3134, 1991

[56] Reed R.P., Schramm R.E., Clark A.F. "Mechanical, thermal, and electrical properties of selected polymers (Mechanical, thermal and electrical properties of polymers as functions of temperature, radiation and frequency for cryogenic environment material and design selection)" Cryogenics, **13**, pp. 67-82, 1973

[57] Dever J.A. "Low Earth orbital atomic oxygen and ultraviolet radiation effects on polymers" NASA TM-103711, 1991

[58] Stewart T.B., Arnold G.S., Hall D.F., Martin M.D. "Absolute rates of vacuum ultraviolet photochemical deposition of organic films" J. Physical Chemistry, **93**/6, p. 2392, 1989

[59] Stewart T.B., Arnold G.S., Hall D.F., Marvin D.C., Hwang W.C., Chandler R.D., Martin H.D. "Photochemical spacecraft self-contamination – laboratory results and system impacts" J. Spacecr. & Rockets, **26**/5, p. 358, 1989

[60] Weihs B., Eesbeek M.v. "Secondary VUV erosion effects on polymers in the ATOX atomic oxygen exposure facility" Proc. 6th International Symposium on Materials in the Space Environment (ISMSE-6), ESA SP-368, pp. 227-283, 1994

[61] Grossman E., Noter Y., Lifshitz Y. "Oxygen and VUV irradiation of polymers: Atomic Force Microscopy (AFM) and complementary studies" Proc. 7th International Symposium on Material in the Space Environment (ISMSE-7), Noordwijk, The Netherlands, pp. 217-223, 1997

[62] Dever J., Messer R., Powers C., Townsend J., Wooldridge E. "Effects of vacuum ultraviolet radiation on thin polyimide films" Proc. 8th International Symposium on Materials in the Space Environment (ISMSE-8) / 5th International Conference on Protection of Materials in the Space Environment (ICPMSE-5), CNES, 2000

[63] Coffey T., Urquhart S.G., Ade H. "Characterisation of the effects of soft x-ray irradiation on polymers" J. Electron Spectroscopy and Related Phenomena, **122**, pp. 65-78, 2002

[64] Milintchouk A., van Eesbeek M., Levadou F. "Soft x-ray radiation as a factor in the degradation of spacecraft materials" 3rd International Space Conference, Toronto, Canada, 1996

[65] Milintchouk A., Van Eesbeek M., Levadou F., Harper T. "Influence of X-ray solar flare radiation on degradation of Teflon in space" J. Spacecraft & Rockets, **34**/4, pp. 542-548, 1997

[66] Milintchouk A., Holmes-Siedle A., Van Eesbeek M., Levadou F. "Degradation of materials under the action of soft X-ray radiation from solar flares" Proceedings of the International Symposium on Materials in the Space Environment 7 (ISMSE-7), Toulouse, France, pp. 87-96, 1997

[67] Banks B.A., de Groh K.K., Stueber T.J., Sechkar E.A. "Ground laboratory soft X-ray durability evaluation of aluminized Teflon FEP thermal control insulation" Sci. Adv. Mat. & Process Eng. Series, **43**, 1998

[68] Dever J.A., Townsend J.A., Gaier J.R., Jalics A.I. "Synchrotron VUV and soft X-ray radiation effects on aluminized Teflon FEP" Sci. Adv.Mat. & Process Eng. Ser., **43**, 1998

[69] Reddy M.R.R. "Review: effect of low earth orbit atomic oxygen on spacecraft materials" J. Materials Science, **30**/2, pp. 281-307, 1995

[70] Koontz S., Leger L., Albyn K., Cross J. "Vacuum ultraviolet radiation/atomic oxygen synergism in materials reactivity" J. Spacecraft and Rockets, **27**, pp. 346-348, 1990

[71] Tagawa M., Yokota K., Ohmae N. "Synergistic study on atomic oxygen-induced erosion of polyethylene with vacuum ultraviolet" J. Spacecraft & Rockets, **41**/3, pp. 345-349, 2004

[72] Skurat V.E., Barbashev E.A., Budashov I.A., Dorofeev Y/I., Nikiforov A.P., Ternovoy A.I., van Eesbeek M., Levadou F. "The separate and combined effects of VUV radiation and fast atomic oxygen on Teflon FEP and silicon carbide" Proc. 7th International Symposium on Materials in the Space Environment (ISMSE-7), Noordwijk, The Netherlands, pp. 267-279, 1997

[73] Verkhovtseva E.T., Yaremenko V.I., Telepnev V.D., Lura F. "Gas-jet simulator of solar VUV and soft X-ray radiation and irradiation effect on some material" International Symposium on Materials in Space Environment 7 (ISMSE-7), Toulouse, France, pp. 119-124, 1997

[74] Dever J.A., Pietromica A.J., Stueber T.J., Sechkar E.A., Messer R.K. "Simulated space vacuum ultraviolet (VUV) exposure testing for polymer films" 39th Aerospace Science Meeting and Exhibit, Reno, Nevada, NASA/TM-2002-211337, AIAA-2001-1054, 2002

[75] Russell D.A., Connell J.W., Fogdall L.B. "Electron, proton, and ultraviolet radiation effects on thermophysical properties of polymeric films" J. Spacecr. & Rockets, **39**/6, pp. 833-838, 2002

[76] Li C., Yang D., He S., Yang S. "Degradation of Teflon film under radiation of protons and electrons" J. Spacecr. & Rockets, **41**/3, pp. 373-376, 2004

[77] Rottman G.J., Woods T.N., McClintock W. "SORCE Solar UV Irradiance Results" Adv. Space Res., **37**/2, pp. 201-208, 2006

[78] Vernazza J.E., Avrett E.H., Loeser R., Astrophys. J., Suppl. **45**, p. 635, 1981

[79] Floyd L.E., Reiser P.A., Crane P.C., Herring L.C., Prinz D.K., Brueckner G.E. "Solar Cycle 22 UV Spectral Irradiance Variability: Current Measurements by SUSIM UARS" Solar Physics, **177**, pp. 79-87, 1998

[80] Minsignori Fossi B.C., Poletto G., Tagliaferri G.L. "An outstanding Lyman-alpha event" Solar Physics, **10**/1, pp. 196-197, 1969

[81] Nusinov A.A., Kazachevskaya T.V., Katyushina V.V., Svidskii P.M., Tsigel'nitskii Y.N., Gonyukh D.A., Afanas'ev A.N., Boldyrev S.I., Lisin D.V., Stepanov A.I. "Measurements of extreme ultraviolet solar radiation in different wavelength intervals onboard the CORONAS satellites: instruments and main results" Solar System Res., **39**/6, pp. 470-478, 2005; Translated from Astronomicheskii Vestnik, **39**/6, pp. 527-536, 2005

[82] Nusinov A.A., Kazachevskaya T.V. "Variations of ultraviolet radiation during large solar flares from CORONAS-F spacecraft observations" Geomagn. Aeron., **45**/3, pp. 398-402, 2005

[83] Martini L., Bischoff K.G.., Pfau G., Stark B., Ulrich Z. "Sharp dips in the flux of the solar Lyman-α line during the flares of August 4, 7, and 11, 1972" Cosmic Res. (USSR) (Engl. Transl.), **12**/5, pp. 670-672; translated from Kosmicheskie Issledovaniia, **12**/5, pp. 736-739, 1974

[84] Kazachevskaya T.V., Avdushin S.I., Gonukh D.A., Lomovsky A.I., Nusinov A.A., Svidsky P.M., Tsigelnitsky Y.N., Oraevsky V.N., Kopaev I.M., Boldirev S.I. "Solar Flux and Spectrum Measurements in the EUV Spectral Region on board CORONAS-I Satellite" Solar Physics, **177**, pp. 175-180, 1998

[85] Bailey S.M., Woods T.N., Eparvier F.G., Solomon S.C. "Observations of the solar soft X-ray irradiance by the student nitric oxide explorer" Adv. Space Res., **37**, pp. 209-218, 2006

[86] Muñoz E., Monroy E., Pau J.L., Calle F., Omnès F., Gibart P. J. "III Nitrides and UV Detection" Phys.: Condens. Matter, **13**, p. 7115, 2001

[87] Razeghi M., Rogalsky A. "Semiconductor ultraviolet detectors" J. Appl. Phys., **79**, 7433-7473, 1996

[88] Hochedez J.-F., Bergonzo P., Castex M.-C., Dhez P., Hainaut O., Sacchi M., Alvarez J., Boyer H., Deneuville A., Gibart P., Guizard B., Kleider J.-P., Lemaire P., Mer C., Monroy E., Muñoz E., Muret P., Omnès F., Pau J.L., Ralchenko V., Tromson D., Verwichte E., Vial J.-C. "Diamond UV Detectors for Future Solar Physics Mission" Diamond and Related Materials **10**/3-7, p. 669, 2001

[89] Monroy E., Calle F., Pau J.L., Muñoz E, Omnès F, Beaumont B., Gibart P. "AlGaN-based UV photodetectors" J. Crystal Growth, **230**, p. 537, 2001

[90] Eds.: Edgar J.H., Strite S., Akasaki I., Amano H., Wetzel C. "Properties, Processing and Applications of Gallium Nitride and Related Semiconductors" EMIS Datareviews Series No. 23, INSPEC, London, p. 634, 1999

[91] Muñoz E., Monroy E., Calle F., Omnès F, Gibart P. Modified from "AlGaN photodiodes for monitoring solar UV radiation" J. of Geo. Res., **105**/D4, p. 4865, 2000

[92] Schreiber P., Dang T., Smith G., Pickenpaugh T., Gehred P., Litton C. "Solar-blind UV region and UV detector development objectives" Proc. SPIE, **3629**, pp. 230-248, 1999

[93] Ulmer M.P., Razeghi M., Bigan, E. "Ultraviolet detectors for astrophysics: present and future" Proc. SPIE, **2397**, pp. 210-217, 1995

[94] Razeghi M., Rogalski A. "Semiconductor ultraviolet detectors" J. Appl. Phys., **79**, pp. 7433-7473, 1996

[95] Pearton S.J., Zolper J.C., Shul R.J., Ren F. "GaN: processing, defects, and devices" J. Appl. Phys, **86**, pp. 1-78, 1999

[96] Dang X.Z., Welty R.J., Qiao D., Asbeck P.M., Lau S.S., Yu E.T., Boutrous K.S., Redwing J.M. "Fabrication and characterisation of enhanced barrier AlGaN/GaN HFET" Electron. Lett., **35**, p. 602, 1999

[97] Walker D., Kumar V., Mi K., Sandvik P., Kung P., Zhang X.H., Razeghi M. "Solar-blind AlGaN photodiodes with very low cutoff wavelength" App. Phys. Lett., **76**/4, p. 403, 2000

[98] Hanzaz M., Bouhdada A., Gibart P., Omnès F. "Impact of the defects on the electrical and optical properties of AlGaN ultraviolet photodetectors" J. of Ap. Phys. **92**/1, pp. 13-18, 2002

[99] Shiojima K., Woodall J.M., Eiting C.J., Grudowski P.A., Dupuis R.D. "Effect of defect density on the electrical characteristics of n-type GaN Schottky contacts" J. Vac. Sci. Technology B, **17**/5, pp. 2030-2033, 1999

[100] Wang C.W., Liao J.Y., Chen C.L., Lin W.K., Su Y.K., Yokoyama M. "Effect of rapid thermal annealing on radio-frequency magnetron-sputtered GaN thin films and Au/GaN Schottky diodes" J. Vac. Sci. Technol. B, **17**, pp. 1545-1548, 1999

[101] Tomiya S., Funato K., Asatsuma T., Hino T., Kijima S., Asano T., Ikeda M. "Dependence of crystallographic tilt and defect distribution on mask material in epitaxial lateral overgrown GaN layers" Appl. Phys. Lett., **77**/5, pp. 636-638, 2000

[102] Tan L.S., Prakesh S., Ng K.M., Raman A., Chua S.J., Wee A.T.S., Lim S.L. "Formation of Ti/Al ohmic contacts on Si-doped GaN epilayers by low temperature annealing" Semicond. Sci. Technol., **15**, pp. 585-588, 2000

[103] Monroy E., Calle F., Pau J.L., Sánchez F.J., Muñoz E., Omnès F., Beaumont B., Gibart P. "Analysis and modelling of $Al_xGa_{1-x}N$-based Schottky barrier photodiodes" J. Appl. Phys., **88**/4, pp. 2081-2091, 2000

[104] Lim B.W., Gangopadhyay S., Yang J.W., Osinsky A., Chen Q., Anwar M.Z., Khan M.A. "8x8 GaN Schottky barrier photodiode array for visible-blind imaging" Electron. Lett., **33**/7, p. 633, 1997

[105] Brown J.D., Matthews J., Harney S., Boney J., Schetzina J.F., Benson J.D., Dang K.V., Nohava T., Yang W., Krishnankutty S. "High-Sensitivity Visible-Blind AlGaN Photodiodes and Photodiode Arrays" MRS Internet J. Nitride Semicond. Res., **5S1**, p. W1.9, 2000

[106] Brown J.D., Boney J., Matthews J., Srinivasan P., Schetzina J.F., Nohave T., Yang W., Krishnankutty S. "UV-Specific (320-365nm) Digital Camera Based on a 128x128 Focal Plane Array of GaN/AlGaN p-i-n Photodiodes" MRS Internet J. Nitride Semiconductor Res., **5**, p. 6, 2000

[107] Ambacher O., Arzberger M., Brunner D., Angerer H., Freudenberg F., Esser N., Wethkamp T., Wilmers K., Richter W., Stutzmann M. "AlGaN-Based Bragg Reflectors" MRS Internet J. Nitride Semiconductor Res., **2**, p. 22, 1997

[108] Monroy E., Omnès F., Calle F. "Wide-bandgap semiconductor ultraviolet detectors" Semicond. Sci. Technol., **18**, pp. R33-R51, 2003

[109] BOLD home page at: http://bold.oma.be/index.php3, contact Jean-Francois Hochedez (hochedez@oma.be)

[110] Hochedez J.-F., Alvarez J., Auret F.D., Bergonzo P., Castex M.-C., Deneuville A., Defise J.M., Fleck B., Gibart P., Goodman S.A., Hainaut O., Kleider J.-P., Lemaire P., Manca J., Monroy E., Muñoz E., Muret P., Nesladek M., Omnes F., Pace E., Pau J.L., Ralchenko V., Roggen J., Schühle U., Van Hoof C. "Recent progresses of the BOLD investigation towards UV detectors for the ESA Solar Orbiter" Diamond and Related Materials, **11**, p. 427, 2002

[111] Solar Orbiter information at: www.esa.int/science/solarorbiter

[112] Solar Probe information at: solarprobe.gsfc.nasa.gov

[113] Klein R., Krumrey M., Richter M., Scholze F., Thornagel R., Ulm G. "Radiometry with synchrotron radiation at the PTB Laboratory at BESSY II" Synchrotron Radiation News, **15**, pp. 23-29, 2002

[114] Ulm G., Wende B. "Radiometry laboratory of Physikalisch-Technische Bundesanstalt at BESSY" Rev. Sci. Instrum., **66**, pp. 2244-2247, 1995

[115] Richter M., Thornagel R., Ulm G. "UV and VUV radiometry at PTB for the calibration of space-based instruments" 4th (Virtual) Thermospheric/Ionospheric Geospheric Research (TIGER) Symposium

[116] "L2D2 Lamps – Deuterium Lamps" Catalogue of Hamamatsu Photonics K.K., Iwata-city, Japan. Also viewable at: http://www.hamamatsu.com

[117] Heltzel S. "Analysis of Simulated Solar Radiation Conditions and its Effects on Coating Materials, used for Thermal Control of Spacecrafts" TOS/QMC Report: 2000/059, ESTEC, 2000

[118] "Operating Manual for the Dual Anode X-ray Sources System", Issue 1, FISONS Instruments, VG Microtech, Uckfield, Sussex

[119] Veronig A.M., Temmer M., Hanslmeier A. "The solar soft X-ray background flux and its relation to flare occurrence" Solar Phys., **219**, p. 125, 2004

[120] Kanaya K., Okayama S. J. "Penetration and energy-loss theory of electrons in solid targets" Phys. D: Appl. Phys., **5**, p. 43-58, 1972

[121] Love G., Scott V.D. "Evaluation of a new correction procedure for quantitative electron probe microanalysis" J. Phys. D: Appl. Phys., **11**, pp. 1369-1376, 1978

[122] Joy D. "A Database of Electron-Solid Interactions" SCANNING, **17**/5, p. 270, 1995 also available at http://web.utk.edu/~srcutk/htm/interact.htm

[123] Image adapted from: Grigis, P.C., Benz A.O. "The spectral evolution of impulsive solar X-ray flares" Astronomy & Astrophysics, **426**/3, pp. 1093-1102, 2004

[124] For a detailed description of the detectors used for the transfer standard see: Kuschnerus, P., Rabus H., Richter M., Scholze F., Werner L., Ulm G. "Characterization of photodiodes as transfer detector standards in the 120nm to 600nm spectral range" Metrologia, **35**/4, pp. 355-362, 1998

[125] Rabus H., Persch V., Ulm G. "Synchrotron-radiation operated cryogenic electrical-substitution radiometer as high-accuracy primary detector standard in the ultraviolet, vacuum ultraviolet and soft X-ray spectral ranges" Appl. Opt., **36**/22, pp. 5421-5440, 1997

[126] Woods T.N., Eparvier F.G., Woodraska D., Rottman G.J., Solomon S.C., Roble R., de Toma G., Lean J., Tobiska W.K., Bailey S.M. "Early results from the TIMED solar EUV experiment SEE" 4th (Virtual) Thermospheric/Ionospheric Geospheric Research (TIGER) Symposium, American Geophysical Union, 2002

[127] http://ssbuv.gsfc.nasa.gov/solar.html#Sec3

[128] ASTM E490-00a(2006) "Standard Solar Constant and Zero Air Mass Solar Spectral irradiance Tables" ASTM International. Available at 'www.astm.org'.

[129] Haberreiter M., Krivova N.A., Schmutz W., Wenzler T. "Reconstruction of the solar UV irradiance back to 1974" Advances in Space Research, **35**, pp. 365-369, 2005

[130] Tobiska W.K., Pryor W.R., Ajello J.M. "Solar hydrogen Lyman-α variation during solar cycles 21 and 22" Geophysical Research Letters, **24**, p. 1123, 1997

[131] Lean J. "The Sun's Variable Radiation and its Relevance for Earth" Annu. Rev. Astron. Astrophys., **35**, pp. 33-67, 1997

[132] Shan W., Ager III J.W., Yu K.M., Walukiewicz W., Haller E.E., Martin M.C., McKinney W.R., Yang W. "Dependence of the fundamental band gap of $Al_xGa_{1-x}N$ on alloy composition and pressure" Journal of Applied Physics, **85**/12, pp. 8505-8507,1999

[133] "Photodiodes" Hamamatsu Photonics K.K., Solid State Division, Catalogue no. KPD0001E07, p. 33, 1998

[134] "Space Station Ionizing Radiation Environment" SSP 30512, Revision C, NASA, 1994

[135] Tribble A.C. "The Space Environment: Implications for Spacecraft Design" Princeton University Press, pp. 206-208, 2003

[136] Ed.: Davies M. "The Standard Handbook for Aeronautical and Astronautical Engineering" McGraw-Hill Companies Inc., p. 16.83, 2003

[137] ibid. p. 16.84

[138] Boldt E., Eds.: McDonald F.B., Fichtel C.E. "High Energy Particles and Quanta in Astrophysics" Cambridge MIT Press, pp. 368-382, 1974

[139] Burrows J.P., Weber M., Buchwitz M., Rozanov V., Ladstätter-Weißenmayer A., Richter A., DeBeek R., Hoogen R., Bramstedt K., Eichmann K.-U., Eisinger M. "The Global Ozone Monitoring Experiment (GOME): Mission Concept and First Scientific Results" J. Atmos. Sci., **56**, pp. 151-175, 1999

[140] Readinger E.D., Mohney S.E. "Environmental Sensitivity of Au Diodes on n-AlGaN" Journal of Electronic Materials, **34**/4, pp. 375-381, 2005

[141] Jang H.W., Baik J.M., Lee M.-K., Shin H.-J., Lee J.-L. "Incorporation of oxygen donors in AlGaN" J. Electrochem. Soc., **151**/8, pp. G536-G540, 2004

[142] Shimamura H., Yamagata I., Suzuki M. "Degradation of Tension-Loaded Polyimide Films in a Space Environment: Results of the Sm/Mpac&Seed Mission" 10th International Symposium on 'Materials in a Space Environment'/8th International Conference on 'Protection of Materials and Structures in a Space Environment', Collioure, 2006 (in print)

[143] Miyazaki E., Yamagata I., Suzuki M. "Results of the Space-Environment Exposure Experiment 'SM/MPAC&SEED' on the International Space Station:(1) Flexible Optical Solar Reflector" 10th International Symposium on 'Materials in a Space Environment'/8th International Conference on 'Protection of Materials and Structures in a Space Environment', Collioure, 2006 (in print)

[144] Rampini R., Grizzaffi L., Lobascio C. "Outgassing kinetics testing of spacecraft materials" Materialwissenschaft und Werkstofftechnik, **34**/4, pp. 359-364, 2003

[145] Minoshima K., Maekawa Y., Komai K. "The Influence of vacuum on fracture and fatigue behaviour in a single aramid fiber" International Journal of Fatigue, **22**/9, pp. 757-765, 2000

[146] "Introductory Guidebook for JEM Exposed Facility Potential Users" JEM-EF experiment payload staff, Space Utilization Engineering Department, Tsukuba Space Centre, NASDA, 1996 (available at: http://idb.exst.jaxa.jp/edata/02110/199810K02110010/199810K02110010.html)

[147] Hochedez J.-F., Schmutz W., Stockman Y., Schühle U., BenMoussa A., Koller S., Haenen K., Berghmans D., Defise J.-M., Halain J.-P., Theissen A., Delouille V., Slemzin V., Gillotay D., Fussen D., Dominique M., Vanhellemont F., McMullin D., Kretzschmar M., Mitrofanov A., Nicula B., Wauters L., Roth H., Rozanov E., Rüedi I., Wehrli C., Soltani A., Amano H., Van der Linden R., Zhukov A., Clette F., Koizumi S., Mortet V., Remes Z., Petersen R., Nesládek M., D'Olieslaeger M., Roggen J., Rochus P. "LYRA, a solar UV radiometer on Proba2" Adv. Space Res., **37**, pp. 303-312, 2006, doi:10.1016/j.asr.2005.10.041

[148] Wilhelm K. "Past and recent observations of the solar upper atmosphere at vacuum-ultraviolet wavelengths" J. Atmospheric & Solar-Terrestrial Physics, **65**/2, pp. 167-189, 2003

[149] Baumann R.C. "The Ariel I Satellite" Proc. Royal Soc. London A, **281**/1387, pp.439-445, 1964

[150] "Orbiting Solar Observatory Satellite" NASA SP-57, 1965

[151] Kreplin R.W., Space Res., **5**, p. 951, 1964

[152] Landini M., Russo D., Tagliaferri G.L. "Solar x-ray flux measured by the 1964-01-D solar radiation satellite during the IQSY" Adv. Space Sci., **15**/2, pp. 231-237, 1967

[153] Jackson J.E., Vette J.I. "OGO Program Summary" NASA SP-7601, 1975 Available at: http://ntrs.nasa.gov/archive/nasa/casi.ntrs.nasa.gov/19760012555_1976012555.pdf

[154] Landini M. et al., Space Res. VII, **2**, p. 1281, 1967

[155] Landini M., Russo D., Tagliaferri G.L. "Atmospheric density measured by the attenuation of solar x-rays monitored on the NRL 1965-16-D satellite" Icarus, **6**, pp. 236-241, 1967

[156] Van Allen, Ness J., J. Geophys. Res., **72**, p. 935, 1967

[157] Kreplin R.W., Horan D.M., Chubb T.A., Friedman H. "Measurements of solar X-ray emission from the OGO 4 spacecraft" Solar Flares and Space Research, pp. 121-130, North Holland Publ. Co., Amsterdam, The Netherlands, 1969

[158] Hudson H.S., Peterson L.E., Schwartz D.A. "Solar and cosmic x-rays above 7.7keV" Solar Phys., **6**, pp. 205-215, 1969

[159] Neupert W.M., White W.A., Gates W.J., Swartz M., Young R.M. "X-ray and extreme ultraviolet (1-400Å) spectroscopy of the sun, from OSO-III" Solar Phy., **6**, pp. 183-192, 1969

[160] Teske R.G. "Observation of the solar soft x-ray component; study of its relation to transient and slowly-varying phenomena observed at other wavelengths" Solar Phys., **6**, pp. 193-204, 1969

[161] Culhane J.L., Sanford P.W., Willmore A.P., Blades J., Nettleship R., IEEE Trans. Nucl. Sci., **NS-14**, p. 38, 1967

[162] Culhane J.L., Phillips K.J.H. "Solar x-ray bursts at energies less than 10keV observed with OSO-4" Solar Phys., **11**, pp. 117-144, 1970

[163] Reeves E.M., Parkinson W.H. "Calibration changes in EUV solar satellite instruments" App. Opt., **9**/5, pp. 1201-1208, 1970

[164] Reeves E.M., Parkinson W.H. "Atlas of extreme ultraviolet spectroheliograms from OSO-IV" Astrophysical Journal Supplementary Series, **21**/181, p. 1, 1970

[165] Meekins J.F., Kreplin R.W., Chubb T.A., Friedman H. "X-ray line and continuum spectra of solar flares from 0.5 to 8.5 angstroms" Science, **162**/3856, pp. 891-895, 1968

[166] Kahler S.W., Meekins J.F., Kreplin R.W., Bowyer C.S. "Temperature and emission-measure profiles of two solar x-ray flares" Astrophysical Journal, **162**, pp. 293-304, 1970

[167] Anderson K.A. "Energetic radiations from solar flares" Final Report, University of California, Berkely, 1971, (TRF B14923)

[168] Kreplin R.W., Horan D.M. "The NRL SOLRAD 9 Satellite Solar Explorer B 1968-17A" NRL Report 6800, 1969

[169] "The Nimbus III User's Guide" TRF B03409

[170] Kelly P.T., Rense W.A. "Solar flares in the EUV observed by OSO-5" Solar Phys., **26**/2, pp. 431-440, 1972

[171] Neupert W.M., Swartz M., Kastner S.O. "Solar flare line emission between 6Å and 25Å"Solar Phys., **31**/1, pp. 171-195, 1973

[172] Vidal-Madjar A., Blamont J.E., Phissamay B. "Solar Lyman alpha changes and related hydrogen density distribution at the Earth's exobase (1969-1970)" J. Geophys. Res., **78**/7, pp. 1115-1144, 1973

[173] Kreplin R.W., Taylor R.G. "Localization of the source of flare X-ray emission during the eclipse of 7 March, 1970" Solar Phys., **21**/2, pp. 452-459, 1971

[174] Doschek G.A., Meekins J.F., Kreplin R.W., Chubb T.A., Friedman H. "Heliumlike calcium emission observed during a solar flare" Astrophysical Journal, **164**, p. 165, 1971

[175] Doschek G.A., Meekins J.F., Cowan R.D. "Further iron-line observations during solar flares" Astrophysical Journal, **177**, p. 261, 1972

[176] Doschek G.A., Meekins J.F., Cowan R.D. "Spectra of solar flares from 8.5Å to 16Å" Solar Phys., **29**/1, pp. 125-141, 1973

[177] Doschek G.A., Meekins J.F., Kreplin R.W., Chubb T.A., Friedman H. "Heliumlike Calcium emission observed during a solar flare" Astrophysical Journal, **164**, pp. 165-180, 1971

[178] Woodgate B.E., Knight D.E., Uribe R., Sheather P., Bowles J., Nettleship R. "Extreme ultraviolet line intensities from the sun" Proc. Roy. Soc. Lon. A, **332**/1590, pp. 291-309, 1973

[179] Macar P.J., Rechavi J., Huber M.C.E., Reeves E.M. "Solar-blind photoelectric detection systems for satellite applications" App. Opt., **9**/3, pp. 581-594, 1970

[180] Watts R.N. "Another successful OSO" Sky and Teles., **38**, p. 230, 1969

[181] Tindo I.P., Mandel'stam S.L., Shuryghin A.I. "Further polarization measurements of the solar flare X-ray emission" Solar Phys., **32**/2, pp. 469-475, 1973

[182] Harrington T.M., Maloy J.O., McKenzie D.L., Peterson L.E. "Design of the solar X-ray instrument for OSO-H" IEEE Trans. Nucl. Sci., **NS-19**, p. 596, 1972

[183] Datlowe D.W., Hudson H.S., Peterson L.E. "Observations of solar x-ray bursts in the energy range 5-15keV" Solar Phys., **35**, p. 193, 1974

[184] Naval Res. Review, **25**, p. 1, 1971

[185] Dalgarno A., Hanson W.B., Spencer N.W., Schmerling E.R. "The Atmosphere Explorer Mission (Atmosphere Explorer mission of lower thermosphere and ionosphere physics investigation, discussing orbit selection)" Radio Sci., **8**/4, pp.263-266, 1973

[186] Heath D.F., Osantowski J.F. "An Extreme UV photometer for solar observations from Atmosphere Explorer" Radio Sci., **8**/4, pp.361-367, 1973

[187] Hinteregger H.E., Bedo D.E., Manson J.E. "The EUV spectrophotometer on Atmosphere Explorer (EUV spectrophotometer onboard Atmosphere Explorer satellites, discussing design, aeronomical mission objectives, constraints and economic factors)" Radio Sci., **8**/4, pp.349-359, 1973

[188] Stilwell D.E., Joyce R.M., Teegarden B.J., Trainor J.H., Streeter G., Bernstein J. "The Pioneer 10/11 and Helios A/B cosmic ray instruments" IEEE Trans. On Nuc. Sci., **NS-22**, pp. 570-574, 1975

[189] Trainor J.H., Stilwell D.E., Joyce R.M., Teegarden B.J., White H.O. "The Helios A/B cosmic ray instrument E7" Raumfahrtforschung, **19**/5, pp. 258-260, 1975

[190] Matsuoka M., Nagai F., Ohki K. "A solar x-ray detector aboard 'Taiyo'" J. Geomag. Geoelectr., **27**/4, 271-278, 1975

[191] Oshio T., Masuoka T., Higashino I., Watanabe N. "An intensity monitor for solar hydrogen lyman-α radiation" J. Geomag. Geoelectr., **27**/4, 271-278, 1975

[192] Hirao K. "The Taiyo Mission" J. Geomag. Geoelectr., **27**/4, 265-270, 1975

[193] Valnicek B., Farnik F., Komarek B., Likin O., Pisarenko N. "Long-term measurements of solar x-rays on board the satellites Prognoz 5 and Prognoz 6" Bull. Astron. Inst. Czech., **30**, 171-173, 1979

[194] Fischer S. "Intershock Project: Science objectives, mission overview, instrumentation and data processing" Pub. No. 60 of the Astronomical Inst. Of the Czechoslovak Academy of Sciences, 351, 1985

[195] Sagdeev R.Z., Balebanov V.M., Zakharov A.V. "The Phobos project: Scientific objectives and experimental methods" Sov. Sci. Rev. E: Astrophys. Space Phys., **6**/1, pp. 1-60, 1988

[196] Wenzel K.-P., Marsden R.G., Page D.E., Smith E.J. "The Ulysses Mission" Astron. Astrophys. Suppl. Ser., **92**/2, pp. 207-219, 1992

[197] Thuillier G., Hersé M., Simon P.C., Labs D., Mandel H., Gillotay D. "Observation of the UV Solar Spectrum Irradiance Between 200 and 350nm During the Atlas 1 Mision by the SOLSPEC Spectrometer" Solar Physics, **171**/2, pp. 283-302, 1997

[198] Sylwester J., Farnik F., Likin O., Kordylewski Z., Siarkowski M., Nowak S., Plocieniak S., Trzebiński W. "Solar Soft/Hard X-ray Photometer-Imager aboard the INTERBALL-Tail Probe" Solar Physics, **197**/2, pp. 337-360, 2000

[199] Ed. Harrison R.A., Fludra A. "The Coronal Diagnostic Spectrometer for the Solar and Heliospheric Observatory" Scientific Report, Astrophysics Division, Rutherford Appleton Laboratories

[200] Lemaire P., Wilhelm K., Axford W.I., Curdt W., Gabriel A.H., Grewing M., Huber M.C.E., Jordan S.D., Kuehne M., Marsch E., Poland A.I., Richter A.K., Thomas R.J., Timothy J.G., Vial J.-C. "SUMER: Temperatures, densities and velocities in the outer solar atmosphere" Proceedings of the first SOHO workshop, ESA SP-348, pp. 13-16, 1992

[201] Wilhelm K., Lemaire P., Curdt W., Schühle U., Marsch E., Poland A.I., Jordan S.D., Thomas R.J., Hassler D.M., Huber M.C.E., Vial J.-C., Kühne M., Siegmund O.H.W., Gabriel A., Timothy J.G., Grewing M., Feldman U., Hollandt J., Brekke P. "First Results of the SUMER Telescope and Spectrometer on SOHO (part 1)" Solar Physics, **170**/1, pp. 75-104, 1997

[202] Kohl J.L., Noci G. "UVCS – the Ultraviolet Coronagraph Spectrometer for SOHO" Proceedings of the first SOHO workshop, ESA SP-348, pp. 23-26, 1992

[203] Zhithik I.A., Kuzin S.V., Sobel'man I.I., Bugaenko O.I., Ignat'ev A.P., Mitrofanov A.V., Oparin S.N., Pertsov A.A., Slemzin V.A., Sukhodrev N.K., Urnov A.M. "Main Results of the SPIRIT

Experiment Onboard the CORONAS-F Satellite" Solar System Research, **39**/6, pp. 442-452, 2005

[204] Hill S.M., Pizzo V.J., Balch C.C., Biesecker D.A., Bornmann P., Hildner R., Lewis L.D., Grubb R.N., Husler M.P., Prendergast K., Vickroy J., Greer S., Defoor T., Wilkinson D.C., Hooker R., Mulligan P., Chipman E., Bysal H., Douglas J.P., Reynolds R., Davis J.M., Wallace K.S., Russell K., Freestone K., Bagdigian D., Page T., Kerns S., Hoffman R., Cauffman S.A., Davis M.A., Studer R., Berthiaume F.E., Saha T.T., Berthiume G.D., Farthing H., Zimmermann F. "The NOAA GOES-12 Solar X-ray Imager (SXI) 1. Instrument, Operations and Data" Solar Physics, **226**, pp. 255-281, 2005

[205] Woods T.N., Rottman G.J., Roble R.G., White O.R., Solomon S.C., Lawrence G.M., Lean J., Tobiska W.K. "Thermosphere-Ionosphere-Mesosphere Energetics and Dynamics (TIMED) Solar EUV Experiment" Proc. SPIE, **2266**, pp. 467-478, 1994

[206] Woods T.N., Bailey S.M., Eparvier F.G., Lawrence M., Lean J., McClintock W.E., Roble R.G., Rottman G.J., Solomon S.C., Tobiska W.K., Ucker G.J., White O.R. "TIMED Solar EUV Experiment" Proc. SPIE, **3442**, pp. 180-191, 1998

[207] Zhang N., Tang H.-s., Chang J., Zhang H.-q., Gan W.-q., Gu F.-u., Shen Q.-z., Xu Y.-l., Cai M.-s., Gong Y.-z. "Preliminary Observing Achievements of Super Soft X-ray Detector and γ-ray Detector Onboard Shenzhou 2" Adv. Space Res., **32**/12, pp. 2579-2583, 2003

[208] Harder J.W., Lawrence G.M., Rottman G.J., Woods T.N. "The Spectral Irradiance Monitor (SIM) for the SORCE Mission" Proc. SPIE, **4135**, pp. 204-214, 2000

[209] Harder J., Lawrence G.M., Rottman G., Woods T. "Solar Spectral Irradiance Monitor (SIM)" Metrologia, **37**/5, pp. 415-418, 2000

[210] McClintock W.E., Rottman G.J., Woods T.N. "Solar Stellar Irradiance Comparison Experiment II (SOLSTICE II) for the NASA Earth Observing System's Solar Radiation and Climate Experiment (SORCE) Mission" Proc. SPIE, **4135**, pp. 225-234, 2000

[211] Powell F.R., Vedder P.W., Lindblom J.F., Powell S.F. "Thin film filter performance for extreme ultraviolet and X-ray applications" Opt. Eng., **26**, p. 614, 1990

[212] Garrett D.L., Tousey R. "Solar XUV grazing incidence spectrograph on Skylab" App. Opt., **16**/4, pp. 898-903, 1977

[213] Tousey R. "Apollo Telescope Mount of Skylab: an overview" App.Opt., **16**/4, pp. 825-836, 1977

[214] Reeves E.M., Huber M.C.E., Timothy J.G. "Extreme UV spectroheliometer on the Apollo Telescope Mount" App. Opt., **16**/4, pp. 837-848, 1977

[215] Underwood J.H., Milligan J.E., deLoach A.C., Hoover R.B. "S056 x-ray telescope experiment on the Skylab Apollo Telescope Mount" App. Opt., **16**/4, pp. 858-869, 1977

[216] Bartoe J.-D.F., Brueckner G.E., Purcell J.D., Tousey R. "Extreme ultraviolet spectrograph ATM experiment SO82B" App. Opt., **16**/4, pp. 879-886, 1977

[217] Bruner E.C., Chipman E.G., Lites B.W., Rottman G.J., Shine R.A., Athay R.G. "Preliminary results from the Orbiting Solar Observatory 8 – transition-zone dynamics over a sunspot" Astrophysical Journal, **210**, pp. L97-L101, 1976

[218] Mosher J.M. "The height structure of solar active regions at X-ray wavelengths as deduced from OSO-8 limb crossing observations" Solar Phys., **64**, 109-119, 1979

[219] Wolfson C.J., Acton L.W., Leibacher J.W., Roethig D.T. "Early evolution of an X-ray emitting solar active region" Solar Phys., **55**, pp. 181-193, 1977

[220] Maran S.P., Thomas R.J. "The last OSO satellite" Sky & Teles., **49**, 355-358, 1975

[221] Feldman U., Doschek G.A., Kreplin R.W. "High resolution x-ray spectra of the 1979 March 25 solar flare" Astrophysical Journal, **238**/1, pp. 365-374, 1980

[222] Woodgate B.E., Tandberg-Hanssen E.A., Bruner E.C., Beckers J.M., Brandt J.C., Henze W., Hyder C.L., Kalet M.W., Kenny P.J., Knox E.D., Michalitsianos A.G., Rehse R., Shine R.A., Tinsley H.D. "The ultraviolet spectrometer and polarimeter on the solar maximum mission" Solar Phys., **65**, pp. 73-90, 1980

[223] Miller M.S., Caruso A.J., Woodgate B.E., Sterk A.A. "Ultraviolet spectrometer and polarimeter for the solar maximum mission" App. Opt., **20**/21, pp. 3805-3814, 1981

[224] Orwig L.E., Frost K.J., Dennis B.R., "The hard x-ray burst spectrometer of the solar maximum mission" Solar Phys., **65**, pp. 25-37, 1980

[225] Forrest D.J., Chupp E.L., Ryan J.M., Cherry M.L., Gleske I.U., Reppin C., Pinkau K., Rieger E., Kanbach G., Kinzer R.L., Share G., Johnson W.N., Kurfess J.D. "The gamma ray spectrometer for the solar maximum mission" Solar Phys., **65**, pp. 15-23, 1980

[226] Van Beek H.R., Hoyng P., Lafleur B., Simnett G.M. "The hard x-ray imaging spectrometer (HXIS)" Solar Phys., **65**, pp. 39-52, 1980

[227] Acton L.W., Culhane J.L., Gabriel A.H., Bentley R.D., Bowles J.A., Firth J.G., Finch M.L., Gilbreth C.W., Guttridge P., Hayes R.W., Joki E.G., Jones B.B., Kent B.J., Leibacher J.W., Nobles R.A., Patrick T.J., Phillips K.J.H., Rapley C.G., Sheather P.H., Sherman J.C., Stark J.P., Springer L.A., Turner R.F., Wolfson C.J. "The soft x-ray polychromator for the solar maximum mission" Solar Phys., **65**, pp. 53-71, 1980

[228] Chipman E.G. "The Solar Maximum Mission" Astrophysical Journal, **244**, pp. L113-L115, 1981

[229] Bohlin J.D., Frost K.J., Burr P.T., Guha A.K., Withroe G.L. "Solar Maximum Mission" Solar Phys., **65**, pp. 5-14, 1980

[230] Reber C.A. "The Upper Atmosphere Research Satellite" Trans. Am. Geophys. Union EOS, **71**/51, 1990

[231] Longdon, N., Spaceflight, **34**, 1992

[232] Strong K.T., Bruner M., Tarbell T., Title A., Wolfson C.J. "TRACE – the Transition Region and Coronal Explorer" Space Sci. Rev., **70**, pp. 119-120, 1994

[233] Tarbell T.D., Bruner M., Jurcevich B., Lemen J., Strong K., Title A., Wolfson J., Golub L., Fisher R. "The Transition Region and Coronal Explorer (TRACE)" Proc. of the Third SOHO Workshop – Solar Dynamic Phenomena and Solar Wind Consequences, ESA SP-373, p. 375, 1994

[234] Handy B.N., Bruner M.E., Tarbell T.D., Title A.M., Wolfson C.J., Laforge M.J., Oliver J.J. "UV Observations with the Transition Region and Coronal Explorer" Solar Physics, **183**, pp. 29-43, 1998

[235] Handy B.N., Acton L.W., Kankelborg C.C., Wolfson C.J., Akin D.J., Bruner M.E., Caravalho R., Catura R.C., Chevalier R., Duncan D.W., Edwards C.G., Feinstein C.N., Freeland S.L., Friedlaender F.M., Hoffmann C.H., Hurlburt N.E., Jurcevich B.K., Katz N.L., Kelly G.A., Lemen J.R., Levay M., Lindgren R.W., Mathur D.P., Meyer S.B., Morrison S.J., Morrison M.D., Nightingale R.W., Pope T.P., Rehse R.A., Schrijver C.J., Shine R.A., Shing L., Strong K.T., Tarbell T.D., Title A.M., Torgerson D.D., Golub L., Bookbinder J.A., Caldwell D., Cheimets P.N., Davis W.N., Deluca E.E., McMullen R.A., Warren H.P., Amato D., Fisher R., Maldonado H., Parkinson C. "The transition region and coronal explorer" Solar Physics, **187**/2, pp. 229-260, 1999

[236] Lin R.P., Dennis B.R., Hurford G.J., Smith D.M., Zehnder A., Harvey P.R., Curtis D.W., Pankow D., Turin P., Bester M., A. Csillaghy, Lewis M., Madden N., Van Beek H.F., Appleby M., Raudorf T., McTiernan J., Ramaty R., Schmahl E., Schwartz R., Krucker S., Abiad R., Quinn T., Berg P., Hashii M., Sterling R., Jackson R., Pratt R., Campbell R.D., Malone D., Landis D., Barrington-Leigh C.P., Slassi-Sennou S., Cork C., Clark D., Amato D., Orwig L., Boyle R., Banks I.S., Shirey K., Tolbert A.K., Zarro D., Snow F., Thomsen K., Henneck R., Mchedlishvili A., Ming P., Fivian M., Jordan J., Wanner R., Crubb J., Preble J., Matranga M., Benz A., Hudson H., Canfield R.C., Holman G.D., Crannell C., Kosugi T., Emslie A.G., Vilmer N., Brown J.C., Johns-Krull C., Aschwanden M., Metcalf T., Conway A. "The Reuven Ramaty High-Energy Solar Spectroscopic Imager (RHESSI)" Solar Physics, **210**, pp. 3-32, 2002

[237] Jain R., Dave H., Kumar S., Deshpande M.R. "Results of one year of observations of solar flares made by 'Solar X-ray Spectrometer (SOXS)' mission" 35th COSPAR Scientific Assembly, p. 744, 2004

[238] Johnson W.C., Parsons J.B., Crew M.C. "Nitrogen compounds of Gallium" J. Phys. Chem. **36**, p. 2561, 1932

[239] Maruska H.P., Tietjen J.J. "The preparation and properties of vapor-deposited single-crystalline GaN" Appl. Phys. Lett. **15**, p. 327, 1969

[240] Pankove J.I., Berkeyheiser J.E. "Properties of Zn-doped GaN II. Photoconductivity" J. Appl. Phys. **47**, p. 3892, 1974

[241] Steigerwald D., Rudaz S., Liu H., Kern R.S., Götz W., Fletcher R. "III-V Nitride Semiconductors for high-performance Blue and Green Light-Emitting Devices" JOM, **49**/9, p. 18, 1997

[242] Ott H. "Das Gitter des Aluminiumnitrids" Zeitschrift für Physik A, **22**/1, pp. 201-214, 1924

[243] Yim W.M., Stofko E.J., Zanzucchi P.J., Pankove J.I., Ettenburg M., Gilbert S.L. "Epitaxially grown AlN and its optical band gap" J. Appl. Phys. **44**, p. 292, 1973

[244] Lyutaya M.D., Bartnitskaya T.S. "Thermal stability of complex nitrides of elements of subgroup IIIB" Inorg. Mater., **9**, p. 1052, 1973

[245] Strite S., Morkoç H. "GaN, AlN, and InN: A review" J. Vac. Sci. Technol. B, **10**/4, p. 1237, 1992

[246] Amano H., Sawaki N., Akasaki I., Toyoda T. "Metalorganic vapor phase epitaxial growth of a high quality GaN film using an AlN buffer layer" Appl. Phys. Lett., **48**, p. 353, 1986

[247] Amano H., Kito M., Hiramatsu K., Akasaki I. "P-type conduction in Mg-doped GaN treated with low-energy electron beeam irradiation (LEEBI)" Jpn. J. Appl. Phys., **28**, pp. L2112-L2114, 1989

[248] Nakamura S. "GaN growth using GaN buffer layer" Jpn. J. Appl. Phys., **30**, pp. L1705-L1707, 1991

[249] Akasaki I., Amano H. "Conductivity control of AlGaN, fabrication of AlGaN/GaN multi-heterostructure and their application to UV/blue light emitting devices" Mater. Res. Soc. Symp. Proc. **242**, p. 383, 1992

[250] Akasaki I., Amano H. "Room temperature ultraviolet/blue light emitting devices based on AlGaN/GaN multi-layered structure" Ext. Abstr. of the 1992 Int. Conf. Solid State Devices and Materials, pp. 327-329, 1992

[251] Khan M.A., Kuznia J.N., Olson D.T., Van Hove J.M., Blasingame M., Reitz L.F. "High-responsivity photoconductive ultraviolet sensors based on insulating single-crystal GaN epilayers" Appl. Phys. Lett., **60**/23, pp. 2917-2919, 1992

[252] Khan M.A., Kuznia J.N., Olson D.T., Blasingame M., Bhattarai A.R. "Schottky barrier photodetector based on Mg-doped p-type GaN films" Appl. Phys. Lett. **63**/18, p. 2455-2456, 1993

[253] Lim B.W., Chen Q.C., Yang J.Y., Khan M.A. "High responsivity intrinsic photoconductors based on $Al_xGa_{1-x}N$" Appl. Phys Lett., **68**, pp. 3761-3762, 1996

[254] Walker D., Zhang X., Saxler A., Kung P., Xu M., Razeghi M. "$Al_xGa_{1-x}N$ ($0 \leq x \leq 1$) ultraviolet photodetectors grown on sapphire by metal-organic chemical-vapor deposition" Appl. Phys. Lett., **70**, pp. 949-951, 1997

[255] Osinsky A., Gangopadhyay S., Lim B.W., Anwar M.Z., Khan M.A., Kuksenkov D., Tempkin H. "Schottky barrier photodetectors based on AlGaN" Appl. Phys. Lett., **72**, pp. 742-744, 1998

[256] Monroy E., Calle F., Muñoz E., Omnes F., Beaumont B., Gibart P., Muñoz J.A., Cusso F. "Ultraviolet Photodetectors based on $Al_xGa_{1-x}N$ Schottky Barriers" MRS Internet J. Nitride Semicond. Res., **3**, p. 9, 1998